



TECHNISCHE
UNIVERSITÄT
DARMSTADT

Synthesis and Characterization of Tailored Gold-based Nanowire Networks for Energy Applications

Vom Fachbereich Material- und Geowissenschaften der Technischen Universität Darmstadt

Zur Erlangung des Grades eines Doktors der Naturwissenschaften (Dr. rer. nat.)

Genehmigte Dissertation von M.Sc. Mohan Li

Darmstadt 2025

1. Gutachten: Prof. Dr. Maria Eugenia Toimil-Molares


2. Gutachten: Prof. Dr. Jan Philipp Hofmann



GSI



MAT



Synthesis and Characterization of Tailored Gold-based Nanowire Networks for Energy Applications

Accepted doctoral thesis by Mohan Li

Date of submission: 02.06.2025

Date of thesis defense: 23.07.2025

Darmstadt, Technische Universität Darmstadt

Jahr der Veröffentlichung auf TUpriints: 2025

Dieses Dokument wird bereitgestellt von tuprints,
E-Publishing-Service der TU Darmstadt

<http://tuprints.ulb.tu-darmstadt.de>

tuprints@ulb.tu-darmstadt.de

Die Veröffentlichung steht unter folgender Creative Commons Lizenz:

Namensnennung 4.0 International

<https://creativecommons.org/licenses/by/4.0/>

This work is licensed under a Creative Commons License:

Attribution 4.0 International

<https://creativecommons.org/licenses/by/4.0/>

Erklärungen laut Promotionsordnung

§ 8 Abs. 1 lit. c PromO

Ich versichere hiermit, dass die elektronische Version meiner Dissertation mit der schriftlichen Version übereinstimmt.

§ 8 Abs. 1 lit. d PromO

Ich versichere hiermit, dass zu einem vorherigen Zeitpunkt noch keine Promotion versucht wurde. In diesem Fall sind nähere Angaben über Zeitpunkt, Hochschule, Dissertationsthema und Ergebnis dieses Versuchs mitzuteilen.

§ 9 Abs. 1 PromO

Ich versichere hiermit, dass die vorliegende Dissertation selbstständig und nur unter Verwendung der angegebenen Quellen verfasst wurde.


§ 9 Abs. 2 PromO

Die Arbeit hat bisher noch nicht zu Prüfungszwecken gedient.

Darmstadt

Mohan Li





雄关漫道真如铁，而今迈步从头越

Life is going to be different from now on...
but the future looks bright!

Abstract

This thesis presents the synthesis and characterization of three types of three-dimensional (3D) free-standing nanostructure assemblies, pure gold (Au), gold-silver ($\text{Au}_{1-x}\text{Ag}_x$, $0 < x < 1$) alloys, and hierarchical nanoporous gold nanowire networks (NWNWs).

The NWNWs are produced by electrodeposition in ion-track etched templates. First, polycarbonate foils are irradiated from four directions with GeV Au ions at the UNILAC accelerator of GSI, creating interconnected ion tracks. Subsequent chemical etching results in membranes with interconnected nanochannels with tunable density number and diameter. Au and $\text{Au}_{1-x}\text{Ag}_x$ alloys are then electrodeposited in the channels. We investigated how nanowire growth rate and atomic composition are influenced by electrolyte compositions and applied potentials. The hierarchical nanoporous NWNWs are created by additional selective dealloying of the Au-Ag alloy NWNWs with Ag content higher than 55 at%. By adjusting NWNW composition and dealloying time, nanoporous NWNWs with tunable ligament and pore sizes are created.


We systematically studied the morphology, composition, crystallinity, and porosity of these three systems, as a function of various synthesis parameters, employing scanning electron microscopy (SEM), energy dispersive x-ray spectroscopy (EDX), transmission electron microscopy (TEM), and x-ray photoelectron spectroscopy (XPS) techniques. The obtained results demonstrate precise and mostly independent control over nanowire diameter (40-200 nm), composition (10-90 at% Ag), porosity (10-98%), and hierarchy.

The synthesized NWNWs exhibit high surface areas and excellent transport properties, making them strong candidates for electrocatalysis. At the same time, their structural and compositional tunability make them ideal model systems to study structure-function relationships in porous materials. We determine their electrochemically active surface area (ECSA), catalytic performance, and cyclic stability during methanol electro-oxidation reaction.

Pure Au NWNWs exhibit around 100 times higher ECSA than the corresponding flat Au film electrode, the measured ECSA values are in good agreement with the theoretically calculated geometrical surface areas. The catalytic reaction of the Au NWNWs towards the methanol oxidation exhibits 5 times higher ECSA-normalized current density than the flat Au film. The $\text{Au}_{1-x}\text{Ag}_x$ NWNWs exhibit composition-dependent catalytic behavior, different from pure Au or pure Ag. For $x < 0.2$, both the methanol oxidation peak potential and current density decrease compared to the pure Au NWNW of identical geometry. Ag-rich NWNWs ($x > 0.5$) and pure Ag NWNWs are inactive.

Hierarchical nanoporous NWNWs obtained by dealloying of $\text{Au}_{1-x}\text{Ag}_x$ ($x > 0.6$) NWNWs retain residual Ag in the nanowires as well as Ag-rich surface shells. Notably, their electro-catalytic performance resembles that of $\text{Au}_{1-x}\text{Ag}_x$ NWNWs with comparable composition. Due to their significantly higher ECSAs, and reduced mass, these nanoporous Au NWNWs outperform pure Au NWNWs in terms of current density normalized by projection flat area.

Surface wettability critically influences nanostructured catalysis by modulating the adsorption and desorption of reactants and products at the catalyst interface, thereby affecting catalytic activity and selectivity. We explore the wettability of the Au NWNWs as a function of porosity using sessile drop measurements. As porosity increases from 20% to 98%, the NWNWs transit from hydrophilic to hydrophobic. Structures with 60% to 80% porosity display super-hydrophilic behavior, while $>90\%$ porous networks exhibit the rose-petal effect, where water droplets are adhered to the surface.



The 3D free-standing structure offers a stable reaction environment, excellent conductivity, and a high specific surface area. The atomic composition can be precisely tailored for specific catalytic reactions. By adjusting the wettability, they can be tailored in the future for reactions involving either liquid or gas-phase reactants. The developed 3D NWNWs exhibit a high degree of structural and compositional tunability, which enables precise control over their physical and chemical properties. This versatility makes them excellent model platforms for systematically investigating the complex interdependencies between structure and function in nanoporous systems. By adjusting various parameters, we can gain deeper insights into how specific structural features influence performance, transport phenomena, and other functional behaviors in nanomaterials.

Zusammenfassung

In dieser Arbeit werden die Synthese und Charakterisierung dreier Typen von dreidimensionalen (3D), freistehenden Nanostruktur-Assemblies vorgestellt: reines Gold (Au), Gold-Silber-Legierungen ($\text{Au}_{1-x}\text{Ag}_x$, $0 < x < 1$) sowie hierarchische nanoporöse Gold-Nanodrahtnetzwerke (NWNWs).

Die Herstellung der NWNWs erfolgt durch Elektroabscheidung in ionenspurgeätzten Templates. Zunächst werden Polycarbonatfolien am UNILAC-Beschleuniger der GSI mit GeV-Au-Ionen aus vier Richtungen bestrahlt, wodurch ein Netzwerk miteinander verbundener Ionenspuren entsteht. Durch anschließendes chemisches Ätzen entstehen Membranen mit vernetzten Nano-Kanälen variabler Dichte und einstellbarem Durchmesser. In diese Kanäle werden anschließend Au und $\text{Au}_{1-x}\text{Ag}_x$ Legierungen elektrochemisch abgeschieden. Es wurde untersucht, wie Wachstumsgeschwindigkeit und atomare Zusammensetzung der Nanodrähte von Elektrolytzusammensetzungen und angelegten Potentialen beeinflusst werden. Die hierarchisch nanoporösen NWNWs entstehen durch selektives Entlegieren der Au-Ag-Nanodrahtnetzwerke mit einem Silbergehalt von mehr als 55 at%. Durch Variation der Zusammensetzung und der Entlegierungszeit lassen sich nanoporöse NWNWs mit gezielt einstellbaren Ligament- und Porengrößen herstellen.


Die Morphologie, Zusammensetzung, Kristallinität und Porosität dieser drei Systeme wurden in Abhängigkeit von den Syntheseparametern systematisch untersucht. Hierfür kamen Rasterelektronenmikroskopie (REM/SEM), energiedispersive Röntgenspektroskopie (EDX), Transmissionselektronenmikroskopie (TEM) und Röntgenphotoelektronenspektroskopie (XPS) zum Einsatz. Die Ergebnisse zeigen eine präzise und weitgehend unabhängige Kontrolle über den Nanodrahtdurchmesser (40–200 nm), die Zusammensetzung (10–90 at% Ag), die Porosität (10–98 %) sowie die hierarchische Struktur.

Die synthetisierten NWNWs weisen eine große spezifische Oberfläche und exzellente Transporteigenschaften auf, wodurch sie vielversprechende Kandidaten für die Elektrokatalyse darstellen. Ihre strukturelle und chemische Einstellbarkeit macht sie zudem zu idealen Modellsystemen zur Untersuchung von Struktur-Funktions-Beziehungen in porösen Materialien. Bestimmt wurden die elektrochemisch aktive Oberfläche (ECSA), die katalytische Leistung sowie die zyklische Stabilität während der Methanol-Elektrooxidation.

Reine Au-NWNWs zeigen eine etwa 100-fach höhere ECSA im Vergleich zu flachen Au-Film-Elektroden; die experimentell ermittelten Werte stimmen dabei gut mit den theoretisch berechneten geometrischen Oberflächen überein. Die katalytische Aktivität der Au-NWNWs gegenüber der Methanoloxidation ist fünfmal höher (ECSA-normalisierte Stromdichte) als die einer flachen Au-Film-Elektrode. Die $\text{Au}_{1-x}\text{Ag}_x$ NWNWs zeigen ein zusammensetzungsabhängiges katalytisches Verhalten, das sich von reinem Au oder reinem Ag unterscheidet. Für $x < 0,2$ nehmen sowohl das Oxidations-Peakpotential als auch die Stromdichte im Vergleich zu Au-NWNWs identischer Geometrie ab. Silberreiche NWNWs ($x > 0,5$) sowie reine Ag-NWNWs sind hingegen katalytisch inaktiv.

Hierarchische nanoporöse NWNWs, die durch Entlegierung von $\text{Au}_{1-x}\text{Ag}_x$ ($x > 0,6$) NWNWs erzeugt werden, enthalten Rest-Silber im Draht sowie silberreiche Oberflächenschichten. Auffällig ist, dass ihre elektro-katalytische Leistung der von $\text{Au}_{1-x}\text{Ag}_x$ NWNWs mit vergleichbarer Zusammensetzung ähnelt. Aufgrund ihrer deutlich höheren ECSA und reduzierten Masse übertreffen diese nanoporösen Au-NWNWs jedoch reine Au-NWNWs in Bezug auf die flächen-normalisierte Stromdichte.

Die Oberflächenbenetzbarkeit beeinflusst die nanostrukturierte Katalyse entscheidend, da sie die Adsorption und Desorption von Reaktanten und Produkten an der Katalysatoroberfläche steuert und somit die katalytische Aktivität und Selektivität bestimmt. Mittels Sessile-Drop-Messungen wurde die



Benetzbarkeit der Au-NWNWs in Abhängigkeit von der Porosität untersucht. Mit steigender Porosität (20–98 %) ändert sich das Verhalten von hydrophil zu hydrophob. Strukturen mit 60–80 % Porosität zeigen superhydrophiles Verhalten, während hochporöse Netzwerke (>90 %) den „Rose-Petal-Effekt“ aufweisen, bei dem Wassertröpfchen an der Oberfläche haften bleiben.

Die 3D-freistehende Struktur bietet eine stabile Reaktionsumgebung, hervorragende Leitfähigkeit und eine hohe spezifische Oberfläche. Die atomare Zusammensetzung kann gezielt auf bestimmte katalytische Reaktionen abgestimmt werden. Durch Anpassung der Benetzbarkeit können die Strukturen zukünftig für Reaktionen mit flüssigen oder gasförmigen Reaktanten maßgeschneidert werden. Die entwickelten 3D-NWNWs weisen insgesamt eine hohe strukturelle und kompositionelle Variabilität auf, die eine präzise Kontrolle ihrer physikalischen und chemischen Eigenschaften erlaubt. Diese Vielseitigkeit macht sie zu exzellenten Modellplattformen, um die komplexen Wechselwirkungen zwischen Struktur und Funktion in nanoporösen Systemen systematisch zu untersuchen. Durch Variation relevanter Parameter lassen sich tiefere Einblicke gewinnen, wie spezifische strukturelle Merkmale die Leistungsfähigkeit, Transportphänomene und weitere funktionale Eigenschaften von Nanomaterialien beeinflussen.

Content

ABSTRACT	I
ZUSAMMENFASSUNG.....	III
CONTENT	V
1. INTRODUCTION	1
1.1 Background	1
1.2 This Work.....	2
2. EXPERIMENTAL METHODS	5
2.1 Fabrication of Etched Ion-Track Membranes.....	5
2.1.1 Irradiation of polymer foils with swift heavy ions	5
2.1.2 UV exposure of irradiated foils	6
2.1.3 Chemical etching of ion tracks	6
2.2 Fabrication of Various Nanowire Networks	8
2.2.1 Sputtering of a thin Au layer	8
2.2.2 Electrodeposition process	8
2.2.3 Electrodeposition of back-electrode layer	9
2.2.4 Electrodeposition of nanowire networks	10
Au NWNW	10
Ag NWNW	12
Au _{1-x} Ag _x alloy NWNW	12
2.2.5 Template removal	13
2.2.6 Dealloying process to fabricate nanoporous Au NWNWs	13
2.3 Characterization Methods	16
2.3.1 High-resolution scanning electron microscopy (HRSEM)	16
2.3.2 Energy dispersive X-ray spectroscopy (EDX)	17
2.3.3 High-resolution transmission electron microscopy (HRTEM)	18
2.3.4 X-ray photoelectron spectroscopy (XPS)	19
2.3.5 Electrochemical measurements	19
2.3.6 Electrochemically active surface area (ECSA) measurement methods	20
Double-layer capacitance measurement	21
Integration of the AuO reduction reaction peak.....	23

2.3.7	Methanol electro-oxidation reaction	24
2.3.8	Contact angle measurements	25
3.	MORPHOLOGICAL AND STRUCTURAL CHARACTERIZATION OF NWNWS	29
3.1	Au Nanowire Networks	29
3.1.1	Homogeneity, morphology, and crystallinity as a function of applied potential	29
3.1.2	Au NWNWs with various wire diameters	32
3.2	Au_{1-x}Ag_x Alloy Nanowire Networks	34
3.2.1	CV for determination of the deposition potential	34
3.2.2	Nanowire composition as a function of the electrodeposition conditions	35
3.2.3	Composition analysis	37
3.3	Nanoporous Au Nanowire Networks	42
3.3.1	Experimental analysis of Au _{1-x} Ag _x alloy nanowire dealloying process	42
	Influence of nanowire composition	42
	Influence of nanowire size	44
3.3.2	XPS analysis of porous Au NWNW after dealloying	47
3.3.3	TEM analysis of porous Au nanowires after dealloying	50
3.3.4	Summary	51
4.	ELECTROCHEMICAL PROPERTIES OF VARIOUS NWNWS	53
4.1	Electrochemically Active Surface Area Measurement	53
4.1.1	Au NWNW	53
4.1.2	Au _{1-x} Ag _x NWNWs	55
4.1.3	Nanoporous NWNW	59
4.1.4	Determination of the DLC reference value	61
	Planar Au film	61
	NWNWs	63
4.2	Methanol Electro-Oxidation	68
4.2.1	Au NWNWs	68
	Influence of electrolyte and reactant concentration	68
	Influence of NWNW geometry	71
	Morphology analysis after catalytic reactions	72
4.2.2	Au _{1-x} Ag _x alloy NWNWs	73
	Influence of atomic composition	74

Influence of electrolyte and reactant concentration	77
Morphology analysis after catalytic reactions	79
4.2.3 Nanoporous Au NWNWs	81
Long-term CV measurements	83
4.3 Summary	86
5. AU NWNW SURFACE WETTING STATE	87
5.1 Au NWNWs Fabrication with Varied Porosity	87
5.2 Contact Angle Measurement	89
5.3 Droplet Sliding Measurement	95
6. CONCLUSION AND OUTLOOK	97
7. BIBLIOGRAPHY	101
LIST OF FIGURES	116
LIST OF TABLES	122
ABBREVIATIONS	123
ACKNOWLEDGEMENTS	125
CURRICULUM VITAE	127
LIST OF PUBLICATIONS	129
ACADEMIC CONFERENCES CONTRIBUTIONS	130



1. Introduction

1.1 Background

The rapid pace of technological advancements has created an increasing demand for innovative materials that can meet the challenges of modern applications. This has significantly driven the field of materials science, leading to the exploration and development of new materials with superior properties. As devices become smaller, faster, and more efficient, the materials used in their construction must also evolve to meet these new challenges. This has led to a surge of interest in nanomaterials, which have been heavily developed over the past 20 years^{1,2}.

Nanomaterials, defined by at least one dimension smaller than 100 nanometers, exhibit unique properties that differ significantly from bulk materials^{3,4}. The drastic increase in surface-to-volume ratio at the nanoscale enhances their reactivity and catalytic properties, making them particularly effective in catalytic applications.^{5,6} Additionally, quantum confinement effects can significantly alter their electrical, optical, and thermal characteristics, broadening their utility across various fields^{7,8}. In catalysis, nanomaterials offer increased active sites due to their high surface area, leading to improved catalytic efficiency and selectivity. Their tunable size, shape, and composition further allow the customization of catalysts for specific reactions, advancing applications in energy conversion, environmental protection, and beyond.

Among these nanostructures, nanowires stand out due to their one-dimensional geometry and high length-to-width aspect ratios, which provide unique advantages in technological applications⁹. This geometry provides a large surface area-to-volume ratio, enhancing their sensitivity in applications such as biosensing and chemical detection. For instance, silicon nanowire-based field-effect transistors have demonstrated superior performance in detecting biomolecules, owing to their efficient charge transport and surface functionalization capabilities¹⁰. In electronics, nanowires facilitate the development of nanoscale devices with improved electrical properties, enabling advancements in transistors and interconnects¹¹. Additionally, their unique optical properties make them suitable for photonic applications, including light-emitting diodes and photodetectors¹². In energy conversion and storage, nanowires enhance the efficiency of photovoltaic cells, boost lithium-ion battery performance, and catalyze reactions in fuel cells. Their high surface area combined with direct electron transport pathways makes them ideal for electrochemical applications, where surface interaction processes are crucial¹³⁻¹⁷. Overall, the structural and functional attributes of nanowires position them as superior candidates over nanoparticles for various technological applications.

The growing interest in nanowires and other nanomaterials has driven the development of various synthesis techniques. The vapor-liquid-solid method employs a metal catalyst to facilitate NW growth from vapor-phase precursors, allowing precise control over size and crystallinity; however, it requires high temperatures and may introduce catalyst contamination¹⁸. Chemical vapor deposition enables the formation of uniform nanowires by decomposing gaseous precursors on a heated substrate, but it involves hazardous gases and demands precise control of reaction conditions¹⁹. Solvothermal and hydrothermal methods involve chemical reactions under high temperature and pressure, enabling the formation of nanowires from diverse materials. These techniques often require extended reaction times and may offer limited control over nanowire orientation²⁰. Template-assisted synthesis employs porous materials like anodic aluminum oxide to guide nanowire growth, allowing precise control over dimensions. However, removing the anodic aluminum oxide template without damaging the nanowires can be difficult, potentially affecting their structural stability²¹. In contrast, ion-track etched polymer

templates are easy to remove, without damaging the nanowires^{22,23}. Template-assisted electrodeposition method stands out as a low-cost, scalable, and ambient-condition process that deposits nanowires onto conductive substrates^{24,25}, allowing precise control over NW length by adjusting deposition time^{22,26}, as demonstrated in studies where the length of nickel nanowires increased proportionally with longer deposition durations, reaching up to 20 μm after 60 minutes²⁷. Electrodeposition is compatible with a wide range of materials, including metals, semiconductors, and alloys, making it suitable for various applications^{26,28-31}.

In comparison with 1D nanowires, three-dimensional (3D) nanowire network (NWNW) assemblies offer enhanced performance in various applications. The interconnected 3D structures provide increased surface area and porosity, improving light absorption and charge transport, which is beneficial in electrochemical and photoelectrochemical applications. For instance, CuO branched nanowires have demonstrated approximately 2.6 times higher photocurrent density in photoelectrochemical water splitting compared to conventional CuO nanowires, due to their larger surface area and improved light absorption³². Additionally, the mechanical stability and electrical reliability of 3D nanowire networks make them suitable for energy storage devices, such as batteries and supercapacitors, where efficient ion diffusion and electron transport are crucial. A study on 3D carbon nitride nanowire scaffolds combined with conducting polymers reported a specific capacitance of 202 Fg^{-1} and maintained 83.5% of initial capacitance after 5000 cycles, highlighting their potential in flexible supercapacitors³³. The ability to tailor geometrical parameters independently in 3D nanostructure assemblies allows for optimization of device performance, surpassing the capabilities of isolated 1D nanowires³⁴⁻³⁶.

Electrochemical and energy conversion devices increasingly rely on 3D nanostructures with engineered surface wettability to optimize performance under diverse operating conditions. Controlled wettability at the nanoscale is essential for regulating mass transport, enhancing interfacial reactions, and improving stability in systems such as fuel cells, batteries, and solar energy devices. In nanostructured catalysts, for instance, surface wettability governs the adsorption and desorption of reactants and products, directly affecting catalytic activity and selectivity. Li et al. demonstrated that increasing hydrophobicity in covalent organic frameworks enhanced Pd-catalyzed hydrogenation of nitroarenes by facilitating interactions with hydrophobic reactants³⁷. In electrocatalysis, Wang et al. showed that tuning wettability on Pd@zeolite surfaces shifted product selectivity in furfural hydrogenation³⁸. Moreover, in real-world environments, solar cell efficiency often declines due to dust accumulation, which blocks sunlight. Superhydrophobic surfaces, with their self-cleaning properties, can mitigate this issue by preventing particle adhesion³⁹. These examples underscore the importance of designing wettability-controlled nanostructures to improve efficiency, selectivity, and adaptability in advanced energy technologies.

1.2 This Work

This work focuses on the synthesis and study of Au-based nanowire networks (NWNWs), including pure Au nanowires, Au-Ag alloyed nanowires, and dealloyed porous nanowires. By combining ion-track nanotechnology, electrodeposition, and dealloying, we create nanostructured tailored porous films with controlled geometry, atomic composition, and morphology. The aim of this work is to explore reproducible, reliable, and stable synthesis methods for various Au-based 3D NWNWs. The networks are characterized with various techniques. Achieving excellent structural and compositional tunability allows us to apply them as porous model systems to study their electrochemical performance as a function of their structural and compositional parameters.

Gold is a precious noble metal, the origin of gold in the universe has been a subject of extensive research, and current scientific consensus supports the idea that gold was formed through cataclysmic astrophysical events, specifically the collision of supernovas and neutron stars, then deposited on earth by meteorites⁴⁰. Gold has been used by humans for over 4,500 years, with ancient Egyptians utilizing it

to create jewelry, statues, and even dental bridges⁴¹. In modern times, gold's applications have expanded significantly into more technical fields, including use in computers, cellphones, and the aerospace industry⁴². Since the beginning of the 21st century, advancements in technology have further pushed the boundaries, leading to the development of micro- and nanostructured gold for specialized applications. Gold nanoparticles are of interest for biomedical applications, where they can be utilized in drug-delivery, radiotherapy, and biomolecular detections^{43,44}. For innovative energy devices, gold is also of huge interest, nanostructured gold has proven promising for energy storage and conversion applications, such as supercapacitor, battery, and water-splitting.⁴⁵⁻⁴⁸ Au nanostructured and porous materials exhibiting high surface areas and excellent transport properties are also strong candidates for electrocatalysis^{6,49-51}.

This thesis is structured in 6 chapters. After this introduction, chapter 2 presents all the experimental and characterization methods applied in this work, as well as relevant employed parameters. This includes the synthesis process of the Au and Au_{1-x}Ag_x NWNWS by electrodeposition in ion-track etched templates, their structural and compositional characterization, as well as the electrochemical techniques applied for the determination of the electrochemically active surface area (ECSA) and the catalytic performance for the methanol electro-oxidation reaction⁵².

Chapter 3 presents the results obtained on the synthesis of NWNWs. We discuss how the electrodeposition conditions are investigated and optimized. We demonstrate that sample morphology, crystallinity, and atomic composition can be controlled through the electrodeposition process, by tuning different parameters such as electrolyte composition, temperature, and electrodeposition potential.

In this chapter, we also discuss the synthesis parameters and characterization of hierarchical nanoporous NWNWs. Hierarchical nanostructures are able to integrate multi-level of porosities, provide even higher specific surface area availability for catalysis reactions, tailored pore size can increase the selectivity towards desired reactions or products⁵³⁻⁵⁵. In this work, we specifically investigate the synthesis and characterization of hierarchical nanoporous NWNWs produced by dealloying the Au_{1-x}Ag_x NWNWs. Dealloying involves selectively removing a chemical element from a solid solution, resulting in a nanoporous crystal. Various mechanisms, such as evaporation and dissolution, drive this process. Despite diverse experimental protocols, the atomic-scale processes driving nanostructure formation are similar, relying on a competition between dissolution and passivation. The special structure of nanoporous gold (NPG) made by dealloying, can uniquely provide catalytically active sites at the atomic scale and a robust scaffold structure at nanoscale⁵⁶. The mechanical behavior has also been extensively studied for stability and sensitivity to heterogeneity^{57,58}, with good uniformity and reproducibility. In this chapter, we present how by dealloying, the Ag atoms in the Au_{1-x}Ag_x NWNWs can be selectively removed, resulting in a network consisting of porous nanowires, this allows us to create a special hierarchical nanostructure with controlled size and porosity. Nanoporous nanowires have a different morphology than cylindrical solid nanowires, they usually possess various size of pores on the nanowire surface and in the core, ranging from a few nm to hundreds of nm. Some wires even show a hollow structure with a tunnel-shaped pore. The goal is to find an optimized set of parameters, that can produce a stable nanoporous NWNW with suitable pore size, and increased surface area. Therefore, various of parameters were investigated, including pristine NWNW geometry, composition, and dealloying time.

Chapter 4 discusses the electrochemical properties of the three types of NWNWs, including their electrochemically active surface area (ECSA), and their catalytic performance towards methanol electro-oxidation reaction. The NWNWs were characterized systematically as a function of geometry, composition, and dealloying time. The influence of electrolyte and reactant concentration on the catalytic performances was also investigated.

One important aspect investigated in this work is the influence of residual Ag in NPG catalysis systems, which is a still an open question in the field. From this perspective, we analyzed detailly the catalytic

performance of $\text{Au}_{1-x}\text{Ag}_x$ NWNWs as a function of the Ag content, then compared the results with the dealloyed nanoporous NWNWs. This comparison allows us to investigate solely the influence of composition, without the additional variation of porosity and surface area, which are always intertwined in traditional NPG thin films.

For catalysis, one property that is not discussed frequently is the wettability of the porous electrode, which is also an influencing factor that could potentially modulate reactants adsorption to the surface, or the catalytic selectivity.

Chapter 5 presents the investigation of NWNW surface wettability as a function of the structural porosity. The main method employed is the sessile drop contact-angle measurement, both static and dynamic, which allows a direct characterization of the surface wetting state. The static characterization shows the water droplet behavior on a horizontal sample surface, while the dynamic characterization involves tilting the sample to different angles to test the droplet adhesion to the sample surface. The results showed a porosity-dependent change, from hydrophilic to superhydrophilic, then change to hydrophobic, as the porosity increases from 20% to 98%⁵⁹.

In chapter 6, we summarize all the important results presented in this work, and provide an outlook to future work in the field of Au-based NWNW catalysis.

2. Experimental Methods

The chapter first introduces the experimental methods applied in this work for the fabrication of nanowire networks, including the different steps to fabricate etched ion-track membranes, and the synthesis processes optimized for the three types of NWNWs, namely pure Au, Au_{1-x}Ag_x, and nanoporous Au. Then, the various characterization techniques employed in this work will be described together with all the relevant experimental parameters required to reproduce the results.

2.1 Fabrication of Etched Ion-Track Membranes

In this work, Au, Ag, and Au_{1-x}Ag_x NWNWs are fabricated by electrodeposition in etched ion-track membranes. This is a template-assisted synthesis method commonly used to fabricate nanowires^{60,61}. It is a bottom-up approach, and the template defines the morphology and dimension of the nanowires, which is known for providing good control of the nanowire structure and dimension, being cost-effective, and applicable for a great variety of materials. Especially for the synthesis of nanowires, the most commonly used templates are polycarbonate (PC) tracked-etched membranes and anodized aluminum oxide (AAO) membranes. Early reports on the fabrication of nanostructures by electrodeposition in polycarbonate (PC) membranes were published by Penner and Martin⁶², and by GSI⁶³.

The steps involved in the fabrication of PC track-etched membranes are: (i) swift heavy-ion irradiation, (ii) UV exposure of the irradiated polymer foils, and (iii) selective chemical etching of the ion tracks. Below, we explain how the three steps are applied to produce polymer membranes with interconnected and well-controlled nanochannels.

2.1.1 Irradiation of polymer foils with swift heavy ions

In this work, 30 PC μm foils (Makrofol N, Bayer AG). were irradiated at the UNILAC linear accelerator of the GSI Helmholtz Centre for Heavy Ion Research in Darmstadt, with Au ions of specific energy up to 11.4 MeV per nucleon (MeV/u). At such high energies, ion beams have a penetration depth in polymers of about $140 \mu\text{m}^2$. On their way through the foil, each ion creates a highly localized nanometer range damaged region called the ion-track. The ion track core has a diameter of about 5-10 nm. In the case of polymers, along the ion penetration trajectory, the polymer chains are damaged by the high energy, and the Au ions will lose energy accordingly.

The interaction of energetic ions with matter is governed by two primary mechanisms: nuclear stopping and electronic stopping, each dominating at different ion energy regimes. At a lower ion energy regime (~ 100 keV), nuclear stopping is the predominant process. In this regime, ions lose energy primarily through elastic collisions with the nuclei of target atoms, resulting in the transfer of kinetic energy to these atoms and causing atomic displacements within the material^{64,65}. As the ion energy increases to the MeV–GeV range, electronic stopping becomes the dominant energy loss mechanism. In this high-energy regime, ions interact predominantly with the electrons of the target material, leading to excitation and ionization processes. The energy transferred to the electronic system can result in the formation of an electron cascade, which subsequently transfers energy to the lattice atoms, potentially causing localized heating and structural changes along the ion's trajectory^{66,67}. The energy losses in the electronic stopping regime are described by the Bethe-Bloch formula:

$$-\frac{dE}{dx} = \frac{e^4(\hbar c)^2}{4\pi\epsilon_0^2 mc^2} n_0 \frac{Z^2}{\beta^2} \left[\ln \left(\frac{2mc^2\beta^2}{(1-\beta^2)I} \right) - \beta^2 \right] \quad 2 - 1$$

where e is the electron charge, m is the electron mass, I is the ionization energy of the target atoms, n_0 is the electron density of the target material, Z is the charge state of accelerated ions, and β is the speed of the accelerated ions, relative to light speed⁶⁸.

The ion fluence (ions/cm²) can be adjusted during irradiation between 1 ion/sample up to $\sim 10^{10}$ ions/cm², the ion beam is adjusted before the irradiation process, to guarantee a homogeneous distribution of ions on the entire surface area. In particular, for the fabrication of membranes with interconnected nanochannels, each foil was irradiated four sequential times from four different directions, as shown in Figure 2.1. The template polymer foil was tilted by 45° to the incoming ion beam. After each irradiation step, the PC foil was rotated 90° around the central axis. After the rotation, the PC foil was ready for the next irradiation. This process will be repeated two more times, which added up to ion tracks in four directions and perpendicular to each other.

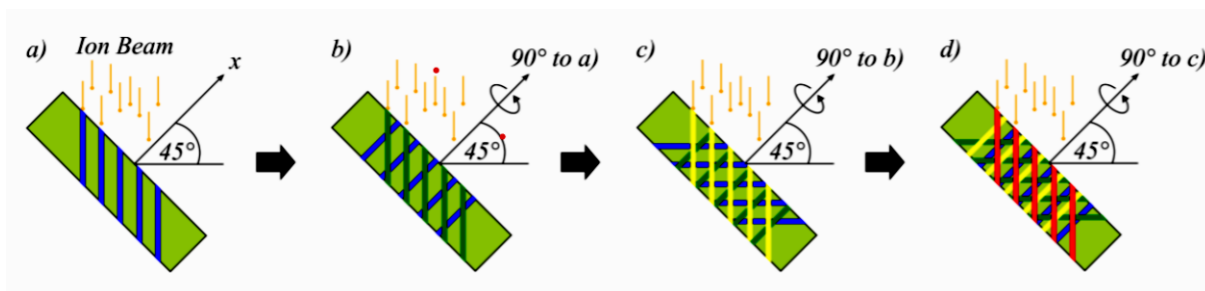


Figure 2.1 Four times irradiation of the PC membrane⁶¹.

In this work, polymer foils were irradiated with several ion fluences, namely $1 \cdot 10^9$ i/cm^2 , $5 \cdot 10^8$ i/cm^2 , and $1 \cdot 10^8$ i/cm^2 for each irradiation direction, leading to a total nominal fluence of $4 \times 1 \cdot 10^9$ i/cm^2 , $4 \times 5 \cdot 10^8$ i/cm^2 , and $4 \times 1 \cdot 10^8$ i/cm^2 for each foil. Due to the angle between the ion beam and the PC foil during the irradiation process, the actual ion track density in the PC foil is lower than the nominal applied ion beam fluence, namely $2.8 \cdot 10^9$ i/cm^2 , $1.4 \cdot 10^9$ i/cm^2 , and 2.8×10^8 i/cm^2 , respectively. The templates used in this work are referred to by the nominal ion beam fluence during irradiation, which has a deviation of around 20%. However, for the calculation of the NWNW surface area and porosity, the template fluence was characterized by SEM analysis of the etched pore numbers per nominal area, to guarantee a reliable theoretical value close to the experimental results.

2.1.2 UV exposure of irradiated foils

Prior to chemical etching, the irradiated foils are exposed to UV light to stabilize and increase the sensitivity of the ion tracks. This UV exposure results in a narrower diameter distribution of the nanochannels⁶⁹. In this work, the irradiated PC foils were exposed to UV light (T-30M Vilber Lourmat lamp, 30W, 312 nm) for one hour on each side.

2.1.3 Chemical etching of ion tracks

To transform an irradiated polymer foil into a porous template, the damaged material along the ion-tracks were selectively etched and enlarged to form pores of well-controlled dimensions. The pore shape and geometry are determined by two factors, the isotropic bulk etching rate (V_B) (dissolution rate of the unirradiated material in the solution), and the anisotropic track etching rate (V_T) (dissolution rate significantly enhanced by the damage produced by the ions). The etching selectivity is determined by the ratio of these two factors, the schematic drawing of the etching pore cross-section along with these two rates are shown in Figure 2.2. The half-angle of the etching pore is given by the function:

$$\sin \alpha = \frac{V_B}{V_T}$$

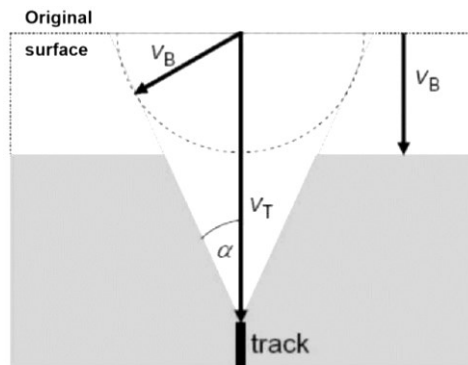


Figure 2.2 Schematic drawing of the pore etching cross-section view¹⁷.

When V_T is slightly higher than V_B ($V_T > V_B$), conical or bi-conical pores are generated, while for $V_T \gg V_B$ cylindrical pores are generated. The etching process for polymer ion tracks is typically performed in aqueous etching solutions. The choice of polymer material also affects the inner surface morphology of the pores. For instance, polycarbonate (PC) foils generally yield smoother pore walls, while polyethylene terephthalate (PET) foils often result in rougher internal surfaces. This difference is attributed to the distinct chemical structures and etching behaviors of these polymers⁷⁰.

Furthermore, the pore shape can be modulated by adjusting etching parameters such as temperature, etchant composition, and the addition of surfactants. For example, incorporating methanol into the alkaline etching solution or applying a transmembrane potential can influence the cone angle of conical nanopores. Additionally, surfactants can adsorb onto the polymer surface during etching, leading to the formation of unique pore geometries like spindle-shaped channels⁷¹⁻⁷⁴.

In this work, only interconnected cylindrical nanochannels were employed. During etching, the nanopore diameter increases proportionally to the etching time. PC foils were etched by immersion in a 6 M NaOH solution at 50 °C. Under these conditions, the etching rate is around 23 - 25 nm/min²². During the etching process, the solution was kept at 50 °C using a water-heated thermostat and was constantly stirred by a magnetic stirring bar. After etching, the templates were rinsed three times, and immersed in de-ionized (DI) water (Millipore Direct 8) for at least 20 min. Then dried with paper towels and stored in a sample box. We applied etching times between 1.6 and 8 min to produce nanochannels with diameters between 40 and 200 nm, respectively.

2.2 Fabrication of Various Nanowire Networks

The nanowire networks were electrodeposited into the interconnected pores of the etched ion-track membranes. The sequential experimental steps in this case are: (i) sputtering of a conductive Au layer on one side of the polymer membrane, (ii) electrodeposition of a thicker Au back-electrode for stability, and (iii) electrodeposition of the nanowires, which are described in the following sections.

2.2.1 Sputtering of a thin Au layer

To electrodeposit material in the ion track-etched pores, a conductive layer has to be prepared on one side of the membrane, which will act as a cathode during the electrodeposition process. The PC foils exhibit a rough side and a smooth side, which originates from the fabrication process. In this case, a thin layer of gold was sputtered on the rough side of the template to attain good adhesion between the PC template and the Au layer. A thin Au layer (thickness ~ 100 nm) was sputtered using an Edwards Sputter Coater S150B with 10^{-1} torr pressure, and with a sputtering current of 30 mA for 200 s. This layer is then reinforced with a thicker electrodeposited Au layer to completely close all the pores and provide a stable substrate for the nanowire network. Details on the preparation of the thicker layer are given in chapter 2.2.3.

2.2.2 Electrodeposition process

Electrodeposition is widely used for the synthesis of numerous materials including metals and alloys. It enables the engineering of surfaces, traditionally being used to fabricate e.g., anti-corrosive coatings or electrical conducting surfaces. Electrodeposition is also a commonly used method for the synthesis of nanostructured metals, alloys, and metal matrix composites. This method can be applied to synthesize multiple nanostructures, such as nanoparticles, nanowires, and thin films^{24,75-77}. There are three main electrodeposition modes, namely potentiostatic deposition, galvanostatic deposition, and pulse-plating deposition. During potentiostatic deposition, a constant potential is applied to the working electrode, while the current between working electrode and counter electrode is recorded as a function of time. During galvanostatic deposition, a constant current is applied, and the potential is recorded. Pulse plating refers to the process during which the deposition potential or deposition current are applied at a certain frequency for a certain amount of time repeatedly^{23,24,75,78}.

A schematic two-electrode electrodeposition cell is shown in Figure 2.3, It consists of two electrodes, an anode, and a cathode, the electrolytic bath, and a power source.

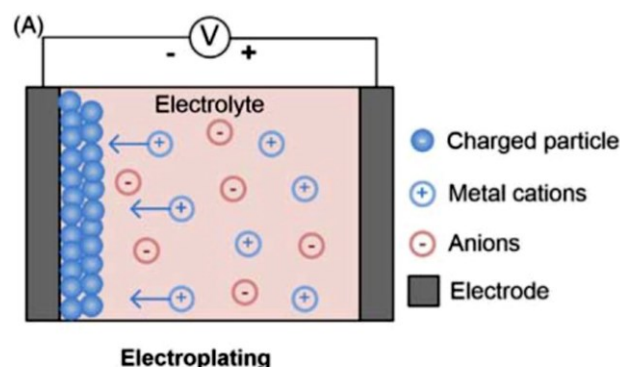


Figure 2.3 Schematic representation of the electroplating process⁷⁵.

The metal ions M^{n+} in the electrolyte can be driven by the potential difference between the two electrodes, and move towards the cathode by migration, diffusion, or convection⁷⁹. The metal ion will be reduced at the cathode surface and be deposited on the substrate, the reaction is represented by this equation:



The metal ions will consume electrons during the reduction reaction, and generate a cathodic current. Accordingly, an oxidation reaction will happen at the anode at the same time and generate an anodic current. If the system reaches the dynamic equilibrium condition, then the two currents will be equal, and the equilibrium potential can be described by the Nernst equation:

$$E_{eq} = E^0 + \frac{RT}{zF} \ln a \quad 2 - 4$$

where E^0 is the standard potential, R is the gas constant, T is the absolute temperature, z is the ion valence, F is the Faraday constant, and a is the metal ion activity. This ion activity a is related to ion concentration.⁷ For the two-electrode system, each electrode is a half-cell, when there is no external contribution, the two half-cells are at dynamic equilibrium. To polarize the interface, an external electrical field needs to be applied to the two electrodes, and a current flow is generated. Thus, an overpotential will be generated due to the two half-cells' potential shifts, this is described by the equation below,

$$\eta = E - E_{o.c.} \quad 2 - 5$$

where η represents the overpotential, E is the external electrical field potential, and $E_{o.c.}$ is the open circuit potential. For this research, a three-electrode setup was used, so the overpotential is measured against a third reference electrode. The overpotential is the main driving force, which generates the polarization of the electrode-electrolyte interface⁶⁸.

In this work, electrodeposition was applied to the reinforcement of Au back-electrode, as well as the growth of pure Au, pure Ag, and $Au_{1-x}Ag_x$ nanowires.

2.2.3 Electrodeposition of back-electrode layer

As mentioned in section 2.1.1, the thin Au layer sputtered on the rough side of the PC template was reinforced by a thicker and more stable Au layer which was produced by electrodeposition. This layer completely closed the pores on one side, which provided good electrical contact and a stable substrate for nanowire growth. The schematic of the employed two-electrode experimental setup is shown in Figure 2.4. A copper ring was in direct contact with the sputtered Au layer, which acted as the working electrode. A gold spiral rod was used as the counter electrode. The electrodeposition was conducted galvanostatically at room temperature, applying a constant current density of 2 mAcm^{-2} . The electrolyte used for back-electrode deposition is a commercial gold sulphite solution (AuSF, 15 g/L Au, METAKEM). The electrodeposition was conducted for 3000 s to deposit a back-electrode layer of thickness $\sim 2 \text{ }\mu\text{m}$, which was stable enough to support the NWNWs during the handling processes.

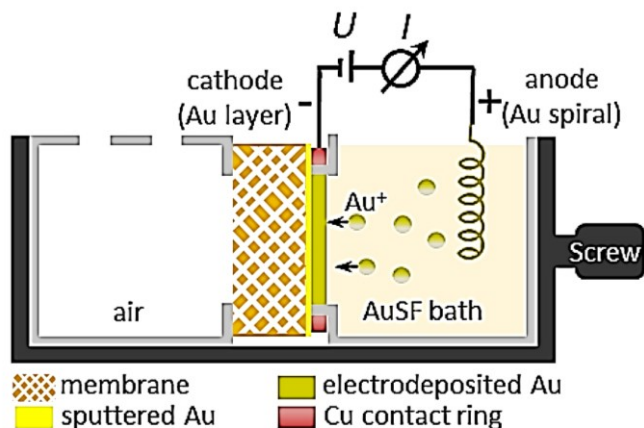


Figure 2.4 Schematic representation of a two-electrode setup for electrodeposition of a Au layer on the sputtered gold of the membrane⁶⁰.

2.2.4 Electrodeposition of nanowire networks

Figure 2.5 shows a schematic of the three-electrode electrochemical cell employed for the electrodeposition of the Au, Ag, and Au_{1-x}Ag_x NWNWs. A platinum (Pt) spiral wire acted as the counter electrode and an Ag/AgCl electrode as the reference electrode (Sensortechnik Meinsberg). The Au back-electrode acted as the working electrode and was contacted via a copper ring. A Gamry potentiostat 600+ was used to apply the voltage during the potentiostatic process. The experimental parameters (voltage, temperature, and electrolyte composition) were investigated and optimized for each of the three types of networks, details are given in the following sections.

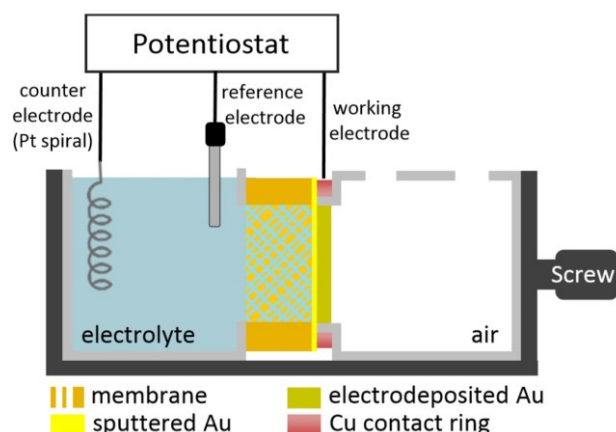
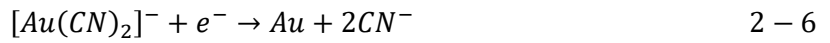


Figure 2.5 Schematic representation of a three-electrode setup consisting of working, counter, and reference electrodes, connected to a potentiostat⁶⁰.

Au NWNW

For the electrodeposition of pure Au NWNWs, the electrolyte consisted of 50 mM potassium dicyanoaurate (KAu(CN)₂, Carl Roth, ≥ 99.5%) and 250 mM sodium carbonate, (Na₂CO₃, Carl Roth, > 99.8%), with 1 vol% surfactant (2A1 Dowfax, Dow). The addition of surfactant resulted in a more

homogeneous nanowire network structure³¹. Na₂CO₃ was added to the electrolyte to maintain an alkaline pH value, which is about 12-13, to prevent the production of the toxic hydrogen cyanide. The Au ion exists as a complex [Au(CN)₂]⁻ in the electrolyte. The gold cyanide electrolyte is very stable at room temperature, the reduction reaction is:



After applying a certain potential, the Au (I) complex will react with one electron and be reduced at the working electrode. Au atoms will be reduced at the bottom of the nanochannels, on the sputtered conductive Au layer, and form nanowires. Before the electrodeposition begins, the electrolyte was filled inside the cell compartment, and the whole cell was heated to 60 °C for 1 hour, to ensure a homogeneous electrolyte temperature inside the pores, and that the pores are completely filled with electrolyte.

To select the deposition potential, cyclic voltammogram (CV) was recorded under the same experimental conditions as employed for nanowire depositions, a representative CV is shown in Figure 2.6, which exhibits a main reduction peak at about -1.1 V, shown as the red dash line, which is in agreement with the reduction potential reported by Alber¹⁷ for the electrodeposition in parallel nanochannels.

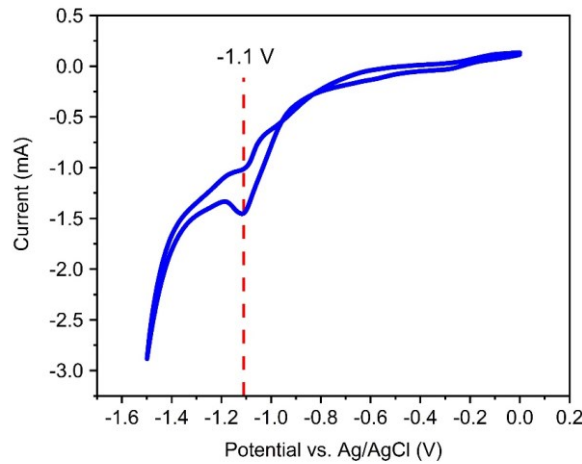


Figure 2.6 CV recorded using a PC template with nanochannel density $d=4 \times 1 \times 10^8 \text{ cm}^{-2}$, and pore diameter 150 nm with a Au back-electrode, in 50 mM KAu(CN)₂ electrolyte with 1% Doxfax 2A1, at temperature 60 °C.

The electrodepositions were performed potentiostatically, applying voltages between $U = -1.1 \text{ V}$ and $U = -0.8 \text{ V}$ vs. Ag/AgCl. The current was recorded during each electrodeposition as a function of time. The deposition time is different according to applied potential, and the actual deposition curve. The deposition process is separated into three stages (Figure 2.7), at first, atoms gradually fill inside the nanochannels and form the NWNW structure. Then after a certain amount of time, which is related to the deposition potential and electrolyte concentration, all the pores will be fulfilled. Once the pores are filled and material starts to be deposited outside the membrane, there is a rapid current increase shown on the $I-t$ curve (Figure 2.8). The depositions were terminated manually as soon as this current increase started, to attain NWNWs of 30 μm height. If the reaction is not stopped in time, caps are formed on top of the nanowires, as shown in Figure 2.7.



Figure 2.7 Schematic drawing of the deposition process of nanowire networks.⁸⁰

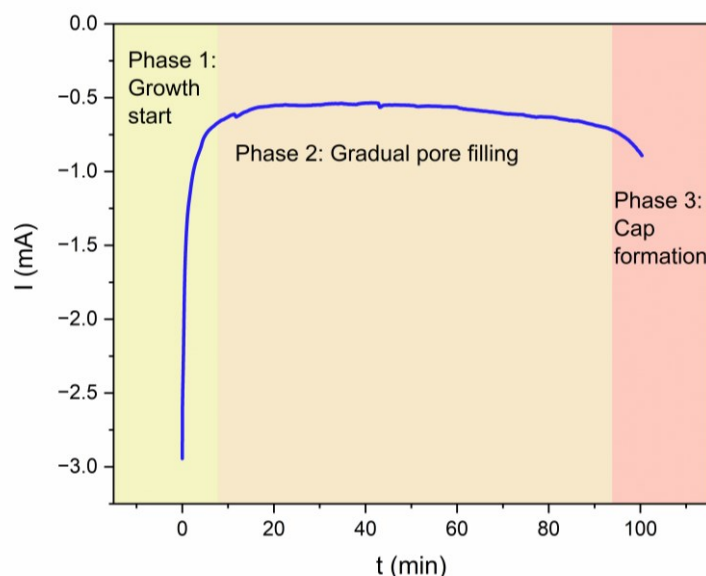
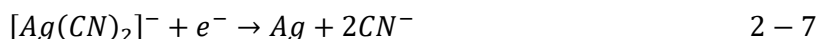


Figure 2.8 Representative I-t curve of NWNW deposition process.

Ag NWNW

Ag NWNW was also deposited potentiostatically, at 60 °C, using 50 mM potassium argentocyanide ($\text{KAg}(\text{CN})_2$, Carl Roth, $\geq 99.5\%$), with 250 mM sodium carbonate (Na_2CO_3 , Carl Roth, $> 99.8\%$) and 1 vol% surfactant (2A1 Dowfax, Dow). The $\text{Ag}(1)$ ion deposition mechanism is the same as Au, one Ag ion will consume one electron and deposit on the substrate, The electrodeposition equation of Ag ion is shown as below:



The other experimental conditions remain the same as Au NWNW deposition. However, Ag and Au ions have different reduction potentials during the electrodeposition process, primarily due to their distinct standard electrode potentials⁸¹. From literature results, we selected $U = -0.8 \text{ V}$ ¹⁷ to deposit Ag NWNWs. The detailed recorded CVs and the corresponding reaction mechanisms will be shown and discussed in section 2.2.4.

$\text{Au}_{1-x}\text{Ag}_x$ alloy NWNW

For the electrodeposition of $\text{Au}_{1-x}\text{Ag}_x$ nanowires, we used an electrolyte consisting of potassium dicyanoaurate ($\text{KAu}(\text{CN})_2$, Carl Roth, $\geq 99.5\%$), potassium argentocyanide ($\text{KAg}(\text{CN})_2$, Carl Roth, $\geq 99.5\%$), 250 mM sodium carbonate (Na_2CO_3 , Carl Roth, $> 99.8\%$), with 1 vol% surfactant (2A1 Dowfax, Dow). In a binary electrodeposition system, in this case, is an Au-Ag alloy system, both Au

and Ag ions will deposit at the same time and form alloyed NWNWs. Both Au and Ag ion form cyanide complex $[Au(CN)_2]^-$ and $[Ag(CN)_2]^-$, their crystallized structures are both face-centered cubic, and they exhibit similar lattice parameters (4.0862 Å for Au and 4.0782 Å for Ag), thus they can form a perfect solid solution⁸². In this case, the composition of the deposited NWNWs, can be adjusted by varying both reduction potential and/or electrolyte composition.

For the electrodeposition of $Au_{1-x}Ag_x$ NWNWs we employed the same amount of sodium carbonate (250 mM) and surfactant (1 vol%), varying the relative contents of Au and Ag ions in the electrolyte, as well as the deposition potential, between $U = -1.1$ V and -0.8 V vs. Ag/AgCl. The summarized electrolyte compositions and the applied deposition potentials are given in Table 2.1. The synthesized samples are analyzed with different characterization methods, and the results are discussed in section 3.2.

Table 2.1 $Au_{1-x}Ag_x$ alloy nanowire network deposition conditions

Electrolyte name	$KAu(CN)_2$ (mM)	$KAg(CN)_2$ (mM)	Au:Ag ratio	Deposition potential (V vs. Ag/AgCl)
10Au1Ag	50	5	10:1	-1.1; -1.0; -0.9; -0.8
9Au1Ag	45	5	9:1	-1.1; -0.8
8Au2Ag	40	10	4:1	-1.1; -0.8
6Au4Ag	30	20	3:2	-1.1; -0.9; -0.8
5Au5Ag	25	25	1:1	-1.1; -0.8
4Au6Ag	20	30	2:3	-1.1; -0.8
3Au7Ag	15	35	3:7	-1.1; -0.8

2.2.5 Template removal

After electrodeposition, the nanowires are released from the polymer template for further characterization. In this case, we employed dichloromethane (DCM, CH_2Cl_2 , Carl Roth, $\geq 99.5\%$) to dissolve the polycarbonate membrane. Each sample was immersed in DCM for around 2 weeks, with at least one time exchange daily, to ensure a complete dissolution of the polymer template, otherwise a thin layer of polymer residual can be observed on the nanowire surface from SEM analysis. Afterwards, the sample is removed from the DCM solution, and then dried out in air. After removal of the polymer template, the NWNW sample remains entire without breaking. It can be easily handled with a tweezer and manipulated for further measurements. Specific sample preparation procedures for further experiments and characterizations (e.g., catalysis, wettability) will be explained in detail in the corresponding chapters.

2.2.6 Dealloying process to fabricate nanoporous Au NWNWs

Dealloying is the selective dissolution of one or more components from an alloy or solid solution, using chemical or electrochemical corrosive methods to remove the less noble component⁸³. This technique

commonly utilizes alloys such as Au-Ag, where the less noble Ag is dissolved to create nanoporous Au. Similarly, Co-Pd alloys are used to generate nanoporous Pd. The two primary dealloying methods are electrochemical and chemical. In electrochemical dealloying, the less noble metal is removed from the alloy by applying an electrical voltage in the electrolyte. This method allows precise control of the pore size and shape, making very fine and even structures. On the other hand, chemical dealloying uses acids or bases to dissolve the less noble metal, which is simple and easy to scale up for large amounts, but it usually makes larger, less uniform pores^{84,85}.

Over the years, it has been shown that dealloying is an effective way to produce a porous structure. A typical pore evolution process is shown in Figure 2.9. During dealloying, the less noble atoms dissolve, allowing the remaining atoms to diffuse along the interface, and the more noble atoms reorganize to form a bicontinuous network of ligaments and pores, and reconstruct a 3D porous structure. Over time, coarsening occurs due to surface diffusion, resulting in the growth of ligaments and pores and a decrease in surface area⁸⁵. This is a competitive process between dissolution and passivation, the pore and ligament size, typically ranging from a few nm to several μm , which can be tuned by balancing dissolution and surface diffusion rates^{56,86,87}.

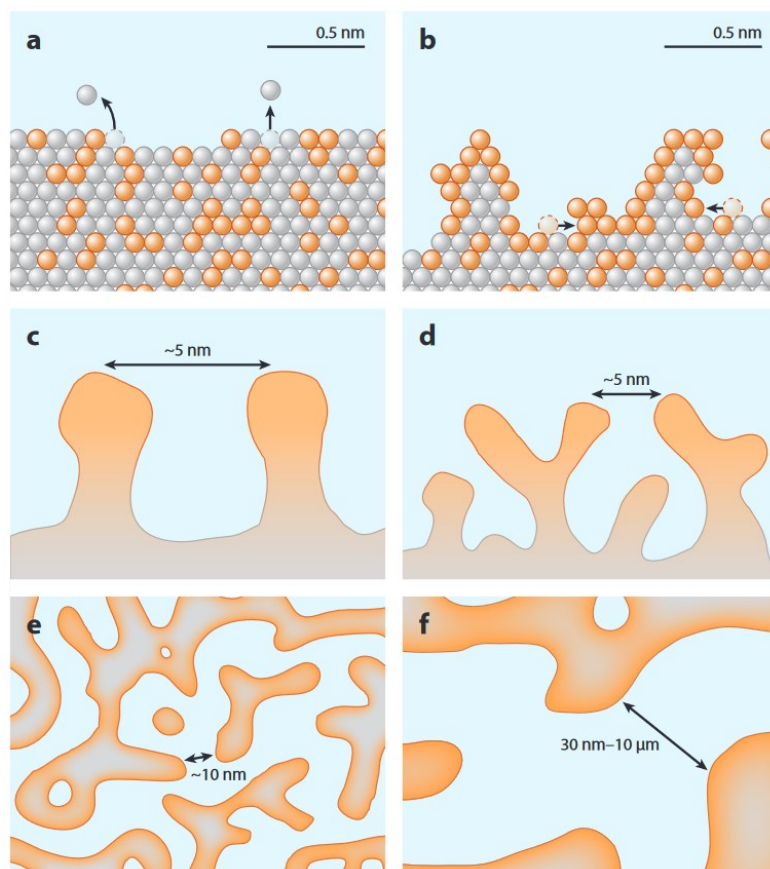


Figure 2.9 Working model for porosity evolution in dealloying in the Ag-Au alloy system (Ag, gray; Au, orange). (a) The rate-limiting step is the formation of terrace vacancies, which then grow into lateral vacancy clusters. (b) As dissolution proceeds layer by layer, surface diffusion passivates low-coordination sites with Au, leading to surface roughening. (c, d) As dealloying continues, there is insufficient Au to totally passivate the increasing surface area, leading to undercutting and bifurcation of ligaments. (e) The result of this process is a bicontinuous porous structure in which ligaments have Au-rich surfaces and Ag-rich interiors. (f) As coarsening increases the length scale of the initial structure, residual Ag atoms are exposed and dissolved, leaving a final structure with much reduced Ag content⁸⁵.

For the AuAg system, the less noble part Ag, has to surpass 55 at% to start the dealloying process, so only $\text{Au}_{1-x}\text{Ag}_x$ NWNWs with more than 60 at% Ag was tested^{88,89}. In this work, we apply chemical dealloying to produce hierarchical porous Au NWNWs. For this, $\text{Au}_{1-x}\text{Ag}_x$ NWNWs of various compositions ($0.6 < x < 0.8$) were placed in a 65% nitric acid (HNO_3) solution to selectively dissolve Ag. Dealloying occurred under the free corrosion conditions for durations from 30 min to 24 hours. Subsequently, the samples were rinsed with DI water for three times, to eliminate any residual acid solution. Finally, the samples were air-dried. All dealloyed samples were analyzed by SEM and EDX, to study the morphological and structural evolution during the dealloying process. Several series of samples, with nanowires varying between 60 nm and 150 nm were synthesized and analyzed, in order to investigate the influence of nanowire size on the dealloying process, and find the optimum geometrical parameters for fabricating free-standing porous Au NWNWs.

2.3 Characterization Methods

To study the morphology, composition, and different properties of the Au, Ag, and $\text{Au}_{1-x}\text{Ag}_x$ nanowire networks synthesized under different experimental conditions, various characterization techniques are applied in this work. High-resolution scanning electron microscopy (HRSEM) was used to determine the morphology of the nanowire networks, along with energy-dispersive X-ray spectroscopy (EDX) for the determination of the elemental composition. The nanowire crystallographic structure was studied by transmission electron microscopy (TEM). In order to test the catalytic performance and to determine the electrochemically active surface area (ECSA) of the Au nanowire networks, cyclic voltammetry (CV) measurements were performed. To study the wettability of the NWNWs we applied contact angle (CA) measurements.

2.3.1 High-resolution scanning electron microscopy (HRSEM)

Scanning electron microscopy (SEM) is widely used to image materials surface characteristics even in the nanometer range, by scanning the specimen with a focused electron beam. In the scanning electron microscope, electrons emitted at the top of the column by an electron gun then accelerated and focused to a beam by passing through several lenses. As shown in Figure 2.10, the beam is scanned over the surface of a sample, which is placed on a stage in the vacuum chamber⁹⁰.

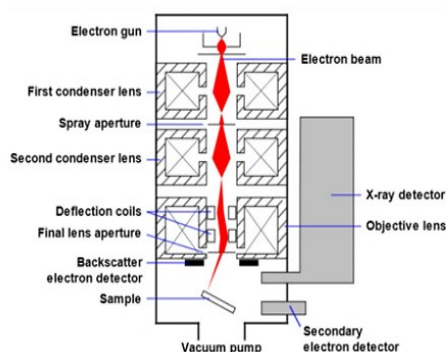


Figure 2.10 Schematic representation of SEM structure⁹⁰.

When the primary electrons hit the sample surface with energy in the keV range, some electrons scattered back from the sample surface due to elastic collisions. During the hitting, the energy of primary electrons is transferred to the sample, which is an inelastic scattering process, ejecting low-energy secondary electrons. Secondary electrons, backscattered electrons, and diffracted backscattered electrons are used to generate a three-dimensional image of the materials' surface topography. During this interaction between the primary electron beam and sample, sample electrons from the valence band and conduction band are excited and return to lower energy states releasing X-rays, which have a characteristic wavelength that is analyzed by energy-dispersive X-ray spectroscopy⁹⁰.

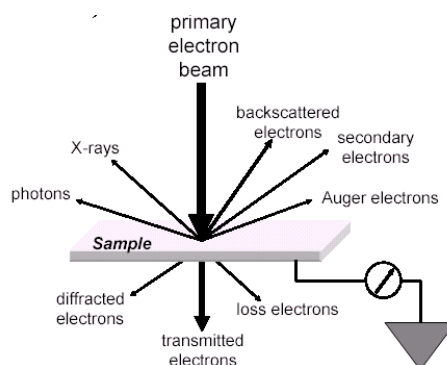


Figure 2.11 Interaction between the electron beam and sample⁹⁰.

SEM is the most important characterization technique in this work, which is used for nanowire morphology, geometry, and structural homogeneity analysis. It is a powerful tool in assisting the optimization of the NWNW fabrication process, as well as analyzing the sample evolution during the electrochemical reactions. In this work, we employed a Zeiss Gemini 500 field emission scanning electron microscope.

2.3.2 Energy dispersive X-ray spectroscopy (EDX)

Energy-dispersive X-ray spectroscopy (EDX) is a chemical analysis method to determine the local elemental composition by analyzing emitted X-rays. The X-rays are generated when the sample is hit by the electron beam, because electrons inside the atom absorb the energy of the primary electrons. The electron of the sample atom is excited to a higher energy level, leaving an electron vacancy inside the atom, which is filled by an electron from a higher level falling down, emitting X-rays. Their energy is determined by the atom, since the energy state positions are a specific material property^{91,92}.

EDX analysis is both a qualitative and quantitative characterization method. EDX spectra contain multiple peaks, whose positions correspond to the energy level of different elements. By integration of the peak line intensity, the relative peak height can be calculated, which represents the elemental content. An example of the EDX spectra is shown in Figure 2.12⁹².

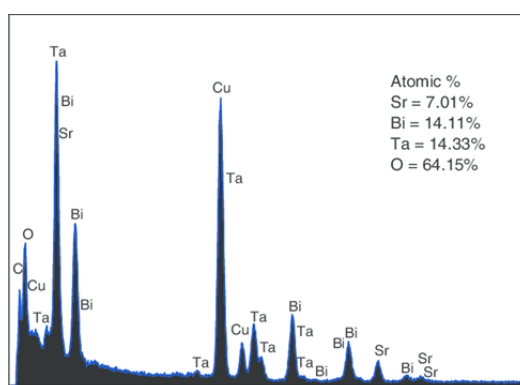


Figure 2.12 EDX spectra from a $\text{SrBi}_2\text{Ta}_2\text{O}_9$ nanotube⁹¹.

SEM and EDX measurements were performed at GSI using a Zeiss Gemini 500 microscope equipped with a Bruker EDX detector. SEM analysis can characterize the nanowire network morphology, including nanowire dimension, structure homogeneity, nanowire surface morphology, and cross-section of the nanowire networks. EDX provides the elemental analysis, especially for the $\text{Au}_{1-x}\text{Ag}_x$ nanowire

networks, which allows us to have a detailed analysis of the atomic composition of the alloyed nanowire networks in different scales, including a detailed scanning and an overview analysis. The sample is fixed on a SEM stub, either using a ring to fix it, or glue on top using a silver paste.

2.3.3 High-resolution transmission electron microscopy (HRTEM)

Transmission electron microscopy (TEM) is a commonly used characterization method to obtain high-resolution analysis in the nanoscale, which is widely applied in materials science and biological science fields. Figure 2.13 shows the schematics of a TEM. An electron beam is generated from the electron gun at the top, and then is focused by several metal apertures and electromagnetic lenses below. At the end of the column, only a small part of the electron beam is focused on the sample, which has a well-defined energy. After the beam passes through the column, only a small portion of the electron beam will focus on the sample, which has a well-defined energy⁹³.

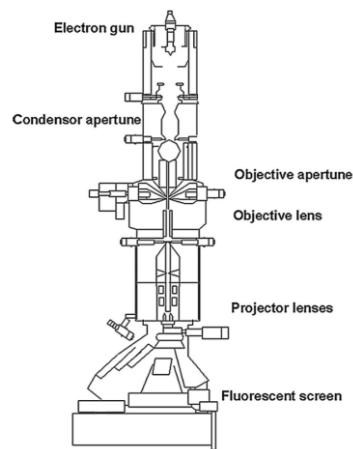


Figure 2.13 Schematic representation of transmission electron microscope⁹³.

Normally, transmission electrons can penetrate through samples thinner than 100 nm, the exact transmission thickness however depends on sample density and composition. There are two observation modes in TEM, bright-field and dark-field imaging. In the bright-field mode, transmitted electrons pass through the aperture and transmit through the specimen, so at thicker spots or where heavier atoms are present, a darker area appears on the screen. However, in the dark-field imaging mode, only diffracted atoms will pass through the aperture, and the transmitted electrons are blocked. Thus, this mode can reveal the crystal information of the specimen. The two observation modes of bright-field and dark-field are demonstrated in Figure 2.14⁹³.

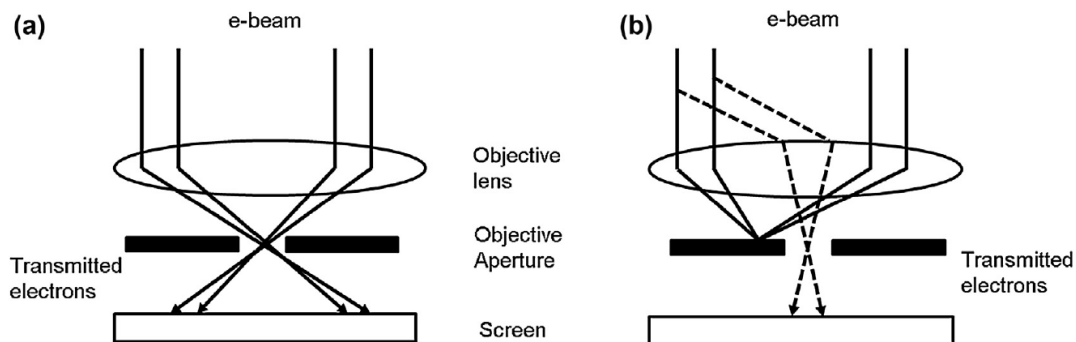


Figure 2.14 Transmitted and diffracted electrons for (a) bright-field and (b) dark-field images in transmission electron microscope⁹³.

For TEM analysis, a small piece ($\sim 3 \text{ mm} \times 5 \text{ mm}$) of the nanowire network sample was cut off and placed in a glass tube filled with a small amount of isopropanol. The tube was inserted in an ultrasonic bath for 2 - 3 min to separate the network structure from the back-electrode layer and break it into small pieces consisting of only a few individual nanowires. Then this nanowire containing suspension was drop-casted on to a copper TEM grid with a pipette. Once the isopropanol evaporates, the sample is ready for TEM characterization. TEM and TEM-EDX measurements were performed by Dr. Wilfried Sigle at the Max Planck Institute for solid state research in Stuttgart, using a JEOL ARM200F TEM.

2.3.4 X-ray photoelectron spectroscopy (XPS)

X-ray Photoelectron Spectroscopy (XPS), also known as electron spectroscopy for chemical analysis (ESCA), is a quantitatively analyzing method focusing on elemental composition and chemical states on a material's surface, providing insights into surface properties within a depth of approximately 1-10 nm. XPS employs high-energy X-ray photons to stimulate electrons within a substrate (Figure 2.15). The ejected electrons are sorted based on their kinetic energies using a hemispherical electron energy analyzer. Then electrons with specific kinetic energies are directed to an electron detector and counted. XPS software generates graphs illustrating the number of electrons versus binding energy. Despite x-rays penetrating deeper into a sample, the photoelectrons exhibit a restricted mean free path, therefore XPS is highly surface-sensitive^{94,95}.

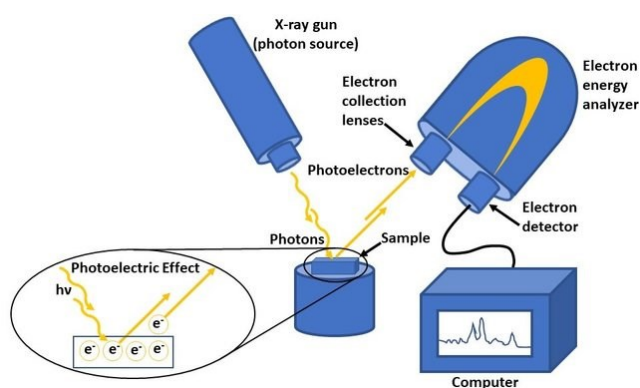


Figure 2.15 Diagram and main components of an XPS system⁹⁴.

In this work, XPS measurement was done in the Surface Science Laboratory at the Technical University of Darmstadt. A SPECS PHOIBOS 150 spectrometer implemented at the DAISY-FUN cluster tool was used. It is equipped with an Al $K\alpha$ X-ray source. Samples were cut into smaller pieces and then used directly for XPS measurements, without extra treatment. The data analysis was performed with CasaXPS. XPS can provide information focused on the nanowire surface, instead of EDX analysis averaging over a number of wires, it can also distinguish the surface oxidation layer, or other impurities and contaminations.

2.3.5 Electrochemical measurements

For nanomaterials using in catalytical applications, it is important to first characterize their electrochemical properties in a controlled experimental condition. These properties include catalytic activity, electrocatalysis, overpotential, durability, selectivity, charge transfer kinetics, surface area, and susceptibility to poisoning or deactivation. Catalysts influence the rate and efficiency of electrochemical reactions, impacting processes like energy conversion and storage. Understanding and optimizing these properties are crucial for designing effective catalysts^{79,96-99}. There is one fundamental method used in various measurements, which is cyclic voltammetry (CV). During a CV measurement, a cyclic potential

is ramped within a certain range to the working electrode with respect to the reference electrode for a certain number of cycles. While the applied potential is varied, different reactions occur at different potentials.

With this method, a current vs. voltage (I - V) diagram is measured. An example is shown in Figure 2.16. When the potential of the working electrode is more positive than the oxidation potential of the redox pair in the electrolyte, then the corresponding species are oxidized, which is indicated by a peak of current increase. Reversely, when the potential of the working electrode is more negative than the reduction potential of the redox couple, the reduction reaction occurs, therefore a reduction peak will appear on the curve. For both oxidation and reduction reactions, anodic and cathodic current peaks are identified on the CV curve. During the CV scan, there are also some potential regions where no reaction happens, this is called the non-faradic region. Within the non-faradic region, there is no peak shown on the CV curve⁹⁹⁻¹⁰¹.

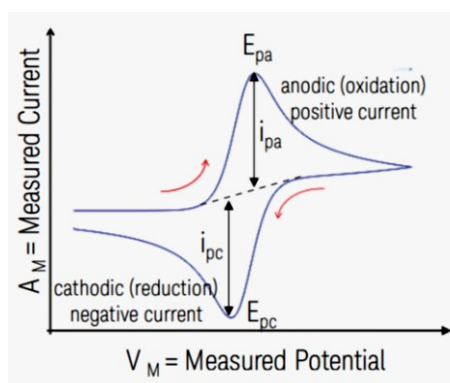


Figure 2.16 Example of a CV curve measurement¹⁰¹.

In this work, all CV measurements are done in a commercial three-electrode cell from Redoxme AG, as shown in Figure 2.17. The setup includes a platinum spiral wire as the counter electrode, a Ag/AgCl (3 M KCl) reference electrode, and a gold coated copper plate in contact with the sample as the working electrode. There is also a pair of gas inlet and outlet tubes, which are used for purging the electrolyte with N₂ gas before every measurement.

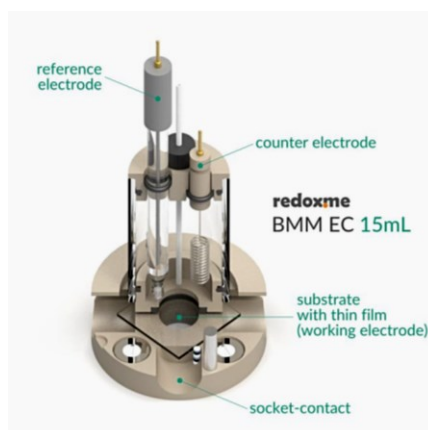


Figure 2.17 The Redoxme BMM EC 15 mL Cell assembly construction.

2.3.6 Electrochemically active surface area (ECSA) measurement methods

To evaluate the catalytical performance of NWNWs, first, the electrochemically active surface area (ECSA) must be determined. In this work, we applied two different methods for the ECSA

determination: (i) the double-layer capacitance measurement and (ii) the integration of the Au oxide reduction peak.

Double-layer capacitance measurement

The electric double-layer is the interface formed between an electrode and the adjacent electrolyte, it forms whenever two conducting phases meet at an interface, which is an intrinsic part of any electrochemical system¹⁰². This was first proposed by Helmholtz in 1853, the double-layer concept was introduced as an interfacial region comprised of two layers of opposite charges separated by a small distance¹⁰³, as shown in Figure 2.18 (a). The electrical double-layer model has since evolved through major contributions by Gouy (1909), Chapman (1913), Stern (1924), and Grahame (1947)^{102,104–106}. As shown in Figure 2.18 (b), Gouy and Chapman expanded the model by accounting for the thermal motion of ions, introducing the concept of a diffuse layer, a region where cations and anions are continuously distributed in the electrolyte due to thermal diffusion. This ion diffusion is influenced by surface charge and entropic factors such as ion adsorption and changes in hydration shells, which together affect the thickness of the electric double layer and result in a “diffuse electric double-layer”. Stern combined the two models, introducing two ion distribution regions: the compact (or Stern) layer and the diffuse layer (Figure 2.18 (c)). In the compact layer, ions are strongly adsorbed onto the electrode, which includes specifically adsorbed ions (usually anions) and non-specifically adsorbed counterions, separated by the inner and outer Helmholtz planes (IHP and OHP). The diffuse layer follows the description from the Gouy–Chapman model.¹⁰⁷

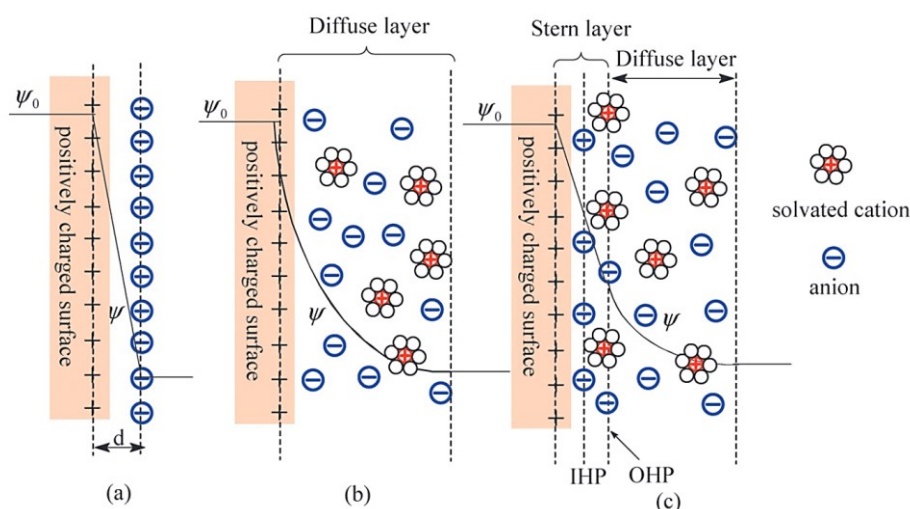


Figure 2.18 Schematic representation of the electrical double-layer using the (a) Helmholtz description, (b) Gouy-Chapman description, and (c) Stern description. IHP stands for the inner Helmholtz plane while OHP refers to the outer Helmholtz plane.¹⁰⁷

In our experiments, we charge this double-layer with an external potential, and then the charge accumulates at the electrode surface. This charge separation behaves like a capacitor, where the electrode and the adjacent ion layer act as two plates. The capacitance of this arrangement, known as the double-layer capacitance, is directly proportional to the surface area of the electrode in contact with the electrolyte.¹⁰⁸ When a potential is applied at the electrode, the ions inside the electrolyte with a reversed charge will be attracted to the electrode surface. So the first layer consists of the surface charge ions, while the second layer is composed of ions attracted to the surface charge via the Coulomb force^{100,109,110}.

During a CV scan, the measurement window is carefully chosen to ensure that no electrochemical reactions occur. Only this reaction-free region, known as the non-faradaic region, can be used to estimate the double-layer capacitance. So, the double-layer charging current can remain constant. The ECSA of an electrode can be determined by the double-layer capacitance (C_{DL}) and the specific capacitance (C_s) according to the equation:

$$ECSA = \frac{C_{DL}}{C_s} \quad 2 - 8$$

The specific capacitance ($C_s [=] \mu\text{Fcm}^{-2}$) is proportional to the surface area, thus crucial in evaluating the ECSA, since small inaccuracy can lead to underestimation or overestimation of the ECSA values.⁴² In this work, we employed a smooth Au thin film as the reference sample for the determination of the specific capacitance, to exclude errors from experimental setups and conditions. First select a suitable non-faradaic region from a CV curve, such as Figure 2.19 (a), then optimize measuring settings by varying different parameters (details will be discussed in section 4.1.4), apply different scan rates within the selected potential range (e.g. from 0.01 V/s to 10 V/s), then the anodic and cathodic current can be extracted from the CV cycles. Last step is to analyze the extracted data and the slope of the linear fitting curve is the capacitance value (Figure 2.19 (c)), which is described by the equation below:

$$C = \frac{i_c}{v} \quad 2 - 9$$

Where C is capacitance, i_c is the capacitive current, and v is the scan rate¹¹¹.

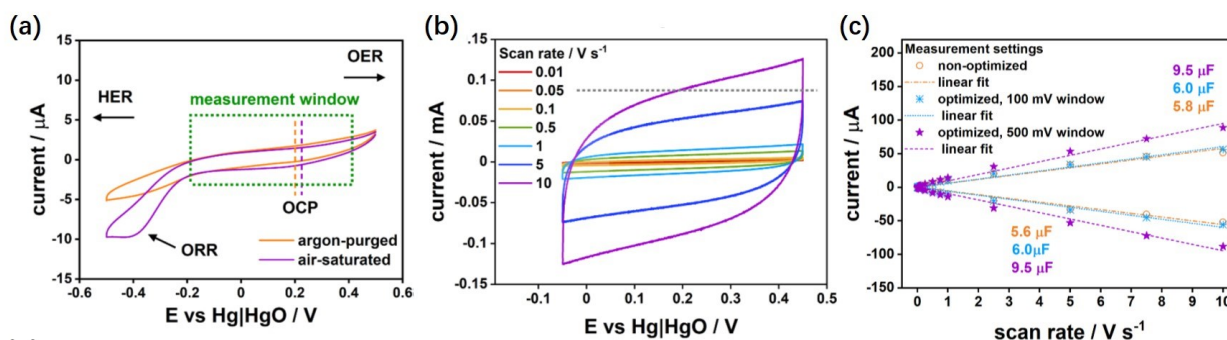


Figure 2.19 Cyclic voltammograms (a) recorded for a glassy carbon electrode in argon-purged 0.1 M NaOH aqueous solution in a wide scan range, (b) with different scan rates within the selected measuring window, (c) anodic and cathodic current as a function of scan rate, dot lines correspond to corresponding linear regression fits. The resulting capacitance values are shown with the colors corresponding to their respective data set¹¹¹.

Real environments can be quite different than an ideal capacitor, since many factors, such as diffusion limitation, uncompensated potential drop, and the selected potential window, influence the measurement. In this work, many parameters were varied to find optimized conditions for the determination of the ECSA of the NWNW by this method, which will be discussed in detail in section 4.1.4. The main advantage of the double-layer capacitance method is its wide applicability. In particular, it can be applied to complex surfaces independently of the surface chemical composition. Therefore, the method is very suitable to determine the ECSA of NWNWs with same geometry but different compositions. But to more accurately evaluate our NWNWs, we also employed a second method for ECSA evaluation, which is only applicable to pure Au samples.

Integration of the AuO reduction reaction peak

Since the ECSA determination is critical for the evaluation of the catalytical performance of the networks, we employed an additional method for ECSA evaluation, i.e., the integration of the Au oxidation reaction peak. This method applies only to pure Au samples, because Ag oxides undergo two steps of reduction reactions, and the reduction peaks of the AuAg alloys can overlap, which makes the separate evaluation difficult.

The ECSA values are determined by integrating the faradaic charge transfer of the Au surface oxide reduction reaction¹¹². Au oxide formation has been studied since the 1960's¹¹³, researchers have found that CV in acidic solutions displays a minimum current prior to oxygen evolution. Charging curves indicate the formation of a monolayer containing one oxygen atom per gold atom. Since this oxide film is restrained to one monolayer, the method can be used to determine the surface area of gold electrodes¹¹⁴.

$$ECSA = \frac{Q_m}{Q_{ref}} \quad 2 - 10$$

where Q_m is the measured charge transfer value, and Q_{ref} is the reference value of the charge transfer used for monolayer of AuO reduction is 1 cm^2 .

We employed a flat Au thin film, produced by electrodeposition, with a thickness of around $2 \mu\text{m}$, as the reference sample. A representative CV recorded in a $0.1 \text{ M H}_2\text{SO}_4$ solution is shown in Figure 2.20. The anodic peaks located at $U = 1.2 - 1.4 \text{ V}$ are attributed to the formation of Au oxide^{115,116}, while the current rising at 1.6 V represents the beginning of O_2 evolution¹¹⁷. The cathodic peak at 0.85 V represents the Au oxide reduction, with the peak area (marked in yellow) representing the total charge transfer during the reduction reaction. During the anodic scan, a monolayer of Au oxide forms on the Au NWNW surface, which is reduced during the cathodic scan. By integration of the reduction peak area and subtraction of the background, the total charge transfer is determined¹¹⁷. A reference value of the faradaic charge of a Au oxide monolayer per unit area was obtained by reference CV measurements under the same experimental conditions using the Au film on the 1 cm^2 reference sample. By integrating the respective reduction peak, a reference charge transfer value of $Q_{ref} = 653 \mu\text{Ccm}^{-2}$ is obtained. This value will be used in section 4.1.1 for determination of the Au NWNWs ECSA. This value is slightly higher than the value available from literature, Leopold and Nahir¹¹⁶ theoretically calculated $448 \mu\text{Ccm}^{-2}$, when assuming the surface is Au(111). The reason for this deviation mostly comes from the intrinsic roughness of our reference sample, which is inevitable in real experimental conditions. Another reason can come from different experimental setups, solution pH, concentration, capacity, and the sweep rate.¹¹⁸ Therefore, in our work, when we control all the parameters to remain the same, then the reference value we obtained can rule out system errors and influences, and give us more reasonable results.

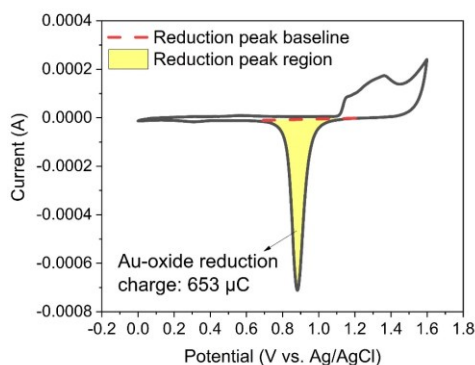


Figure 2.20 CV recorded in $0.1 \text{ M H}_2\text{SO}_4$ for a 1 cm^2 flat Au reference sample⁵².

In chapter 4.1.4 we will also discuss the parameters used for ECSA determination, and which set of parameters can lead to more optimized results. Also, a comparison of the ECSA values obtained by the two methods will be presented and discussed in that section.

2.3.7 Methanol electro-oxidation reaction

Direct methanol fuel cell is a very promising choice of energy source for portable devices and transportation vehicles, such as automobiles¹¹⁹. These applications require simple resources, with non-hazardous waste, and function at low temperatures, while providing high specific energy⁹⁶. In order to improve the performance of methanol/ethanol fuel cells, it's very important to find suitable catalysts to increase the reaction rate.

A representative scheme of the methanol oxidation process in a fuel cell is shown in Figure 2.21. A direct methanol fuel cell consists of two electrodes, including an anode, where methanol is fed along with water, and a cathode, where oxygen goes in. The anode and cathode are separated by an ionic conductor, the cell can be filled with an acidic or alkaline electrolyte⁹⁶.

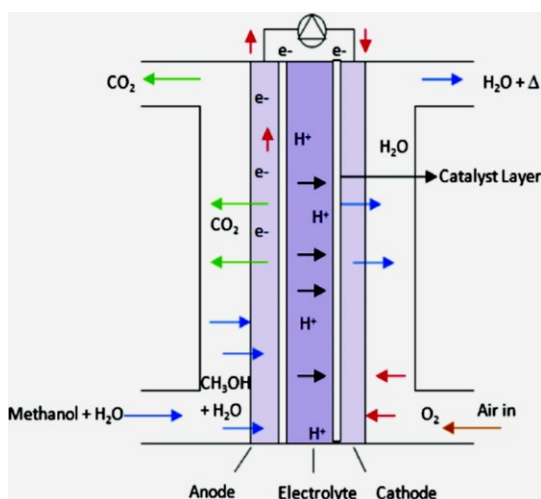
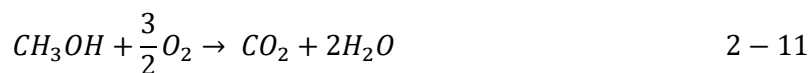
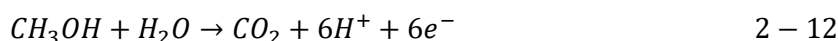


Figure 2.21 Schematic figure of a methanol fuel cell¹²⁰.

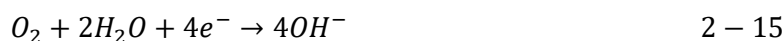
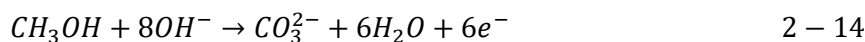
The oxidation of methanol will happen at the anode, which can produce electrical energy with carbon dioxide emissions. While at the cathode, oxygen is consumed and reduced, with H₂O as a product. The complete reaction is shown below:



The anodic and cathodic reactions are different as a function of pH.¹²¹ In the acidic electrolyte, the reactions at the anode and cathode are:



But if the electrolyte is alkaline, such as sodium hydroxide and potassium hydroxide, then the reaction equations at the anode and cathode are:



The anode corresponds to the negative electrode, while the cathode is the positive electrode, and the potential difference between the two electrodes is called the cell potential¹²².

In this thesis, to characterize the catalytic performance of Au, Ag, Au_{1-x}Ag_x, and nanoporous Au NWNWs, the setup details are given in section 2.3.5. To properly characterize the catalytic ability of various NWNWs against methanol oxidation, alkaline electrolytes with different concentrations were used, namely 0.1 M, 0.5 M, and 1 M potassium hydroxide (KOH) solutions.

2.3.8 Contact angle measurements

The surface wetting state is impacted by the unique characteristics of nanostructures, which include nanoparticles, nanowires, and other nanoscale features. Their defining attributes include high surface area, intricate surface roughness, and various surface chemical composition. When liquids are brought into contact with a surface, they exhibit a certain wetting behavior. For example, a drop of water either spreads over the surface or is repelled by it. This wetting behavior is typically described and characterized by a technical term called the contact angle (CA). The CA on a surface is the angle formed at the three-phase contact line, where a liquid, a solid, and a gas phase (usually air) meet. It quantifies the wetting behavior of the liquid on the solid surface. For conventional cases, a high CA ($90^\circ < \theta < 180^\circ$) signifies non-wetting or hydrophobic behavior, where the liquid forms a nearly spherical droplet with minimal surface adhesion. Conversely, a low CA ($\theta < 90^\circ$) characterizes wetting or hydrophilic behavior, where the liquid spreads extensively across the surface^{123–125}.

The CA of a drop on a solid is given by the Young equation

$$\cos(\vartheta_0) = \frac{\gamma_s - \gamma_{SL}}{\gamma_L} \quad 2 - 16$$

where γ_s is the surface energy of solid, γ_L is the surface energy of the liquid, and γ_{SL} is the energy of solid-liquid interface. Classical models, including the Wenzel and Cassie-Baxter models, provide a theoretical framework to explain how surface roughness influences wetting.

The Wenzel theory describes a chemically homogeneous surface:

$$\cos(\vartheta_{eff}) = r \cdot \cos(\vartheta_0) \quad 2 - 17$$

ϑ_{eff} is the macroscopic contact angle of the rough surface, r is the roughness factor, and ϑ_0 is the given by the Young equation.

The Cassie-Baxter theory differs from the Wenzel theory, which can describe a chemically heterogeneous surface, with two compositions, each with a certain surface fraction:

$$\cos(\vartheta_{eff}) = f_1 \cdot \cos(\vartheta_1) + f_2 \cos(\vartheta_2) \quad 2 - 18$$

where the effective contact angle is affected by the contact angle of two materials and their surface fraction f_1 and f_2 .

However, the Cassie-Baxter theory can also be developed and applied on a single-phased rough surface with texture, where the surface is only partially wetted, with air pockets trapped in the asperities. In such a case, the contact angles of the solid and liquid phase are ϑ_0 and 0, respectively:

$$\cos(\vartheta_{eff}) = 1 - r \cdot f + r \cdot f \cdot \cos(\vartheta_0) \quad 2 - 19$$

Where r is the roughness factor of the wetted area, f is the area fraction of the wetted area, so $r \cdot f$ is also called the solid fraction Φ_s ^{125–127}.

In addition to CA, the adhesion of the water droplets to the surface is also of interest. The adhesion indicates whether the drop rolls off on an inclined surface or remains stuck to one spot. Two different states can be distinguished here. A hydrophobic surface can either have a low adhesion to water, or a

strong adhesion to water. When a droplet is placed on an inclined surface, the contact angles at two sides show different behavior, as shown in Figure 2.22, the minimum value of the CA, called the receding CA, θ_{rec} , and a maximum value of the CA, called the advancing CA, θ_{adv} . The difference between the advancing and receding CAs is called CA hysteresis, $\Delta\theta_{hys}$. A low adhesion between the water droplet and the surface leads to a low contact angle hysteresis and vice versa¹²⁸.

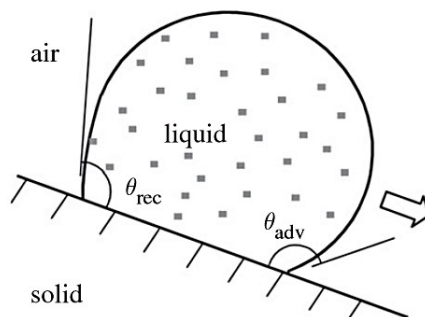


Figure 2.22 Schematic of a droplet on a tilted surface showing advancing (θ_{adv}) and receding (θ_{rec}) contact angle (CA). The difference between these angles is the CA hysteresis¹²⁸.

There are many unique wetting behaviors existing in natural surfaces, such as the lotus effect and the rose petal effect, they showed different mechanism than traditional theories. The lotus effect shows a hydrophobic behavior, where the droplet will roll off the tilted surface, which means very low surface adhesion and low contact angle hysteresis.⁵⁹ However, the rose petal surface shows a very different phenomenon, it exhibits a high contact angle droplet, with a high adhesion, the droplet is pinned on the surface, and forms a high contact angle hysteresis, which is a special wetting phenomenon, someone explained it as the Cassie-impregnating^{126,128-130}. These effects are results of special surface structure, with certain roughness both in the micrometer and nanometer range.

Current theory only provides partial solution to the ever-developing field of complex surfaces. With diverse combinations of different hydrophilic and hydrophobic nanostructures, they can achieve many unique functions. In this work, we are interested to see how 3D NWNW structure can influence surface wetting behavior. For this, we fabricated a series of Au NWNWs with different nanowire sizes and densities, to explore the interactions between capillary imbibition and wetting behavior on patterned nanostructures. CA measurements were only carried out on pure Au NWNWs, considering gold is a material suitable for model study, which is chemically stable, and does not oxidize in air. Despite the hydrophilic nature of gold, NWNWs with different geometry exhibited various wetting states, details are discussed in section 5.2.

CA measurements of the NWNWs were carried out on an optical tensiometer (Biolin Scientific Figure 2.23), using the static sessile drop method. Droplets of deionized water (Milli-Q Direct 8) of 2, 4, 6, and 15 μL volume were used. Droplets were formed at the pipette tip, and then placed on the sample surface. The photographs were taken at five different spots on the sample surface for each sample, each measurement was recorded for 10 s after the droplet was placed.

For the tilting contact angle measurements, the advancing angle (θ_{adv}) and receding angle (θ_{rec}) were measured at tilted 0, 15, 30, 45, 60, 75, and 90 degrees, with 4 and 15 μL droplets. There is no contact line movement observed, so we use the CA hysteresis ($\Delta\theta_{hys}$) when the sample is tilted 90°.



Figure 2.23 Photo of the Optical Tensiometer Theta Lite.

3. Morphological and Structural Characterization of NWNWs

This chapter presents the results of a detailed characterization of the three types of electrodeposited NWNWs (i.e., pure Au, $\text{Au}_{1-x}\text{Ag}_x$, and porous Au) by various complementary methods, namely SEM, EDX, TEM, and XPS. The goal of these investigations is to understand how the different synthesis parameters influence the sample morphology and composition, as well as to provide the optimized conditions for the synthesis of the tailored, stable, homogeneous, and functional NWNWs.

3.1 Au Nanowire Networks

3.1.1 Homogeneity, morphology, and crystallinity as a function of applied potential

Au NWNWs were electrodeposited employing a 50 mM $\text{KAu}(\text{CN})_2$ electrolyte cyanide-based electrolyte under potentiostatic deposition conditions at 60 °C (details in section 2.2.4). The electrodeposition process was monitored via current-vs.-time ($I-t$) curves (Figure 3.1 (a)). Aiming at fabricating homogeneous Au NWNWs on the entire sample area (diameter xx mm) we first studied the influence of the applied potential on the growth rate and on the morphology of the NWNW. Different potentials ranging from $U = -1.1$ V to $U = -0.7$ V (vs. Ag/AgCl) were applied. To allow direct comparison, etched ion-track templates with the same set of parameters were employed, i.e., pore diameter of 150 nm and total nanochannel density of $4 \times 10^8 \text{ cm}^{-2}$. The experimental results reveal a very strong influence of the deposition potential on both the Au NWNW growth rate and the resulting morphology.

Figure 3.1 (a) shows that at high potentials, e.g., $U = -1.1$ V (purple) the growth is very fast. The current increases rapidly during the growth in the channels and even more rapidly after 13 min, indicating that some nanochannels were already completely filled and so-called caps formed on the membrane surface. This fast growth results in inhomogeneous filling and thus poor interconnectivity, with a rather inhomogeneous and unstable network structure (Figure 3.1 (b)). At $U = -1.0$ V (orange), the growth rate is slightly decreased. Au nanowires are deposited in the channels for ~1 h, and the overall homogeneity is improved (Figure 3.1 (c)). However, not all channels are filled at the same rate, and thus some areas with fewer nanowires were observed. At lower potentials, namely $U = -0.9$ V (green) and $U = -0.8$ V (pink), the network homogeneity is significantly improved resulting in a dense network structure, see Figure 3.1 (d, f).

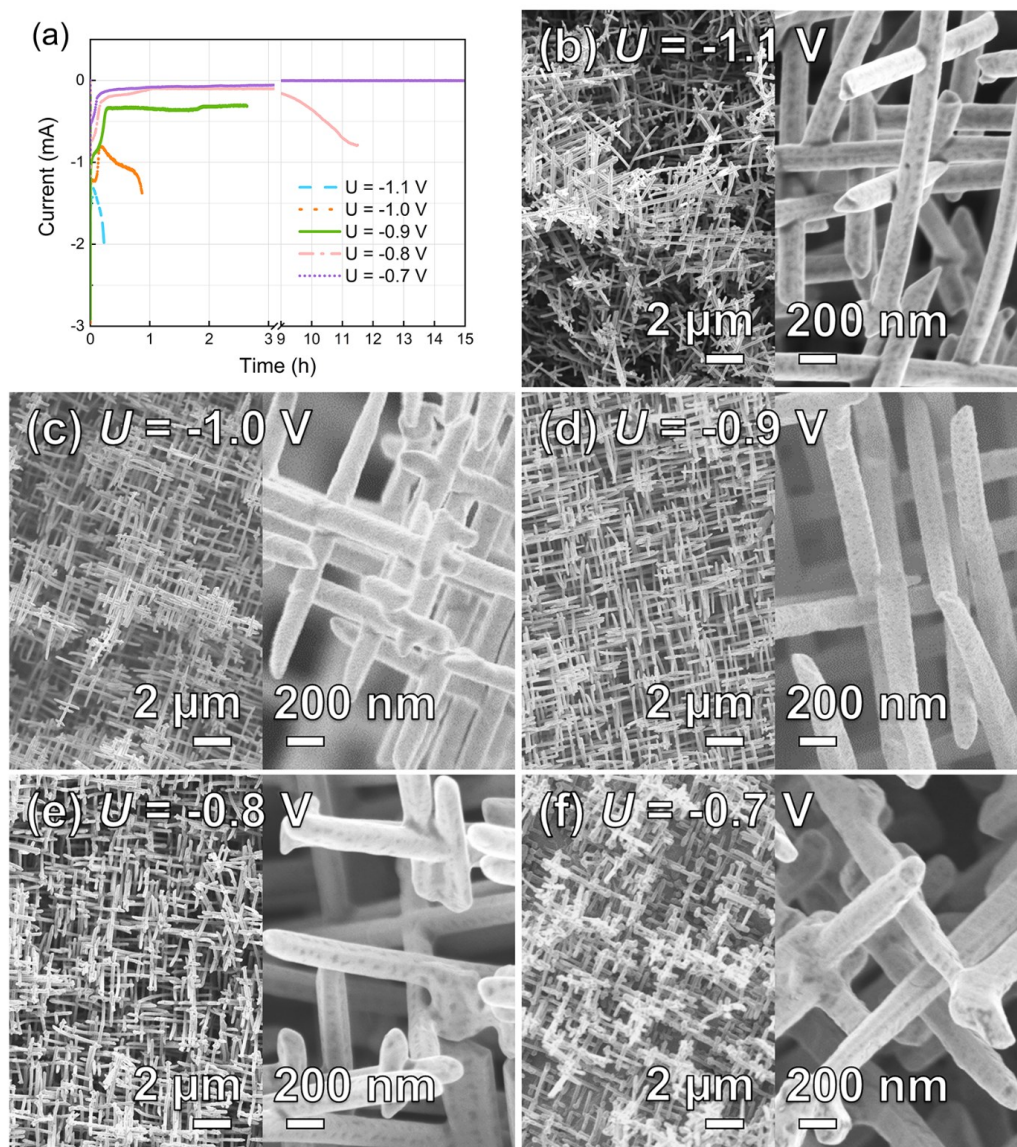


Figure 3.1 (a) Current-vs.-time (I - t) curves recorded for various applied potentials during the potentiostatic deposition of Au NWNWs, and the corresponding SEM images, (b) $U = -1.1$ V, (c) $U = -1.0$ V, (d) $U = -0.9$ V, (e) $U = -0.8$ V, (f) $U = -0.7$ V vs. Ag/AgCl. The large magnification SEM images reveal cylindrical monodispersed nanowires.

Cross-section SEM images of the Au NWNWs further demonstrate the homogeneity increase with decreasing applied potential (Figure 3.2). It can be seen that with decreasing potential, the duration for complete channel filling gets longer and longer. At $U = -0.7$ V, the template is not completely filled even after 15 hours. At such long deposition times, a constant ion concentration in the electrolyte cannot be guaranteed because the whole setup is heated and the electrolyte solution evaporates over time. Based on these observations, an optimal deposition potential of $U = -0.9$ V was selected for the following experiments, which delivers an optimized morphology and is time-efficient.



Figure 3.2 SEM images of cross-sections of Au NWNW deposited at (a) $U = -1.1$ V, (b) $U = -1.0$ V (c) $U = -0.9$ V vs. Ag/AgCl. The orange arrows indicate some branches of nanowires grow higher than average, and the inhomogeneity decrease, from a to c, as the deposition potential is less negative.

The nanowire diameter was determined from the SEM images. By measuring the diameter of 100 wires, we calculated an average diameter of 148 ± 13 nm, i.e., a diameter spread distribution smaller than 10%. This was done for each sample, since the diameter of the wire determines the geometrical and electrochemically active surface area of the entire network. Their surface structure, in addition, can influence the catalytic activity. EDX analysis shows that the nanowires consist of pure gold (Figure 3.3). No impurities were detected except a small peak of carbon, which is ascribed to the polymer residuals left from the PC template removal.

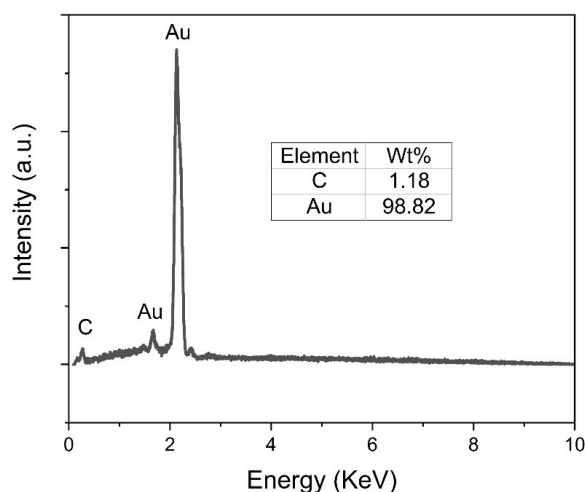


Figure 3.3 EDX spectrum of a Au NWNW deposited at $U = -0.9$ V vs. Ag/AgCl.

The crystallinity of the Au nanowires was analyzed by TEM. Figure 3.4 shows representative TEM images of segments of the Au NWNW deposited at $U = -1.0$ V, -0.9 V and -0.8 V vs. Ag/AgCl. By TEM dark-field imaging, grain boundaries (GB) were identified and marked with red lines in Figure 3.4. Nanowires deposited at -1.0 V (Figure 3.4 (a-c)) are single crystalline on a length of about 0.5 to 1 μm , which indicates a bamboo-like crystalline structure. At less negative deposition potential ($U = -0.9$ V in Figure 3.4 (d-f) and $U = -0.8$ V in Figure 3.4 (g-i)), the size of the grains is larger and the wires exhibit fewer grain boundaries consistent with a smaller nanowire growth rate as discussed above (Figure 3.1 (a)). It is also worth noting that no grain boundaries were found at the nanowire crossing junctions, so the presence of crossing nanochannels seems not to affect the nanowire crystallinity.

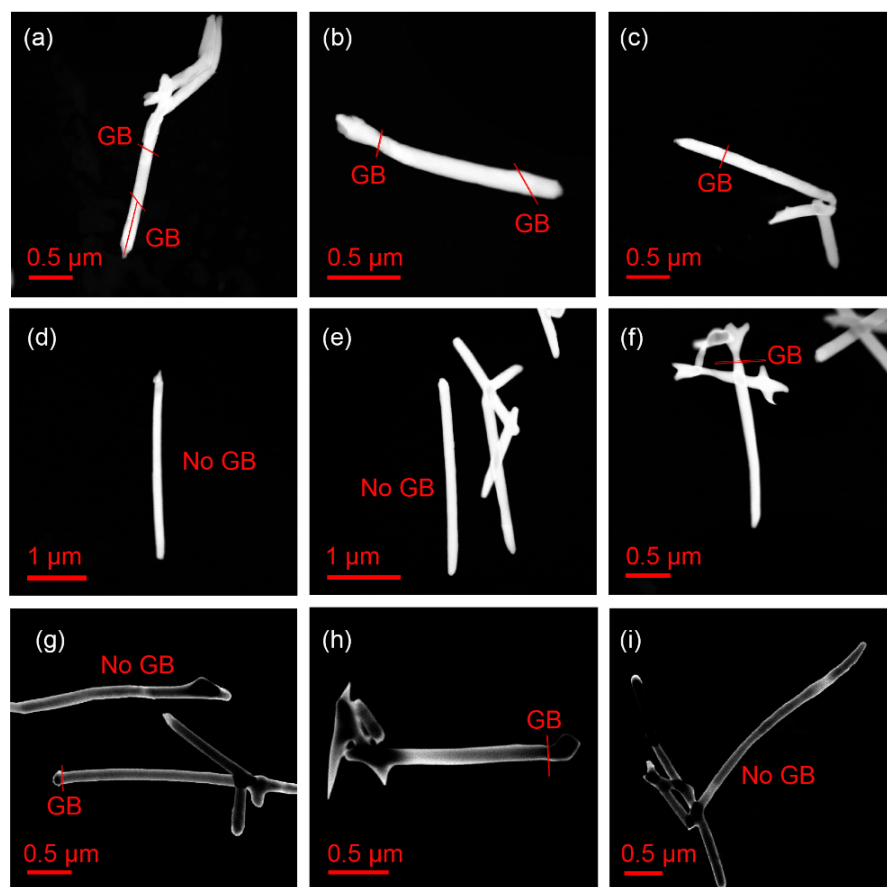


Figure 3.4 TEM dark-field images of fragments of Au nanowire networks deposited at (a-c) $U = -1.0$ V, (d-f) $U = -0.9$ V, which are high-angle annular dark-field imaging, and (g-i) $U = -0.8$ V vs. Ag/AgCl, are medium-angle annular dark-field imaging. The red lines mark the positions where grain boundaries (GB) were observed.

3.1.2 Au NWNWs with various wire diameters

After optimization of the electrodeposition process using templates with 150 nm diameter channels and density of $4 \times 10^8 \text{ cm}^{-2}$, we fabricated a series of membranes with the same channel density and diameters ranging from 40 nm to 200 nm. As shown in Figure 3.5, a series of Au NWNWs with nanowires ranging from 40 nm to 200 nm can be successfully synthesized with the 50 mM $\text{KAu}(\text{CN})_2$ electrolyte, applying -0.9 V vs. Ag/AgCl. This series of electrodepositions proved that the optimized conditions can be applied to fabricate NWNWs with different densities and nanowire diameters. This allowed the fabrication of NWNWs with tailored geometry for the further investigation of their properties to be implemented in various applications.

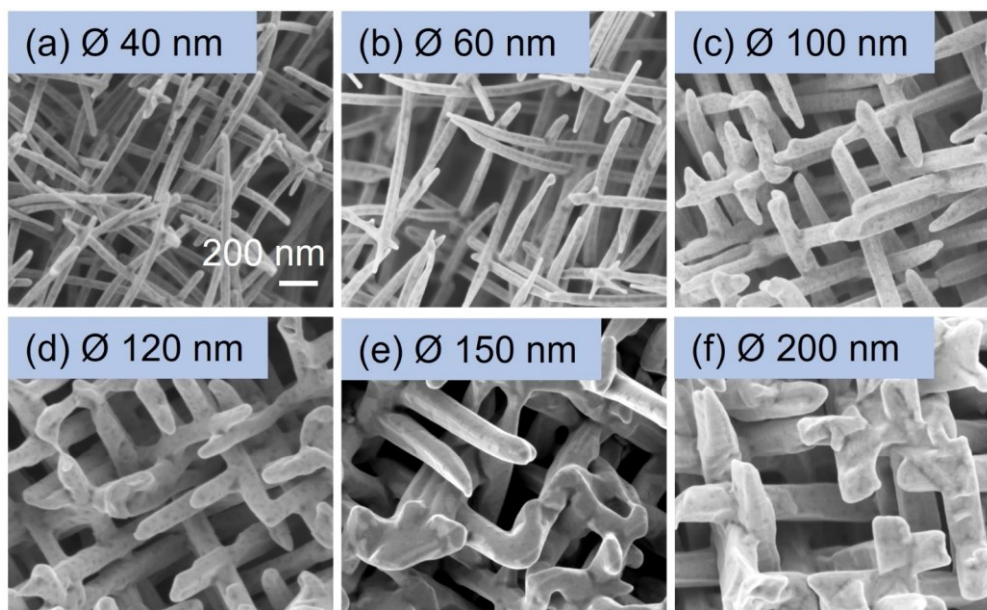


Figure 3.5 SEM images of Au NWNWs with different nanowire diameters, density of $2 \times 10^9 \text{ cm}^{-2}$.

In summary, we demonstrate that the deposition potential has a direct influence on the growth rate of Au NWNWs, and the overall homogeneity of the network. For potentiostatic deposition of the Au NWNWs, a voltage of $U = -0.9 \text{ V}$ vs. Ag/AgCl yields the best compromise between optimal network properties and suitable growth duration. NWNWs deposited under these conditions exhibit a bamboo like crystalline structure, consisting of micrometer sized single-crystalline sections.

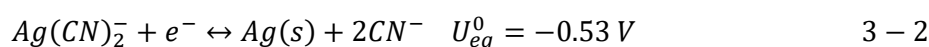
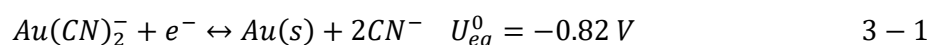
3.2 Au_{1-x}Ag_x Alloy Nanowire Networks

To fabricate Au_{1-x}Ag_x NWNWs, with controlled composition, we investigated the influence of two parameters in the following sections, including the Au:Ag ion ratio in the cyanide-based electrolyte, and the applied potential.

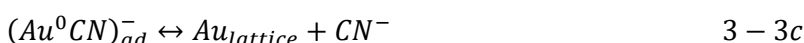
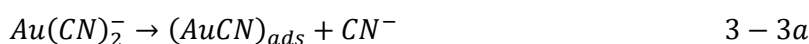
3.2.1 CV for determination of the deposition potential

First, we measured the CVs (scan rate: 50 mV/s) for both KAu(CN)₂ and KAg(CN)₂ (Carl Roth) electrolytes between $U = 0$ and -1.5 V vs Ag/AgCl, as explained in section 2.3.5. The employed etched ion-track membranes were prepared under identical conditions (nanochannel diameter = 150 nm, density = 4×10^8 cm⁻², with Au back-electrode).

The relevant standard reduction potentials vs. Ag/AgCl, for $Au(CN)_2^-$ and $Ag(CN)_2^-$ are:



At small overpotentials, the reaction proceeds through an adsorbed $(Au^0CN)_{ad}^-$ intermediate, which also applies to Ag:



These reactions happen before the actual reduction peak, then at more negative potentials will the direct reduction reaction happen¹³¹. The equilibrium potential for the $Ag(CN)_2^-/Ag$ couple is always more positive than the $Au(CN)_2^-/Au$ couple¹³²⁻¹³⁴. We can see from Figure 3.6 that the two different ions are reduced at different potentials vs. Ag/AgCl. From the orange curve, we can see the reduction peak of Ag initiates from -0.3 V while reaching the highest reduction current at around -0.67 V. For the reduction of Au, the onset potential is around -0.8 V, with the peak potential reaching -1.15 V. These values are corresponding to literatures^{23,133}, while defining the deposition window of Au_{1-x}Ag_x alloy NWNWs.

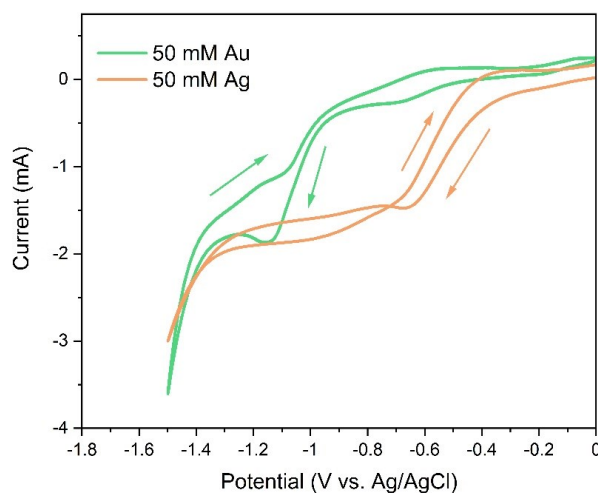


Figure 3.6 Cyclic voltammograms for electrolytes containing 50 mM KAu(CN)₂/ 50 mM KAg(CN)₂ with 250 mM Na₂CO₃ at 60 °C.

The reduction peak potential signals the diffusion and transport limitation at the electrode surface, beyond this potential, the deposition rate of the ions cannot be further increased. Based on the CV results, more negative potentials should lead to more Au-rich depositions. Therefore, the first tests were carried out between $U = -1.1$ V and -0.8 V, with the electrolyte containing 50 mM Au and 5 mM Ag ions.

3.2.2 Nanowire composition as a function of the electrodeposition conditions

Figure 3.7 shows the recorded EDX spectra for nanowire networks deposited at $U = -1.1$, -1.0 , -0.9 , and -0.8 V vs. Ag/AgCl, together with the corresponding SEM images and the average composition. The composition for every sample was obtained by averaging the values of five EDX scans on different sample positions. When nanowires are deposited with the most negative potential at -1.1 V, which is very close to the reduction peak of Au, then the nanowires consist of 89 at% Au and 11 at% Ag. The results show that the Ag content in the nanowires increases for less negative applied potentials. When deposited at -0.8 V, the Au content decreased to 73 at%, and the Ag content increased to 27 at%. All nanowires show homogeneous growth and uniform size distribution, as well as good interconnectivity. This means the change of nanowire composition will not affect the sample morphology.

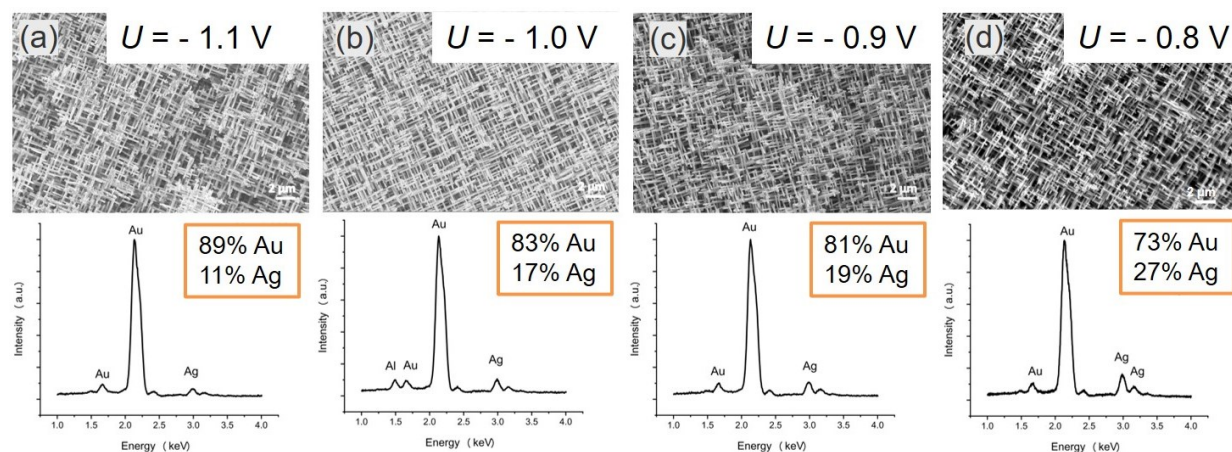


Figure 3.7 SEM image and EDX spectrum of $\text{Au}_{1-x}\text{Ag}_x$ NWNWs deposited at (a) $U = -1.1$ V, (b) $U = -1.0$ V, (c) $U = -0.9$ V, (d) $U = -0.8$ V vs. Ag/AgCl, using electrolyte 50 mM Au + 5 mM Ag.

With the electrolyte containing the metal ion ratio of $[\text{Au}(\text{CN})_2]^+ : [\text{Ag}(\text{CN})_2]^+ = 10:1$, and within the potential range that is required to achieve homogeneous nanowire growth over the entire area, the Ag content can be varied by 17%, between ~ 11 at% and ~ 27 at% Ag. Therefore, to synthesize $\text{Au}_{1-x}\text{Ag}_x$ NWNW with higher Ag content, the Ag ion concentration in the electrolyte has to be further increased. We electrodeposited NWNWs with electrolyte metal ion ratios varying between 10:1 and 3:7. The highest Ag concentration (80 at% Ag and 20 at% Au) was attained using an electrolyte containing 70% Ag ions and applying $U = -0.8$ V vs. Ag/AgCl.

Table 3.1 summarizes the parameters applied, namely electrolyte concentrations and applied potentials, together with the average atomic composition of the NWNWs determined by EDX. The data evidenced the following trend: the electrolyte concentration adjusts the composition of the NWNWs roughly, while the applied potential further finely tunes the targeted composition. The less negative potential will lead to a higher concentration of Ag in the nanowires. By combining these two parameters, we successfully fabricated $\text{Au}_{1-x}\text{Ag}_x$ NWNWs with ($0.1 < x < 0.9$) covering a wide range of compositions.

Table 3.1 Au_{1-x}Ag_x NWNWs electrodeposition conditions and the corresponding nanowire composition

Electrolyte metal ion ratio	KAu(CN) ₂ (mM)	KAg(CN) ₂ (mM)	Deposition potential (V vs. Ag/AgCl)	Sample name	χ _{Ag} in nanowire (at%)	χ _{Ag} in nanowire (at%)
1:0	50	0	-0.9	Au ₁ Ag ₀	100	0
9:1	45	5	-1.1	Au _{0.9} Ag _{0.1}	93	7
9:1	45	5	-0.8	Au _{0.8} Ag _{0.2}	78	22
4:1	40	10	-0.8	Au _{0.7} Ag _{0.3}	63	37
3:2	30	20	-0.9	Au _{0.5} Ag _{0.5}	52	48
3:2	30	20	-0.8	Au _{0.4} Ag _{0.6}	43	57
2:3	20	30	-0.8	Au _{0.3} Ag _{0.7}	27	73
3:7	15	35	-0.8	Au _{0.2} Ag _{0.8}	20	80
0:1	0	50	-0.8	Au ₀ Ag ₁	5	95

Figure 3.8 shows the χ_{Ag} in the NWNWs, determined by EDX, as a function of the Ag ion concentration in the electrolyte, for two different applied potentials, namely $U = -0.8$ V (brown triangles) and $U = -1.1$ V (blue circles). It is seen that the Ag at% in the wire increases almost linearly with the Ag ion concentration in the electrolyte for both voltages. When comparing the brown and blue symbols, we see that for the same electrolyte the less negative potential at -0.8 V yields nanowires with around 20 at% more Ag in the nanowires. By this series of tests, precise control of nanowire composition can be achieved.

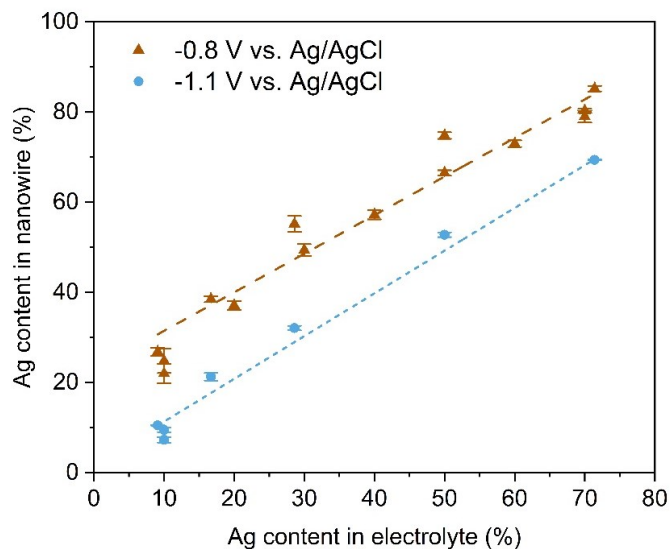


Figure 3.8 Nanowire composition as a function of Ag concentration in the electrolytes at two different deposition potentials. $U = -0.8$ V (brown triangle dot), and $U = -1.1$ V (blue round dot), the error bar comes from the five EDX measurements, and the dashed line is the linear fitting of the data points.

3.2.3 Composition analysis

To analyze the detailed composition of the alloyed nanowires, small sections of the nanowires were analyzed by EDX mapping, which can display the local elemental composition of the sample. In this case, we can see from Figure 3.9 that the distribution of both Au and Ag atoms is very homogeneous, across the nanowires.

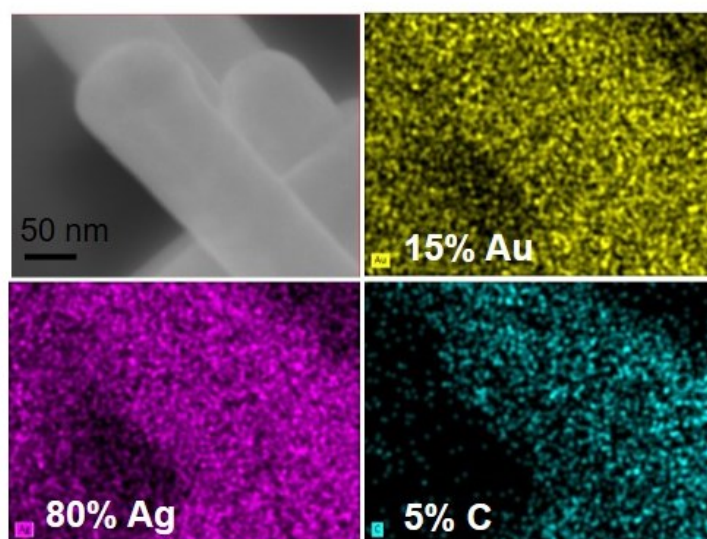


Figure 3.9 EDX mapping of a selected area of a representative NWNW, showing the atomic distribution of Au (yellow), Ag (pink), and C (blue).

Further on, we compared the composition analysis from EDX and XPS. By EDX we analyzed the average composition of the NWNW over a certain area. Figure 3.10 shows the EDX spectra recorded for $\text{Au}_{1-x}\text{Ag}_x$ NWNWs synthesized under different conditions. From top to bottom, the height of the Au

and Ag peaks increases and decreases, respectively, in a systematic manner, indicating an increasing Au content in the nanowire. When we do the EDX measurement from the top direction of the sample, the electron beam can penetrate several micrometers deep into the sample, which means the measured value comes from averaging thousands of nanowires. We found the EDX spectrum from pure Ag NWNW also has a small Au peak, this could originate from the Au substrate, since the NWNW on top is a highly porous structure that electron beam can potentially penetrate through.

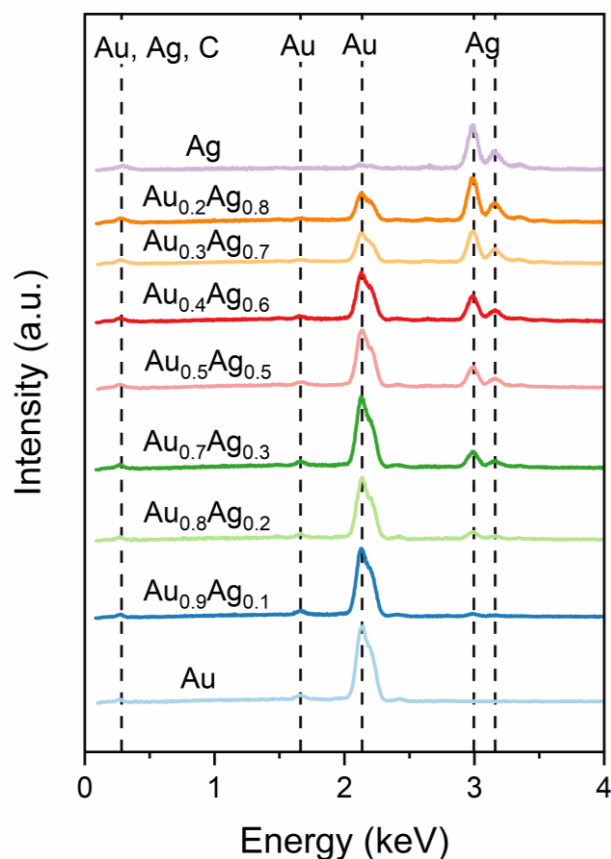


Figure 3.10 EDX spectrums of different composition $Au_{1-x}Ag_x$ NWNWs.

Considering EDX only provides average nanowire composition over a certain area, we analyzed five selected samples by XPS analysis to obtain surface composition values. Figure 3.11 shows the recorded XPS, showing major peaks from Au 4f, Au 4d, Ag 3d, and Ag 3p and three smaller peaks from oxygen, carbon and sodium. We assume carbon and oxygen are normal contamination from air and storage, while sodium can come from our deposition electrolyte (Na_2CO_3), or the surfactant (Dowfax 2A1) mixed inside. Dowfax 2A1 is an anionic surfactant composed primarily of an alkyl diphenyloxide disulfonate, with water and sodium sulfate as minor components¹³⁵.

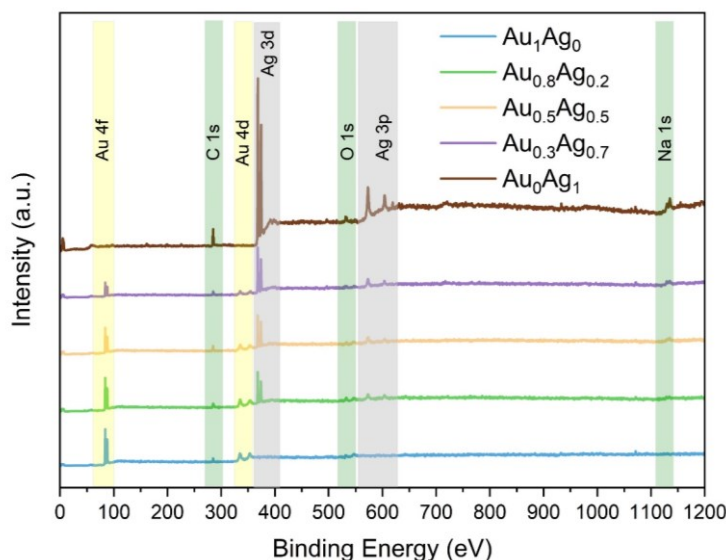


Figure 3.11 XPS spectrum survey of five $\text{Au}_{1-x}\text{Ag}_x$ NWNWs with different compositions.

Figure 3.12 shows a more resolved scan of the peak Au 4f and Ag 3d peaks. As expected, the intensity of the Au 4f peak decreases, and the Ag 3d peak increases with decreasing Au content in the NWNWs. The Ag NWNW sample ($x=0$) shows the Ag $3d_{5/2}$ at 368.2 eV, which represents pure Ag without oxidation. In turn, the Ag $3d_{5/2}$ peak of the $\text{Au}_{1-x}\text{Ag}_x$ alloy NWNWs is slightly shifted towards 368.0 eV, which may indicate a change of chemical state. The Au 4f peak is also slightly shifted to higher binding energies from the pure Au sample (83.95 eV) to $\text{Au}_{0.3}\text{Ag}_{0.7}$ sample (84.05 eV). This is strong evidence that metallic alloys have slightly different peak binding energy than pure metals.

These shifts are attributed to the chemical shift phenomenon, where the electron binding energy is sensitive to the electronic environment of the atom. In an alloy, the atoms of a metal are surrounded by different types of atoms than in the pure element, which changes the local electron density, leading to a chemical shift in binding energy^{136,137}. For instance, studies have demonstrated that the Au 4f peaks in Au–Ag nanostructures shift to higher binding energies as the structures evolve from nanoparticles to nanocages and further to nanoframes, with a total displacement of 0.5 eV¹³⁸. Similarly, the binding energy of the Ag $3d_{5/2}$ peak shifts depending on the oxidation state and the formation of the AuAg alloy, indicating changes in the chemical environment¹³⁹.

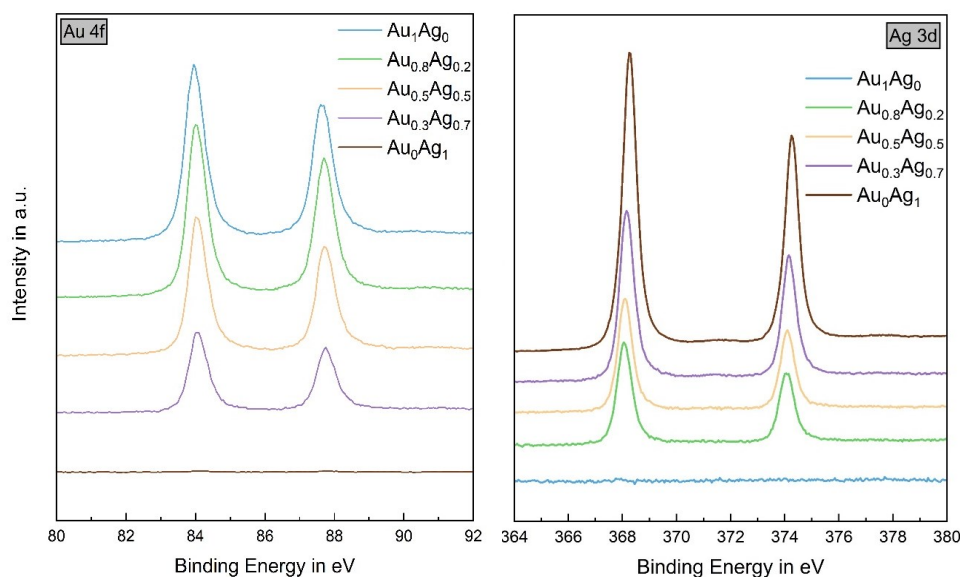


Figure 3.12 XPS spectrum of $\text{Au}_{1-x}\text{Ag}_x$ NWNWs at Au 4f (left) and Ag 3d (right) peak positions.

When we compare the composition of the same sample series determined from these two different methods, we saw the values are slightly different. The results of this comparative study, as shown in Table 3.2, reveal that the values of pure Au NWNW is the same from two measurements, but the results of AuAg NWNWs from XPS shows slightly lower Au content. However, for the pure Ag NWNW, both methods detected a trace of Au, which should not appear, we attribute this to the influence from the Au substrate under the highly porous NWNWs, as well as the deviation caused by the spectrum background and the detection limitations from the two methods.

While both EDX and XPS are widely used for elemental analysis, each technique has inherent limitations that affect quantitative accuracy. EDX provides rapid compositional analysis with relatively deep penetration ($\sim\mu\text{m}$ scale), but it suffers from matrix effects, peak overlap, and limited sensitivity to light elements^{92,140}. In contrast, XPS offers higher surface sensitivity (typically 1–10 nm) and chemical state information, but it is less accurate for quantifying heavier elements and is influenced by surface contamination and charging effects^{141,142}. Due to their fundamentally different probing mechanisms, the comparison between the two measurements has to be interpreted with caution. Therefore, discrepancies between EDX and XPS results are expected, and the variations between the two reflect the complementary nature of the techniques rather than measurement errors.

In conclusion, within the experimental errors there is an excellent agreement in composition analysis, and we cannot identify any significant difference between the average composition of the NWNWs and the nanowire surface composition.

Table 3.2 Comparison of the atomic composition values determined for $\text{Au}_{1-x}\text{Ag}_x$ NWNWs by XPS and EDX.

Sample	$\chi_{\text{Au}} - \text{XPS}$ (at%)	$\chi_{\text{Ag}} - \text{XPS}$ (at%)	$\chi_{\text{Au}} - \text{EDX}$ (at%)	$\chi_{\text{Ag}} - \text{EDX}$ (at%)
Au	100	0	100	0
$\text{Au}_{0.8}\text{Ag}_{0.2}$	73 ± 1	27 ± 1	78 ± 2	22 ± 2
$\text{Au}_{0.5}\text{Ag}_{0.5}$	47 ± 2	53 ± 2	52 ± 3	48 ± 3
$\text{Au}_{0.3}\text{Ag}_{0.7}$	24 ± 2	76 ± 2	27 ± 1	73 ± 1
Ag	1 ± 1	99 ± 1	3 ± 1	97 ± 1

In addition to the XPS measurements, we analyzed the $\text{Au}_{0.8}\text{Ag}_{0.2}$ NWNWs sample by TEM-EDX. Figure 3.13 shows the line scans measured for four nanowires. For each wire, the TEM image and the corresponding line scan across the nanowire surface inwards is shown. We see that atomic composition of the single wires from shell to core, and the results show slight fluctuation, for around 10 at%. This fluctuation is in agreement with the EDX results, and the deviation is accepted for electrodeposition process. Therefore, the reason for the measurement differences from XPS and EDX can be the intrinsic differences from different methods. Also, this proves our assumption that the detector can receive some signal from the sample substrate, which is pure gold, because the network structure has a 90% porosity, hence increase the overall measured Au content.

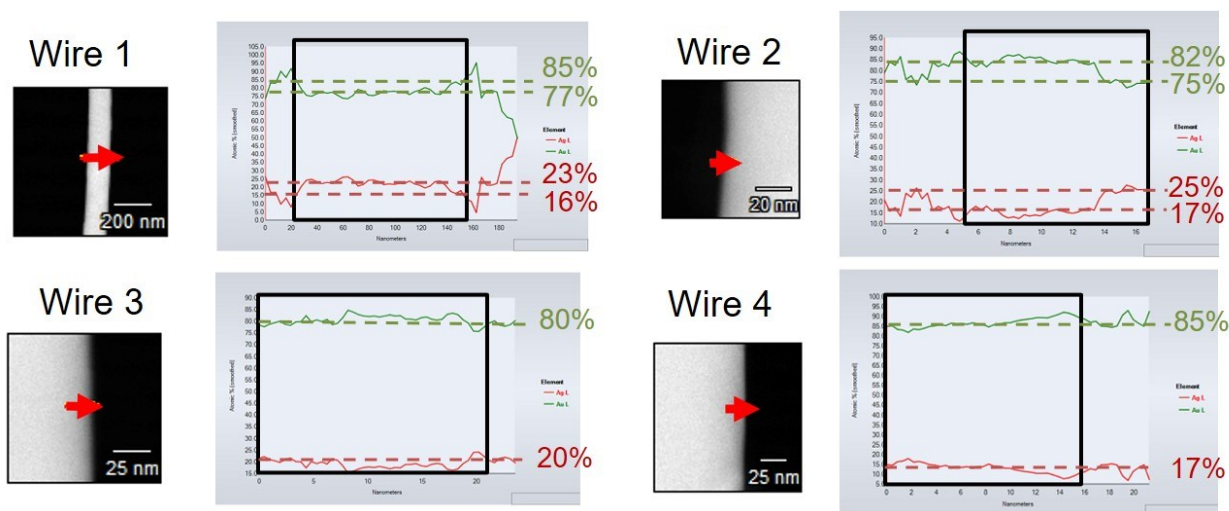


Figure 3.13 TEM line scan of four single nanowires atomic composition distributions, green lines represent the atomic composition of Au, and the red lines represent the atomic composition of Ag, the black box represents the measurement on the nanowire.

In summary, we successfully synthesized $\text{Au}_{1-x}\text{Ag}_x$ NWNWs with controlled composition from 10 at% to 90 at% Ag, by combination of deposition potential and varied electrolyte concentration. Through different analysis methods, the NWNWs show homogeneous composition distribution in a single wire and through a large area.

3.3 Nanoporous Au Nanowire Networks

In this section, the fabrication and characterization of NWNWs of porous nanowires by selective dealloying of Ag from the $\text{Au}_{1-x}\text{Ag}_x$ alloy NWNWs is presented. $\text{Au}_{1-x}\text{Ag}_x$ NWNWs are suitable candidate for dealloying, as we showed in the previous section, they form a homogeneous solid solution at all concentrations⁵⁶. Our goal is to produce porous Au nanowires that retain their 3D network structure with even larger surface area, while simultaneously reducing both the sample weight and the gold usage, which would also reduce costs. Furthermore, we want to explore to which extent we can tailor the hierarchical porosity of these NWNWs. We systematically investigated the influence of the most important parameters on the morphology and mechanical stability of the porous NWNWs, including the nanowire size, Ag at% in the NWNWs, and the dealloying time.

3.3.1 Experimental analysis of $\text{Au}_{1-x}\text{Ag}_x$ alloy nanowire dealloying process

In the case of $\text{Au}_{1-x}\text{Ag}_x$ bulk and thin films, the minimum Ag concentration for successfully dealloying yielding a porous structure is ~ 55 at% Ag and 45 at% Au¹⁴³, while the most commonly used composition to fabricate nanoporous gold is 75 at% Ag with 25 at% Au.⁵⁶ However, in the case of nanowires, they exhibit much higher surface-to-volume ratio, which could potentially lead to different diffusion mechanisms. Therefore, it is important for us to experimentally test different composition and dimension parameters to understand the process in nano-scale.

To explore how does the $\text{Au}_{1-x}\text{Ag}_x$ NWNWs behave during the dealloying process, with different compositions at different dealloying time, we designed a series of experiments, with three different precursor alloys, and three different diameters of nanowires, with ex-situ SEM and EDX analysis at every time point, to fully understand the process, and find out the most suitable protocol of fabricating stable nanoporous nanowires. We will discuss how these two parameters influence the nanowire dealloying process in the following sections. The synthesis parameters of the $\text{Au}_{1-x}\text{Ag}_x$ NWNWs were selected based on the results discussed in section 3.2 with desired compositions. The dealloying conditions are given in section 2.2.6, by using 65% nitric acid at room temperature.

Influence of nanowire composition

We synthesized $\text{Au}_{0.4}\text{Ag}_{0.6}$, $\text{Au}_{0.3}\text{Ag}_{0.7}$, and $\text{Au}_{0.2}\text{Ag}_{0.8}$ NWNWs, with the same nanowire density $2 \times 10^9 \text{ cm}^{-2}$, and the same nanowire diameter 150 nm. The three samples were dealloyed in concentrated nitric acid, under the same conditions. Figure 3.14 shows SEM images of the three samples before and after dealloying for 1h, 4h, 8h, and 24h. The composition was determined by EDX and is marked at the bottom of every image. The images before dealloying show that the nanowires of the three samples exhibit the same initial morphology and geometry.

Figure 3.14 first row shows the ex-situ analysis of the $\text{Au}_{0.4}\text{Ag}_{0.6}$ NWNW sample dealloying process, we can see that the Ag at% decreases gradually with time, and the pores on the nanowire surface first grow larger gradually, then begin to roughen. At the beginning, it consists of 63 at% Ag, the dealloying happened quite inhomogeneous at the beginning (at 1 h), the pores are not distributed evenly on the nanowire surface, even after 24 hours, there is still 19 at% Ag left, also the pores are roughened, some of them are even closed, so this precursor alloy has too little Ag to have a fast dealloying process, which cannot create a porous structure with low Ag concentration and high surface area.

Figure 3.14 middle row shows the $\text{Au}_{0.3}\text{Ag}_{0.7}$ NWNW dealloying process, for this sample, it is evident that the dealloying rate is higher than for the previous sample. When the Ag concentration increased to 70 at% at the initial stage, after dealloying for 1 hour, there was only 9 at% Ag left, and pores appeared homogeneously on the nanowire surface. We can see that the pore size gradually increases from 1 h to

8 h, and the network structure remains free-standing. After 24 hours, there is less than 1 at% left in the sample, but we have also observed a severe roughening morphology, and many pores are closed due to the surface diffusion.

Figure 3.14 bottom row shows the $\text{Au}_{0.2}\text{Ag}_{0.8}$ NWNW, when the Ag concentration further increased to 77 at%, we observed a very fast pore evolution after just 1 h, with homogeneous pore distribution. However, this fast volume loss caused the network structure to collapse, the crossing junctions are already partially destroyed after 1 hour. After 24 hours, the wire size is severely shrunk, and the porous surface is roughened. We can clearly observe the strong surface diffusion process here, with the closing of the pores. The reason can be that the large specific surface area strongly facilitated the diffusion process.

This series of testing showed a direct visualization of the $\text{Au}_{1-x}\text{Ag}_x$ NWNWs dealloying evolution process as a function of time. The comparison between the three precursor alloys illustrated that the initial composition is an important factor, which can largely affect the dealloying process, including the composition change as well as the pore evolution. Higher Ag content (e.g., 80 at%) in the Au-Ag precursor leads to faster dealloying but causes more volume and stability loss. Lower Ag content (e.g., 60 at%) slows dealloying but inhomogeneous pores. From the experimental point of view, $\text{Au}_{0.3}\text{Ag}_{0.7}$ is a more suitable choice to produce a porous NWNW with an appropriate dealloying rate, without collapsing or inhomogeneous pore distribution.

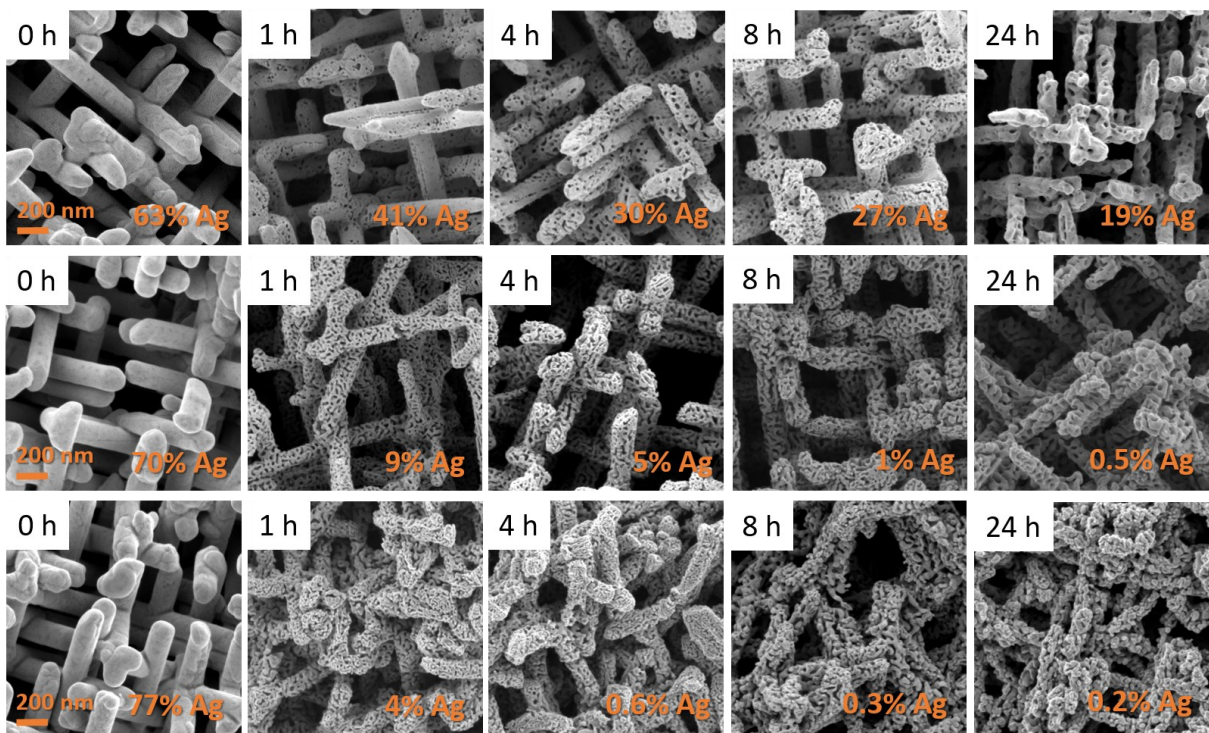


Figure 3.14 SEM images of $\text{Au}_{1-x}\text{Ag}_x$ alloy nanowire dealloying process, with three different composition precursor alloy.

Figure 3.15, it shows how the sample composition change with different dealloying time, we can see that the higher the initial Ag concentration, the faster the dealloying goes. And the less Ag is remained inside the nanowires after 24 hours.

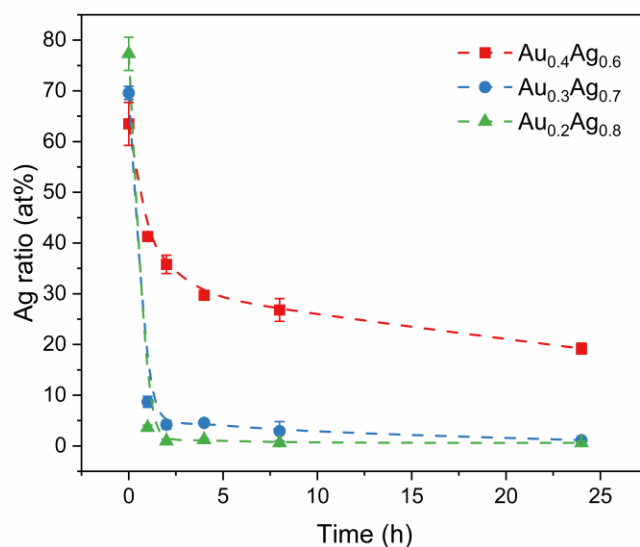


Figure 3.15 Nanowire composition change with dealloying time

In summary, with this NWNW geometry (nanowire diameter 150 nm, density $2 \times 10^9 \text{ cm}^{-2}$), the most suitable composition would be 70 at% Ag with 30 at% Au to produce a stable porous NWNW sample. But the dealloying time must be strictly controlled to limit the surface diffusion (shorter than 8 hours), since the diffusion will severely coarsen the structure and cause the loss of surface area in the end.

Influence of nanowire size

Another important factor could also potentially influence the dealloying process as well as the pore size evolution, is the nanowire diameter. Therefore, we synthesized $\text{Au}_{1-x}\text{Ag}_x$ NWNWs with three different nanowire diameters 150 nm, 100 nm, and 60 nm, each with two different composition precursors. Together with ex-situ SEM and EDX analysis of all samples.

In addition to the results showed in the last section, we synthesized two other NWNWs with 150 diameter nanowires, with initial composition of 58 at% and 65 at% Ag, as shown in Figure 3.16. We observed similar process as discussed in the last chapter, the 58 at% Ag sample showed slower dissolution of Ag, with 25 at% Ag still left after 24 hours. During the dealloying process, we can see how the pores start to evolve on nanowire surface, along with the nanowire size shrinkage. After 24 hours, the nanowire size decreased from 150 nm to around 112 ± 5 nm. For the 65 at% Ag sample, the dealloying proceeded much faster, the Ag concentration decrease trend can fit well in the curves in Figure 3.15. With higher initial Ag concentration, after 24 hours dealloying, the nanowire size is further decreased to 100 ± 10 nm, due to more Ag dissolution.

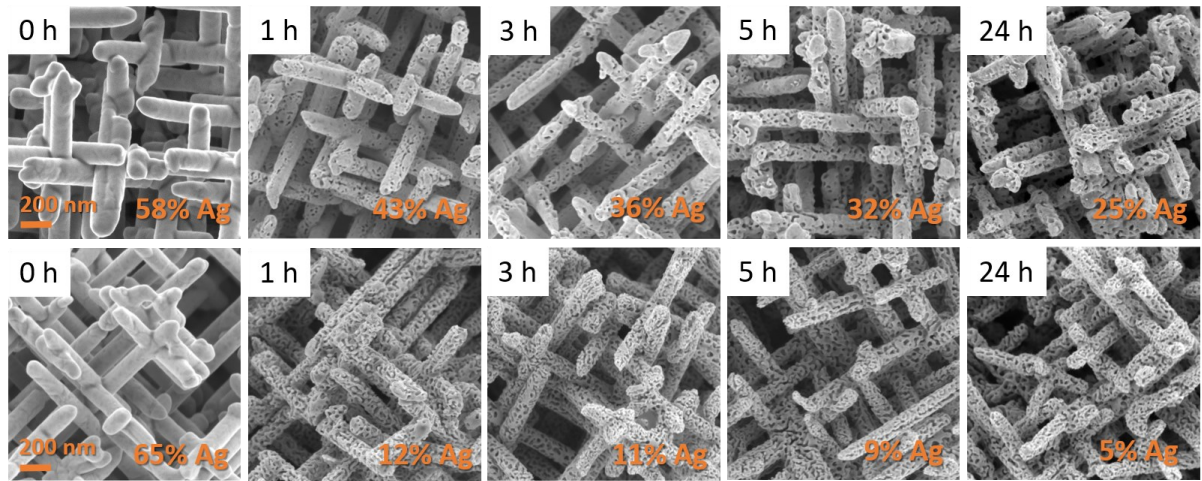


Figure 3.16 SEM images of 150 nm diameter nanowire dealloying process of nanowire morphology evolution with time (from left to right) of two different composition precursor alloy.

Figure 3.17 shows the dealloying process of 100 nm $\text{Au}_{1-x}\text{Ag}_x$ NWNWs, with initial Ag concentration of 61 at% and 68 at%. With initial only 61 at% Ag, the nanowires showed homogeneous pores evolve on the surface only after one hour, with 24 at % of Ag in the nanowires, which is much faster and much less Ag residual compare to the 150 nm NWNWs with similar composition. But after 24 hours, the porous nanowires are severely coarsened, the nanowire size is largely decreased to 56 ± 10 nm, from which we observed lots of transverse pores on the nanowires. The nanowires showed bending morphology with partial network collapse, with the loss of interconnecting points. When the initial Ag concentration increased to 68 at%, there is already large pores shown after 1 hour of dealloying, with only 6% Ag left in the nanowires, resulting in a collapse of the network structure, due to the large volume loss. The structure collapse can be observed everywhere, also in the crossing junctions. Such an instability can result in an effective reduction of the total surface area. After 24 hours dealloying, there are almost no pores observed on the surface, due to roughening and merging caused by diffusion. The sample consists thus of very rough nanowires with diameter 42 ± 12 nm, partially discontinuous. In summary, when the nanowire size is decreased to 100 nm, the network structure possesses even higher surface to volume ratio, with fewer crossing junctions. These factors result in a faster dissolution of Ag and a decrease of structural stability when compare with 150 nm NWNWs.

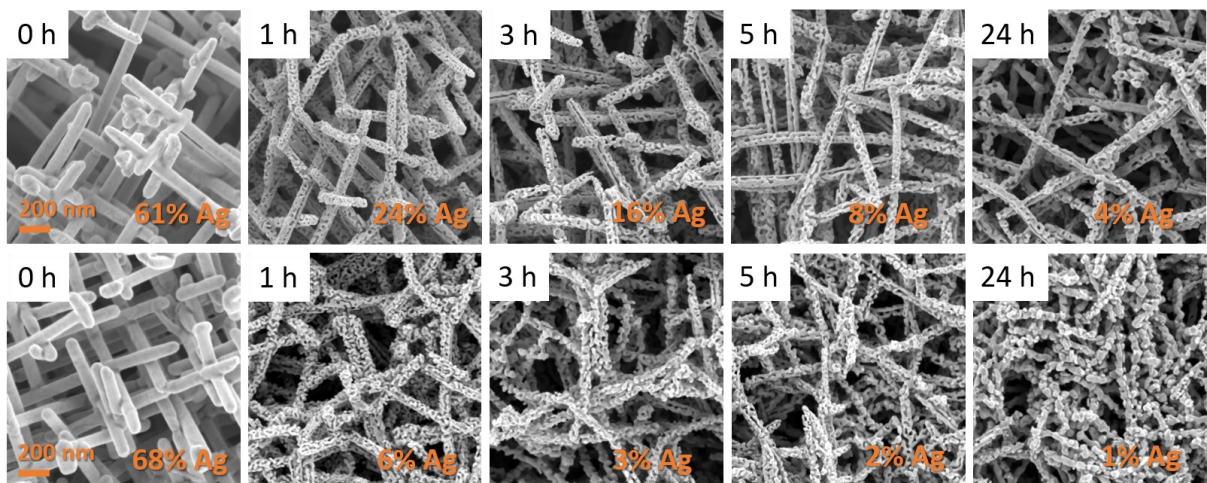


Figure 3.17 SEM images of 100 nm diameter nanowire dealloying process of nanowire morphology evolution with time (from left to right) of two different composition precursor alloy.

Figure 3.18 shows the SEM images of NWNWs with nanowire diameter 60 nm dealloyed under the same conditions, with initial composition of 62 at% and 68 at% Ag. With initial 62 at% Ag, we saw a fast and homogeneous pore evolution even after 1 hour, and we already observe coarsening effect after 5 hours. This demonstrates that with higher surface to volume ratio, both dissolution and diffusion is largely facilitated. While the network structural stability is also more affected, there is already collapsing observed after one hour, which is highly unfavorable if we aim for a stable network structure. Also, this is not beneficial for catalytic applications, there will be no space for the sample to access electrolytes and reactants. With initial 68 at% Ag, there is almost no Ag detectable after 24 hours dealloying, there is already pore closing observed after 3 hours, and the network structure is completely lost after 5 hours. In summary, both series showed faster Ag dissolution compare to the NWNWs with larger nanowire diameters, but the destroy of the network structure is not desirable for the following catalysis tests.

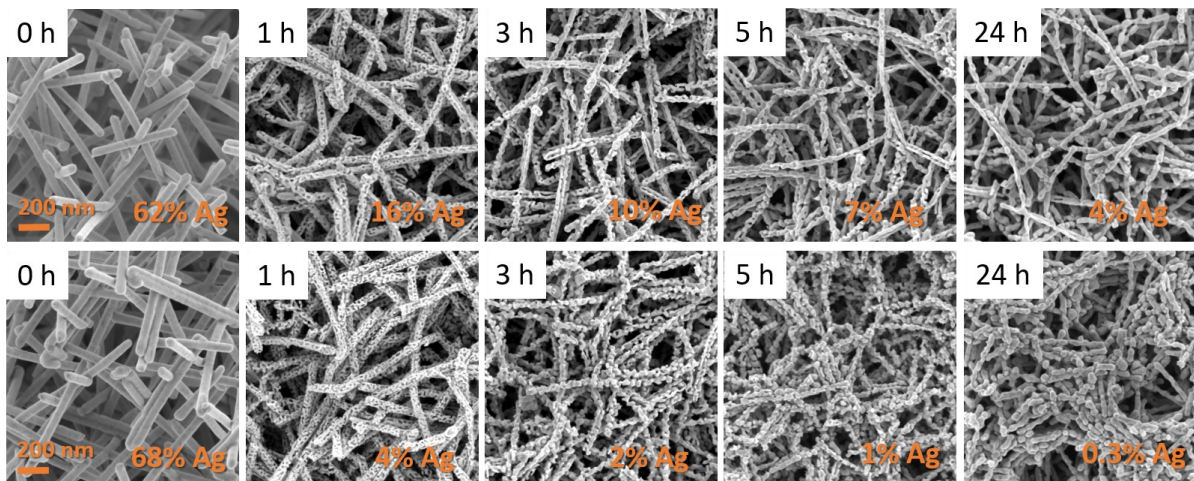


Figure 3.18 SEM images of 60 nm diameter nanowire dealloying process of nanowire morphology evolution with time (from left to right) of two different composition precursor alloy.

Figure 3.19 shows all sample composition change with different dealloying time, it is obvious that with the same initial Ag concentration, the smaller nanowires have a faster Ag dissolution rate, when there is more surface exposed to the corrosion solution. As we can see, the Ag dissolution is the fastest at the beginning (0 to 3 hours), shown by the high slope of the dash lines. With the increase of dealloying time, the dissolution becomes slower, then will enter a plateau after 6 to 8 hours. The smaller the nanowire, it will enter this plateau sooner. When we compare the different initial compositions, with more Ag atoms on the surface, the driven force to start the Ag dissolution is larger, which results in the faster dealloying speed.

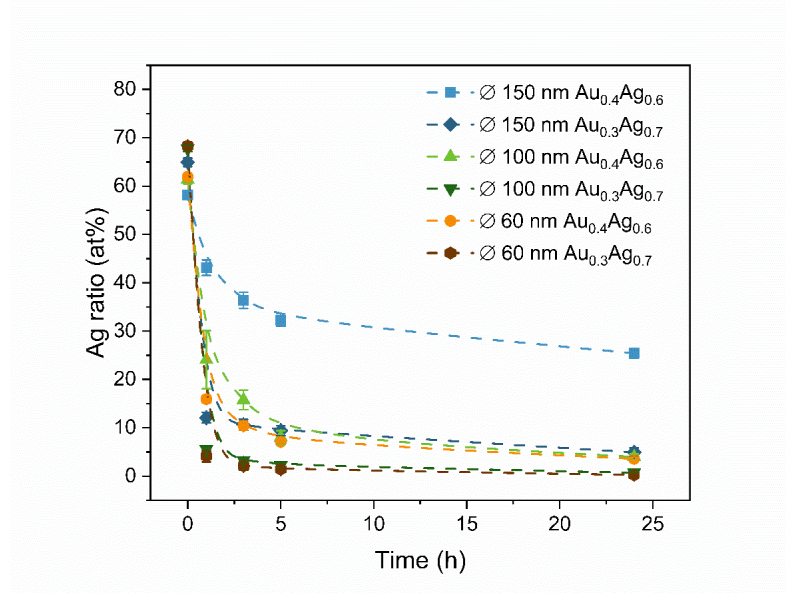


Figure 3.19 Nanowire composition change with dealloying time

In summary, different nanowires showed different composition change and morphology evolution during the dealloying process. All suffer from similar diffusion-caused coarsening effects, which are more pronounced with smaller nanowire diameter. The results reveal that dealloying can cause mechanical instability of the NWNW. In these cases, the volume loss caused during Ag dissolution resulted in the partial loss of connecting junctions (or reduced connection size) between the nanowires, thus degrading the self-supporting ability of the network structure. This can be avoided by using initial $\text{Au}_{1-x}\text{Ag}_x$ NWNWs with larger solid fraction and more connecting junctions, that yield better mechanical stability that can be maintained after the free corrosion process. Thus, for further experiments on the catalytical performance of the porous NWNWs, we synthesized a porous NWNW with 150 nm diameter nanowires and density of $2 \times 10^9 \text{ cm}^{-2}$, the results will be discussed in section 4.2.3.

3.3.2 XPS analysis of porous Au NWNW after dealloying

From the past research about nanoporous Au bulk or thin film samples, they reported that after dealloying, the sample surface composition is different from the bulk. From Zielasek¹⁴⁴, they found that there is 4.4% Ag present at the surface, while only 0.7% of the whole nanoporous gold foam. Similar results were reported by Schaefer¹⁴⁵ and Wittstock¹⁴⁶. They all reported that the nanoporous gold produced by free corrosion in strong acid solutions exhibited a Ag-rich shell. Similarly, we employed XPS to analyze the surface composition of the dealloyed NWNWs and compare it to the EDX results, which provides the average composition.

Since catalytical reactions happen mostly at the top surface layer of the sample, it is essential to clarify the possible presence of a Ag-rich shell on the nanowires of the NWNW. To study the surface composition of the dealloyed nanowires, we performed XPS analysis. Due to the detection limitation depth of photoelectrons¹⁴², XPS is very suitable to study the surface composition only up to several nanometers thick.

Figure 3.20 shows the XPS results of a pristine $\text{Au}_{0.3}\text{Ag}_{0.7}$ NWNW (black) and two samples after dealloying with 1 (red) and 6 hours (blue). All samples exhibit the main Au and Ag peaks, as well as smaller carbon and oxygen peaks, attributed to surface contamination.

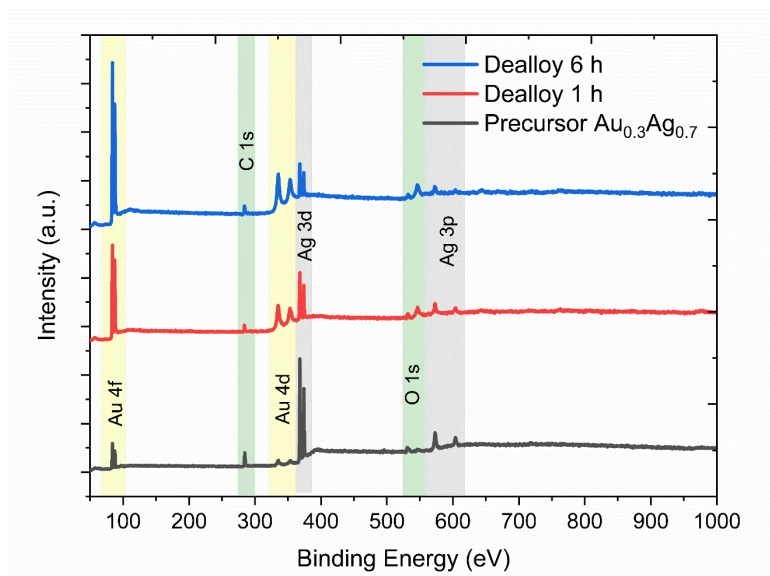


Figure 3.20 Overall XPS survey spectra of precursor $\text{Au}_{0.3}\text{Ag}_{0.7}$ NWNW sample (black), after dealloy 1 hour (red), and after dealloy 6 hours (blue) in concentrated nitric acid.

Figure 3.21 shows XPS spectra recorded around the Ag 3d and Au 4f peak positions. Figure 3.21 (a) shows that the Ag 3d peaks shift after the dealloying process, the Ag $3d_{5/2}$ peak shifts from 368 eV to 367.8 eV. The peak of the initial sample (368.0 eV) corresponds to pure Ag, while the shifted peak after dealloying can be attributed to Ag_2O (367.7 eV) or AgO (367.2 eV), after oxidation by the strong acidic solution. This is in agreement with results from Wittstock and et al.¹⁴⁶, that the oxidized Ag species can lead to a change to more negative binding energy relative to Ag(0). The binding energy of the Ag nanowire is also different than bulk Ag, where the Ag $3d_{5/2}$ peak should have the Ag(0) peak energy at 368.2 eV, and the Ag(1) should be shifted to 368.7 eV¹⁴⁷.

Figure 3.21 (b) shows the Au 4f peaks, in this case, the spectra reveals also a peak shift between the initial sample and the dealloyed samples. For the pristine sample, the Au $4f_{7/2}$ peak is, as expected for Au(0) located at 84 eV. For the dealloyed samples, in turn, a shift to higher binding energies should be expected corresponding to the oxidation states of Au gold^{148,149}, which is not the case here. The Au $4f_{7/2}$ peak from two dealloyed samples shifts slightly to lower binding energy around 83.89 eV (1 h) and 83.95 eV (6 h), respectively. From the results of Hansch¹¹⁵, they did not observe any peak shift caused by the dealloying process, since Au cannot be oxidized in nitric acid. But the peak position here is similar to the pure Au NWNW sample, so the peak shift may represent some Au atoms on the surface are freed from the alloy form and going back to pure Au atoms binding with Au only.

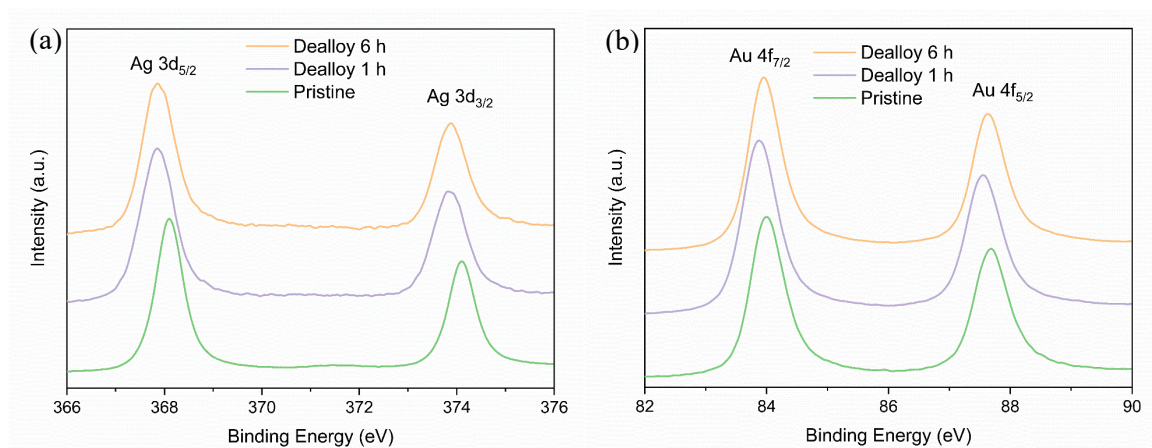


Figure 3.21 XPS spectra of (a) Ag 3d, and (b) Au 4f peaks of sample $\text{Au}_{0.3}\text{Ag}_{0.7}$ NWNW (green), after dealloying for 1 hour (purple), and after dealloying 6 hours (orange), all normalized by peak intensity.

Next, we compared the composition values obtained from the XPS spectra with the results from the EDX analysis for the $\text{Au}_{0.3}\text{Ag}_{0.7}$ NWNW before and after dealloying. The summary for the three samples is presented in Table 3.3. The $\text{Au}_{0.3}\text{Ag}_{0.7}$ NWNW before dealloying shows only slightly higher Ag concentration from XPS than EDX, which is in good agreement considering the probing differences from two methods. However, for the dealloyed samples, the Ag concentration measured from XPS is more than 10 at% higher than from EDX. Considering the detection depth difference between the two methods, as mentioned previously, XPS provides information of the composition at the surface, from a penetration depth of only several nm, but the EDX analysis here used 15 keV electron beam, which can penetrate through several micrometers thick. The main reason for this difference can be the Ag enrichment on the porous nanowire surface than in the core, as mentioned at the beginning of this section, a Ag-rich shell has been reported by many studies before^{115,144,146}, the Ag enrichments especially form on the ligaments surface and form clusters¹⁵⁰, causing the XPS measurements to show a higher Ag concentration on the surface than the bulk. This effect was found both by chemical and electrochemical dealloying methods to fabricate nanoporous structure, which should be taken into consideration especially when testing the samples for catalytic reactions. The second reason can be the substrate effect. After the dealloying process, the network porosity further increased to around 80%, then more electrons can reach the sample substrate, EDX detector can also receive partial signals from the substrate, thus generating an even higher Au at% value than the actual nanowire composition.

Table 3.3 Pristine and dealloyed NWNWs composition analysis by XPS and EDX.

Sample/ Composition	$\chi_{\text{Au}} - \text{XPS}$ (at%)	$\chi_{\text{Ag}} - \text{XPS}$ (at%)	$\chi_{\text{Au}} - \text{EDX}$ (at%)	$\chi_{\text{Ag}} - \text{EDX}$ (at%)
Pristine $\text{Au}_{0.3}\text{Ag}_{0.7}$ NWNW	21 ± 2	79 ± 2	27 ± 1	73 ± 1
Dealloy 1 hour	68 ± 1	32 ± 1	87 ± 2	13 ± 2
Dealloy 6 hours	83 ± 1	17 ± 1	97 ± 1	3 ± 1

In summary, XPS measurement results provide unique information about the porous nanowire surface, the XPS spectra shows a Ag-rich shell of the porous nanowires after the dealloying process, which is around 10-20% higher than the bulk composition. This Ag-rich surface layer may cause different catalytic effects than expected, since alloys can catalyze the methanol oxidation reactions differently than single metals. However, the current dealloying protocol cannot produce a completely Ag free porous Au NWNW without destroying the network structure or coarsening all the pores on the surface. Therefore, the catalytic results from porous NWNWs have to be carefully examined to discuss influential factors from various aspects.

3.3.3 TEM analysis of porous Au nanowires after dealloying

In order to further analyze the crystallographic information of the porous nanowires, we did TEM analysis of the single nanowires. For this, the networks were broken apart in an ultrasonic bath, then drop casted onto TEM grids for HRTEM analysis. Figure 3.22 shows the TEM images of the $\text{Au}_{0.3}\text{Ag}_{0.7}$ NWNW dealloyed for 1 hour at different magnifications. We can see from Figure 3.22 (a) that the pores extend into the core of the nanowire. Some pores even penetrate through the nanowires, creating a hollow structure. The image reveals also planar defects along the nanowire, which seem to have been maintained during the formation of the pores throughout the dealloying process, keeping their directions and shape. To have a closer look at the crystal defects, we did high-magnification imaging, as shown in Figure 3.22 (b) and (c). These images reveal that the planar defects are a series of micro-twins and stacking faults closely packed together.

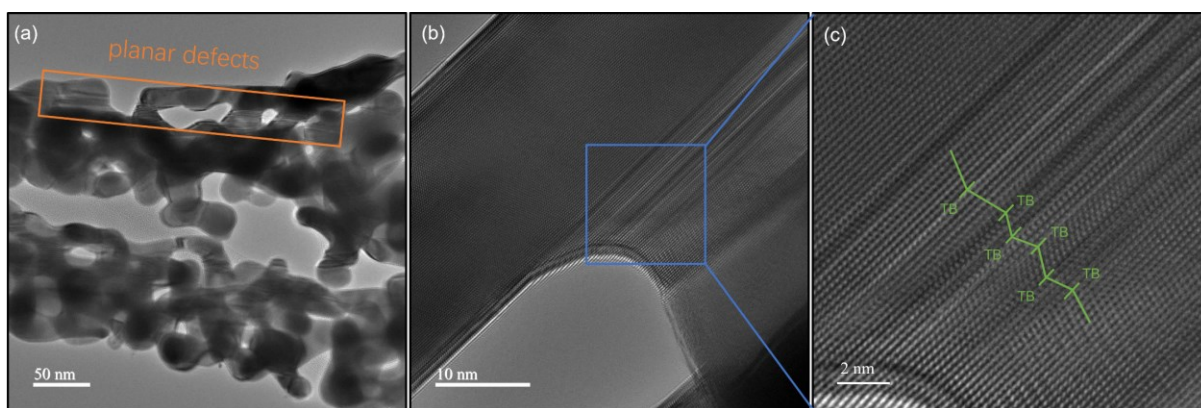


Figure 3.22 TEM images of nanoporous Au nanowires after dealloying for 1 hour.

We did the same analysis with the second sample, which is the $\text{Au}_{0.3}\text{Ag}_{0.7}$ NWNW dealloyed for 6 hours. Figure 3.23 (a) shows that the nanowire size is profoundly shrunk. As the Ag atoms continue being dissolved, the pores get larger and the porous structure is coarsened over time. The hollow structure has disappeared compared to Figure 3.22 (a), and the ligaments on the nanowires have lost interconnections. It seems that the nanowire stability is largely affected by the longer dealloying time, since in some images the nanowires turned into a mixture of nanowire broken segments. In this sample, we also saw a series of stacking faults, as well as some twinings overlaying each other, as shown in Figure 3.23 (b, c). It is certain that our porous nanowires have lots of defects, but due to the thickness of the sample, and being multi-crystalline, it is difficult to distinguish all of the defects clearly.

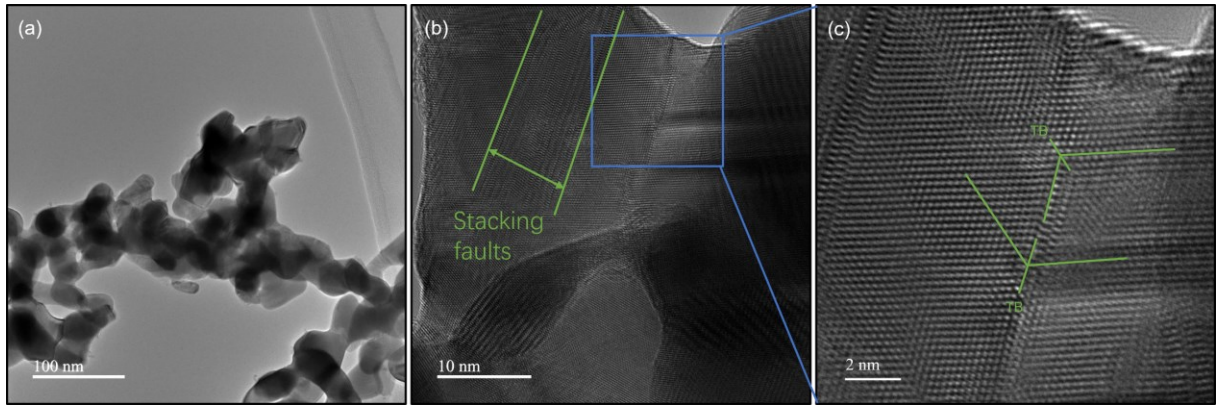


Figure 3.23 TEM images of nanoporous Au nanowires after dealloying for 6 hours.

Figure 3.24 shows electron diffraction patterns obtained for the samples dealloyed for 1 h (a) and 6 h (b). By measuring the distance from the reflections to the center, we calculated the lattice plane distances, and subsequently identified the corresponding planes. Their miller indexes are marked within the figures. The diffraction patterns show multiple reflection points instead of rings, which indicates that the sample is not fine polycrystalline but instead consists of single-crystalline sections.

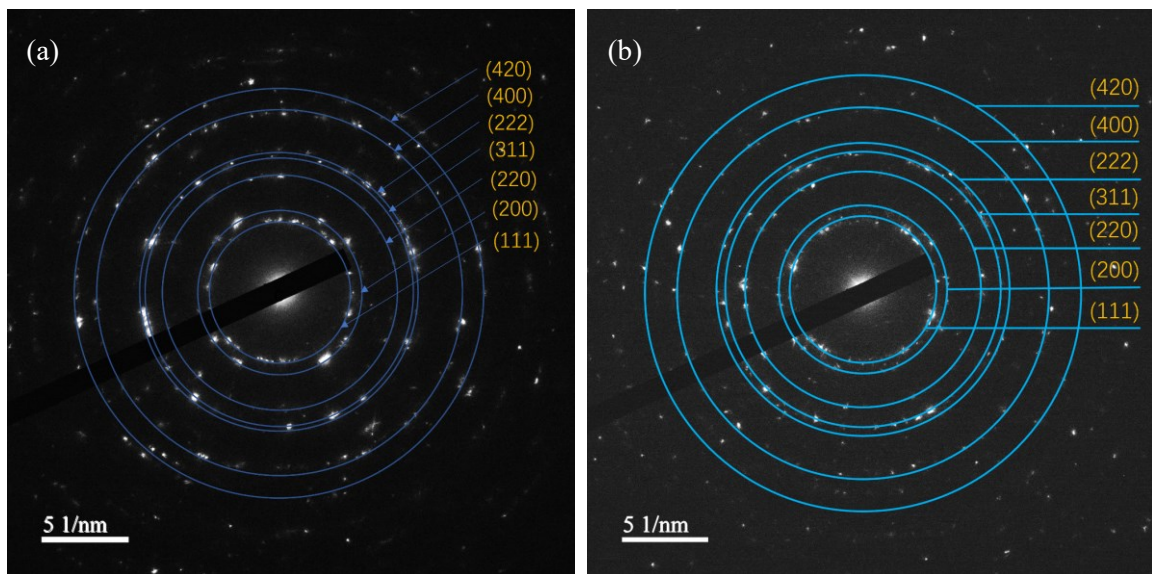


Figure 3.24 Diffraction pattern of dealloyed nanowires: (a) dealloyed for 1 hour, (b) dealloyed for 6 hours.

3.3.4 Summary

Nanoporous nanowire networks have been successfully synthesized by dealloying. From the series of testing, we learned both precursor composition, as well as the nanowire size, can lead to a different dealloying and pore evolution process. In general, we can see the pore size increases with the dealloying time increase, and then the porous structure gets coarsening also with time. By dealloying NWNWs with identical geometrical parameters and three different compositions, we demonstrate that the initial composition has to be optimized in order to create a stable porous nanowire network. When the sacrificial Ag content is too low, the Ag atoms cannot be dealloyed efficiently, while when the Ag content is too high, the large volume loss results in the collapse of the network structure. Systematic EDX and XPS measurements revealed that the free corrosion process results in a Ag-rich surface layer

for all initial compositions. The TEM analysis revealed that the porous nanowires exhibit many crystallographic defects, especially planar defects, including stacking faults and twinings. The TEM images reveal that the pores formed during dealloying can exist within one single crystal. In summary, to produce a stable porous NWNW, all the parameters have to coordinate with each other to yield the most ideal sample morphology and composition.

4. Electrochemical Properties of Various NWNWs

In this chapter, we characterize the electrochemical properties of three types of NWNW samples, namely the pure Au NWNWs, the $\text{Au}_{1-x}\text{Ag}_x$ alloy NWNWs, and the nanoporous NWNWs. First, we discuss the determination of the electrochemically active surface area (ECSA) by two different methods. The ECSA determination is essential to characterize the NWNW structure in electrochemical reactions scientifically and understand how they react in different electrolytes. Second, the NWNWs are tested in alkaline electrolytes to catalyze the methanol oxidation reaction. The influence of different parameters such as NWNW geometry, atomic composition, and electrolyte concentration is systematically investigated. Third, we present the sample characterization by SEM and EDX before and after the catalytic reactions, which is performed to study how the morphology or compositions of the samples are affected by the specific reactions.

4.1 Electrochemically Active Surface Area Measurement

When characterizing a catalyst, first the ECSA should be determined. The ECSA indicates the availability of the geometrical surface area toward electrochemical reactions. An ideal catalyst for a certain reaction should exhibit high ECSAs and a large number of active sites. This is why nanomaterials are advantageous in the catalysis field, because nanostructuring can provide very high specific surface areas compared with traditional bulk materials.^{4,5,144} In this work, two different methods for measuring the ECSA of NWNWs were used. The integration of the faradaic charge transfer of the Au surface oxide reduction reaction was applied for the Au NWNWs. The double-layer capacitance (DLC) method was applied for the $\text{Au}_{1-x}\text{Ag}_x$ NWNWs and the nanoporous Au NWNWs. The first method can only be applied to pure Au samples, while the second one can be applied regardless of the surface chemical composition. Details about the DLC measurements are provided in section 4.1.4, obtained ECSA values are always compared with the theoretically calculated surface area values (S_{GEO}).

4.1.1 Au NWNW

The ECSA of three Au NWNWs with nanowire diameters 80, 130, and 170 nm, with the same wire density = $4 \times 10^8 \text{ cm}^{-2}$, were estimated by applying the AuO reduction peak area integration method. With the increase of nanowire diameter, the total S_{GEO} increases accordingly, assuming all the nanowire surface can participate in the reaction, the measured ECSA should also increase. To systematically measure their ECSA, all three samples are measured under the same conditions. Figure 4.1 shows representative SEM images of the three samples, we can see when the nanowire diameter is smaller than 100 nm (Figure 4.1 (a)), the wires tend to bend due to the lower number of crossing junctions, and they cannot maintain the original orientations (45° to the horizontal plane) of the nanochannels in the template. When the nanowire diameter increases to 130 nm, the nanowires can maintain their 45° orientation better, but still show slight bending at some positions. When the nanowire diameter is 170 nm, the wires are well connected and they appear straight.

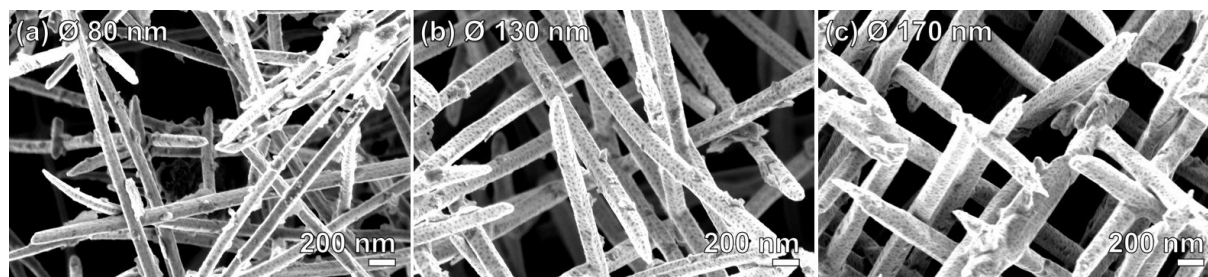


Figure 4.1 SEM image of Au NWNWs with the same density ($4 \times 10^8 \text{ cm}^{-2}$), and different diameters (a) 80 nm, (b) 130 nm, and (c) 170 nm.

In order to calculate the theoretical geometrical surface area (S_{GEO}) of the NWNWs, we require the planar area, the nanowire density, as well as the average nanowire diameter and length. Thus, for every sample, we determined the size distribution by measuring the diameter of 100 nanowires from SEM images. The results are summarized in Figure 4.2. The average nanowire diameter is 86 ± 14 , 131 ± 15 , and 170 ± 17 nm, respectively. The results show around 10% diameter deviation, which is a standard deviation from the etching process. As explained in section 2.1.1, during the ion irradiation process, the high energy ion will break the polymer chains along its trajectory path, which leaves many broken bonds and carboxy groups, and they are especially easy to dissolve in the concentrated alkaline etching solutions. However, the random breakages are not locally uniform, thus the local etching rate is slightly varied, which makes the nanochannel diameter along the ion penetration path also deviate.

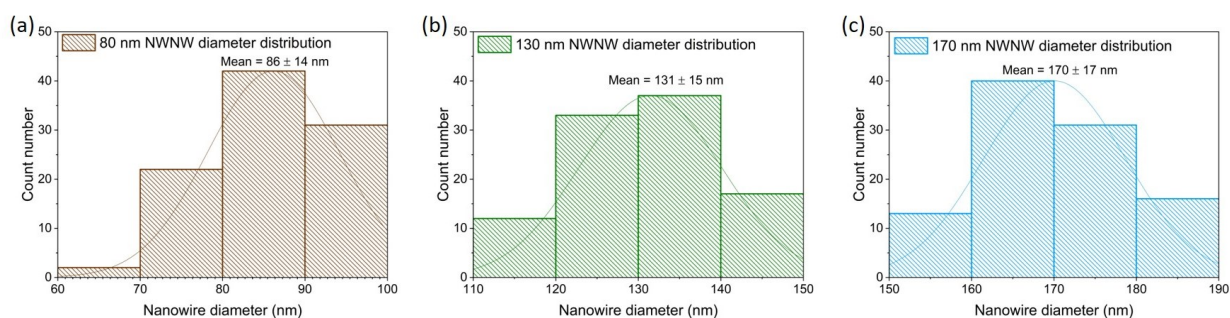


Figure 4.2 Nanowire diameter distribution charts of Au NWNWs.

Next, we measured the ECSA measurements of these three samples using the AuO reduction peak integration method. Figure 4.3 shows the CVs recorded in 0.1 M H_2SO_4 solution. The anodic peaks locate at $U = 1.2 - 1.4$ V (Figure 4.3 (a)–(c)) are attributed to the formation of Au oxide^{115,116}, the cathodic peak at $U = 0.85$ V is assigned to the Au oxide reduction. With the integration of the reduction peak, we were able to calculate faradic transfer for the three samples, as the values are shown on each figure. The faradic charge we obtained is proportional to the sample ECSA. In this case, we employed the reference value from a smooth Au film sample, with 1 cm^2 flat area. By integrating the respective reduction peak, a reference charge-transfer value of $Q_{\text{ref}} = 653 \mu\text{Ccm}^{-2}$ was obtained (Figure 2.20). By comparing the integrated charge transfer from Figure 4.3 (a-c), and the reference value, the ECSA of all three samples can be calculated. The Au NWNWs have a ECSA of 20.8, 30.1, and 40.3 cm^2 , respectively. The measured ECSA increases systematically with the nanowire diameter increase.

Figure 4.3 (d) shows the comparison between the measured ECSA values (purple bars) with the estimated S_{GEO} (following equation 4-1) (pink bars) of three Au NWNWs. The error bars of ECSA represents fluctuations from different CV cycles. The error bars of the S_{GEO} include the nanowire

diameter distribution, and the crossing points of nanowires. Taking into account these uncertainties, for all nanowire diameters, measured ECSA is in good agreement with the calculated S_{GEO} .

In summary, the ECSA values we obtained with the optimized experimental conditions correlate well with the calculated S_{GEO} values, which increase systematically with the increase nanowire diameter, indicating that the entire highly interconnected 3D Au NWNW contributed to the reaction. These results highlight the potential of the NWNWs in catalytic applications. By designing the Au NWNW sample with an optimized S_{GEO} , better catalytic performance can potentially be achieved.

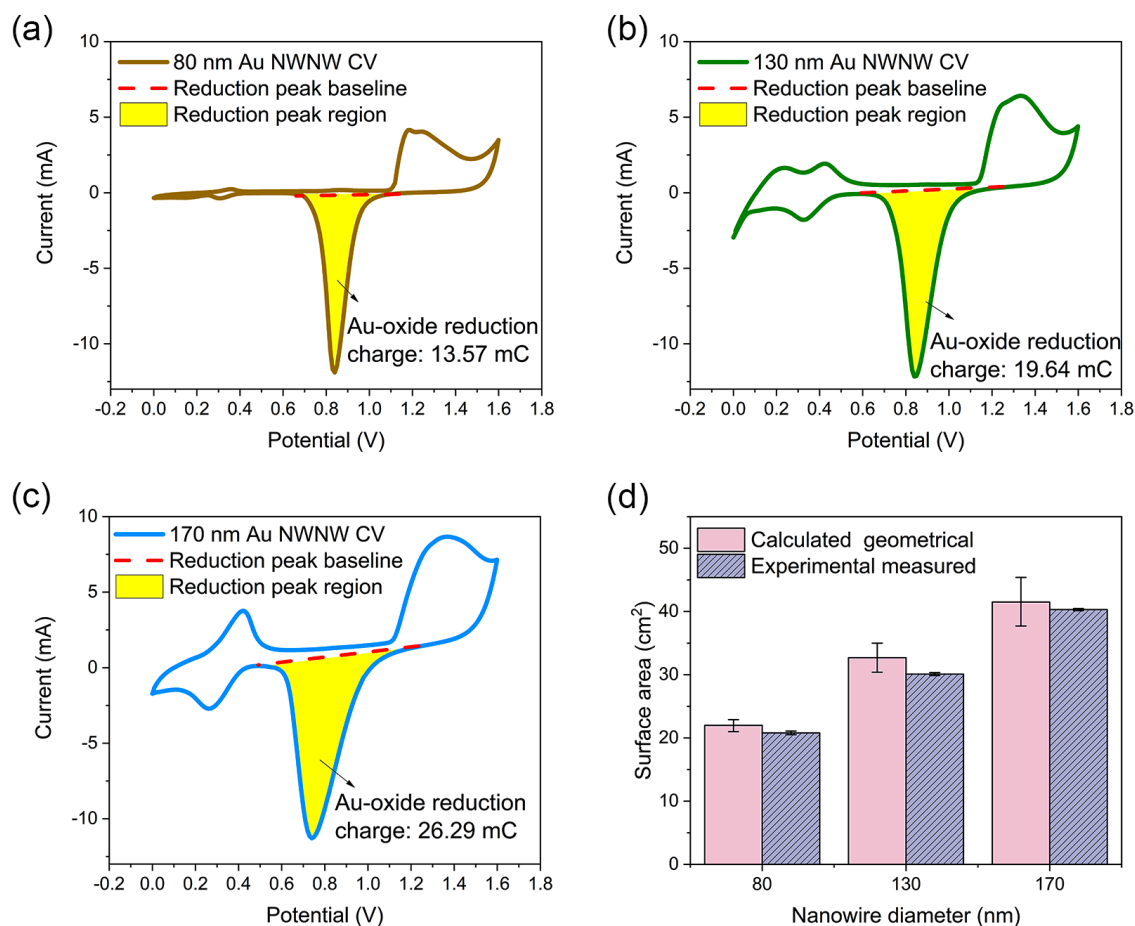


Figure 4.3 CVs recorded in 0.1 M H_2SO_4 for Au NWNWs of different nanowire diameters: (a) 80 nm, (b) 130 nm, and (c) 170 nm (room temperature, scan rate = 100 mV s^{-1}). The red dashed line defines the baseline for the reduction peak integration, the yellow area represents the Au oxide reduction peak region providing the electrochemically active surface area. (d) Experimental (ECSA) and calculated (S_{GEO}) surface area values of the Au NWNWs as a function of nanowire diameter.

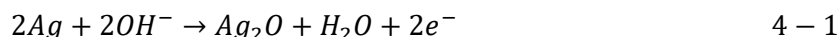
4.1.2 $\text{Au}_{1-x}\text{Ag}_x$ NWNWs

For the $\text{Au}_{1-x}\text{Ag}_x$ NWNWs, due to the surface composition change, we cannot simply apply the AuO reduction method to measure ECSA as the pure Au NWNWs. In the same acidic media, Ag will undergo two-step oxidation reactions during the anodic scan, first Ag is oxidized to Ag_2O , then further oxidized to AgO. During the cathodic scan, the Ag oxides will also be reduced in two steps, as in two separate reduction peaks. For a Au-Ag alloy, the Au and Ag oxides will reduce simultaneously, leading to a composite reduction peak. The total charge under this peak reflects the combined surface area of both

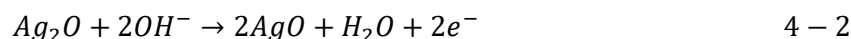
metals, while the charge densities of the Au and Ag oxides reduction are different. This difference does not allow a straightforward calculation of ECSA for each metal individually^{56,151,152}.

Therefore, in this section, DLC method was applied for $Au_{1-x}Ag_x$ NWNWs in alkaline media, applying the parameters discussed in section 4.1.4. First, a representative CV of one pure Ag NWNW was recorded in 0.1 M KOH, to identify the reactions and the non-faradic region, as shown in Figure 4.4.

The anodic peak a_1 and a_2 are attributed to the formation of $[Ag(OH)_2]^-$, and then the electro-oxidation of Ag to Ag_2O ¹⁵³:



Then the next peak a_3 is attributed to further oxidation of AgO ¹⁵³:



During the cathodic scan, we can also see multiple reduction peaks, from c_1 to c_2 , they represent a series of silver oxides reduction reactions from AgO to Ag_2O , then back to pure Ag.

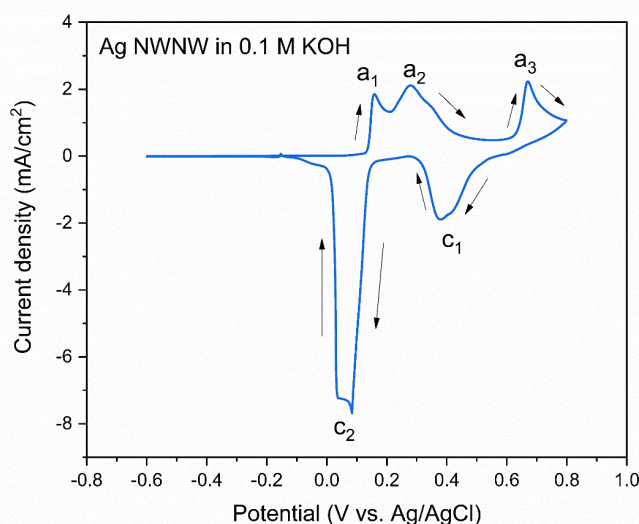


Figure 4.4 Cyclic voltammogram of the Ag NWNW in 0.1 M KOH solution at a scan rate of 50 mV/s.

For the DLC method, it is important to select a measurement window, from Figure 4.4 we can identify a non-faradic region from $U = -0.2$ V to -0.6 V. Since we selected $U = -0.4$ V to -0.6 V for the pure Au NWNW, and this also overlays with the non-faradic region of pure Ag, we applied the same measurement window of $U = -0.4$ V to -0.6 V for $Au_{1-x}Ag_x$ NWNWs.

Figure 4.5 (a) shows a representative CV in 0.1 M KOH solution at room temperature, and repeated CV cycles with different scan rates from 5 to 50 mV/s are conducted, as shown in Figure 4.5 (b). Two series of $Au_{1-x}Ag_x$ NWNWs with low-density (4×10^8 cm⁻²) and high-density (2×10^9 cm⁻²) templates were fabricated and tested, All the samples were measured with the same parameters in the same setup, to make the results comparable. their DLC plots are shown in Figure 4.5 (c, d).

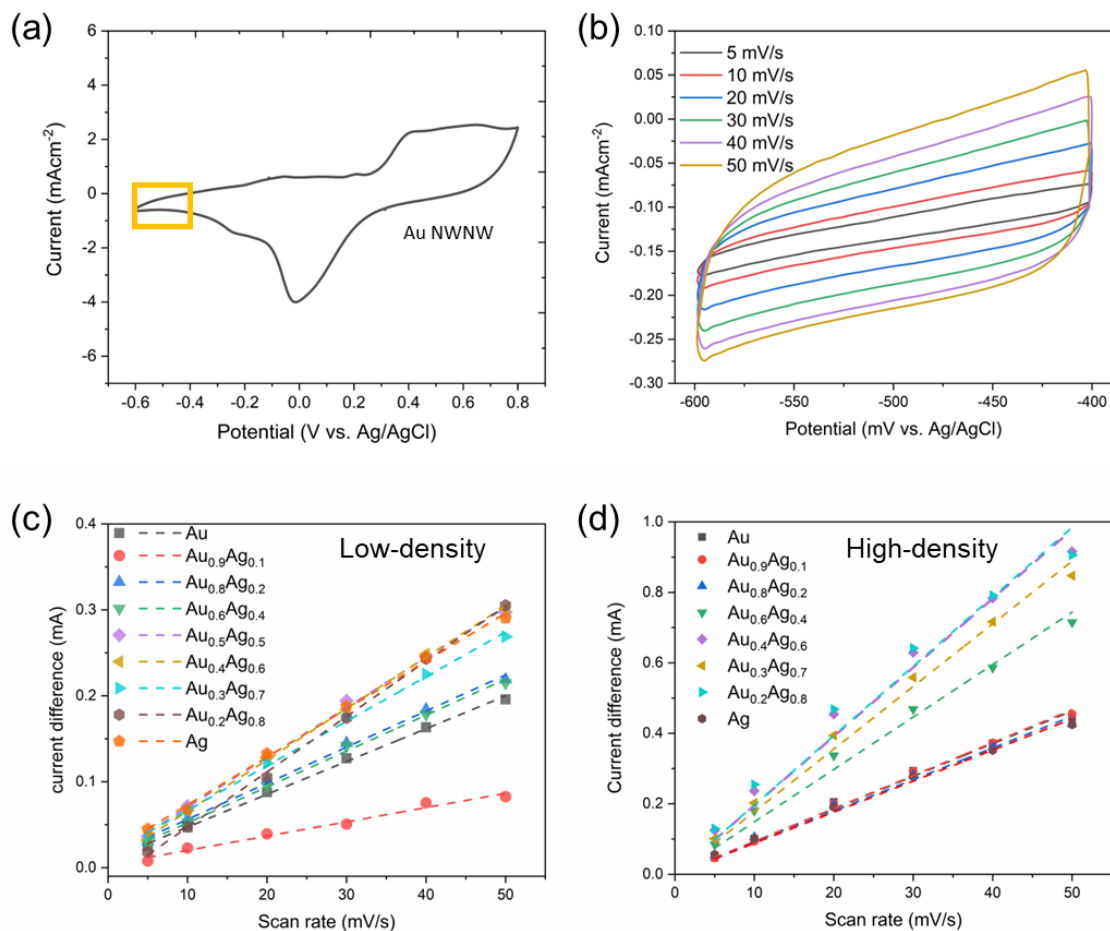


Figure 4.5 Cyclic voltammograms (a) recorded for a Au NWNW in argon-purged 0.1 M KOH solution in a wide scan range, (b) with different scan rates within the selected measuring window, anodic and cathodic current difference as function of scan rate, of the low-density (c) and high-density (d) series, dash lines correspond to corresponding linear fits.

The measured DLC values with the corresponding ECSA values are listed in Table 4.1, this was calculated by the obtained reference value $DLC_{ref} = 74 \mu F cm^{-2}$. Both series of Au_{1-x}Ag_x NWNWs were fabricated with 150 nm nanochannels. The calculated S_{GEO} for the low-density series is $53 \pm 4 cm^2$, while for the high-density series is $263 \pm 21 cm^2$. If the irradiation fluence deviation (20%) and nanowire size distribution (10%) are to be considered, then the surface area deviation will be much larger.

For the low-density series, we can see the Au_{0.9}Ag_{0.1} NWNW shows the smallest DLC, this is caused by the very negative deposition potential ($U = -1.1 V$), which led to a fast deposition rate, that the nanowire growth is rather inhomogeneous, thus resulted in a smaller surface area. When we compare the whole series together, the Ag-rich (Ag at% > 50%) NWNWs tend to have higher ECSA than the Au-rich samples, even though they were fabricated with the same templates. This may be caused by different filling rates of the nanochannels. The pure Au and the Au_{0.9}Ag_{0.1} NWNW were deposited at -0.9 V, and -1.1 V, respectively, while the other samples were deposited at -0.8 V. Less negative deposition potentials can lead to more homogeneous growth NWNWs, which were proved in section 3.1.1. However, even with a 100% nanochannel filling rate, this cannot explain why the values are 30-50% higher than the estimated S_{GEO} .

For the high-density series, we see the same trend, that the Ag-rich samples have higher ECSA than Au-rich samples. Except, the Ag NWNW has a similar ECSA as the Au NWNW, and both values are only around half of the S_{GEO} . Because both samples were deposited near their ion reduction potential, that led to a smaller nanochannel filling rate. Another reason can be the nanochannels overlaying with each other, lead to a smaller surface area than estimated. Despite the differences between the samples, unlike the low-density series, the values are within the range of the estimated S_{GEO} value.

When comparing the two series together, the low-density NWNWs ECSA seems to be overestimated, while the high-density NWNWs ECSA correspond well with the thermotical estimation. We attribute this difference to the selection of the Au NWNW reference samples. As discussed in section 4.1.4, the Au NWNW references we selected have the same density as the high-density series ($2 \times 10^9 \text{ cm}^{-2}$). When comparing the Au thin film to the Au NWNW, we observed that the determined DLC of the NWNW samples appeared lower than expected. This discrepancy is attributed to diffusion and mass transport limitations inherent to the nanostructured geometry. However, in the case of low-density NWNW samples, where the nanowire spacing is significantly larger due to a five times lower density, these diffusion and transport limitations are less pronounced. Consequently, if we apply a reference sample that is more strongly affected by diffusion limitations to compensate for the DLC underestimation in NWNW structures, as a result, we overestimated the ECSA of the less diffusion limited low-density NWNWs.

Table 4.1 Double-layer capacitance and the corresponding ECSA of $\text{Au}_{1-x}\text{Ag}_x$ NWNWs.

Low-density NWNW			High-density NWNW		
Sample name	DLC (mF)	ECSA (cm^2)	Sample name	DLC (mF)	ECSA (cm^2)
Au	3.8	51.4	Au	9.3	125.7
$\text{Au}_{0.9}\text{Ag}_{0.1}$	1.7	23.0	$\text{Au}_{0.9}\text{Ag}_{0.1}$	9.4	127.0
$\text{Au}_{0.8}\text{Ag}_{0.2}$	4.2	56.8	$\text{Au}_{0.8}\text{Ag}_{0.2}$	9.0	121.6
$\text{Au}_{0.6}\text{Ag}_{0.4}$	4.2	56.8	$\text{Au}_{0.6}\text{Ag}_{0.4}$	14.9	201.4
$\text{Au}_{0.5}\text{Ag}_{0.5}$	5.8	78.4	$\text{Au}_{0.4}\text{Ag}_{0.6}$	19.7	266.2
$\text{Au}_{0.4}\text{Ag}_{0.6}$	6.0	81.1	$\text{Au}_{0.3}\text{Ag}_{0.7}$	17.8	240.5
$\text{Au}_{0.3}\text{Ag}_{0.7}$	5.2	70.3	$\text{Au}_{0.2}\text{Ag}_{0.8}$	19.7	266.2
$\text{Au}_{0.2}\text{Ag}_{0.8}$	6.4	86.5	Ag	8.9	120.3
Ag	5.6	75.7			

In summary, the DLC method can be applied to $\text{Au}_{1-x}\text{Ag}_x$ NWNWs, the measured values are proportional to the ECSA as expected, and the results were not influenced by the sample surface composition variation. However, the selection of the reference value is very critical, as it can directly impact the ECSA results, which can lead to underestimation if not considering diffusion and mass transportation limitations in nanostructures. On the contrary, if we try to compensate too much, then it can lead to overestimation of the ECSA.

4.1.3 Nanoporous NWNW

For nanoporous NWNWs, we applied the same method as the $\text{Au}_{1-x}\text{Ag}_x$ NWNWs, due to the presence of residual Ag from the dealloying process, and possible AgO from the oxidation caused by the dealloying solution (65% HNO_3). As mentioned in section 3.3.1, NWNWs with Ag at% ~ 70 -80% can start a fast dealloying process without undergoing significant pore coarsening and structural instabilizing. Therefore, we only tested the $\text{Au}_{0.2}\text{Ag}_{0.8}$ and $\text{Au}_{0.3}\text{Ag}_{0.7}$ NWNWs as dealloying precursors, with nanowire diameter of 150 nm, and density of $2 \times 10^9 \text{ cm}^{-2}$. Thus, when growing homogenously, they should exhibit a S_{GEO} of $263 \pm 21 \text{ cm}^2$ in 1 cm^2 projection area.

Figure 4.6 shows the SEM images of the $\text{Au}_{0.3}\text{Ag}_{0.7}$ and $\text{Au}_{0.2}\text{Ag}_{0.8}$ NWNWs before and after dealloying of different times, before dealloying, two pristine samples exhibit the same morphology with the same nanowire size. The SEM images show that after the $\text{Au}_{0.3}\text{Ag}_{0.7}$ NWNWs were dealloyed for 1 and 6 h (Figure 4.6 (b, c)), the pore size increases with dealloying time, resulting in slightly different pore sizes. After the $\text{Au}_{0.2}\text{Ag}_{0.8}$ NWNW was dealloyed for 30 min (Figure 4.6 (e)), it exhibited the smallest pores on the nanowire surface, but the network structure started collapsing due to the volume loss.

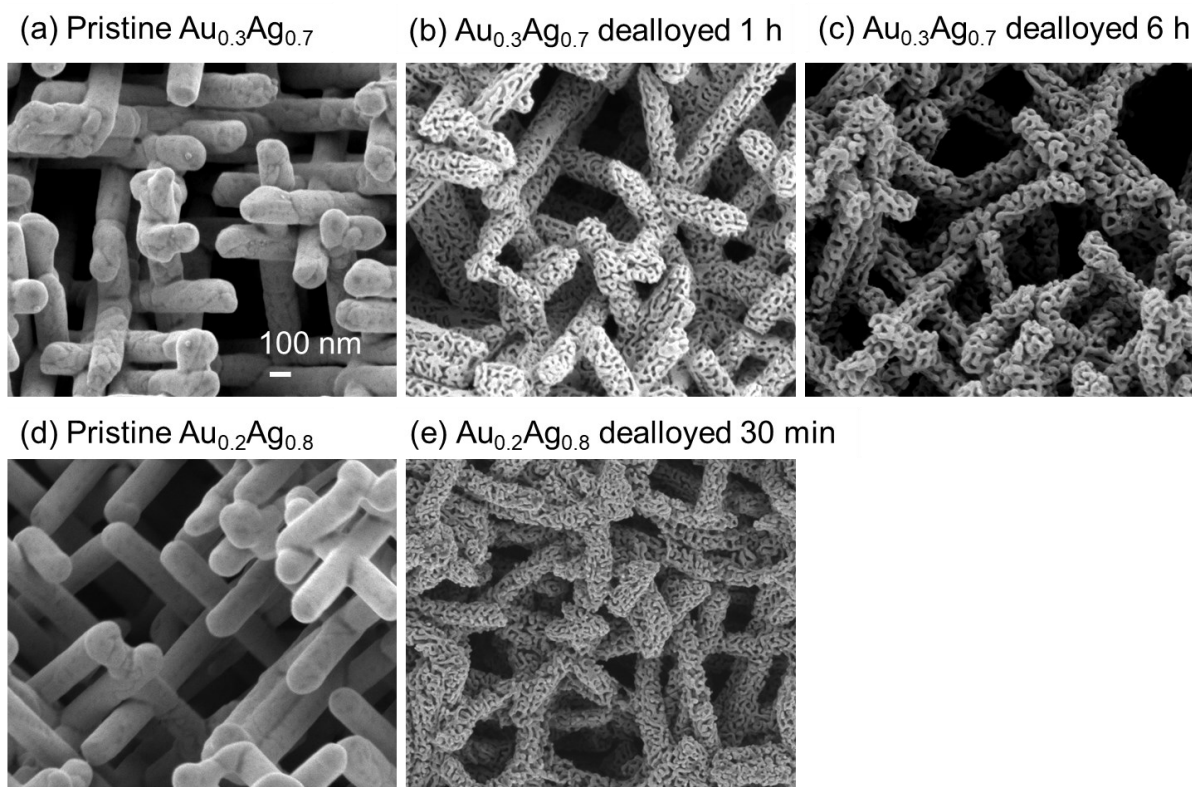


Figure 4.6 SEM images of (a) $\text{Au}_{0.3}\text{Ag}_{0.7}$ NWNW before dealloying, (b) dealloyed for 1 h, (c) dealloyed for 6 h, (d) $\text{Au}_{0.2}\text{Ag}_{0.8}$ NWNW before dealloying, (e) dealloyed for 30 min.

Figure 4.7 (a-c) show the DLC CVs recorded for the three dealloyed samples, the curve shapes are similar, the anodic/ cathodic current increases with the increase of scan rate. Figure 4.7 (d) plots the current difference as a function of the scan rate. As mentioned before, the slope of the linear fitting corresponds to the capacitance value. The DLC values and the corresponding ECSA values are given in Table 4.2. For the ECSA calculations, we applied the reference value $DLC_{ref} = 74 \mu F cm^{-2}$ (determination details are discussed in section 4.1.4).

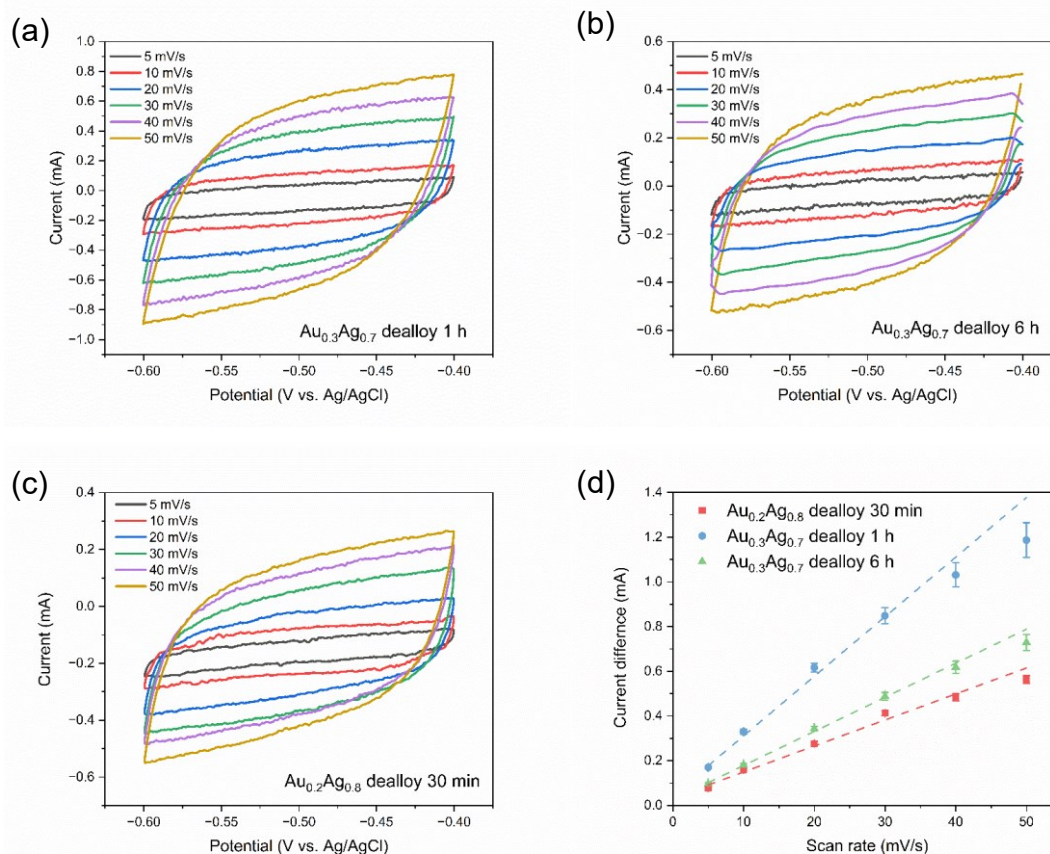


Figure 4.7 Cyclic voltammograms of dealloyed NWNWs, (a) Au_{0.3}Ag_{0.7} NWNW dealloyed 1 h, (b) Au_{0.3}Ag_{0.7} NWNW dealloyed 6 h, (c) Au_{0.2}Ag_{0.8} NWNW dealloyed 30 min, and (d) anodic and cathodic current difference as a function of scan rate of three samples, dash lines correspond to corresponding linear fits.

Table 4.2. Measured DLC and ECSA values of pristine and dealloyed NWNWs.

Sample name	DLC (mF)	ECSA (cm ²)
Pristine Au _{0.3} Ag _{0.7} NWNW	17.8	240.5
Au _{0.3} Ag _{0.7} NWNW dealloyed 1 h	25.8	348.6
Au _{0.3} Ag _{0.7} NWNW dealloyed 6 h	15.4	208.1
Pristine Au _{0.2} Ag _{0.8} NWNW	19.7	266.2
Au _{0.2} Ag _{0.8} NWNW dealloyed 30 min	12.2	164.8

The theoretical surface area value of a pristine NWNW before dealloying is around $263 \pm 21 \text{ cm}^2$ in 1 cm^2 projection area, which is in good agreement with the ECSA value of the pristine $\text{Au}_{0.3}\text{Ag}_{0.7}$ and $\text{Au}_{0.2}\text{Ag}_{0.8}$ NWNWs, which is 240.5 and 266.2 cm^2 , respectively.

After 1 h dealloying, the porous NWNW exhibited an ECSA 40% higher than the pristine sample. If we consider the weight loss due to the dissolution of Ag atoms and the surface area increase, then the specific surface area per unit weight increased from $0.6 \text{ m}^2\text{g}^{-1}$ to $2.8 \text{ m}^2\text{g}^{-1}$, i.e., around 5 times larger. After 6 h dealloying, the ECSA decreased compared to both the pristine sample and the 1 h dealloyed sample. This can be attributed to the coarsening of the porous structure due to surface diffusion and partial collapse of the network structure, effects which are evidenced in the SEM images of this sample (Figure 4.7 (c)).

Finally, the $\text{Au}_{0.2}\text{Ag}_{0.8}$ NWNW after 30 min dealloying yielded an ECSA value of 164.8 cm^2 , which is around 40% smaller than the pristine sample. This ECSA decrease is mainly caused by the volume loss during the dealloying process, partly also because of the network structure collapsing. They also exhibit very small pores at nanowire surface. The fact that the ECSA decreased indicates that these pores do not participate effectively in the reactions.

In conclusion, by optimizing the composition and dealloying conditions of $\text{Au}_{1-x}\text{Ag}_x$ NWNWs, the ECSA can be significantly increased. Both geometry and composition of the pristine NWNWs need to be carefully designed to produce a stable porous NWNW while increasing the surface area.

4.1.4 Determination of the DLC reference value

As explained in previous sections, two methods were applied for measuring the ECSA of the NWNWs. The first method applies integrating the faradaic charge transfer of the Au surface oxide reduction reaction, the second method applies measuring the double-layer capacitance of the sample surface. In this section, the two methods will be compared using the pure Au NWNW. The ECSA measured by AuO reduction reaction is treated as the standard value, since the excellent agreement between the ECSA values and S_{GEO} values as shown in section 4.1.1. This comparison helped us to compare the optimized conditions for the DLC determination of our NWNWs.

Both methods were introduced in section 2.3.6. We will first compare the two methods applied on a planar Au film, and discuss the results of a planar electrode without diffusion limitation. Then we will compare the two methods on two identical NWNW samples, fabricated with the same geometry and electrodeposition. This allows us to compare how the NWNW geometry can influence the measurement results.

Planar Au film

The planar Au film was produced with the same protocol as the Au back-electrode layer, it is around $2 \mu\text{m}$ thick, and exhibits a shiny surface finish, with only 1 cm^2 flat area exposed to the measurement electrolyte. A representative CV was recorded in $0.1 \text{ M H}_2\text{SO}_4$ solution, as shown in Figure 4.8 (a). During the anodic scan, first H^+ is absorbed, then the oxidation of Au takes place at around $U = 1.3 \text{ V}$. The oxygen evolution reaction starts at around $U = 1.5 \text{ V}$. During the cathodic scan, the Au oxides reduction peak locates at around $U = 0.75 \text{ V}$. During one CV scan, only the top monolayer of Au atoms on the sample surface will be oxidized and then reduced, therefore the reaction charge transfer can be used to calculate how many atoms are involved in the reaction, and subsequently calculate the surface area that participated in the reactions. From the CV, the reduction peak area was integrated into a charge transfer of 4.3 mC . As discussed in section 2.3.6, we choose to apply the value used in the literature $Q = 448 \mu\text{Ccm}^{-2}$ ^{116,117}, from this value, we can calculate that this reference planar Au film has a ECSA of 9.6 cm^2 .

Then we measured the same Au film sample in basic solutions (Figure 4.8 (b)), CVs were recorded in 0.1 M (orange) and 1 M KOH (green). As expected, they exhibit different current values for different electrolyte concentrations, but similar reaction peak potentials. During the anodic scan, the OH⁻ is first absorbed on the Au atoms, then Au atoms are oxidized at around $U = 0.4-0.5$ V, then the oxygen evolution starts at around $U = 0.8$ V. During the cathodic scan, AuO is reduced, and we can identify a non-faradic region at -0.4 to -0.6 V.

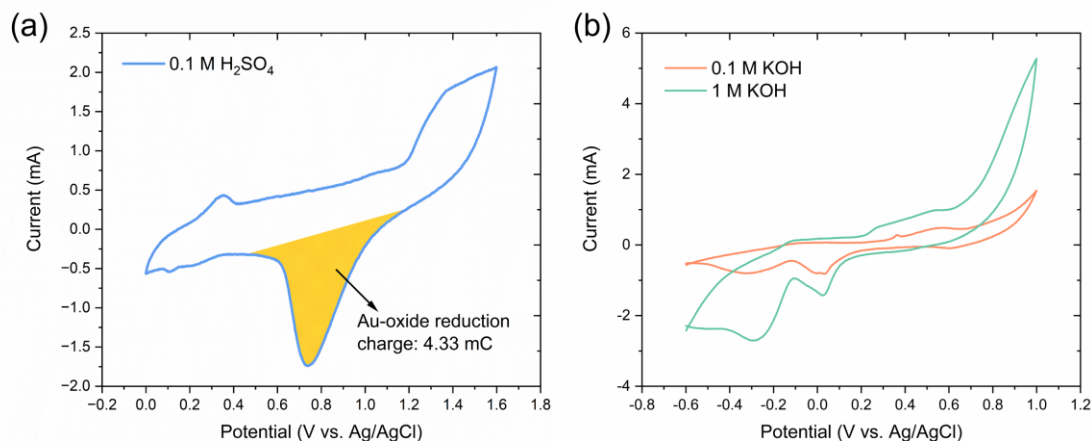


Figure 4.8 CV of Au thin film reference sample in (a) 0.1 M H₂SO₄, and (b) in 0.1 M/ 1 M KOH solutions.

To determine the DLC, a series of CV cycles are recorded within the non-faradic region at different scan rates, as shown in Figure 4.9 (a). From each CV cycle, the current difference between the anodic curve and the cathodic curve was measured. Then the current differences were plotted against the scan rate, as shown in Figure 4.9 (b). The slope of the linear fit curve represents the DLC. From this, we derived the DLC of this planar Au film sample, which is 1.04 mF.

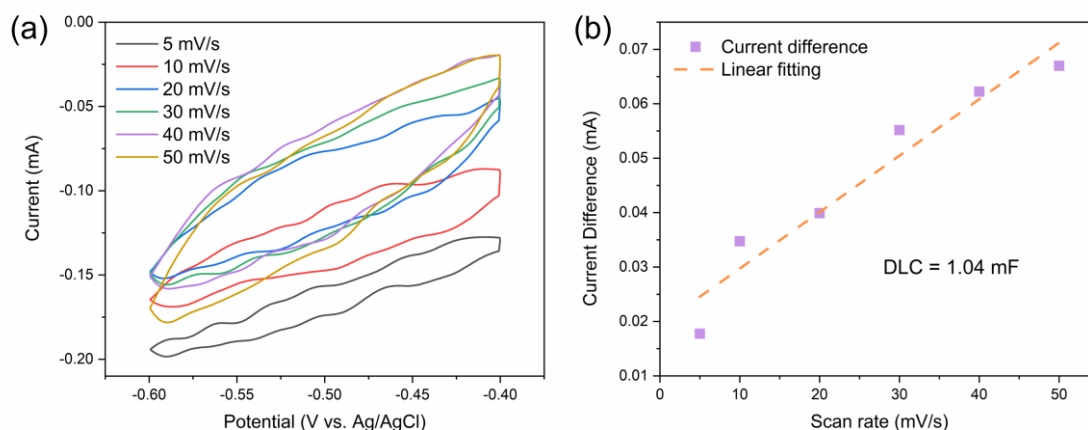


Figure 4.9 (a) CVs of the planar Au film reference sample in the non-faradic region for DLC measurements with different scan rates, the starting and end points of each cycle were joined by a vertical line, (b) plot of current difference vs. scan rate.

To summarize the measurement results together. Applying the faradaic charge transfer method, we estimated that the 4.3 mC transferred charge corresponds to the surface area of 9.6 cm². Applying the

DLC method, we measured a DLC for the same reference Au film of 1.0 mF. When we compare the two results together, the measured DLC of 1.0 mF is also correspond to the ECSA of 9.6 cm². From the DLC results we can derive a reference value of the $DLC_{ref} = 108 \mu F cm^{-2}$.

NWNWs

In the following, we exemplarily apply these methods to determine the ECSA of two NWNWs with the same theoretically calculated geometrical surface area (S_{GEO}). The two Au NWNW samples were fabricated with the same templates, e.g., with the same irradiation fluence ($2 \cdot 10^9 \text{ cm}^{-2}$) and the same etching time (6 min corresponding to a channel diameter of $\sim \text{Ø } 150 \text{ nm}$). Then the nanowires were deposited with the sample electrolyte and the same potential. They exhibit the same morphology under the SEM analysis, and the deposition curves showed only 7% difference in faradic charge, indicating that they have very similar surface area. The S_{GEO} is $263 \pm 21 \text{ cm}^2$, according to the calculation below:

$$S_{GEO} = ((\pi \times r_{nw}^2) + (2\pi \times r_{nw} \times L_{nw})) \times f_{nw} \quad 4 - 3$$

Where r_{nw} is the radius of the nanowire, L_{nw} is the length of the nanowire, which is 1.41 times larger than the template thickness, because the wires are 45° tilted. The f_{nw} is the density of nanowires. This calculation corresponds to the surface area of a NWNW within 1 cm² flat area, and does not consider the interconnections or nanowire roughness. The error bar comes from the crossing junctions between the nanowires.

The charge transfer of the AuO reduction reaction for the first Au NWNW is measured in 0.1 M H₂SO₄. On the CVs displayed in Figure 4.10 (a), we can see that the curves showed similar peaks as the reference Au thin film sample, the reduction peak is located at around $U = 0.6 \text{ V}$, and the corresponding integrated peak area has a faradic change of 58.3 mC. When we utilize the reference charge transfer value $Q = 448 \mu C cm^{-2}$, we can calculate the sample ECSA is 130.1 cm². Please notice that even though the electrodeposited NWNW has a circular diameter of 1.5 cm, these measurements are performed in the commercial electrochemical cell with an exposure area of 1 cm². This means that this Au NWNW has 130.1 cm² ECSA participating in the electrochemical reactions within a 1 cm² flat projection area.

For the second Au NWNW, the CV was recorded in 0.1 M KOH, as shown in Figure 4.10. The first OH⁻ absorption on Au atoms takes place at $U = 0.4 \text{ V}$, while Au gets oxidized at $U = 0.6 \text{ V}$. The reduction peak of AuO is located at a similar position (0.1 V), as measured for the Au thin film reference sample (0.1 V). For consistent DLC measurement, the measurement window was also selected between -0.4 V and -0.6 V, under the same parameters.

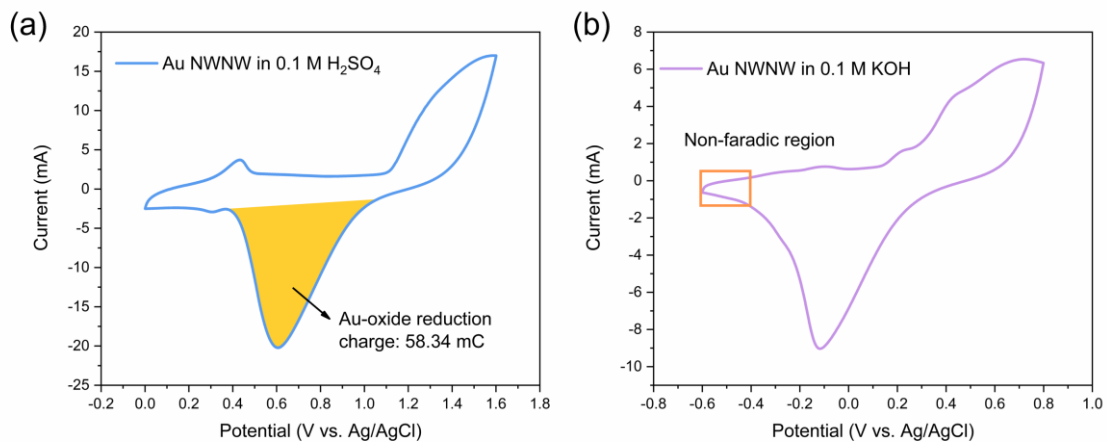


Figure 4.10 CV of Au NWNW samples in (a) 0.1 M H₂SO₄, and (b) in 0.1 M KOH solutions.

As shown in Figure 4.11 (a), repeated CVs were measured with scan rates from 5 to 50 mV/s, resulting in almost square-shaped curves, the measured current difference between the anodic scan and the cathodic scan was plotted against the scan rate in Figure 4.11 (b). The slope of the linear fit is the estimated DLC of this Au NWNW sample. In this case, this Au NWNW has a measured DLC=9.59 mF.

When the two Au NWNW samples were fabricated with the same parameters (e.g., geometry and electrodeposition), there can be 10% intrinsic surface area difference from the fabrication process. If we assume the two Au NWNWs have exactly the same surface area, and thus the same ECSA values. Therefore, the 9.6 mC DLC is corresponds to the ECSA of to 130.1 cm², which was determined from the AuO reduction method. We can obtain the normalized reference value derived from the DLC results, for this sample geometry, is $DLC_{ref} = 74 \mu Fcm^{-2}$.

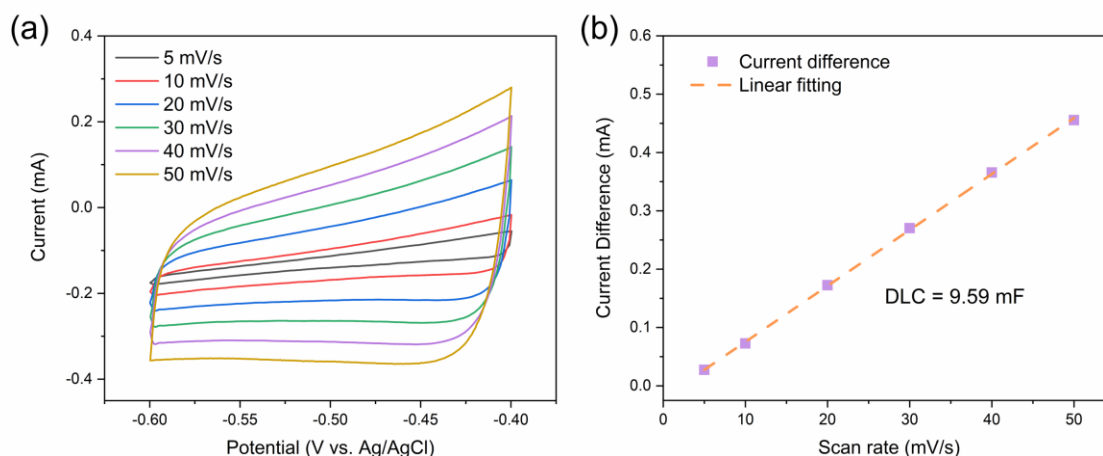


Figure 4.11 (a) CVs of Au NWNW in the non-faradic region for DLC measurements with different scan rates, (b) plot of current difference vs. scan rate.

Table 4.3 summarizes all the measured and calculated ECSA values discussed above. When we compare the DLC reference values from the planar Au film and Au NWNW, we can see the one from thin film is around 30% higher than the one derived from NWNW. If we use the DLC_{ref} from the thin film, then we will estimate an ECSA of the NWNW sample of only 89 cm². Then the DLC method will lead to an underestimation of 30%.

There can be many reasons for this deviation, one major problem is the diffusion or transport limitation in nanostructures. The measurements are conducted and analyzed under the assumption that ion transport to the surface is not rate-limiting. However, in nanostructured electrodes, there are often diffusion limitations and restricted ion accessibility. Recent studies have shown that in mesoporous and nanoporous architectures, ion transport within confined structures becomes increasingly hindered, particularly at higher scan rates, resulting in lower apparent capacitance and consequently an underestimation of the true ECSA^{154,155}.

Table 4.3 ECSA measurement comparison from two methods

Sample	Planar Au film		Au NWNW	
	AuO reduction	DLC	AuO reduction	DLC
Faradic charge (mC)/ Capacitance (mF)	4.3	1.0	58.3	9.6
Reference value (μCcm^{-2})/ (μFcm^{-2})	448	108	448	74
ECSA (cm^2)	9.6	9.6	130.1	130.1

Many ECSA measurements are often determined by the DLC method, and the suitability of this method has been in debate^{100,114,156}. Different ways of improving the measurement setup and parameters to arrive at a more reliable and scientific value were also reported^{100,111}. In this work, since we need to apply this method for the AuAg samples, we adapted some suggestions from Molares and Risch¹¹¹, where we placed our setup in a Faraday cage, to prevent any electromagnetic interference, and tested different parameters to compare the results, then tried to find the most optimized protocol for ECSA measurements.

In particular, we studied the influence of the scan window width, and IR compensation, which refers to the voltage drop caused by the resistance of the electrolyte solution between the working and reference electrodes. First, we compared a narrow window of 100 mV with a wide window of 200 mV, as shown in Figure.12 (a) and (b). Clearly, the wider scan window can lead to larger current differences, this is in agreement with the results of Molares and Risch¹¹¹, they suggested the scan window should be as large as possible to obtain meaningful results. Figure.12 (c) shows the CVs recorded with IR compensation (the system resistance is 27 Ω), because the IR drop can cause a change in the measured current. It can be seen that there is no significant difference between applying (c) or not applying (b) IR compensation, thus we did not apply IR compensation for the DLC CV measurements.

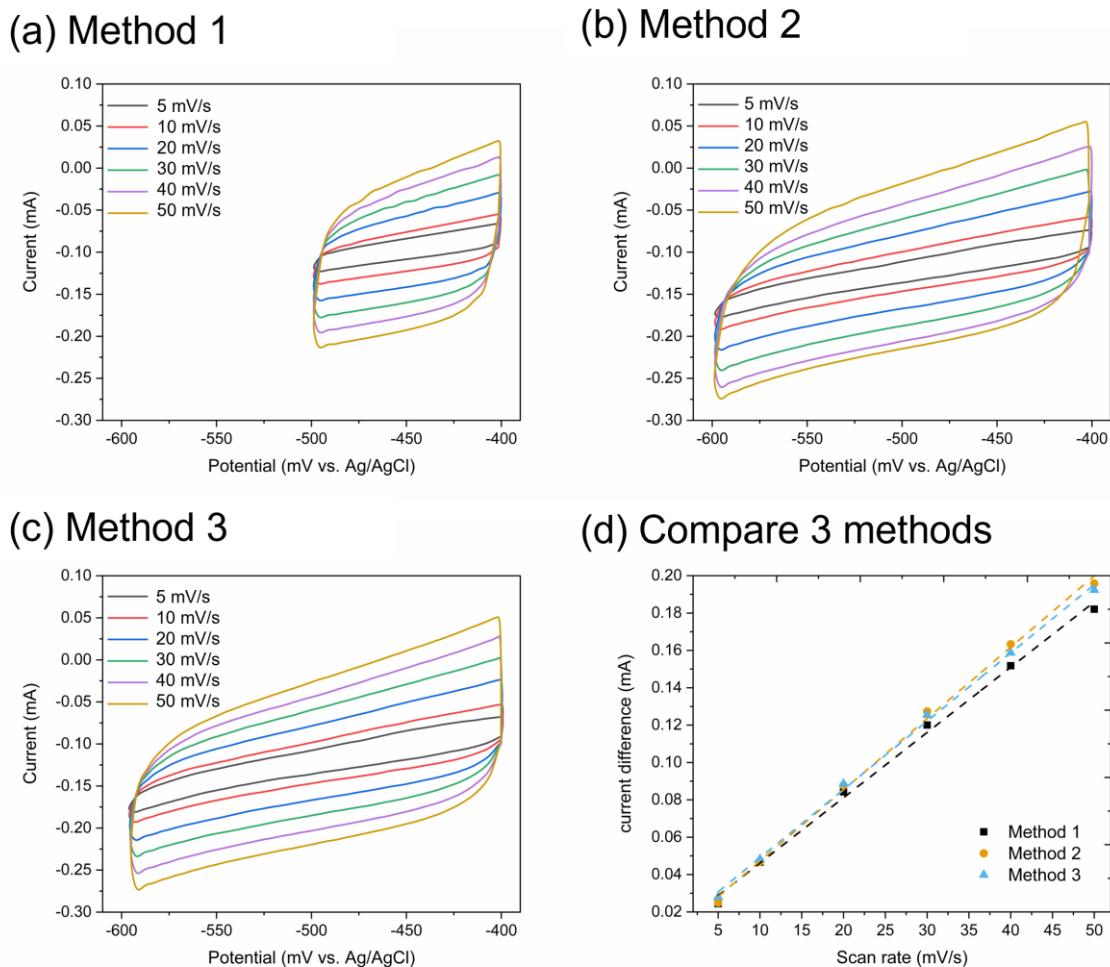


Figure.12 CVs of DLC measurements of a Au NWNW sample, with three different conditions: (a) narrow scan window, (b) wide scan window, (c) wide scan window with IR compensation.

Figure.12 (d) shows the current differences as a function of the scan rate for the three measurements. From the slope, we estimated the DLC values, which are given in Table 4.4. The values show that selecting the widest possible potential window results in a slightly larger DLC value. Since from previous results, we already know that the DLC method can lead to an underestimation of the ECSA, so it is only reasonable to choose the set of parameters that can lead to the largest value.

Table 4.4 DLC values obtained from CVs in Figure.12.

Method	1.	2.	3.
DLC (mF)	3.5	3.8	3.7

In summary, in this section we presented the two processes followed for the selection of the experimental conditions applied for the determination of the ECSA. We compared how different methods are designed and conducted on Au thin film and Au NWNW samples. Measurements reported in section 4.1.1 had

revealed an excellent agreement between the ECSA and S_{GEO} surface area values, indicating the reliability of the AuO reduction method for the ECSA determination of the Au NWNWs.

However, we found out the DLC method can lead to an underestimation of the ECSA value of the NWNWs, even after the optimization of the measurement parameters. Therefore, for the DLC measurement of the $\text{Au}_{1-x}\text{Ag}_x$ and nanoporous Au NWNWs, we should be aware that the actual surface area can deviate from the measured ECSA values, and the more complex the structure, the larger the deviation. From previous studies, there are many different reference values from different measurements, the C_{DLC} values are typically within 22–130 μFcm^{-2} in alkaline media^{108,156–164}. While in this work, for a NWNW sample, we employ the reference value calculated from the Au NWNW sample, $\text{DLC}_{\text{ref}} = 74 \mu\text{Fcm}^{-2}$, this value is within the range from literatures. Given that every measurement method even after careful optimization and evaluation, can still have limitations and deliver false result, a thorough consideration and optimization of the measurement parameters should be always undertaken.

4.2 Methanol Electro-Oxidation

NWNWs with large specific surface areas and tunable geometry as well as electrical, thermal, and chemical properties are of interest for catalysis. In this section, we explore the suitability and performance of the three types of NWNWs as catalysts, applying a well-known reaction, the electro-oxidation of methanol. Through this reaction, we use the NWNWs as a model system to investigate the influence of tailorable parameters such as nanowire diameter, density, composition, and hierarchy on their electrochemical catalytic performance.

4.2.1 Au NWNWs

Au NWNWs are chemically stable and thus ideal model systems to investigate the influence of the geometrical parameters on the electrocatalytic performance. In this section, we will discuss how different Au NWNWs can show different performances towards the methanol oxidation reaction. For this, we synthesize Au NWNWs with tailored geometry, varying systematically only the NW diameter and maintaining all other parameters the same. Thus, all NWNWs were deposited under identical conditions, i.e., using the same electrolyte and deposition potential to ensure a homogeneous network structure. Then they are all tested under the same conditions, details are explained in section 2.3.7.

Influence of electrolyte and reactant concentration

We start the catalytic test with a pure Au NWNW, with $4 \times 10^8 \text{ cm}^{-2}$ fluence, and 150 nm diameter nanowires, deposited at -0.9 V vs Ag/AgCl, all nanowires are well interconnected together. This sample has a $S_{\text{GEO}} = 53 \pm 4 \text{ cm}^2$ and measured ECSA = 51.4 cm^2 . Figure 4.13 (a) shows the CVs recorded in 0.1 M KOH (black dashed lines) electrolyte, with varied methanol concentration (solid lines).

The respective current density values were determined by dividing the recorded current values by the nominal area of the sample (same as the area of the reference sample, i.e., 1 cm^2). The methanol oxidation process involves two reactions: In the lower potential range, methanol is oxidized to formate, while in the higher potential region, formate is further oxidized to carbonate¹⁶⁵. In Figure 4.13 (black dashed line), at $U = 0.35\text{--}0.6 \text{ V}$, two anodic peaks are superimposed forming a plateau, corresponding to the formation of Au–OH and AuO. The cathodic peak located at $U = 0.02 \text{ V}$, is attributed to the stripping of Au–OH, and the reduction of AuO. The CV recorded in KOH electrolyte containing 1 M MeOH (blue solid line) exhibits one anodic peak at $U = 0.46 \text{ V}$, which corresponds to the oxidation peak for methanol to formate on the Au surface¹⁶⁶, for which the peak current density was around 3.5 mAcm^{-2} . When the methanol concentration increased to 2 M and 3 M, the oxidation peak current density increased accordingly to 4.7 and 5.7 mAcm^{-2} . In Figure 4.13 (b), the peak current densities of Figure 4.13 (a) are plotted against the methanol concentration (green), which shows that the oxidation peak current density increases proportionally to the methanol concentration. The oxidation peak potential from Figure 4.13 (a) was also plotted against the methanol concentration, as shown in Figure 4.13 (b) red squares, which shows a shift of the anodic peak potential, that increases from 0.47 V to 0.6 V with the methanol concentration increasing. This may be caused by the increase in unoxidized organic residue absorbed on the surface, which required a higher potential for oxidation,¹⁶⁷ or by an increase in the IR-drop.¹⁶⁸ It is worth noticing that in spite of the high methanol concentrations, no saturation of the peak current density was reached.

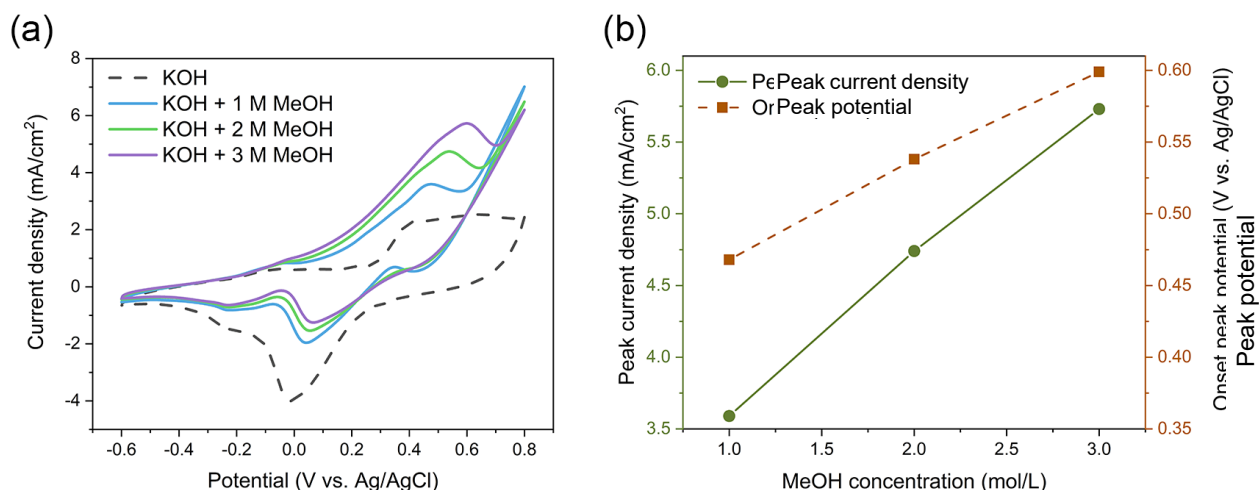


Figure 4.13 (a) CVs of 4×10^8 cm⁻² density Au NWNW recorded in 0.1 M KOH with 0/1/2/3 M MeOH with scan rate 50 mV s⁻¹, (b) anodic peak current density and onset potential as a function of the methanol concentration.

The influence of the KOH electrolyte concentration was tested with another Au NWNW with same nanowire diameter (150 nm) and higher nanowire density (2×10^9 cm⁻²), corresponding to a S_{GEO} of 263 ± 21 cm² in a 1 cm² nominal area, and measured ECSA = 125.7 cm². Figure 4.14 shows the CVs recorded in 0.1, 0.5, and 1 M KOH electrolytes, with different concentration of methanol, 0 (black dash), 0.5 (red), 1 (blue), and 2 M (green). The current density was normalized by the flat projection area.

In Figure 4.14 (a), the CVs show the performance of a high-density Au NWNW in 0.1 M KOH, when we compare it with Figure 4.14 (a), the only difference is the nanowire density increase. If we compare the CVs carefully, and only look at the anodic peak in 0.1 M KOH with 1 M methanol, we can see the methanol oxidation peak current density per nominal area increased from 3.6 to 8.3 mAcm⁻², mainly due to the ECSA increased from 51.4 to 125.7 cm². But the peak potential is also increased from 0.47 V to 0.64 V, meaning when the surface area is larger, it needs higher activation energy for the oxidation reaction to happen. Therefore, we can conclude from the two figures, that the peak potential and peak current will both increase with the increase of surface area.

Figure 4.14 (b, c) show the same high-density Au NWNW in 0.5 M, and 1 M KOH electrolyte, in both figures, the methanol oxidation peak current density increases with the methanol concentration increase, this is the same effect as observed for the low-density Au NWNW. With 1 M KOH with 2 M KOH, we can reach up to 24.4 mAcm⁻². When we compare Figure 4.14 (b, c) with (a), we see that with 1 M methanol in the electrolyte, the oxidation peak current densities increase from 8.3 to 13.5 and 16.1 mAcm⁻², respectively. This evidences that higher KOH concentration can facilitate the methanol oxidation reaction.

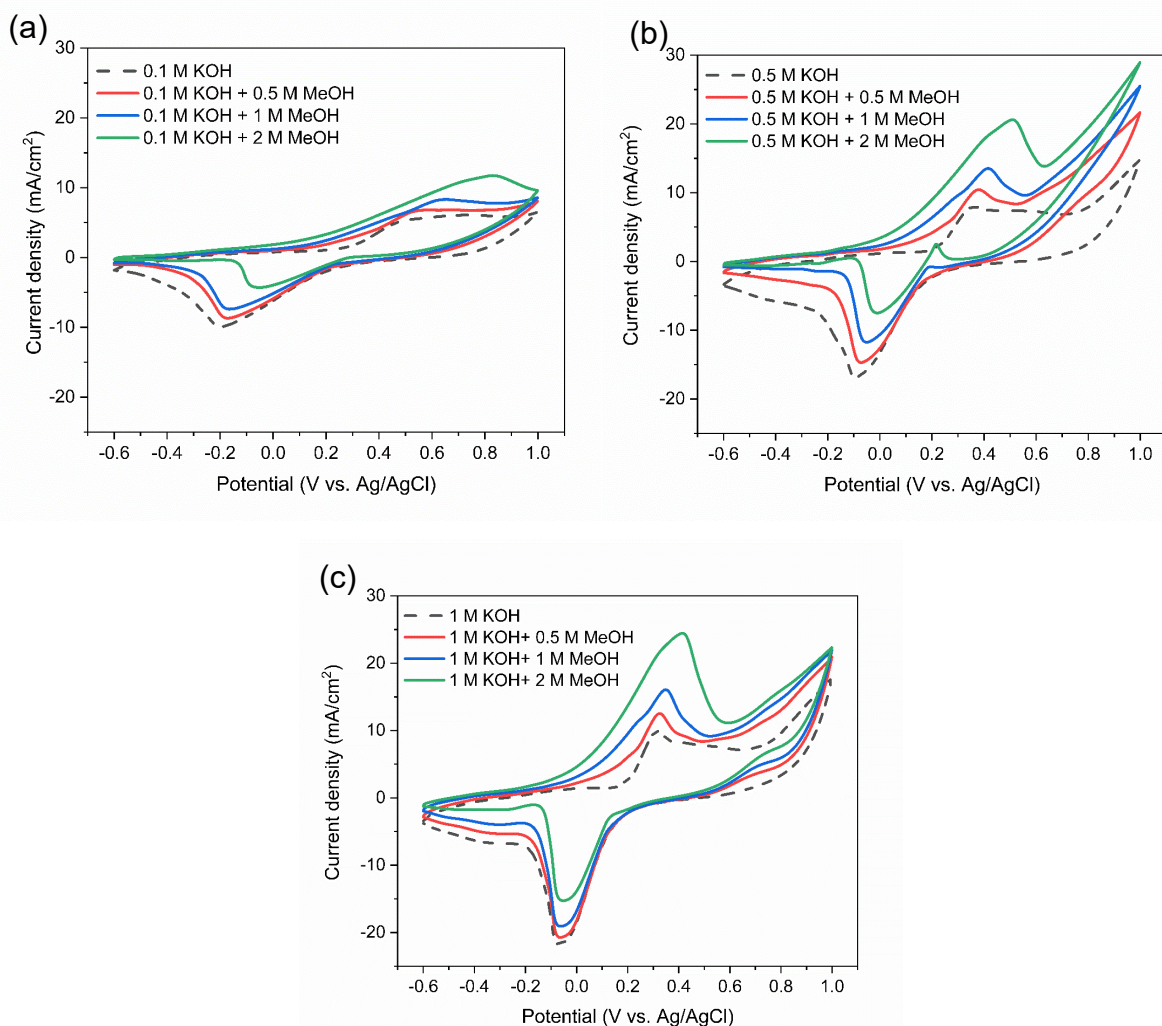


Figure 4.14 CVs of Au NWNW with nanowire diameter of 150 nm, and density of $2 \times 10^9 \text{ cm}^{-2}$ recorded in (a) 0.1 M KOH, (b) 0.5 M KOH, and (c) 1 M KOH electrolyte, with 0 M (black dash line), 0.5 M (red solid line), 1 M (blue solid line), and 2 M (green solid line) MeOH with scan rate 50 mV s^{-1} .

To compare the methanol oxidation peaks from Figure 4.14 more directly, in Figure 4.15, we plotted the peak current density (a) and peak potential (b) against different methanol concentrations. From Figure 4.15 (a), we can see that with the same KOH concentration, the current density increase is almost linear to the increase of methanol concentration in the electrolyte. However, when the methanol concentration is constant, and the KOH concentration increases from 0.1 M to 1 M, the current density increase is around 2 times. This is in agreement with reported studies, that a higher concentration of KOH provides more OH^- , which enhances the reaction rate by improving the mass transport, and accelerating the formation of reactive intermediates^{169,170}. There was a study that reported excessively high KOH concentrations may lead to inhibitory effects, due to OH^- adsorption on the catalyst surface¹⁷¹, but this was not observed in this work.

Figure 4.15 (b) shows the peak potential change with different KOH and methanol concentration. With 1 M methanol, when the KOH concentration increases from 0.1 M to 0.5 M, then to 1 M, the peak potential decreases from 0.64 V to 0.42 V, then to 0.35 V. And we observed this potential decrease for every methanol concentration. This demonstrates that the increasing KOH concentration can lower the

oxidation peak potential, and no saturation was observed. The peak onset potentials are also lowered accordingly, which could mean that the reaction barrier for methanol oxidation on Au NWNW is decreased. Studies suggested this could be due to the abundant OH^- can facilitate deprotonation steps during methanol oxidation, thereby enhancing reaction kinetics^{172,173}.

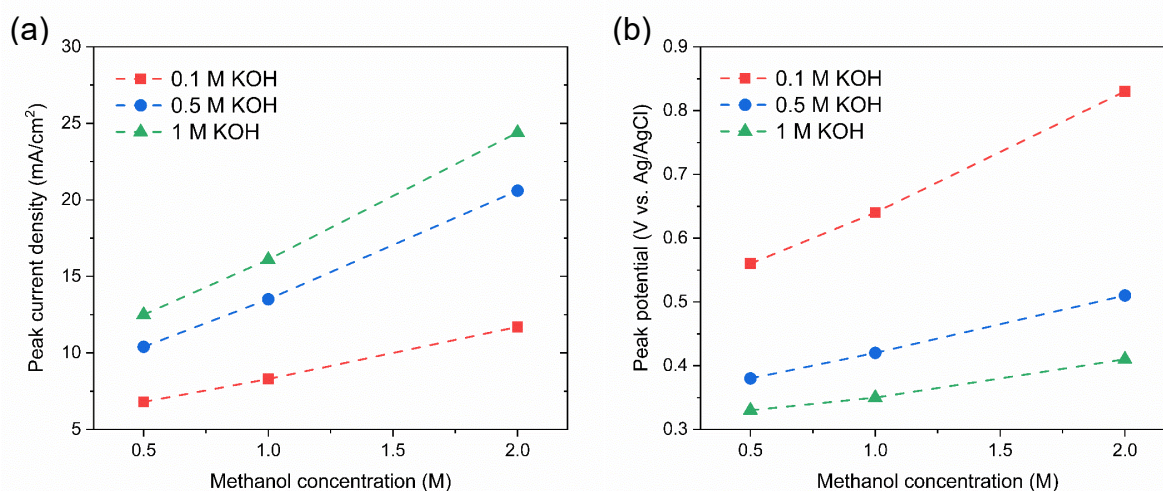


Figure 4.15 (a) anodic peak current density, and (b) peak potential as a function of the methanol concentration from Figure 4.14, with three different KOH electrolyte concentration: 0.1 M (red), 0.5 M (blue), and 1 M (green).

Influence of NWNW geometry

Figure 4.16 shows the CVs recorded of three Au NWNWs, with density of $4 \times 10^8 \text{ cm}^{-2}$, and nanowire diameters of 80, 130, and 170 nm, in 0.1 M KOH with and without 0.5 M methanol. For each Au NWNW sample, 200 CV cycles in the KOH electrolyte with methanol were run for 3 h, to test their long-term stability.

Figure 4.16 (a) shows the Au NWNW with 80 nm diameter nanowires, the solid blue curve shows the 10th CV cycle of the methanol oxidation in KOH, the oxidation peak locates at $U = 0.4 \text{ V}$ with a peak current density of $\sim 1.9 \text{ mAcm}^{-2}$, with the second anodic peak at $U = 0.6 \text{ V}$ for methanol oxidation on AuO, and formate oxidation to carbonate.¹⁶⁹ Figure 4.16 (b) and (c) show the CVs recorded for Au NWNWs with wire diameters of 130 and 170 nm, respectively. For these two samples, the methanol oxidation peak current density increases to 2.5 and 3.9 mAcm^{-2} , respectively. For all three samples, The CV curve for the 200th cycle was nearly the same as for the 10th cycle, two major anodic and cathodic peaks were slightly shifted, whereby the change in the peak current density was smaller than 5%, and the peak potential was shifted only 0.02 V. These minor changes give evidence that during the overall 200 cycles, the reactions did not severely modify the samples and that the Au NWNWs are stable units and thus have potential for long-term electrochemical performance.

Figure 4.16 (d) summarizes the current density values recorded for all the methanol oxidation peaks of the Au NWNWs in reference to both the nominal area and ECSA. With the nanowire diameter increasing, the anodic peak current density increased accordingly, this is due to the ECSA increase. Compared with the planar Au reference sample, the oxidation peak current density values per nominal area of the Au NWNW with nanowire diameters of 80, 130, and 170 nm were 86, 132, and 205 times higher, respectively. When divided by the measured ECSA of the Au NWNWs, the current density was still 4 times higher than for the reference sample. The Au NWNWs are electrochemically more active in the catalytic reactions towards methanol electro-oxidation compared to the planar smooth sample.

Thus, the large surface area of the 3D networks resulted in larger current densities, while the additional increase was attributed to the high electrochemical activity of the nanowire surface. The obtained values were comparable to those obtained by Graf et al.¹⁷⁴ for nanoporous gold samples, which exhibited a peak current density of 0.042–0.127 mAcm⁻² normalized to ECSA (in 1 M KOH + 1 M methanol electrolyte).¹⁷⁴

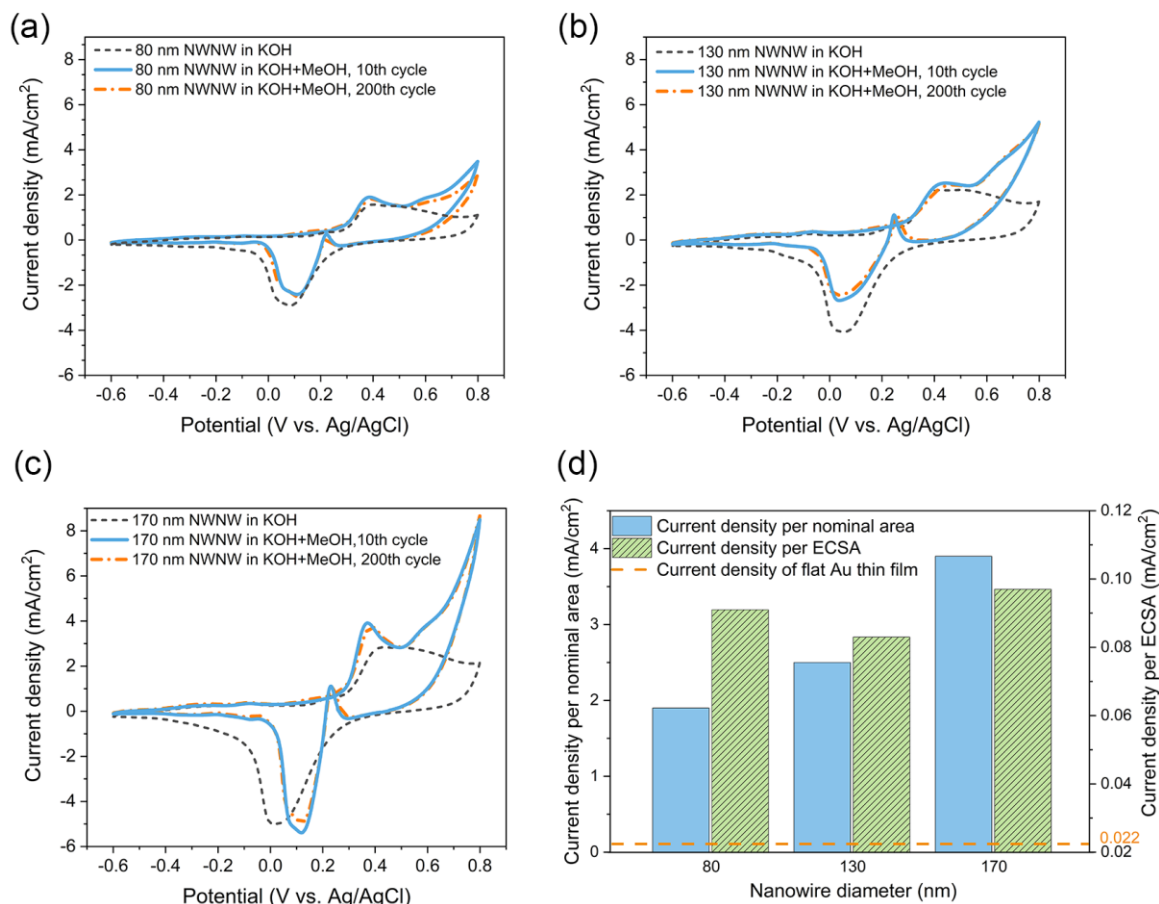


Figure 4.16 CVs recorded in 0.1 M KOH (black dash line) and in 0.1 M KOH + 0.5 M MeOH electrolyte. The graphs display the 10th cycle (blue solid line), and the 200th cycle (orange dash-dot line) for (a) 80 nm, (b) 130 nm, and (c) 170 nm diameter nanowires. (d) Methanol electro-oxidation peak current density divided by nominal area (blue) and ECSA (shaded green) for this three Au NWNWs. The orange dash line represents the methanol oxidation peak current density of the smooth Au thin film reference sample.

Morphology analysis after catalytic reactions

Morphological changes of the Au NWNWs that may have occurred during the CV measurements were investigated by SEM characterization before and after the methanol electrooxidation. The SEM images in Figure 4.17 reveal that the NWNWs maintained their original 3D interconnected structure throughout the 3 h long process, while the individual nanowires exhibited clear changes in morphology, especially at the upper tips. At the nanowire tips, faceted crystals were formed with larger sizes compared to the initial wire diameters. Such morphology changes have been reported before, e.g. by Ar'an-Ais, et al., who showed that both the shape and morphology of Pt nanoparticles were drastically degraded after 1000 CV cycles in a 0.5 M H₂SO₄ solution.¹⁷⁵ Surface restructuring was also reported by Cui, et al. for

porous PtCu nanotubes after 250 cycles in 0.1 M HClO₄ solution.¹⁷⁶ In our case, since the long nanowire sections (length \sim 27–28 μ m) below the tips remained unchanged, the overall surface area change was smaller than 4.5%. Thus, it should be emphasized that the catalytic performance of the Au NWNWs was not affected by the observed changes in the tip morphology, as evidenced by the excellent stability of the CV curves between the 10th and the 200th cycles.

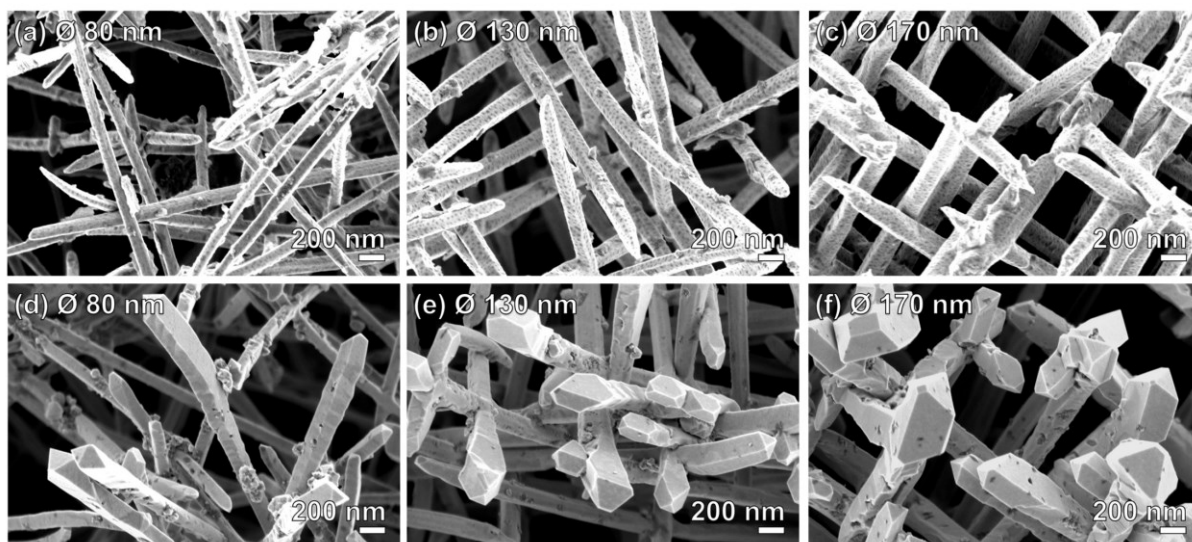


Figure 4.17 SEM images of Au NWNW deposited at $U = -0.9$ V vs. Ag/AgCl with different nanowire diameters, (a) and (d) 80 nm, (b) and (e) 130 nm, (c) and (f) 170 nm, before (a–c) and after (d–f) 200 CV cycles during methanol oxidation reaction measurements.

To summarize, Au NWNWs were tested as catalysts towards methanol oxidation reactions. By comparing the performance of tailored Au NWNWs, synthesized with an independent variation of their nanowire diameter, leaving all other parameters constant (nanowire length and density), we demonstrate that the methanol oxidation peak current is proportional to the increase of ECSA. In addition, the current density also increases with increasing concentration of methanol and KOH electrolyte. The peak potential, on the other hand, increases with increasing ECSA and increasing methanol concentration, but decreases with increasing KOH concentration. Therefore, a high concentration alkaline electrolyte can be very beneficial for methanol oxidation catalytic reactions. Au NWNWs exhibited remarkable long-term stability during CV measurements, only minor changes are observed at nanowire tips, but the oxidation peak current remains constant.

4.2.2 Au_{1-x}Ag_x alloy NWNWs

Alloys, which are composed of two or more metallic elements, often exhibit unique properties different than their original single metals. In particular, alloy catalysts can exhibit unique advantages, including enhanced catalytic activity, selectivity, and stability.^{177,178} The combination of different metals in an alloy catalyst can lead to synergistic effects, which can result from various factors, such as improved electronic properties, optimized geometric arrangements of active sites, and better resistance to deactivation or poisoning.^{5,179–181} Additionally, the tunability of alloy compositions allows for fine-tuning of catalytic properties to suit specific reactions.^{182–185} In this section, we will explore how Au_{1-x}Ag_x alloy NWNWs will behave differently than single Au and Ag metals, especially focus on the methanol electro-oxidation reaction in alkaline electrolytes.

This is also a fundamental approach to understand the influence of residual silver to the catalytic activity of nanoporous gold. There is a debate in the nanoporous gold research community, about whether the

residual silver can facilitate or decrease the catalytic activity of nanoporous gold, and how much content of Ag will lead to which influence^{186,187}. With our unique NWNW system, we can investigate this in an excellent and systematic manner, because we can tune the parameters independently by synthesizing “model porous systems” (the solid NWNWs) with controlled Ag composition. And separate the influence of composition from porosity variations.

In this section we first investigate how surface composition influences methanol oxidation reactions, by characterizing NWNWs with identical geometrical parameters, but tailored atomic composition. The composition was controlled via the electrodeposition process, as described in section 3.2. We then examine how variations in electrolyte and reactant concentrations affect the catalytic reaction and assess whether these parameters follow the same trends previously observed for pure Au NWNWs (section 4.1.1).

Influence of atomic composition

First series of NWNWs were fabricated with $4 \times 10^8 \text{ cm}^{-2}$ fluence template, etched with $\text{\O} 150 \text{ nm}$ nanochannels. The chemical composition was tuned by the electrodeposition parameters listed in chapter 3.2, and the sample atomic composition shown in this chapter were characterized by SEM-EDX analysis. Some examples of the sample morphology are shown in Figure 4.18.

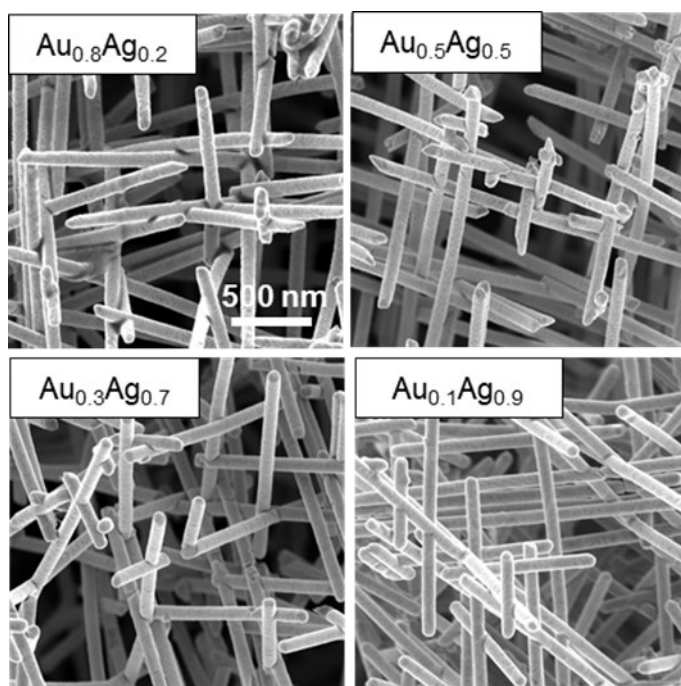


Figure 4.18 SEM images of $\text{Au}_{1-x}\text{Ag}_x$ NWNWs with density of $4 \times 10^8 \text{ cm}^{-2}$, nanowire diameter of 150 nm, and different atomic compositions.

Figure 4.19 shows the CVs of $\text{Au}_{1-x}\text{Ag}_x$ NWNWs with controlled Ag % at (namely 0, 0.1, 0.2, 0.5, 0.7, 0.8, and 1), in 0.1 M KOH electrolyte, with and without different concentration of methanol. First, we compare the CVs recorded only in KOH (black solid line). As Au and Ag get oxidized at different potentials, and Au only has one-step oxidation (Figure 4.13 (a)), but Ag undergoes two-step oxidations (Figure 4.19 (f)), this also applies to the oxide reduction peaks showed during the cathodic scan. Interestingly, the shape of the CVs recorded for AuAg alloys (b-e) are closer to that of the pure Au NWNWs at all Ag concentrations, exhibiting one oxidation peak during the anodic scan and one broad

reduction peak as the envelope of multiple reduction peaks. The oxidation peak shifts slightly to higher potentials, with the Ag composition increase.

Next, we analyze the effect of the addition of methanol for the various NWNWs. Figure 4.19 (a) shows the CVs recorded for the $\text{Au}_{0.9}\text{Ag}_{0.1}$ NWNW with various concentrations of methanol. The methanol oxidation peak is clearly shown at $U = 0.25$ V, increasing clearly when varying the methanol concentration from 0.1 (red dashed line) to 2 M (gold dashed line). This is different than pure Au NWNW (Figure 4.13), where the methanol oxidation peak is located at around $U = 0.5$ V to 0.6 V. Apart from the main oxidation peak, there another oxygen evolution peak appeared rising from 0.6 V, which also shows current increase with the methanol concentration increase. Figure 4.19 (b) shows the CV recorded for $\text{Au}_{0.8}\text{Ag}_{0.2}$ NWNW, which shows a small oxidation peak at $U = 0.15$ V, this can be identified by the corresponding current density increases slightly with increasing methanol concentration. There is also an oxygen evolution peak observed, which has a similar current as the $\text{Au}_{0.9}\text{Ag}_{0.1}$ NWNW. These two CVs recorded for $\text{Au}_{1-x}\text{Ag}_x$ NWNWs with small Ag content (up to 20 %) reveal that the methanol oxidation potential can be shifted to lower values by alloying, however at the expenses of the peak current density, which is significantly lower than for pure Au (4.6 mAcm^{-2}).

Figure 4.19 (c-e) present the CVs recorded for $\text{Au}_{1-x}\text{Ag}_x$ NWNWs with $x > 0.5$. It is noticeable that the CVs show the oxidation peaks corresponding to the oxidation of $\text{Au}_{1-x}\text{Ag}_x$ alloys, but no methanol oxidation peak can be observed, i.e., the current density does not vary significantly or systematically with increasing methanol concentration in the investigated potential range. Also, the oxygen evolution peak decreases with the Ag content increase. Figure 4.19 (f) shows the CVs recorded for the pure Ag NWNW, there is no methanol oxidation peak shown in the measured potential range.

In conclusion, the obtained data revealed a strong dependence of the methanol oxidation reaction on the NWNW composition. At low Ag concentrations, Ag at% < 20%, a synergistic effect is shown on the Au-rich alloys NWNWs. This special effect can lower the methanol oxidation peak potential, indicating that it can lower the reaction barrier, but at the expense of the oxidation peak current density. When the Ag composition is too high (higher than 50 at%), the catalytic activity cannot be observed.

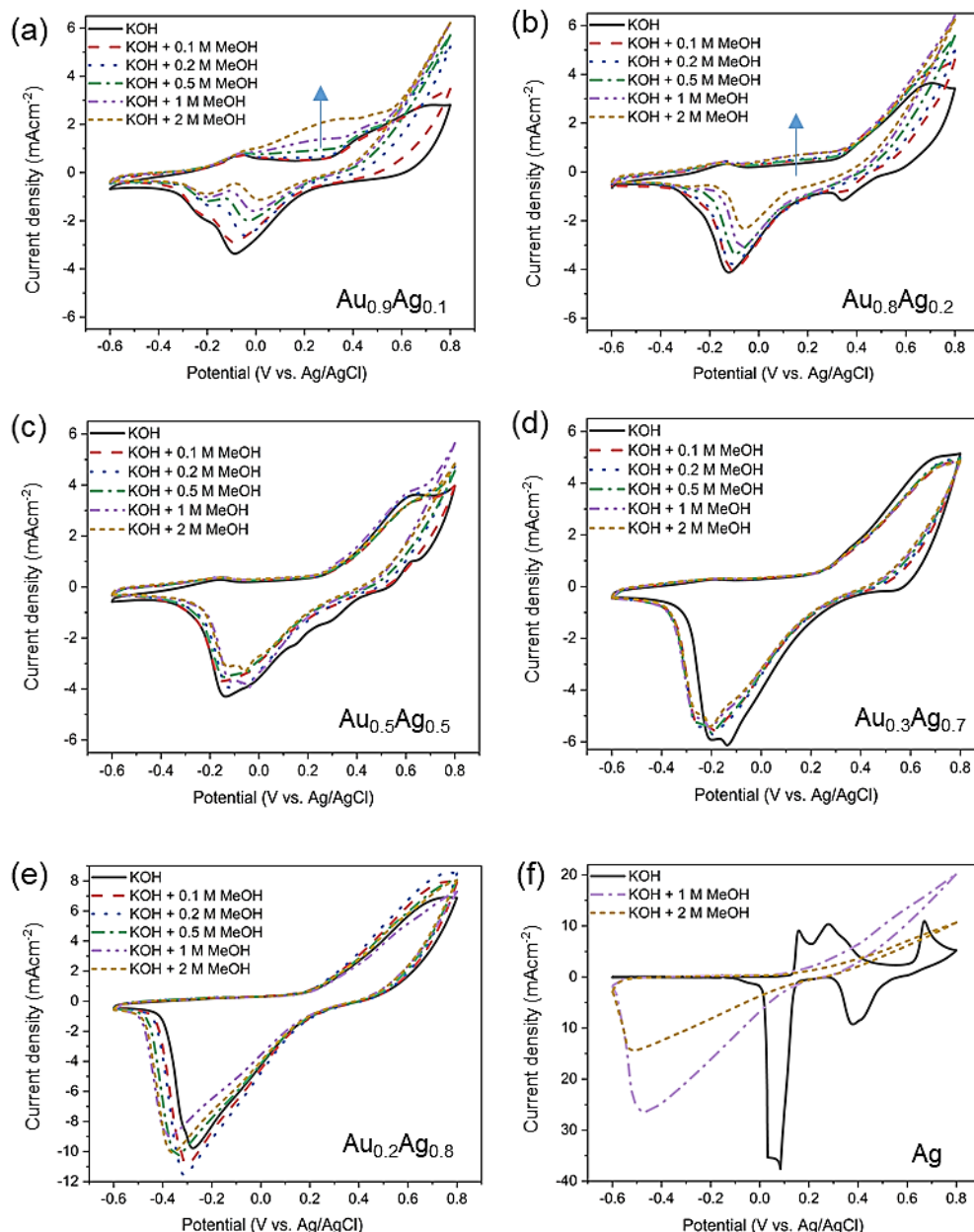


Figure 4.19 CVs recorded for (a) $\text{Au}_{0.9}\text{Ag}_{0.1}$, (b) $\text{Au}_{0.8}\text{Ag}_{0.2}$, (c) $\text{Au}_{0.5}\text{Ag}_{0.5}$, (d) $\text{Au}_{0.3}\text{Ag}_{0.7}$, (e) $\text{Au}_{0.2}\text{Ag}_{0.8}$, (f) Au_0Ag_1 NWNWs, in 0.1 M KOH electrolyte with different concentration of methanol, scan rate = 50 mV/s, at room temperature.

From past studies, Olaya and Wittstock, et al., reported dealloyed nanoporous gold shows different performance after removing the residual Ag by cycling in H_2SO_4 , as shown in Figure 4.20, for lower Ag content ($\chi_{\text{Ag}} < 1\%$), the peak onset potential is shifted to more positive values. At the same time, the peak I_{a1} current is higher. They hypothesize Ag can promote the oxidative adsorption of the methoxide, as well as the OH^- adsorption on the surface, thus Ag plays an active role in the first steps of the methanol oxidation reaction¹⁸⁷. This is in partial agreement of what we observed, that $\text{Au}_{0.9}\text{Ag}_{0.1}$ sample showed higher peak current density than $\text{Au}_{0.8}\text{Ag}_{0.2}$ sample. The adsorption promotion effect can help explain the lower peak potential and lower peak onset potential of $\text{Au}_{0.9}\text{Ag}_{0.1}$ NWNW compare to pure Au

NWNW, with better supply of the OH^- to the methanol oxidation reaction, the reaction barrier can be lowered.

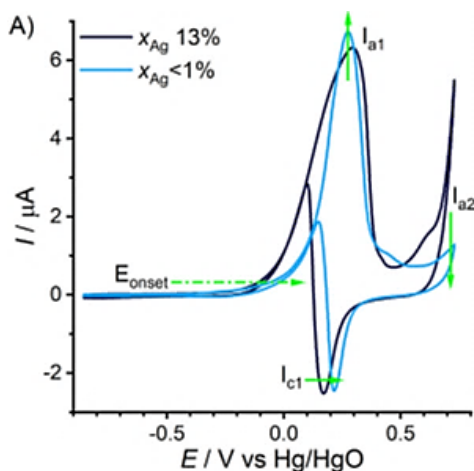


Figure 4.20 CVs of “as-prepared” NPG (curve in black) and NPG “after cycling in H_2SO_4 ” (curve in blue) in 1 M MeOH + 0.25 M KOH¹⁸⁷.

Influence of electrolyte and reactant concentration

After investigating the effect of Ag content independently on the methanol oxidation reaction, using a relatively low concentration of KOH, i.e., 0.1 M. We investigated the effect of the KOH concentration by increasing the concentration further to 0.5 and 1 M. Another series of $\text{Au}_{1-x}\text{Ag}_x$ NWNWs were fabricated with density of $2 \times 10^9 \text{ cm}^{-2}$, and nanowire diameter of 150 nm.

Figure 4.21 (a-c) show the CVs recorded for the $\text{Au}_{0.9}\text{Ag}_{0.1}$ NWNW in (a) 0.1 M, (b) 0.5 M, and (c) 1 M KOH, without methanol (black solid line), and with 0.5 M (red), 1 M (blue), and 2 M methanol (green). The series of CVs reveal that an increase of KOH concentration from 0.1 M to 1 M contributes to a significant increase of the methanol oxidation peak current density. For example, for 2 M MeOH in the electrolyte (green curves), the peak current density increases from ~ 5 to $\sim 20 \text{ mAcm}^{-2}$, as shown in Figure 4.21 (a) and (c), respectively, while the peak potential slightly shifts to lower potentials, from $U = 0.45 \text{ V}$ to 0.4 V . This is similar as observed for Au NWNW, where the peak potential also shifts to lower potentials with the KOH concentration increase (Figure 4.14). There is also a promotion effect of the oxygen evolution reaction, as the current rising starts from 0.7 V , and increases with the KOH concentration.

Figure 4.21 (d-f) show the CVs recorded for the $\text{Au}_{0.8}\text{Ag}_{0.2}$ NWNW. In this case, when increasing the KOH concentration from 0.1 M (d) to 1 M (f), the peak current density for 2 M MeOH increases from ~ 7 to $\sim 23 \text{ mAcm}^{-2}$, while the peak potential decreases from $U = 0.45 \text{ V}$ to 0.35 V . Therefore, both samples showed higher methanol oxidation current with the increasing of the KOH concentration. It should be noticed that the oxygen evolution in this case starts at around 0.6 V and the current can reach to 50 mA at $U = 1 \text{ V}$. This indicates that the oxygen evolution reaction is strongly promoted, with both the increasing concentration of KOH and methanol. This has been reported before, that methanol can facilitate oxygen evolution reaction by enhancing adsorption of intermediates, leading to the generation of additional OH^- , and lowering the energy barrier, thus increase the overall current density^{167,171,188,189}.

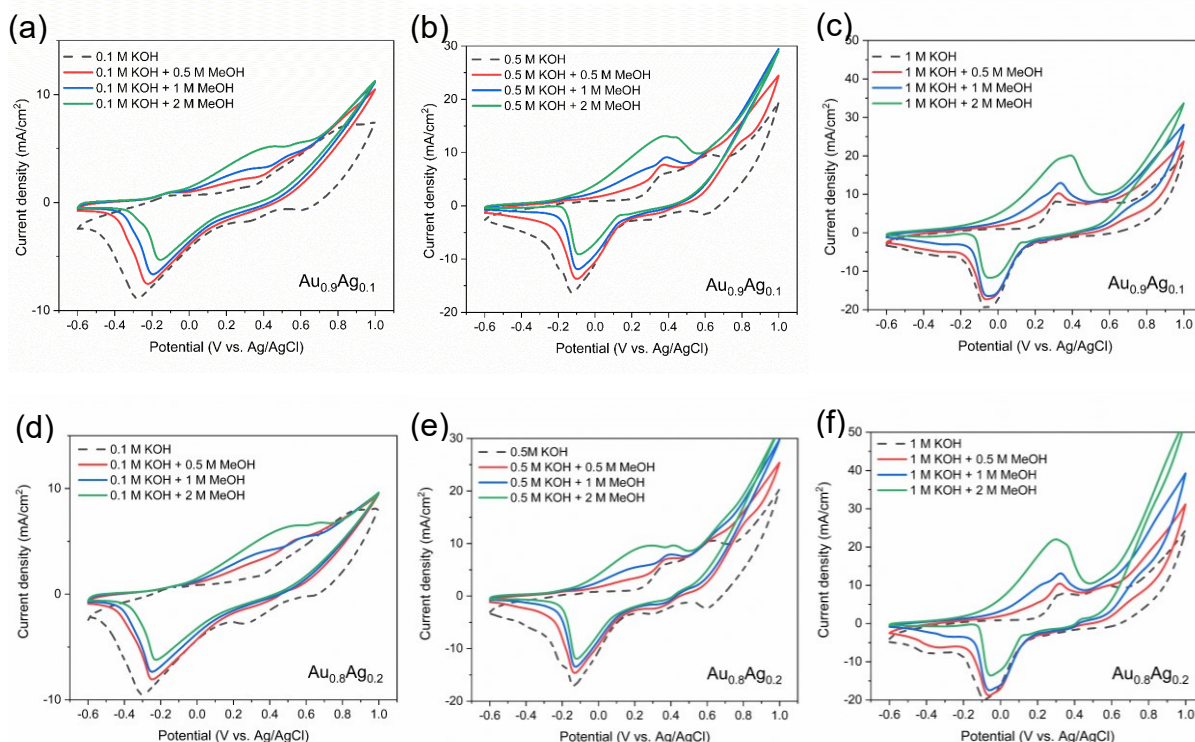


Figure 4.21 CVs recorded for $\text{Au}_{0.9}\text{Ag}_{0.1}$ NWNW in (a) 0.1 M, (b) 0.5 M, (c) 1 M KOH with different concentration methanol, and $\text{Au}_{0.8}\text{Ag}_{0.2}$ NWNW in (d) 0.1 M, (e) 0.5 M, (f) 1 M KOH with different concentration methanol.

Figure 4.22 shows the CVs recorded for $\text{Au}_{1-x}\text{Ag}_x$ NWNWs ($x \geq 0.4$) in 1 M KOH, with different concentration of methanol. Figure 4.22 (a) shows the CVs of $\text{Au}_{0.6}\text{Ag}_{0.4}$ NWNW, the CV in KOH (black dash line) shows multiple oxidation and reduction peaks, which correspond to the one step oxidation/reduction of Au and two step oxidation/reduction of Ag atoms on the nanowire surface. But when we add methanol into the electrolyte, there is no methanol oxidation peak can be observed, the metal oxidation peak is even decreased with higher methanol concentration. There is another oxygen evolution peak observed starting from 0.7 V, which can reach up to 60 mA at 1 V. Figure 4.22 (b) shows the CVs of $\text{Au}_{0.4}\text{Ag}_{0.6}$ NWNW, there is no methanol oxidation peak can be observed, the oxygen evolution peak is also decreased compare to the $\text{Au}_{0.6}\text{Ag}_{0.4}$ NWNW. The $\text{Au}_{0.3}\text{Ag}_{0.7}$ and $\text{Au}_{0.2}\text{Ag}_{0.8}$ NWNWs shown in Figure 4.22 (c, d) are neither active for methanol oxidation nor for the oxygen evolution reaction.

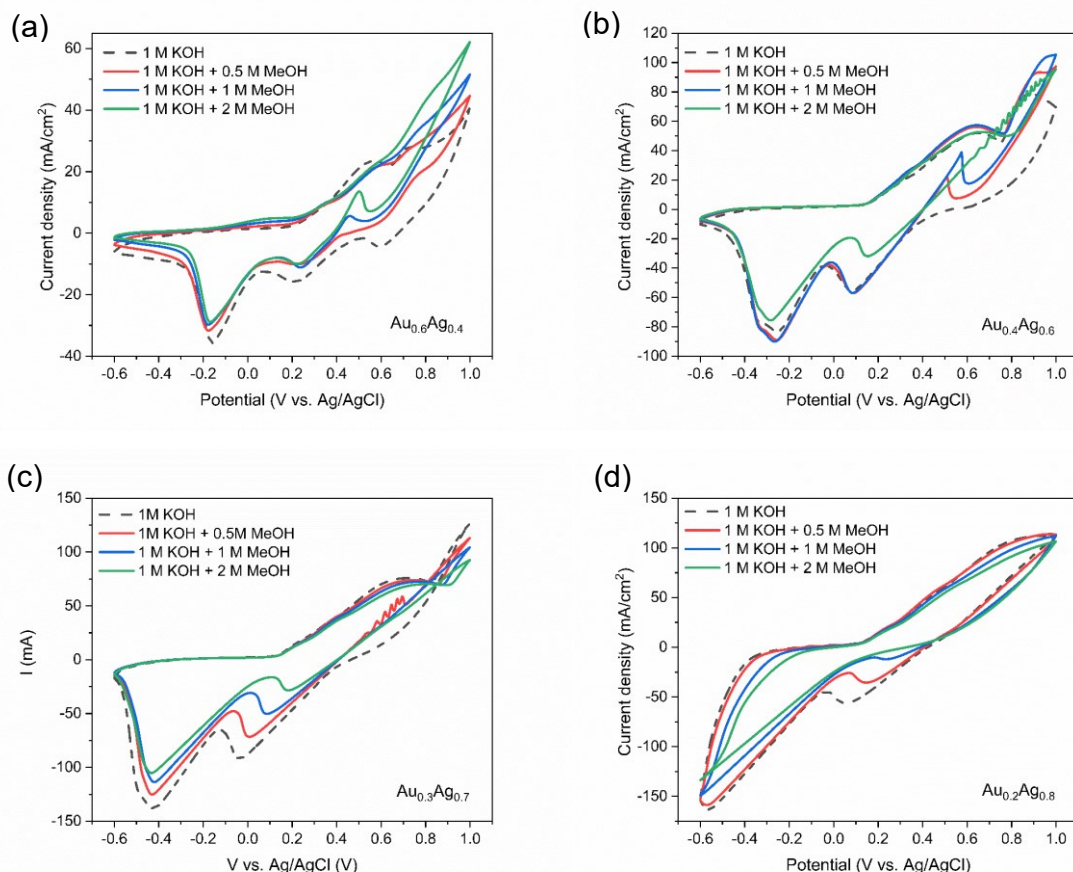


Figure 4.22 CVs recorded for (a) $\text{Au}_{0.6}\text{Ag}_{0.4}$, (b) $\text{Au}_{0.4}\text{Ag}_{0.6}$, (c) $\text{Au}_{0.3}\text{Ag}_{0.7}$, (d) $\text{Au}_{0.2}\text{Ag}_{0.8}$ NWNWs in 1 M KOH with different concentration of methanol.

In summary, in higher concentration KOH, $\text{Au}_{1-x}\text{Ag}_x$ NWNWs with Ag at% < 20% can catalyze the methanol oxidation reaction with higher current density, and lower peak potential, but higher Ag at% samples do not show a methanol oxidation peak even with higher KOH concentration. The oxygen evolution reaction can be promoted with both higher concentration of KOH and methanol, for NWNWs with Ag at% < 30%.

Morphology analysis after catalytic reactions

Figure 4.23 shows SEM images after the catalysis tests. The morphology analysis before the reaction was presented in Figure 4.18, all nanowires exhibit similar morphology with uniform diameter of 150 nm and smooth surface. However, after the catalysis reactions, these SEM images reveal composition-dependent morphology changes. The nanowires in the Au-rich NWNWs shown in Figure 4.23 (a) and (b) remain mostly unchanged, revealing changes mostly at the nanowire tip. These changes are more severe for the Ag-rich samples in Figure 4.23 (c, e), display the fine-grained particles agglomerate at the top surface. The SEM image in Figure 4.23 (f) reveals that in the case of pure Ag, the NWNW geometry has been completely lost, which shows only agglomeration of fine-grained particles.

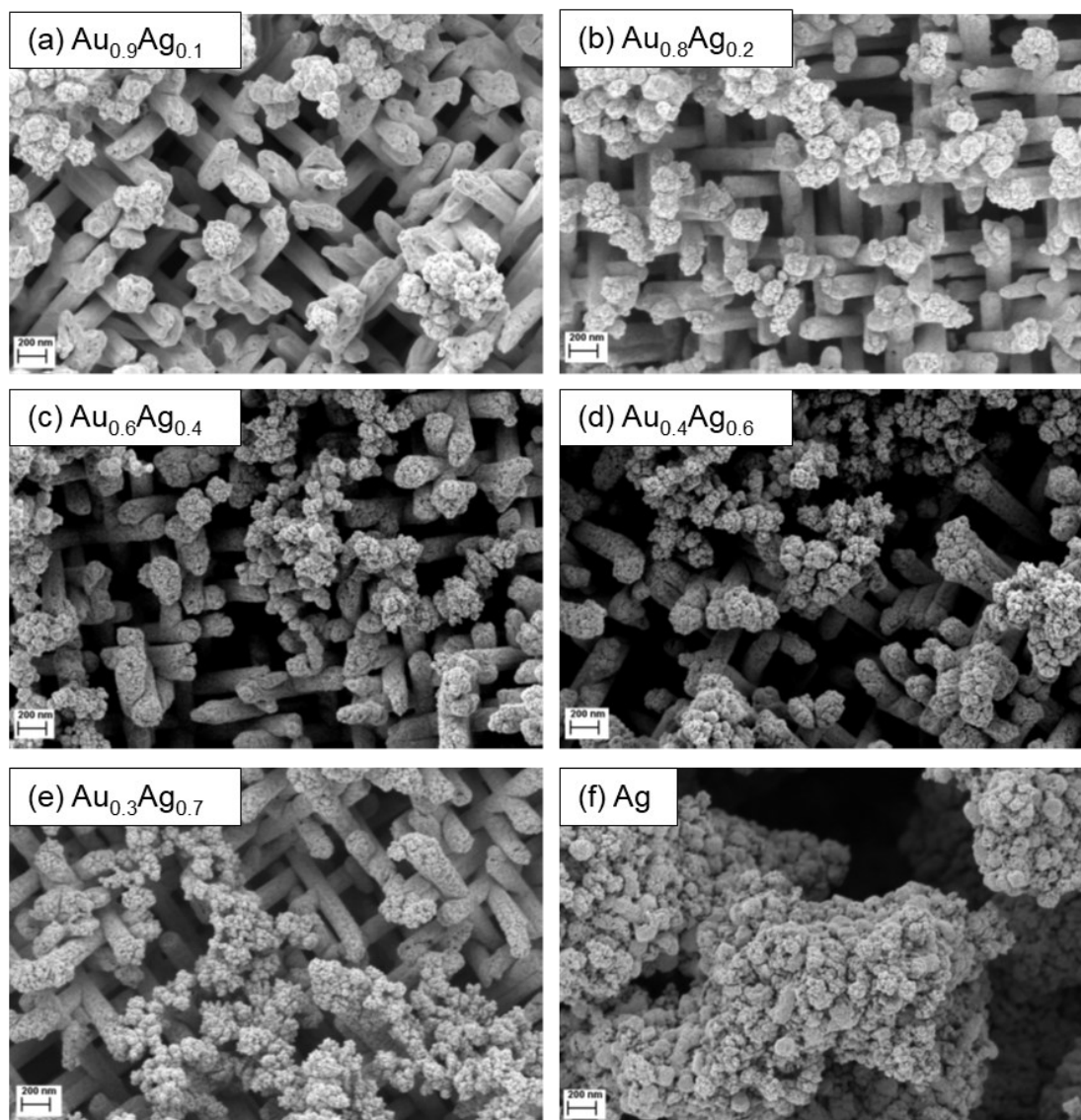


Figure 4.23 SEM pictures of $Au_{1-x}Ag_x$ NWNWs with different compositions after catalyzing the methanol oxidation reaction.

Since the duration and conditions of the catalytical reactions were tested the same for all samples, these results seem to indicate that the stability of the NWNW during the electrochemical reaction decreases with increasing Ag concentration.

To confirm that whether the diffusion of Ag atoms is responsible for these strong morphology changes, we performed EDX mappings of the $Au_{0.3}Ag_{0.7}$ NWNW after the reaction, collecting information about the local atomic distribution. Figure 4.24 shows the SEM image of the selected area (left), the center of the SEM image are some agglomerated particles, and the corresponding EDX mapping (middle) shows a Ag rich region in the middle. From the line scan (right), we can also see the middle part has 80 at% Ag, while the outer region only has 40 – 60 at% Ag. The EDX data indicates that during the methanol oxidation reaction, Ag atoms are oxidized, diffusing from the nanowires and forming particles agglomerate around and between the nanowires. It seems that the agglomeration occurs preferably at the top of the surface. However, more measurements at longer reaction times should be performed in the future to clarify this aspect.

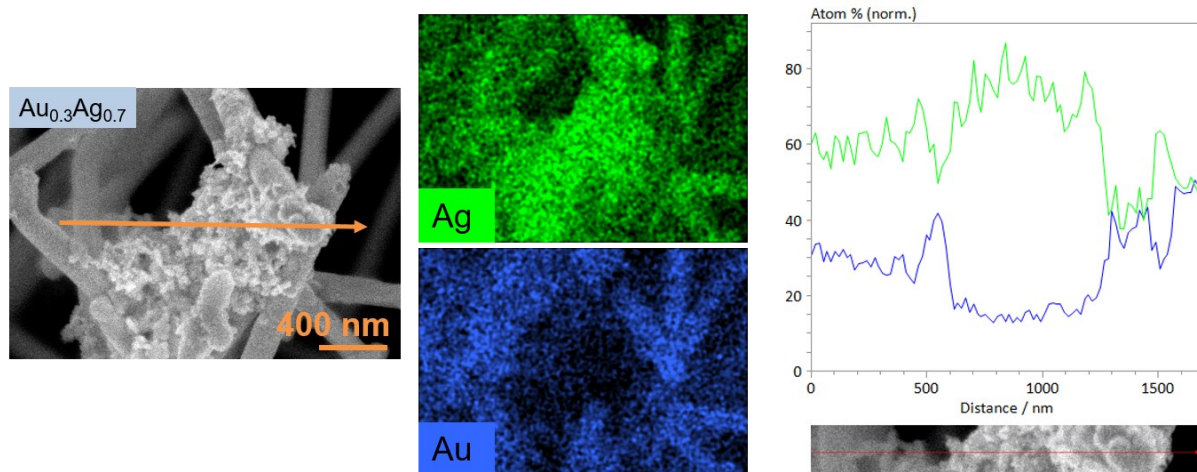


Figure 4.24 EDX mapping and line scan of a $\text{Au}_{0.3}\text{Ag}_{0.7}$ NWNW sample, SEM image (left) with the arrow represents the line scan, elemental mapping (middle) of Au (green) and Ag (blue), and quantitative line scan (right).

In this section, we synthesized $\text{Au}_{1-x}\text{Ag}_x$ NWNWs with identical geometrical parameters and tailored compositions ranging from pure Au to pure Ag, and characterized their catalytic performance, geometrical and compositional stability with respect to the methanol oxidation reaction. We systematically analyzed CVs recorded using different concentrations of both alkaline electrolytes and methanol. We found out that for all concentrations applied, only the Au-rich samples are active towards the methanol oxidation reaction in the investigated potential range. For $\text{Au}_{1-x}\text{Ag}_x$ NWNWs with $x < 20\%$, the methanol oxidation reaction starts at lower onset potentials, but unfortunately at the expense of lower current density. The geometry of the Au-rich NWNWs is maintained after 50 repeated CV cycles. For $\text{Au}_{1-x}\text{Ag}_x$ NWNWs with higher Ag content ($> 20\%$) the morphological and geometrical stability decreases gradually due to the formation of Ag-rich fine-grained particles, and agglomerates around and in between the nanowires. The NWNW geometry of the pure Ag samples disappeared completely.

4.2.3 Nanoporous Au NWNWs

In this section, the methanol oxidation reaction is tested on two selected dealloyed nanoporous Au NWNWs. Mechanically stable networks were fabricated by dealloying for 1 h and 6 h of two $\text{Au}_{0.3}\text{Ag}_{0.7}$ NWNWs, with nanowire density $2 \times 10^9 \text{ cm}^{-2}$, and nanowire diameter 150 nm. Figure 4.25 shows the representative SEM images of the employed samples. Details on the synthesis of these networks were presented in section 3.3.1. The dealloying process obviously increases the porosity significantly. This provides a unique opportunity to investigate the influence of nano sized pores, in particular, hierarchical porosity for NWNWs with otherwise similar geometry and composition on the electrochemical methanol oxidation reaction. Increasing porosity is a relatively widely applied approach to improve catalytic performance, however, systematic studies on the influence of porosity are challenging since most samples do not exhibit tailored parameters but rather a wide distribution of feature sizes.

Figure 4.25 (a) shows the $\text{Au}_{0.3}\text{Ag}_{0.7}$ NWNWs after dealloying for 1 hour. It exhibits straight wires and homogeneously distributed nanopores. We determined an average residual Ag content of 12 at% (over the sample) by EDX analysis, and a surface composition of 32 at% Ag by XPS analysis, indicating the presence of a Ag-rich surface layer, that may disturb the reactions. Figure 4.25 (b) shows the SEM image of a $\text{Au}_{0.3}\text{Ag}_{0.7}$ NWNWs after dealloying for 6 hours. This sample exhibits slightly bent nanowires and larger pores appear on nanowire surface. The EDX analysis showed that the average bulk Ag composition was 4 at%, while the surface composition contains around 14 at% Ag by XPS analysis

(summarized in Table 4.5). This indicates that the applied free dealloying process yields a higher Ag atom concentration on the nanowire surface, which should be considered when evaluating the electrochemical results.

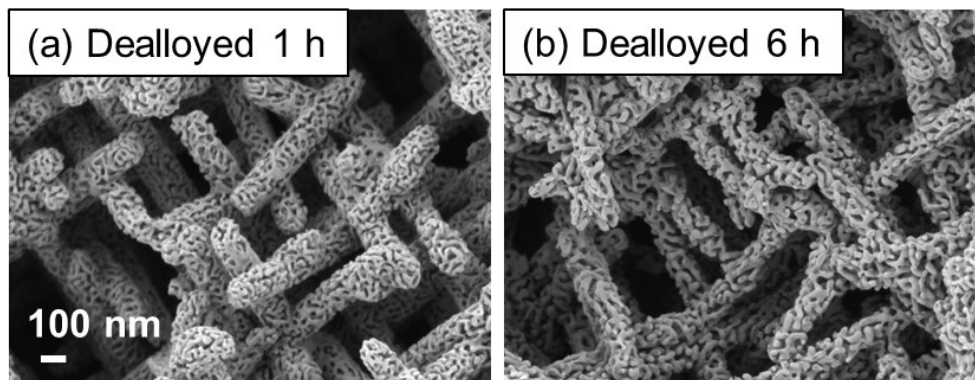


Figure 4.25 SEM image of $\text{Au}_{0.3}\text{Ag}_{0.7}$ NWNWs dealloyed for (a) 1 h and (b) 6 h.

We tested the two samples toward the methanol oxidation reaction. To be able to compare their performance, we employed the same experimental conditions as the Au and $\text{Au}_{1-x}\text{Ag}_x$ NWNWs using KOH solutions with three different concentrations, namely 0.1, 0.5, and 1 M, and different amounts of methanol in the solution.

Figure 4.26 shows the CVs recorded for the $\text{Au}_{0.3}\text{Ag}_{0.7}$ NWNWs after dealloying for 1 hour. The graphs show that, with increasing KOH concentration, the methanol oxidation peak current density increases systematically. In 0.1 M KOH (Figure 4.26 (a)), the methanol oxidation peak current density is around 15 mAcm^{-2} with 2 M methanol. With the KOH concentration increase to 1 M, the peak current increases to around 25 mAcm^{-2} with 2 M methanol. In the same time, the oxidation peak potential gradually shifts from 0.7 V to 0.4 V, which is the same trend as observed before.

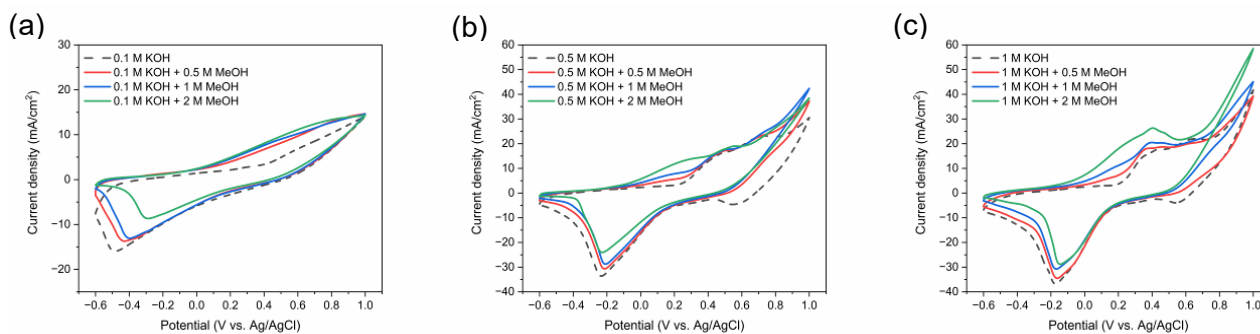


Figure 4.26 CVs recorded for $\text{Au}_{0.3}\text{Ag}_{0.7}$ NWNW dealloyed for 1 h, tested in (a) 0.1 M KOH, (b) 0.5 M KOH, (c) 1 M KOH with different concentration of methanol.

Figure 4.27 shows the CVs recorded for the $\text{Au}_{0.3}\text{Ag}_{0.7}$ NWNWs after dealloying for 6 hours. In 0.1 M KOH solution, the methanol oxidation peak current is around 8 mAcm^{-2} with 2 M methanol. With the KOH concentration increase to 1 M, the peak current increases to around 20 mAcm^{-2} with 2 M methanol. Similarly, we can observe the peak potential shifts from 0.6 V to 0.4 V.

In the previous section, we demonstrated that the $\text{Au}_{1-x}\text{Ag}_x$ ($x < 0.2$) alloys can oxidize methanol at a lower potential than pure Au. This finding can also apply with the dealloyed samples, with similar Ag content on the nanowire surface, so the methanol oxidation peak is also at a rather low potential.

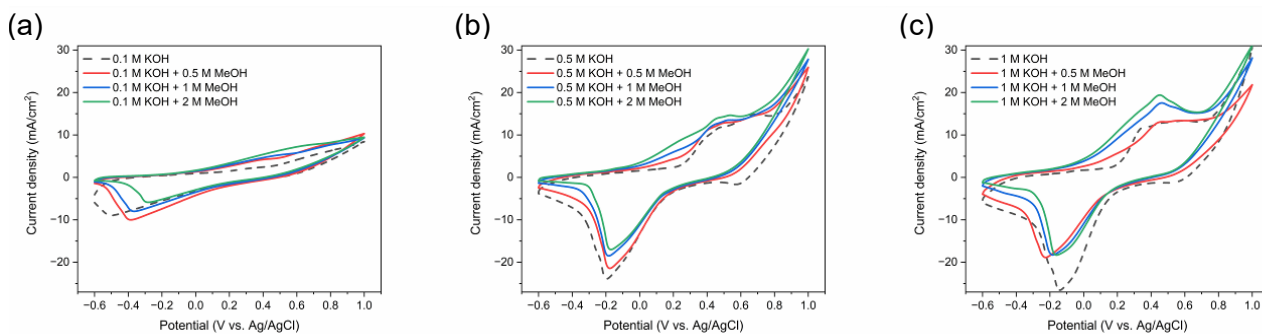


Figure 4.27 CVs recorded for $\text{Au}_{0.3}\text{Ag}_{0.7}$ NWNW dealloyed for 6 h, tested in (a) 0.1 M KOH, (b) 0.5 M KOH, (c) 1 M KOH with different concentration of methanol.

Long-term CV measurements

The long-term stability of the two selected types of nanoporous NWNWs were investigated by recording 300 CVs under the experimental conditions that had yielded the highest current density values, i.e., in 1 M KOH solution with 3 M methanol. The tests were carried out in a large cell containing 80 ml KOH electrolyte, to guarantee sufficient reactant supply during the tests, and the electrolyte was constantly stirred during whole testing period. The CV curves are shown in Figure 4.28, selected CVs are plotted, namely 1st, 2nd, 3rd, 10th, 50th, 150th, 200th, 250th and 300th, for comparison in each case.

Figure 4.28 (a) shows the CVs recorded for the $\text{Au}_{0.3}\text{Ag}_{0.7}$ NWNWs after dealloying for 1 hour. We can see the methanol oxidation peak shows the highest current density in the 1st CV cycle, which is 130 mAcm^{-2} at $U = 0.9 \text{ V}$, while the CV curve in pure KOH only shows a Au/Ag oxidation peak current density of $\sim 15 \text{ mAcm}^{-2}$. During the first three cycles, the current density dropped strongly from 130 to 80 mAcm^{-2} , this is mainly due to the fast consumption of methanol. During the CV cycles, we can see lots of bubbles evolve inside the electrochemical cell, which is a sign of the high reaction rate. The bubbles also caused the fluctuations of the current, which can be seen from the fluctuating curve recorded in 1st CV of KOH with methanol in Figure 4.28 (a). Because the network structure is rather dense, there is a diffusion limitation of molecules moving through the pore. Therefore, even though the electrolyte was constantly stirred by the magnetic stirrer, methanol cannot be supplied in time for the oxidation reaction, thus result in the fast decrease of the current.

From the 3rd to the 10th cycle, the anodic peak gradually shifting to more positive potentials, which is beyond 1 V, therefore we can only see a linear curve during the anodic scan. This may due to the loss of Ag atoms on the nanowire surface. From our previous CV results of the $\text{Au}_{1-x}\text{Ag}_x$ NWNWs, we know that with AuAg alloys can catalyze the methanol oxidation at a lower potential. Therefore, the potential shift could due to the decrease of Ag atoms on the surface.

From the 10th to 50th cycle, we can see the anodic peak shifting back to a lower potential range, as well as the cycles afterwards, this is mainly due to the decrease of surface area, that both the anodic potential and current decrease simultaneously. This can be confirmed by DLC measurement, as shown in Figure 4.29, after 300 CV cycles, the DLC decreased 50%, which means the ECSA also decreased 50% after the long-term CV test.

Figure 4.28 (b) shows the CVs recorded for the $\text{Au}_{0.3}\text{Ag}_{0.7}$ NWNWs after dealloying for 6 hours. The 1st CV cycle with KOH and methanol also shows the highest peak current $\sim 100 \text{ mAcm}^{-2}$ at $U = 0.7 \text{ V}$. From the 1st to the 300th cycle, the peak current density decreases accordingly. After 300th cycle, the peak current decreases to $\sim 45 \text{ mAcm}^{-2}$ at $U = 0.4 \text{ V}$. This is also caused by the ECSA decrease during the CV cycle, details are shown in Figure 4.29.

The current from the 6 h dealloyed sample is slightly lower than the 1 h dealloyed sample, this is mainly due to the smaller ECSA, which also caused a smaller peak potential. The measured DLC is around 25% lower than the 1 h dealloyed sample (Figure 4.29), this indicates a high ECSA is the key factor to achieve a high catalytic current.

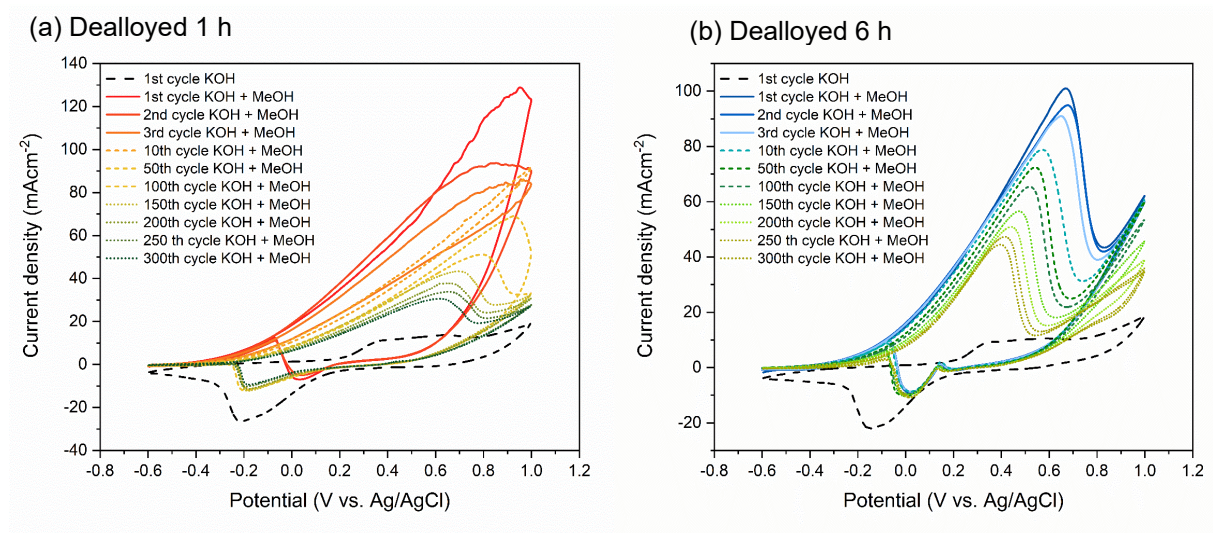


Figure 4.28 CVs recorded for porous Au NWNWs fabricated by dealloying $Au_{0.3}Ag_{0.7}$ NWNWs for (a) 1 h, and (b) 6 h. The CVs were measured in 1 M KOH solution with addition of 3 M MeOH.

Figure 4.29 shows the DLC change before and after the 300 cycles, which is directly proportional to the ECSA values. The data shows both samples have a ECSA decrease of around 50%, as discussed before, this is the main reason for the anodic peak current density decrease.

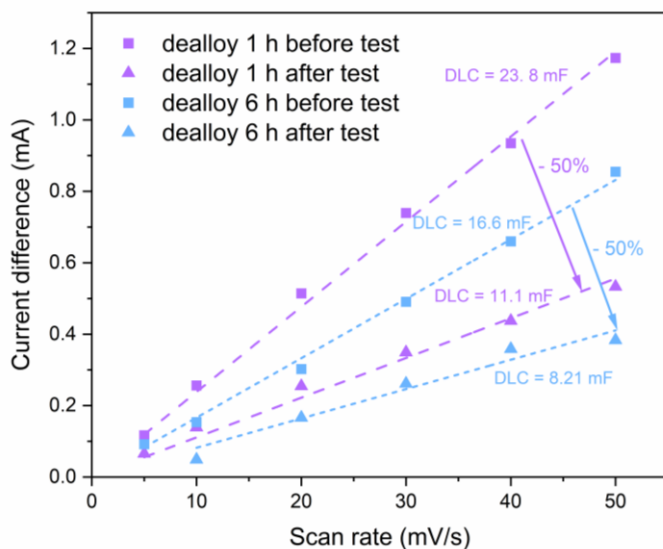


Figure 4.29 DLC measurements of two porous Au NWNW samples before and after the long-term CV tests.

After the long-term cyclic tests, we analyzed the nanoporous NWNWs morphology change with SEM, as shown in Figure 4.30, there are some crystals formed on the nanowire tip. We can see at the top

surface of the sample, some pores on the nanowire surface start to close, and the nanoporous structure get coarsened. This will certainly decrease the sample surface area, which is in agreement with the DLC measurement results.

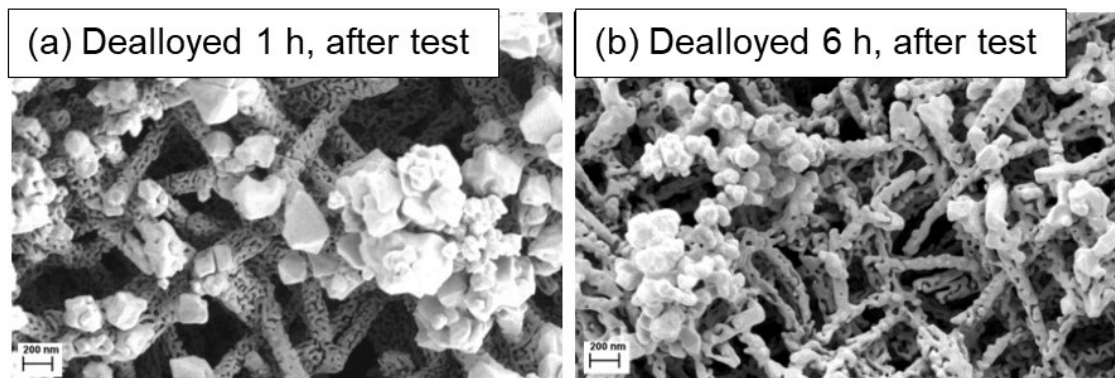


Figure 4.30 SEM images of the nanoporous NWNWS after the long-term CV tests.

In section 3.3, we discussed the atomic composition of the nanoporous NWNWs, and the distribution inhomogeneity from nanowire surface to core. Before the cyclic test, the porous nanowires consist of a Ag-rich shell, which is much larger than the Ag concentration in sample bulk. After the long-term cyclic test, there is a significant decrease of the Ag concentration, both on the surface and through the whole sample. The high oxidation potential can separate the Ag atoms from the porous nanowires, some of which redeposited on the nanowire tip and formed the crystals, while some get lost into the electrolyte. This could be another reason for the high Ag concentration detected by XPS, since XPS is especially sensitive to the top surface of the sample. The Ag atom concentration is also an influencing factor for the catalytic performance of the nanoporous NWNWs, which can lower the methanol oxidation potential, but also result in a lower current density. Therefore, the measured anodic peak current density and potential during the long-term CV tests were influenced by many different factors, including the ECSA values, the pore size, the surface atomic composition, as well as the methanol concentration in the electrolyte. However, to understand all the results observed in this section, more experiments are needed in the future. For example, the reaction products should be analyzed by gas chromatography and nuclear magnetic resonance.

Table 4.5 Dealloyed nanoporous NWNWs composition change before and after the long-term CV test

Sample name	1 h dealloyed nanoporous NWNW		6 h dealloyed nanoporous NWNW	
Composition	χ_{Ag} before test (at%)	χ_{Ag} after test (at%)	χ_{Ag} before test (at%)	χ_{Ag} after test (at%)
EDX	12±1.1	4±1.7	3±0.9	1±0.2
XPS	32	14	17	8

4.3 Summary

In this chapter, we present our investigation of the electrochemical performance of three series of NWNWs towards the methanol oxidation reaction, selected as the model reaction. The three types of NWNWs were pure Au NWNWs, $\text{Au}_{1-x}\text{Ag}_x$ alloyed NWNWs, and nanoporous NWNWs obtained after dealloying the $\text{Au}_{1-x}\text{Ag}_x$ NWNWs. We determined the ECSA of all NWNWs. The ECSA of the pure Au NWNWs was quantified as a function of nanowire diameter by the AuO reduction peak charge integration method. We found out an excellent agreement between the ECSA and the estimated S_{GEO} of the samples, which increased with increasing nanowire diameter, from 20.8 to 40.3 cm^2 on a planar 1 cm^2 area. The ECSA of the $\text{Au}_{1-x}\text{Ag}_x$ NWNWs was determined by the DLC method, which shows the ECSA of the NWNWs increase accordingly as the density increase, and both methods prove to be partially suitable for our samples, as every method has its own flaws, that we must judge it critically. The choice of a reference sample can largely influence the characterization results.

We varied many parameters during the studies, including the geometrical size, atomic composition, and electrolyte concentration, to test and compare how they can vary the catalytic performance of the samples.

Au NWNWs were employed to quantify the influence of the nanowire diameter, nanowire density, methanol concentration, and KOH concentration. The nanowire diameter increase directly leads to the increase of ECSA, which generates a higher methanol oxidation current density. This also leads to a shift of peak potential to higher voltages. On the other hand, the increase of KOH concentration can facilitate the methanol oxidation reaction by increasing the current density and lowering the peak potential.

$\text{Au}_{1-x}\text{Ag}_x$ NWNWs were applied to investigate the effect of the presence of Ag in tailored quantities on the oxidation of methanol. From the current results, only Au-rich ($\chi_{\text{Ag}} < 20$ at%) samples are active for catalyzing the methanol oxidation, which can lower the peak potential, but in sacrifice of a small decrease of the current density. For NWNWs with higher Ag content ($\chi_{\text{Ag}} > 50$ at%), the samples did not exhibit activity towards the methanol oxidation reaction.

Then, we fabricated nanoporous NWNWs by the dealloying method. This effectively decreased the Ag content, while significantly increased the ECSA by a factor of 3. The nanoporous NWNWs yielded higher current densities than the corresponding $\text{Au}_{1-x}\text{Ag}_x$ NWNWs with similar Ag concentrations. In addition, the nanoporous NWNWs exhibited lower methanol oxidation peak potentials than the pure Au NWNWs. However, the nanoporous NWNWs exhibited lower cyclic stability than the cylindrical solid Au NWNWs, as the fine nanostructure is easily coarsened with the high potentials. Also, the network structural stability is damaged by the dealloying process, a higher density NWNW should be able to provide more crossing junctions and higher mechanical stability. Another problem is the nanoporous nanowires still have a rather high Ag content residual after dealloying, which can significantly decrease the methanol oxidation current density. Therefore, in future works, the dealloying process should be further optimized to decrease the Ag content in the dealloyed NWNWs as much as possible, while not coarsening the nanoporous structure. Based on our studies, the goal can be to synthesize nanoporous NWNW with less than 5 at% Ag on the surface. In the meantime, nanowire density and nanowire diameter should be adjusted accordingly to guarantee sufficient NW crossing junctions that grant NWNW stability during dealloying.

5. Au NWNW Surface Wetting State

Wetting phenomena on solid surfaces, particularly when considering nanostructured surfaces, evidence intriguing and complex interactions with water and other liquids that have captivated the attention of researchers in various scientific fields^{190–195}. It has been demonstrated that the surface wetting state is impacted by the unique characteristics of nanostructures present on the surfaces, including nanoparticles, nanowires, and other nanoscale features^{192,194,196,197}, and in particular by parameters such as surface-area-to-volume ratio, intricate surface roughness, and the surface chemical composition^{14,198–201}. For electrochemical reactions, if the reaction requires stable contact with gas phase reactants, hydrophobic surfaces will have the advantage of continuously collecting gas and absorbing it onto the electrode surface²⁰². In contrast, when the reactions require constant contact with the liquid phase reactants, hydrophilic or super-hydrophilic surfaces should be considered, which can lead to a faster release of the gas products, without clogging the surfaces with large bubbles, thus improving the reaction efficiency²⁰³.

In this chapter, we will discuss the wettability of our NWNW structure with controlled geometry and porosity, where it shows a porosity dependent wetting state change (Figure 5.1). The wetting behavior of nanostructured materials is important for a wide range of technological applications ranging from liquid transport, and microfluidic devices, sensors, to catalysis^{204,205}.

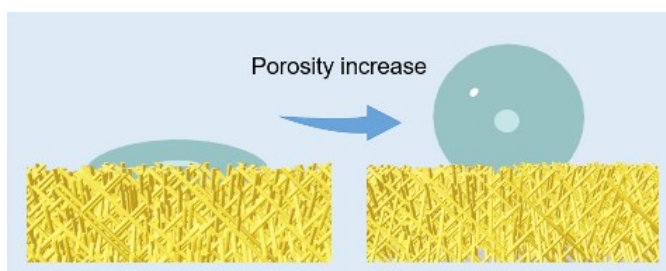


Figure 5.1 Schematics of water droplets sitting on top of the 3D Au NWNW structure with the surface wetting states transition from low contact angle, hydrophilic (left) to high contact angle, hydrophobic (right), as the structural porosity increases⁵⁹.

5.1 Au NWNWs Fabrication with Varied Porosity

By electrodeposition in etched ion-track membranes and subsequent dissolution of the PC membranes, we fabricated two series of free-standing Au NWNWs: a “low-density” series consisting of NWNWs with density $(2.3 \pm 0.3) \times 10^8$ wires cm^{-2} and nanowire diameters ranging between 60 and 200 nm, and a “high-density” series $(1.3 \pm 0.1) \times 10^9$ wires cm^{-2} , with nanowire diameters between 40 and 200 nm. The nanowire density was estimated from SEM analysis of the density of pores on the corresponding PC template foils. The minimum nanowire diameter value was selected to guarantee the interconnectivity and stability of the NWNWs. Especially for the low-density series, nanowires with diameters smaller than 60 nm provided too few interconnection points to form a stable network structure. Figure 5.2 shows the top and side view of two representative samples, with the variation of wire density and wire diameter, we were able to tune the network structure porosity from 98% to 20%.

The network porosity was calculated based on the measured nanowire diameter, network height, and nanowire density. The crossing junctions were not included in the calculation. Thus, only the wire density and nanowire diameter variations are considered. The detailed calculation was done through the equation below:

$$\Phi = 1 - \frac{V_{nw}}{V_{tot}} = 1 - \frac{\pi \times r_{nw}^2 \times L_{nw} \times f_{nw}}{h} \quad 5 - 1$$

V_{nw} is the volume of all the nanowires, V_{tot} is the total volume of the space, h is the height of the network structure, while L_{nw} is the length of the nanowire, which is 1.41 times longer than h , because the wires are 45° tilted. The f_{nw} is the density of nanowires.

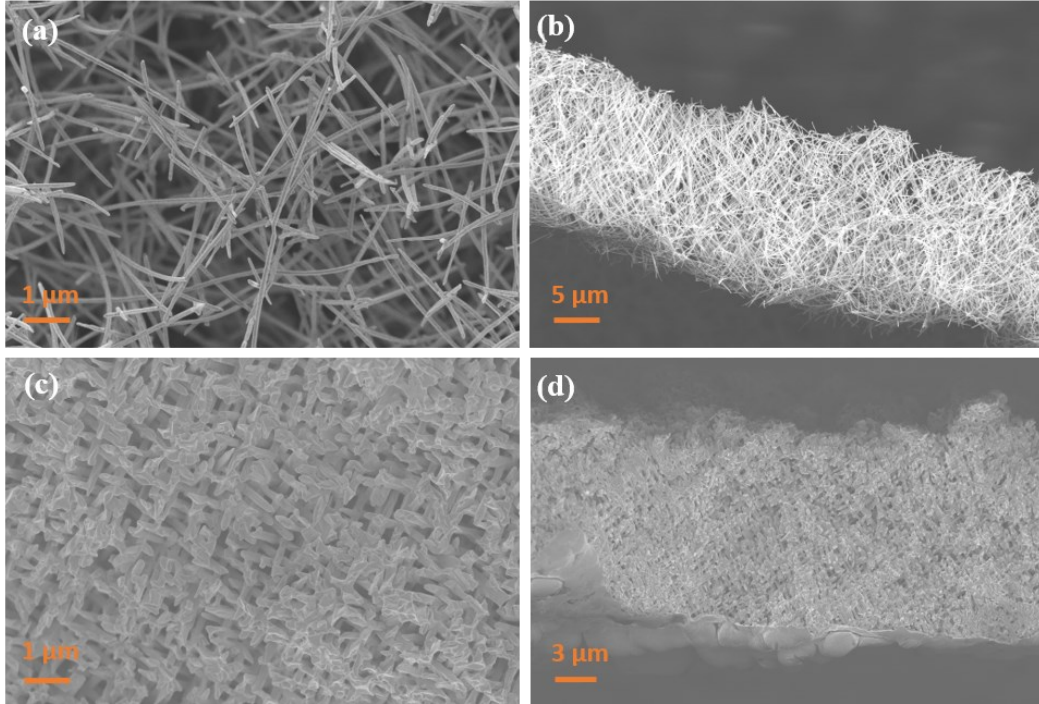


Figure 5.2 Representative SEM images of (a, b) one low-density Au NWNW with 100 nm wire diameter and 95% porosity, and (c, d) one high-density Au NWNW with 200 nm wire diameter and 28% porosity. (a)/(c) and (b)/(d) display top- and side views, respectively.

It is worth emphasizing that NWNWs with porosities as high as 98% have been achieved. Figure 5.2 (a, b) show a representative sample with 95% porosity, the structure of these highly porous Au NWNWs is still self-supporting and mechanically stable. After the nanowires are freed from templates, since the highly porous NWNW is formed by thin wires and low wire density, the thinnest nanowires cannot maintain the original orientations, given by the template, and they rather bend appearing at times curved along their length (Figure 5.2 (b)). With increasing wire density and wire diameter, the network structure becomes denser (Figure 5.2 (c, d)), the nanowires can maintain their 45° orientation, and the average spacings between adjacent nanowires decrease with increasing wire density and diameter.

5.2 Contact Angle Measurement

We first compared the contact angle change within each series, with the nanowire diameter increase from 60 to 200 nm, the results plots of the “low-density” series are shown in Figure 5.3. The increase in NW diameter is evident in the SEM images taken under the same magnification. While the thinner nanowires (Figure 5.3 (b, c)) exhibit a bending morphology, the thicker ones (Figure 5.3 (d, e), diameter > 130 nm) appear straight, maintaining the original template channel orientation. The NWNWs with the smallest wire diameters (60-100 nm) exhibit an average contact angle of around 130°. For thicker nanowire diameters (100-200 nm), the contact angle of the various NWNWs varies between 110° and 130°. For NWNWs with wire diameters above 200 nm a larger distribution of contact angles was observed including a transition to hydrophilic states.

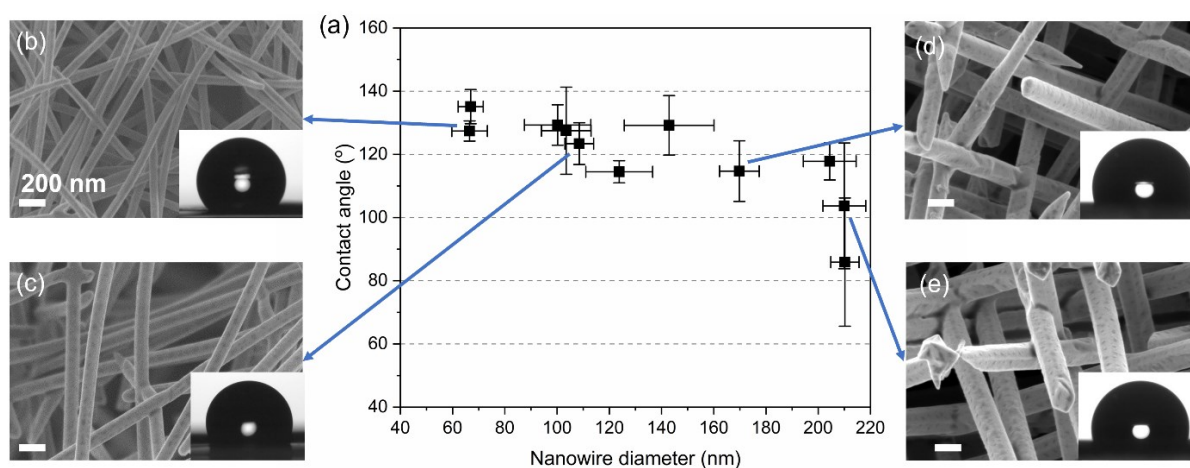


Figure 5.3 (a) Contact angle measured for low-density NWNWs with tailored nanowire diameter between 60 and 210 nm, and porosity ranging between 98% and 86%, respectively. SEM images show selected networks with nanowire diameter (b) 60 nm, (c) 100 nm, (d) 160 nm, (e) 210 nm, the scale bar is 200 nm. The insets show the sessile drop on the corresponding sample surface. The error bars are given by the standard deviation of five contact angle measurements on various positions of the same sample.

Figure 5.4 displays the contact angle measurements of the high-density series of Au NWNWs, with wire diameters ranging from 40 nm to 200 nm. The NWNWs of this series exhibit more crossing junctions than the low-density NWNWs, so nanowires with diameters between 60 and 200 nm can still maintain their orientation. The sample with the thinnest nanowires ($\text{\O} \sim 40$ nm) displays bending wires and exhibits a rather high contact angle ($120^\circ - 130^\circ$). When the wire diameter increases to around 60 nm, we observed a transition stage, the contact angle ranging from 10° to 120° , this large deviation may be a result of the nanowire diameter distribution ($\sim 10\%$) combined with the local randomly distributed spacing and pores between nanowires. When the wire diameter reaches around 100 nm, the samples show super-hydrophilicity, where the contact angle is smaller than 10° , and we observed a swift droplet spreading all over the surface. When the wire diameter further increases, the contact angle again rises and stabilizes at around 40° , which is similar to a bulk gold surface²⁰⁶.

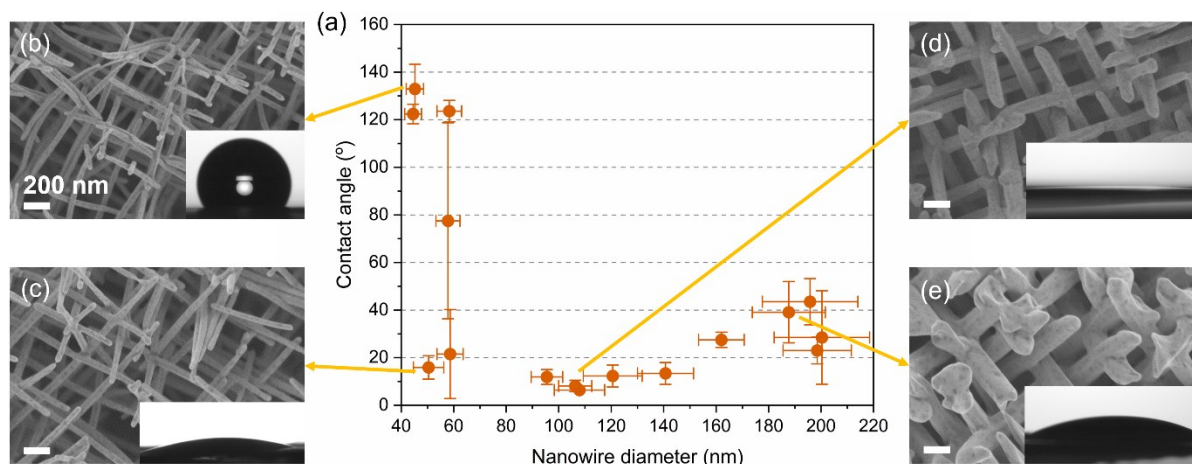


Figure 5.4 (a) Contact angle measured for high-density Au NWNWs with tailored nanowire diameter between 40 and 200 nm, and porosity ranging between 96% and 28%, respectively. SEM images show selected networks with nanowire diameter (b) \varnothing 40 nm, (c) \varnothing 60 nm, (d) \varnothing 110 nm, (e) \varnothing 180 nm, the scale bar is 200 nm. The insets show the sessile drop on the corresponding sample surface. The error bars are given by the standard deviation of five contact angle measurements on various positions of the same sample.

For comparison, we fabricated two different planar Au reference surfaces, shown in Figure 5.5. The first one is a \sim 300 nm thick smooth Au layer sputtered on a Si wafer. The sputtered Au surface exhibits hydrophilicity with a contact angle of around 40° , which represents the hydrophilic nature of Au, and is in agreement with reported literature values^{197,206}. The second one is an electrodeposited Au thin film substrate layer, which adopted the roughness of the polycarbonate template surface. This Au thin film shows a higher contact angle ($\sim 90^\circ$) attributed to the surface roughness. Obviously, the wettability of these two pure Au surfaces differs dramatically from the Au NWNW structure, evidencing that the special wetting phenomena of NWNW are mainly the result of this 3D nanostructure.

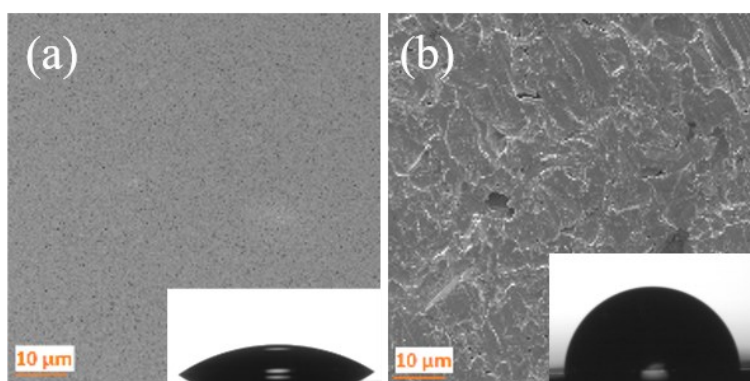


Figure 5.5 SEM images of (a) Au sputtered silicon wafer, and (b) Au substrate layer with insets of sessile drop for contact angle measurement.

To further study and understand the wettability transition by NWNW geometry variation, we plotted the contact angle of each NWNW against the calculated porosity, as shown in Figure 5.6.

For all low-density NWNWs, the porosity ranges from 98% to 85%, and the contact angle decreases with decreasing porosity. All samples with porosity higher than 95%, exhibit high contact angles above 120° independent of the NW density. However, for porosities between 80% and 95%, the samples

display mixed wetting behaviors, i.e., hydrophobic and hydrophilic in a sequential manner. This indicates that the water droplet is very sensitive to the surface microstructure, resulting in an unstable wetting behavior within this porosity range. Here, the contact angle varies widely between 120° and 10° . We define this phase as a transition state, in which the NWNW transits from hydrophobic to hydrophilic behavior. This transition regime can be originated from the random distribution of ions (i.e., the distribution of nanowires), which is especially noticeable at high porosities, where nanowire density and diameter are smaller, leading to larger distribution of interwire distances and subsequent local deviations from the original 45° nanowire orientation, which in turn affects the measured apparent contact angles. When the porosity is lower than 80%, the samples became super-hydrophilic with contact angles smaller than 10° . Further decrease of the porosity to between 60% and 20% leads to a slight increase in the contact angle to around 20° to 50° .

This suggests that, as the porosity decreases, the interplay between the pore size distribution, surface structure, and drop contact line becomes increasingly significant in determining the wetting behavior. Following Bico et al. 2001²⁰⁷, modeling the interfacial energies leads to a condition for a critical contact angle of imbibition. For a porous medium with interconnected channels or pores, this condition states that when the structure is invaded by liquids, the contact angle is smaller than 90° . Since the contact angle with smooth gold is around 40° to 60° , imbibition should theoretically occur for all the samples. However, as pointed out in the review article by Gambaryan-Roisman 2014²⁰⁸, this model does not account for the influence of local substrate structures. The local structure governs the local position of the contact line. In addition, rather strong contact line pinning can lead to a metastable state of the drop on the substrate.

From our experimental results, we observed stable hydrophobic behavior for very high porosity ($> 90\%$) samples, while samples with porosities between 80% and 90% exhibit strong fluctuations in measured contact angles. We attribute this behavior to the fact that at this porosity range, where bending nanowires cannot maintain the original 45° wire orientation, local differences in nanowire orientation and distribution result in a variety of contact angles (Figure 5.2). We hypothesize that, for the hydrophobic samples, with very high porosity nanostructures, air may become trapped within the pores beneath the drop²⁰⁹. Below a certain porosity (i.e., smaller interwire distances), the drop is sometimes pinned to the structures and therefore resulting in a hydrophilic contact angle.

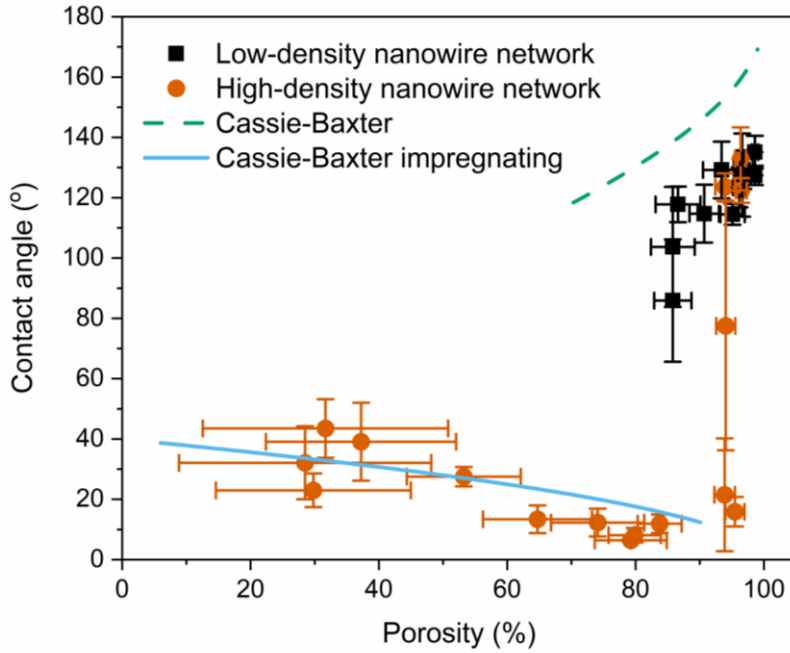


Figure 5.6 Measured contact angle values versus the NWNW porosity visualizing the influence of the network porosity on wetting state transition. The corresponding values estimated with the models of Cassie-Baxter (solid blue line) and Cassie-Baxter impregnating (dash green line) are also shown.

Assuming that for the hydrophobic NWNWs, the drop sits on top of the bending nanowire structure with air trapped beneath, we can use the Cassie-Baxter equation,

$$\cos(\theta^*) = -1 + f_s \cdot (\cos\theta_Y + 1) \tag{5-2}$$

to calculate the apparent contact angle, where f_s is surface roughness, and θ_Y is the contact angle for the smooth gold surface, obtaining the green dash line in Figure 5.6. It can be seen on the graph that the Cassie-Baxter model quantifies the trend of the low-density samples very well. The discrepancy between the predicted and measured contact angle values is around 20° for the hydrophobic samples. We attribute this systematic shift in contact angle values to the complex surface morphology of the designed NWNWs, in contrast to the simplifications assumed by the theoretical models²¹⁰.

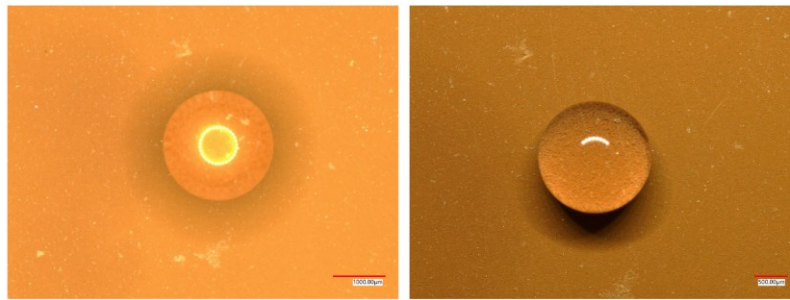
To model the hemi-wicking of the drop for lower-porosity NWNWs, we apply the impregnating Cassie-Baxter model²¹⁰,

$$\cos(\theta^*) = 1 + f_s(\cos\theta_Y - 1) \tag{5-3}$$

obtaining the blue line in Figure 5.6, and demonstrating a very good agreement between the model prediction and the measured contact angles.

These results show a clear dependency between the effective porosity of the NWNWs and their wettability, with both high-density and low-density series. For very high-porosity NWNWs, the droplet sits on top of the structure with trapped air, leading to a clear hydrophobic behavior (Figure 5.7), while for lower porosity NWNWs, imbibition is energetically favorable, with the liquid spreading across the rough hydrophilic surface driven by capillarity (Figure 5.8, Figure 5.9). In addition, we found the hydrophobic samples do not exhibit a classical behavior as traditional hydrophobic surfaces, but there is a high adhesion between the droplet and the sample surface, so we performed additional measurements to examine the adhesion between the droplet and sample surface.

Top view: the darker ring around it is the light shadow



View from side: there is no wetting can be observed

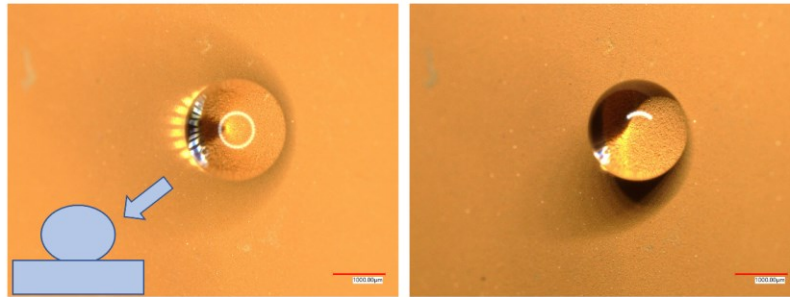


Figure 5.7 Photos of a 5 μL droplet on top of a hydrophobic nanowire network sample by Keyence optical microscope, scale bar is 1 mm. Nanowire diameter 104 nm, density $2.3 \times 10^8 \text{ cm}^{-2}$, with porosity of 97%.

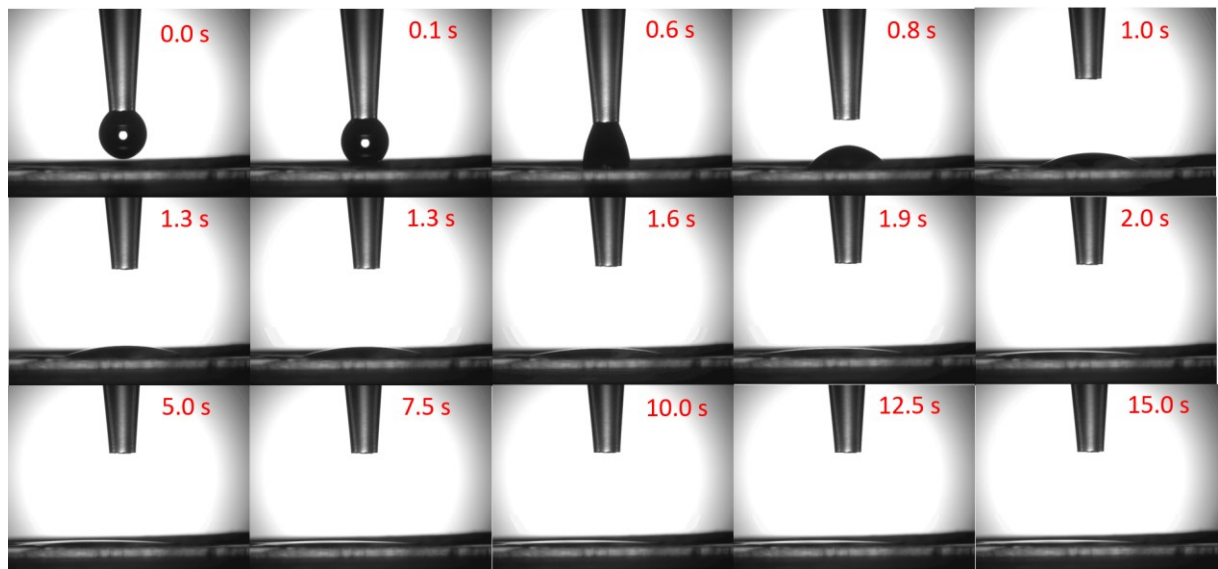


Figure 5.8 Photos of the sessile drop contact angle measurement by the high-speed camera on the Biolin Scientific Theta-lite tensiometer. On a hydrophilic NWNW sample, with nanowire diameter 106 nm, density $1.3 \times 10^9 \text{ cm}^{-2}$, and porosity of 80%.



Figure 5.9 Photos of a 5 μL droplet on top of a hydrophilic nanowire network sample by Keyence optical microscope, a wetted ring around the droplet can be observed, scale bar is 1 mm. Nanowire diameter 120 nm, density $1.3 \times 10^9 \text{ cm}^{-2}$, with porosity of 74%.

5.3 Droplet Sliding Measurement

To study the droplet adhesion on sample surface, the highly porous samples were mounted on a tilting stage, and the advancing and receding angles were measured. Figure 6 shows the representative results obtained for a high-porosity low-density NWNW with 60 nm diameter nanowires. We employed two droplet sizes, 4 and 15 μL , for each sample, and they showed similar behavior, displayed in Figure 5.10 (a, b), respectively. The images evidence that with increasing tilting angle, the droplet advancing angle slightly increases, while the receding angle largely decreases. Moreover, the measurements show a very high contact angle hysteresis. The contact angle hysteresis is the difference between advancing and receding angles:

$$\theta_{hys} = \theta_{adv} - \theta_{rec} \quad 5 - 4$$

Normally this angle is defined when the droplet contact line movement is observed during the tilting process, but we cannot observe this movement during the entire process, so the value from the sample tilted at 90° is used. We can observe a contact angle of 135° with a contact angle hysteresis of 35° ($4 \mu\text{L}$ droplet) and 80° ($15 \mu\text{L}$ droplet). This demonstrates an extremely high adhesion of the droplet to the substrate. Moreover, we performed the same measurement with a $4 \mu\text{L}$ droplet on a fresh rose petal, where we observed a contact angle around 130° . And the θ_{hys} is 25° when tilted 90° ($4 \mu\text{L}$ droplet), while for our Au NWNW sample, the θ_{hys} is 34° under the same conditions. This may indicate that our sample possesses a higher water droplet adhesion than a fresh rose petal.

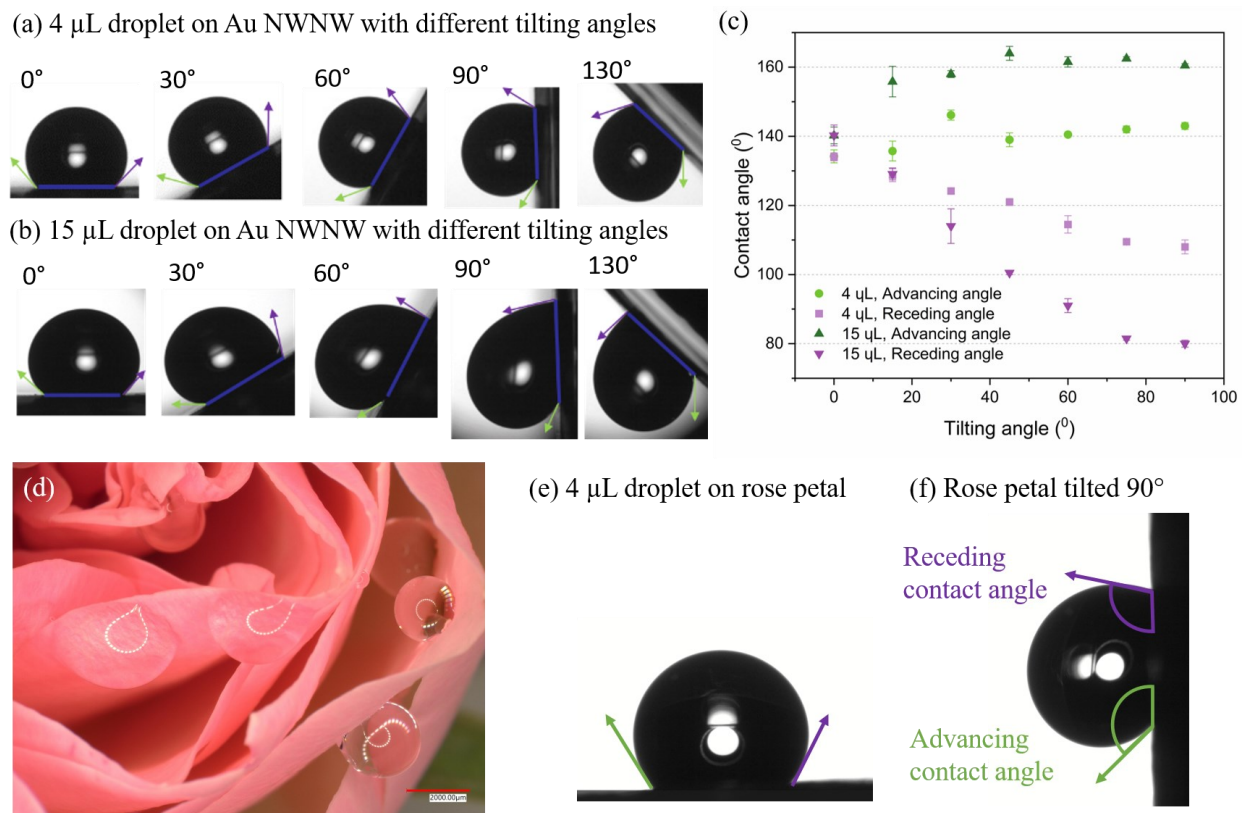


Figure 5.10 (a) $4 \mu\text{L}$ and (b) $15 \mu\text{L}$ water droplet sitting on Au NWNW surface with different tilting angles, (c) plots of two volume water droplets advancing (green) and receding (purple) contact angles as a function of stage tilting angle, (d) optical image of a rose with multiple droplets attached on the petals, (e, f) images of a $4 \mu\text{L}$ water droplet on one rose petal surface (e) horizontal position, and (f) tilted 90° with advancing (green) and receding (purple) angles.

This phenomenon we observed is very similar to the rose-petal effect, as shown in Figure 5.10 (d-f), where the surface exhibits high contact angle and high contact angle hysteresis. There are certain similarities between the structural geometry of the rose petal and of our NWNWs. The rose petal consists of a periodic array of micro pillars, which are up to 25 μm high, with sub-micro sized folds (0.5 - 1 μm) on their surface. The pillars have angles of up to 50° with slight variations of the inclination angle. It offers, therefore, a special combination of surface micro- and nanostructures^{130,211,212}. Meanwhile, our highly porous network structures exhibit total heights of around 20 - 30 μm and nanowire inclinations of 45° with a certain inclination distribution due to the bending of the nanowires mentioned above, and displayed in Figure 5.2 (a). The interwire distance for the highly porous networks is around 0.5 - 0.8 μm , resembling the size of the rose petals pillars folds.

There were several extensive theoretical research studies about the origin of the rose-petal effect¹²⁸. Traditionally, Cassie-Baxter theory is applied to describe situations when the liquid cannot wet the surface structure, and some air pockets are formed and trapped inside, which makes the surface hydrophobic with high contact angle. On petal surface, due to the high structural porosity, air pockets are trapped beneath the water droplet, so water cannot fulfill the whole nanostructure, resulting in a high contact angle and high adhesion^{128,211}. On the other hand, Gao¹²⁶ and Jiang²¹³ observed, that liquid can be in direct contact with the petal surface micropillars, exhibiting the Wenzel regime at microscale. In summary, the rose-petal effect is attributed to a combined state between the Wenzel and Cassie-Baxter wetting regimes.

More generally, it has been previously discussed in literatures^{208,210,214}, that complex surfaces can be defined by multiple roughness levels. In the case of the NWNWs investigated in this work, the first level is defined by the wires and their interwire distance (quantified as porosity in this work), while the second level is defined by the intrinsic hydrophilicity of the material. Consistently, our results indicate that the wettability of the NWNW is influenced by the different factors of its complex structure and thus describing the behavior of NWNWs requires a combination of Wenzel, Cassie-Baxter, and impregnating Cassie-Baxter theories.

It is important to mention that the Au nanowire networks exhibit a very stable performance. Thanks to the chemical stability and non-oxidative nature of gold, a high contact angle and high adhesion are exhibited after one year of storage in air. This long-term stability makes this special nanostructure an ideal candidate for potential applications, such as for lab-on-a-chip devices or microelectronics, where they need controlled movement or positioning of tiny liquid droplets on superhydrophobic surfaces²¹⁵.

In summary, we demonstrated that 3D Au NWNWs exhibit a clear porosity-dependent wettability change, as a function of their geometrical parameters. Thanks to a systematic and independent variation of nanowire density and diameter, we could show that the NWNWs with low-porosity (< 60%) show hydrophilicity (CA = 20°-50°), while the medium-porosity samples from 60% to 80% show superhydrophilicity (CA < 10°), where the hemi-wicking effect plays a major role. The NWNWs with porosity higher than 95% exhibit very high contact angles (120° - 130°) and high adhesion of water droplets to the sample surface, which revealed three major aspects of the rose-petal effect: high contact angle, high adhesion, and high contact angle hysteresis. Our results also demonstrated that the developed tailored porous Au material exhibits long-term stability, controlled wetting states, and good reproducibility. This innovative method offers a new way for enhanced control over surface properties, opening up new possibilities for various applications where tailored wetting behavior is desirable, such as microelectronics, optical devices, and energy harvesting devices^{14,216,217}.

6. Conclusion and Outlook

In this work, we demonstrate the successful synthesis of three distinct types of NWNWs based on electrodeposition in track-etched polymer membranes: pure Au, Au-Ag alloy, and hierarchical nanoporous NWNWs. We present a comprehensive analysis of how key synthesis parameters influence the geometry, composition, and crystallinity of both Au and $\text{Au}_{1-x}\text{Ag}_x$ NWNWs. These characteristics were systematically studied using a range of techniques, including HRSEM, EDX, XPS, TEM, and X-ray diffraction. The obtained results highlight the high versatility and robustness of the fabrication approach, demonstrating its capability for producing NWNWs with precisely controlled structural and compositional features tailored for specific applications.

Pure Au NWNWs exhibited very good interconnectivity and stability. Systematic electrodeposition experiments showed that the overall homogeneity of the NWNW depends on the potential applied. At more negative deposition potentials, the deposition rate is faster and the growth tends to be inhomogeneous, resulting in large height variations. At less negative potentials ($U = -0.9$ and $U = -0.8$ V vs. Ag/AgCl) the NWNWs grew homogeneously over the entire planar area of up to 3 cm^2 . The nanowire crystallinity is also influenced by the deposition potential, more negative potentials leading to smaller grain size. The optimized electrodeposition conditions were then successfully applied with track-etched templates with different combinations of nanochannel density and diameter. This allowed us to fabricate series of Au NWNWs with tailored porosity ranging from 20% to 98%. All synthesized networks were free-standing and mechanically stable after the template dissolution.

The $\text{Au}_{1-x}\text{Ag}_x$ NWNWs were successfully synthesized across a wide compositional range, from 10 at% to 90 at% Ag. This tunability was achieved by adjusting the electrodeposition potential and electrolyte composition, leveraging the different reduction potentials of Au and Ag ions to precisely control their relative deposition rates. This method proved to be highly reproducible across various template characteristics. TEM analysis confirmed a homogeneous atomic distribution within single nanowires, with only minor ($\sim 5\%$) compositional variations along their length and width. Thanks to the crystallographic similarities of Au and Ag, the alloyed nanowires formed solid solutions with high quality, under the optimum deposition conditions.

Hierarchical nanoporous Au NWNWs were fabricated by dealloying $\text{Au}_{1-x}\text{Ag}_x$ ($x > 0.6$) NWNWs in concentrated nitric acid solution at room temperature. To investigate the dealloying behavior, NWNWs with various diameters and precursor alloy compositions were studied. The results showed that thinner wires ($\text{Ø} \sim 60 \text{ nm}$) undergo faster Ag dissolution, but the associated diffusion process leads to rapid surface roughening and severe volume loss at the crossing junctions between nanowires, often resulting in network collapse. In contrast, thicker nanowires ($\text{Ø} \sim 150 \text{ nm}$) dealloy more slowly and exhibit substantially better structural stability, remaining interconnected despite volume reduction. Free corrosion leads to Ag enrichment at the surface layer, as confirmed by EDX and XPS analysis. TEM revealed that the porous nanowires, remain predominantly single-crystalline. The porous structure also forms within individual crystals and is characterized by numerous planar defects such as stacking faults and twins. Our findings indicate that increasing the nanowire density in the pristine alloyed NWNWs in future works could improve the mechanical stability post-dealloying. Providing more crossing junctions and adjusting the dealloying conditions accordingly, should enable the fabrication of nanoporous NWNWs with thinner wires and smaller pore dimensions while maintaining structural stability.

Recognizing its potential impact on catalytical performance, we investigated the surface wettability of the Au NWNWs as a function of structural porosity. The 3D Au NWNWs displayed a pronounced porosity-dependent wetting behavior, enabled by the independent tuning of nanowire density and diameter. Low-porosity networks ($< 60\%$) exhibited hydrophilic behavior with contact angles between

20° and 50°, while medium-porosity samples (60% - 80%) demonstrated superhydrophilicity ($CA < 10^\circ$), where the hemi-wicking effect plays a major role. Highly porous NWNWs (> 95%) showed large contact angles (120° - 130°) combined with strong droplet adhesion and significant CA hysteresis – three major aspects of the rose-petal effect. These results confirm that the tailored Au NWNWs offer stable, controllable, and reproducible wetting properties, highlighting their potential for applications for specific surface designs.

Thanks to the high reproducibility of the NWNW synthesis methods developed in this work, and the large specific surface area inherent to their special 3D architecture, these NWNWs are well-suited as model systems for catalysis experiments. Accordingly, we systematically evaluated the electrochemical properties of three series of NWNWs. For each series, first their electrochemically active surface area (ECSA) was measured. We used two different methods: charge integration from the AuO reduction peak and double-layer capacitance measurements. These methods, suitable for different material systems, were benchmarked against reference samples to assess their consistency and limitations. Both approaches showed distinct advantages and must be interpreted critically, however they consistently indicated that the entire nanowire network surface actively participates in electrochemical reactions.

The measured ECSA values increased systematically with both nanowire diameter and density, reflecting the expected scaling of active surface area. Slight discrepancies between measured ECSAs and theoretical geometric surface areas were determined, most probably due to unaccounted crossing junctions, nanowire overlap, and/or diffusion limitations within the complex 3D architectures. Nevertheless, the good agreement between theoretical and experimental values reinforces the reliability of the characterization method and provides a strong foundation for further optimizing the geometry of the NWNWs and evaluating the catalytic performance of the NWNWs.

The catalytic performance of the NWNWs was evaluated in alkaline media of varying KOH electrolyte concentrations by testing their activity toward the methanol oxidation reaction. For pure Au NWNWs, we systematically investigated the influence of geometric parameters, including nanowire diameter and density. Each sample was initially tested in pure KOH solution to identify characteristic Au oxidation and reduction peaks. Subsequently, methanol was added at different concentrations into the electrochemical cell, to monitor the emergence and evolution of the methanol oxidation reaction peak. As the ECSA increased, the methanol oxidation peak current increased. The increase was quantified for both increasing nanowire diameter and increasing nanowire density, while all other geometrical parameters were kept constant. The methanol oxidation peak potential also increases with the increasing ECSA. Notably, increasing the KOH concentration from 0.1 M to 1 M led to significant decrease in the methanol oxidation peak potential and a substantial increase in current density. These results indicate that a higher concentration of OH⁻ in the electrolyte lowers the reaction barrier and significantly enhances the efficiency of the methanol oxidation reaction.

To assess the influence of alloying on the catalytic behavior of Au NWNWs, Au_{1-x}Ag_x NWNWs with varying atomic compositions and identical geometrical parameters were systematically studied. Samples with low Ag content (< 30 at%) exhibited a significant decrease in the methanol oxidation onset potential, indicating that the incorporation of Ag facilitates the reaction by lowering the activation barrier. However, this comes at the cost of a slight lower current density, suggesting that Ag partially hinders the catalytic activity at the reaction sites. For samples with higher Ag content (> 40 at%), no catalytic activity toward methanol oxidation reaction was observed. This indicates that as more Ag atoms present on the surface, the catalytic reaction is being suppressed. These findings highlight the importance of precise compositional tuning for optimal catalytic performance.

In alloyed Au_{1-x}Ag_x NWNWs, the methanol oxidation reaction also benefits from higher KOH concentration, showing lower peak potentials and enhanced current densities. This behavior is similar to pure Au NWNWs, although the effect is less pronounced. Au-rich samples demonstrated good

chemical and structural stability over multiple CV cycles. However, as the Ag content is increased, structural and electrochemical stability decreased gradually. In Ag-rich NWNWs, Ag atoms tended to dissolve and redeposit on the surface, forming Ag particles. Pure Ag NWNWs were completely degraded under high oxidation potentials, confirming that they are unsuitable for methanol oxidation catalysis under these conditions.

The dealloyed nanoporous NWNWs exhibited ECSAs up to three times higher than their pristine counterparts, due to the formation of small pores on the nanowire surfaces. However, for non-optimized parameters, the structural mechanical stability is compromised during the dealloying process, led to complete or partial localized network collapse, yielding ECSA values smaller than the pristine $\text{Au}_{1-x}\text{Ag}_x$ alloyed NWNW sample. CV measurements revealed electrochemical features consistent with the presence of residual Ag, with oxidation and reaction peak positions closely matching those $\text{Au}_{1-x}\text{Ag}_x$ NWNWs of comparable composition. This observation is also supported by XPS analysis, which confirms a residual Ag-rich surface layer.

The nanoporous NWNWs demonstrated higher current densities than the $\text{Au}_{1-x}\text{Ag}_x$ alloyed NWNWs, and lower methanol oxidation peak potentials compared to pure Au NWNWs, suggesting a synergetic effect by combination from the hierarchical porosity and residual Ag. However, the nanoporous NWNWs exhibited limited cyclic stability, as the fine porous structure coarsened under high oxidation potentials, diminishing long-term catalytic performance.

According to previous results on nanoporous Au¹¹⁵, the free corrosion process yields the lowest specific surface area, both in terms of flat projection area and weight. Future development of this project should focus on optimizing the dealloying protocol, comparing chemical and electrochemical dealloying methods. The goal is to identify conditions that maximize ECSA and minimize residual Ag content. Importantly, our results indicate that pursuing the smallest ligament size or pore size is not necessarily advantageous. Pores smaller than 10 nm were shown to have minimal impact on the catalytic activity and contributed little to ECSA increase. An ideal target would be the fabrication of nanoporous NWNW with less than 5 at% residual Ag on the surface and ligament sizes below 30 nm. Such a structure is expected to combine high surface area and improved catalytical efficiency for the methanol oxidation reaction.

The next step should be to evaluate the most promising NWNW samples in a working fuel cell environment. This includes testing under controlled electrolyte flow conditions, analyzing their performance across a range of applied potentials, and accurately measuring reaction currents. Long-term stability assessments will be especially important for determining their viability for further developments. In-situ analytical measurements will also be beneficial for identifying the reaction potentials and products.

Additionally, conducting stress tests under extreme conditions, such as high or cryogenic temperatures, vacuum environments, or under severe irradiation environments would provide valuable insights into their robustness. Au exhibits chemical stability, resistance to oxidation, and proven resilience under high vacuum and irradiation conditions (as demonstrated in previous studies²¹⁸), these NWNWs may hold potential for advanced applications, including in space or harsh-environment technologies.

7. Bibliography

- (1) *Nanomaterials for Advanced Technologies*; Katiyar, J. K., Panwar, V., Ahlawat, N., Eds.; Springer Nature: Singapore, 2022. <https://doi.org/10.1007/978-981-19-1384-6>.
- (2) R. Rao, C. N.; K. Cheetham, A. Science and Technology of Nanomaterials: Current Status and Future Prospects. *Journal of Materials Chemistry* **2001**, *11* (12), 2887–2894. <https://doi.org/10.1039/B105058N>.
- (3) Balasubramanian, G. Advances in Nanomaterials. Fundamentals, Properties and Applications. **2016**, *79*, 180. <https://doi.org/10.1007/978-81-322-2668-0>.
- (4) Wang, J.; Gu, H. Novel Metal Nanomaterials and Their Catalytic Applications. *Molecules* **2015**, *20* (9), 17070–17092. <https://doi.org/10.3390/molecules200917070>.
- (5) Liu, L.; Corma, A. Metal Catalysts for Heterogeneous Catalysis: From Single Atoms to Nanoclusters and Nanoparticles. *Chem. Rev.* **2018**, *118* (10), 4981–5079. <https://doi.org/10.1021/acs.chemrev.7b00776>.
- (6) Graf, M.; Jalas, D.; Weissmüller, J.; Petrov, A. Y.; Eich, M. Surface-to-Volume Ratio Drives Photoelectron Injection from Nanoscale Gold into Electrolyte. *ACS Catalysis* **2019**, *9* (4), 3366–3374. <https://doi.org/10.1021/acscatal.9b00384>.
- (7) Edvinsson, T. Optical Quantum Confinement and Photocatalytic Properties in Two-, One- and Zero-Dimensional Nanostructures. *Royal Society Open Science* **2018**, *5* (9), 180387. <https://doi.org/10.1098/rsos.180387>.
- (8) Ghosh, C. K. Quantum Effect on Properties of Nanomaterials. In *Introduction to Nano: Basics to Nanoscience and Nanotechnology*; Sengupta, A., Sarkar, C. K., Eds.; Springer: Berlin, Heidelberg, 2015; pp 73–111. https://doi.org/10.1007/978-3-662-47314-6_5.
- (9) Kline, T. R.; Tian, M.; Wang, J.; Sen, A.; Chan, M. W. H.; Mallouk, T. E. Template-Grown Metal Nanowires. *Inorganic Chemistry* **2006**, *45* (19), 7555–7565. <https://doi.org/10.1021/ic0601384>.
- (10) Shen, M.-Y.; Li, B.-R.; Li, Y.-K. Silicon Nanowire Field-Effect-Transistor Based Biosensors: From Sensitive to Ultra-Sensitive. *Biosensors and Bioelectronics* **2014**, *60*, 101–111. <https://doi.org/10.1016/j.bios.2014.03.057>.
- (11) Jia, C.; Lin, Z.; Huang, Y.; Duan, X. Nanowire Electronics: From Nanoscale to Macroscale. *Chem. Rev.* **2019**, *119* (15), 9074–9135. <https://doi.org/10.1021/acs.chemrev.9b00164>.
- (12) Quan, L. N.; Kang, J.; Ning, C.-Z.; Yang, P. Nanowires for Photonics. *Chem. Rev.* **2019**, *119* (15), 9153–9169. <https://doi.org/10.1021/acs.chemrev.9b00240>.
- (13) Guo, S.; Li, D.; Zhu, H.; Zhang, S.; Markovic, N. M.; Stamenkovic, V. R.; Sun, S. FePt and CoPt Nanowires as Efficient Catalysts for the Oxygen Reduction Reaction. *Angewandte Chemie - International Edition* **2013**, *52* (12), 3465–3468. <https://doi.org/10.1002/anie.201209871>.
- (14) Chen, Y.; Yang, S.; Liu, H.; Zhang, W.; Cao, R. An Unusual Network of α -MnO₂ Nanowires with Structure-Induced Hydrophilicity and Conductivity for Improved Electrocatalysis. *Chinese Journal of Catalysis* **2021**, *42* (10), 1724–1731. [https://doi.org/10.1016/S1872-2067\(21\)63793-2](https://doi.org/10.1016/S1872-2067(21)63793-2).
- (15) An, T.; Gong, S.; Ling, Y.; Dong, D.; Zhao, Y.; Cheng, W. Dynamically Functioning and Highly Stretchable Epidermal Supercapacitor Based on Vertically Aligned Gold Nanowire Skins. *EcoMat* **2020**, *2* (2). <https://doi.org/10.1002/eom2.12022>.
- (16) Kostowskyj, M. A.; Gilliam, R. J.; Kirk, D. W.; Thorpe, S. J. Silver Nanowire Catalysts for Alkaline Fuel Cells. *International Journal of Hydrogen Energy* **2008**, *33* (20), 5773–5778. <https://doi.org/10.1016/j.ijhydene.2008.05.040>.

- (17) Alber, I. Synthesis and Plasmonic Properties of Metallic Nanowires and Nanowire Dimers, University Heidelberg, 2012. <https://doi.org/10.11588/heidok.00014035>.
- (18) Pinion, C. W.; Christesen, J. D.; Cahoon, J. F. Understanding the Vapor–Liquid–Solid Mechanism of Si Nanowire Growth and Doping to Synthetically Encode Precise Nanoscale Morphology. *J. Mater. Chem. C* **2016**, *4* (18), 3890–3897. <https://doi.org/10.1039/C5TC03898G>.
- (19) Dobkin, D. M.; Zuraw, M. K. *Principles of Chemical Vapor Deposition*; Springer Netherlands: Dordrecht, 2003. <https://doi.org/10.1007/978-94-017-0369-7>.
- (20) Cheng, S. L.; Syu, J. H.; Liao, S. Y.; Lin, C. F.; Yeh, P. Y. Growth Kinetics and Wettability Conversion of Vertically-Aligned ZnO Nanowires Synthesized by a Hydrothermal Method. *RSC Adv.* **2015**, *5* (83), 67752–67758. <https://doi.org/10.1039/C5RA08535G>.
- (21) Ganapathi, A.; Swaminathan, P.; Neelakantan, L. Anodic Aluminum Oxide Template Assisted Synthesis of Copper Nanowires Using a Galvanic Displacement Process for Electrochemical Denitrification. *ACS Appl. Nano Mater.* **2019**, *2* (9), 5981–5988. <https://doi.org/10.1021/acsanm.9b01409>.
- (22) Toimil-Molares, M. E. Characterization and Properties of Micro- and Nanowires of Controlled Size, Composition, and Geometry Fabricated by Electrodeposition and Ion-Track Technology. *Beilstein Journal of Nanotechnology* **2012**, *3* (1), 860–883. <https://doi.org/10.3762/bjnano.3.97>.
- (23) Schubert, I.; Burr, L.; Trautmann, C.; Toimil-Molares, M. E. Growth and Morphological Analysis of Segmented AuAg Alloy Nanowires Created by Pulsed Electrodeposition in Ion-Track Etched Membranes. *Beilstein J. Nanotechnol.* **2015**, *6*, 1272–1280. <https://doi.org/10.3762/bjnano.6.131>.
- (24) Sobha Jayakrishnan, D. Electrodeposition: The Versatile Technique for Nanomaterials. In *Corrosion Protection and Control Using Nanomaterials*; Woodhead Publishing Limited, 2012; pp 86–125. <https://doi.org/10.1533/9780857095800.1.86>.
- (25) Fernández-González, C.; Guzmán-Mínguez, J. C.; Guedeja-Marrón, A.; García-Martín, E.; Foerster, M.; Niño, M. Á.; Aballe, L.; Quesada, A.; Pérez, L.; Ruiz-Gómez, S. Scaling Up the Production of Electrodeposited Nanowires: A Roadmap towards Applications. *Nanomaterials (Basel)* **2021**, *11* (7), 1657. <https://doi.org/10.3390/nano11071657>.
- (26) Ulrich, N.; Schäfer, M.; Römer, M.; Straub, S. D.; Zhang, S.; Brötz, J.; Trautmann, C.; Scheu, C.; Etzold, B. J. M.; Toimil-Molares, M. E. Cu Nanowire Networks with Well-Defined Geometrical Parameters for Catalytic Electrochemical CO₂ Reduction. *ACS Appl. Nano Mater.* **2023**, *6* (6), 4190–4200. <https://doi.org/10.1021/acsanm.2c05232>.
- (27) Li, X.; Wang, Y.; Song, G.; Peng, Z.; Yu, Y.; She, X.; Li, J. Synthesis and Growth Mechanism of Ni Nanotubes and Nanowires. *Nanoscale Res Lett* **2009**, *4* (9), 1015. <https://doi.org/10.1007/s11671-009-9348-0>.
- (28) Gu, Y.; Liu, J.; Qu, S.; Deng, Y.; Han, X.; Hu, W.; Zhong, C. Electrodeposition of Alloys and Compounds from High-Temperature Molten Salts. *Journal of Alloys and Compounds* **2017**, *690*, 228–238. <https://doi.org/10.1016/j.jallcom.2016.08.104>.
- (29) Ojo, A. A.; Dharmadasa, I. M. Electroplating of Semiconductor Materials for Applications in Large Area Electronics: A Review. *Coatings* **2018**, *8* (8), 262. <https://doi.org/10.3390/coatings8080262>.
- (30) Movsesyan, L.; Maijenburg, A. W.; Goethals, N.; Sigle, W.; Spende, A.; Yang, F.; Kaiser, B.; Jaegermann, W.; Park, S. Y.; Mul, G.; Trautmann, C.; Toimil-Molares, M. E. ZnO Nanowire Networks as Photoanode Model Systems for Photoelectrochemical Applications. *Nanomaterials* **2018**, *8* (9). <https://doi.org/10.3390/nano8090693>.

- (31) Wagner, M. F. P.; Völklein, F.; Reith, H.; Trautmann, C.; Toimil-Molares, M. E. Fabrication and Thermoelectrical Characterization of Three-Dimensional Nanowire Networks. *physica status solidi (a)* **2016**, *213* (3), 610–619. <https://doi.org/10.1002/PSSA.201532616>.
- (32) Dong, W. J.; Lim, K. W.; Cho, H. W.; Yoo, C. J.; Ham, J.; Cho, W. S.; Park, J. Y.; Lee, J.-L. Three-Dimensional Cu-Based Nanostructures for Photoelectrochemical Water Splitting and Electrochemical Carbon Dioxide Reduction. *ACS Appl. Energy Mater.* **2024**, *7* (15), 6569–6577. <https://doi.org/10.1021/acsaem.4c01197>.
- (33) Tang, Z.; Zhang, X.; Duan, L.; Wu, A.; Lü, W. Three-Dimensional Carbon Nitride Nanowire Scaffold for Flexible Supercapacitors. *Nanoscale Res Lett* **2019**, *14* (1), 98. <https://doi.org/10.1186/s11671-019-2932-z>.
- (34) Zhao, H.; Lei, Y. 3D Nanostructures for the Next Generation of High-Performance Nanodevices for Electrochemical Energy Conversion and Storage. *Advanced Energy Materials* **2020**, *10* (28), 2001460. <https://doi.org/10.1002/aenm.202001460>.
- (35) Wagner, M. F. P.; Voss, K.-O.; Trautmann, C.; Toimil-Molares, M. E. Three-Dimensional Nanowire Networks Fabricated by Ion Track Nanotechnology and Their Applications. *EPJ Techn Instrum* **2023**, *10* (1), 1–11. <https://doi.org/10.1140/epjti/s40485-023-00090-9>.
- (36) Jiang, H.; See Lee, P.; Li, C. 3D Carbon Based Nanostructures for Advanced Supercapacitors. *Energy & Environmental Science* **2013**, *6* (1), 41–53. <https://doi.org/10.1039/C2EE23284G>.
- (37) Li, X.; Li, H.; Li, C.; Wang, M.; Yang, Q. Tuning the Surface Wettability of Pd/COFs for Selective Hydrogenation. *ChemCatChem* **2023**, *15* (12), e202300002. <https://doi.org/10.1002/cctc.202300002>.
- (38) Wang, C.; Liu, Z.; Wang, L.; Dong, X.; Zhang, J.; Wang, G.; Han, S.; Meng, X.; Zheng, A.; Xiao, F.-S. Importance of Zeolite Wettability for Selective Hydrogenation of Furfural over Pd@Zeolite Catalysts. *ACS Catal.* **2018**, *8* (1), 474–481. <https://doi.org/10.1021/acscatal.7b03443>.
- (39) Liang, Z.; Zhou, Z.; Zhao, L.; Dong, B.; Wang, S. Fabrication of Transparent, Durable and Self-Cleaning Superhydrophobic Coatings for Solar Cells. *New J. Chem.* **2020**, *44* (34), 14481–14489. <https://doi.org/10.1039/D0NJ01402H>.
- (40) Bandyopadhyay, D.; Kar, K. *Supernovae, Neutron Star Physics and Nucleosynthesis*; Astronomy and Astrophysics Library; Springer International Publishing: Cham, 2022. <https://doi.org/10.1007/978-3-030-95171-9>.
- (41) Bernstein, P. L. *The Power of Gold: The History of an Obsession*; John Wiley & Sons, 2012.
- (42) Kenny, S. L. *Gold: A Cultural Encyclopedia*; Bloomsbury Publishing USA, 2011.
- (43) Bansal, S. A.; Kumar, V.; Karimi, J.; Singh, A. P.; Kumar, S. Role of Gold Nanoparticles in Advanced Biomedical Applications. *Nanoscale Adv.* **2020**, *2* (9), 3764–3787. <https://doi.org/10.1039/D0NA00472C>.
- (44) Daraee, H.; Eatemadi, A.; Abbasi, E.; Fekri Aval, S.; Kouhi, M.; Akbarzadeh, A. Application of Gold Nanoparticles in Biomedical and Drug Delivery. *Artificial Cells, Nanomedicine, and Biotechnology* **2016**, *44* (1), 410–422. <https://doi.org/10.3109/21691401.2014.955107>.
- (45) Kim, S. H. Nanoporous Gold for Energy Applications. *The Chemical Record* **2021**, *21* (5), 1199–1215. <https://doi.org/10.1002/tcr.202100015>.
- (46) Gonçalves, J. M.; Kumar, A.; da Silva, M. I.; Toma, H. E.; Martins, P. R.; Araki, K.; Bertotti, M.; Angnes, L. Nanoporous Gold-Based Materials for Electrochemical Energy Storage and Conversion. *Energy Technology* **2021**, *9* (5), 2000927. <https://doi.org/10.1002/ente.202000927>.
- (47) Kim, S.-I.; Kim, S.-W.; Jung, K.; Kim, J.-B.; Jang, J.-H. Ideal Nanoporous Gold Based Supercapacitors with Theoretical Capacitance and High Energy/Power Density. *Nano Energy* **2016**, *24*, 17–24. <https://doi.org/10.1016/j.nanoen.2016.03.027>.

- (48) Qi, Z.; Biener, J.; Biener, M. Surface Oxide-Derived Nanoporous Gold Catalysts for Electrochemical CO₂-to-CO Reduction. *ACS Applied Energy Materials* **2019**, *2* (11), 7717–7721. <https://doi.org/10.1021/acsaem.9b00355>.
- (49) Hashmi, A. S. K.; Hutchings, G. J. Gold Catalysis. *Angewandte Chemie - International Edition* **2006**, *45* (47), 7896–7936. <https://doi.org/10.1002/anie.200602454>.
- (50) Lu, X.; Yu, T.; Wang, H.; Qian, L.; Lei, P. Electrochemical Fabrication and Reactivation of Nanoporous Gold with Abundant Surface Steps for CO₂ Reduction. *ACS Catalysis* **2020**, *10* (15), 8860–8869. <https://doi.org/10.1021/acscatal.0c00627>.
- (51) Wittstock, G.; Bäumer, M.; Dononelli, W.; Klüner, T.; Lühns, L.; Mahr, C.; Moskaleva, L. V.; Oezaslan, M.; Risse, T.; Rosenauer, A.; Staubitz, A.; Weissmüller, J.; Wittstock, A. Nanoporous Gold: From Structure Evolution to Functional Properties in Catalysis and Electrochemistry. *Chemical Reviews* **2023**, *123* (10), 6716–6792. <https://doi.org/10.1021/ACS.CHEMREV.2C00751>/ASSET/IMAGES/LARGE/CR2C00751_0037.JPEG.
- (52) Li, M.; Ulrich, N.; Schubert, I.; Sigle, W.; Peter Wagner, M. F.; Trautmann, C.; Toimil-Molares, M. E. Three-Dimensional Free-Standing Gold Nanowire Networks as a Platform for Catalytic Applications. *RSC Advances* **2023**, *13* (7), 4721–4728. <https://doi.org/10.1039/D2RA08035D>.
- (53) Wu, C.; Wang, D.; Guo, J.; Zavabeti, A.; Xiao, P.; Li, G. K. Hollow Hierarchical Pd/HNC Nanoreactor as a High-Performance Catalyst for CO₂ Hydrogenation to Formate. *Energy Fuels* **2024**, *38* (4), 3357–3368. <https://doi.org/10.1021/acs.energyfuels.3c05193>.
- (54) Fang, B.; Kim, J. H.; Kim, M.-S.; Yu, J.-S. Hierarchical Nanostructured Carbons with Meso-Macroporosity: Design, Characterization, and Applications. *Acc. Chem. Res.* **2013**, *46* (7), 1397–1406. <https://doi.org/10.1021/ar300253f>.
- (55) Hung, C.-T.; Duan, L.; Zhao, T.; Liu, L.; Xia, Y.; Liu, Y.; Qiu, P.; Wang, R.; Zhao, Z.; Li, W.; Zhao, D. Gradient Hierarchically Porous Structure for Rapid Capillary-Assisted Catalysis. *J. Am. Chem. Soc.* **2022**, *144* (13), 6091–6099. <https://doi.org/10.1021/jacs.2c01444>.
- (56) Wittstock, G.; Bäumer, M.; Dononelli, W.; Klüner, T.; Lühns, L.; Mahr, C.; Moskaleva, L. V.; Oezaslan, M.; Risse, T.; Rosenauer, A.; Staubitz, A.; Weissmüller, J.; Wittstock, A. Nanoporous Gold: From Structure Evolution to Functional Properties in Catalysis and Electrochemistry. *Chemical Reviews* **2023**, *123* (10), 6716–6792. <https://doi.org/10.1021/acs.chemrev.2c00751>.
- (57) Hakamada, M.; Mabuchi, M. Mechanical Strength of Nanoporous Gold Fabricated by Dealloying. *Scripta Materialia* **2007**, *56* (11), 1003–1006. <https://doi.org/10.1016/j.scriptamat.2007.01.046>.
- (58) Tan, Y. H.; Davis, J. A.; Fujikawa, K.; Ganesh, N. V.; Demchenko, A. V.; Stine, K. J. Surface Area and Pore Size Characteristics of Nanoporous Gold Subjected to Thermal, Mechanical, or Surface Modification Studied Using Gas Adsorption Isotherms, Cyclic Voltammetry, Thermogravimetric Analysis, and Scanning Electron Microscopy. *Journal of Materials Chemistry* **2012**, *22* (14), 6733–6745. <https://doi.org/10.1039/C2JM16633J>.
- (59) Li, M.; Bonart, H.; Zellner, D.; Toimil-Molares, M. E. 3D Gold Nanowire Networks with Tailorable Surface Wetting State: From Rose-Petal Effect to Super-Hydrophilicity. *Small* **2025**, 2411971. <https://doi.org/10.1002/SMLL.202411971>.
- (60) Movsesyan, L. Template-Assisted Growth and Characterization of ZnO-Based Nanowire Arrays and 3D Networks. **2017**.
- (61) Wagner, M. F. P. Bi and Sb Nanowire Assemblies for Thermoelectric Applications, Technische Universität Darmstadt, 2018.

- (62) Penner, R. M.; Martin, C. R. Preparation and Electrochemical Characterization of Ultramicroelectrode Ensembles. *Analytical Chemistry* **1987**, *59* (21), 2625–2630. <https://doi.org/10.1021/ac00148a020>.
- (63) Dobrev, D.; Vetter, J.; Angert, N.; Neumann, R. Electrochemical Growth of Copper Single Crystals in Pores of Polymer Ion-Track Membranes. *Applied Physics A: Materials Science and Processing* **1999**, *69* (2), 233–237. <https://doi.org/10.1007/s003390050995>.
- (64) Wilhelm, R. A.; Grande, P. L. Unraveling Energy Loss Processes of Low Energy Heavy Ions in 2D Materials. *Commun Phys* **2019**, *2* (1), 1–8. <https://doi.org/10.1038/s42005-019-0188-7>.
- (65) Sigmund, P. Nuclear Stopping. In *Stopping of Heavy Ions: A Theoretical Approach*; Sigmund, P., Ed.; Springer: Berlin, Heidelberg, 2004; pp 85–94. https://doi.org/10.1007/978-3-540-44471-8_10.
- (66) Zhang, Y.; Weber, W. J. Ion Irradiation and Modification: The Role of Coupled Electronic and Nuclear Energy Dissipation and Subsequent Nonequilibrium Processes in Materials. *Applied Physics Reviews* **2020**, *7* (4), 041307. <https://doi.org/10.1063/5.0027462>.
- (67) Sand, A. E.; Ullah, R.; Correa, A. A. Heavy Ion Ranges from First-Principles Electron Dynamics. *npj Comput Mater* **2019**, *5* (1), 1–7. <https://doi.org/10.1038/s41524-019-0180-5>.
- (68) Burr, L. Ion-Track Technology Based Synthesis and Characterization of Gold and Gold Alloys Nanowires and Nanocones. **2016**.
- (69) Pépy, G.; Boesecke, P.; Kuklin, A.; Manceau, E.; Schiedt, B.; Siwy, Z.; Toulemonde, M.; Trautmann, C. Cylindrical Nanochannels in Ion-Track Polycarbonate Membranes Studied by Small-Angle X-Ray Scattering. In *Journal of Applied Crystallography*; 2007; Vol. 40. <https://doi.org/10.1107/S0021889807000088>.
- (70) Ceccio, G.; Vacik, J.; Siegel, J.; Cannavó, A.; Choukourov, A.; Pleskunov, P.; Tosca, M.; Fink, D. Etching and Doping of Pores in Polyethylene Terephthalate Analyzed by Ion Transmission Spectroscopy and Nuclear Depth Profiling. *Membranes (Basel)* **2022**, *12* (11), 1061. <https://doi.org/10.3390/membranes12111061>.
- (71) Kaya, D.; Keçeci, K. Review—Track-Etched Nanoporous Polymer Membranes as Sensors: A Review. *Journal of The Electrochemical Society* **2020**, *167* (3), 037543. <https://doi.org/10.1149/1945-7111/AB67A7>.
- (72) Apel, P. Y.; Ramirez, P.; Blonskaya, I. V.; Orelovitch, O. L.; Sartowska, B. A. Accurate Characterization of Single Track-Etched, Conical Nanopores. *Physical Chemistry Chemical Physics* **2014**, *16* (29), 15214–15223. <https://doi.org/10.1039/C4CP01686F>.
- (73) Ali, M.; Ahmed, I.; Ramirez, P.; Nasir, S.; Cervera, J.; Niemeyer, C. M.; Ensinger, W. Fluoride-Induced Modulation of Ionic Transport in Asymmetric Nanopores Functionalized with “Caged” Fluorescein Moieties. *Nanoscale* **2016**, *8* (16), 8583–8590. <https://doi.org/10.1039/C6NR00292G>.
- (74) Apel, P. Yu.; Blonskaya, I. V.; Orelovich, O. L.; Akimenko, S. N.; Sartowska, B.; Dmitriev, S. N. Factors Determining Pore Shape in Polycarbonate Track Membranes. *Colloid J* **2004**, *66* (6), 649–656. <https://doi.org/10.1007/s10595-005-0001-z>.
- (75) Karatutlu, A.; Barhoum, A.; Sapelkin, A. *Liquid-Phase Synthesis of Nanoparticles and Nanostructured Materials*; Elsevier Inc., 2018. <https://doi.org/10.1016/B978-0-323-51254-1.00001-4>.
- (76) Li, M.; Bo, X.; Mu, Z.; Zhang, Y.; Guo, L. Electrodeposition of Nickel Oxide and Platinum Nanoparticles on Electrochemically Reduced Graphene Oxide Film as a Nonenzymatic Glucose Sensor. *Sensors and Actuators, B: Chemical* **2014**, *192*, 261–268. <https://doi.org/10.1016/j.snb.2013.10.140>.

- (77) Movsesyan, L.; Schubert, I.; Yeranyan, L.; Trautmann, C.; Toimil-Molares, M. E. Influence of Electrodeposition Parameters on the Structure and Morphology of ZnO Nanowire Arrays and Networks Synthesized in Etched Ion-Track Membranes. *Semiconductor Science and Technology* **2015**, *31* (1). <https://doi.org/10.1088/0268-1242/31/1/014006>.
- (78) Paunovic, Milan.; Schlesinger, Mordechai. *Modern Electroplating*.; Wiley, 2010.
- (79) Geoffrey Prentice. Electrochemical Engineering. In *Encyclopedia of Physical Science and Technology (Third Edition)*; Academic Press, 2003; pp 143–159. <https://doi.org/10.1016/B0-12-227410-5/00205-2>.
- (80) Ulrich, N. Copper Nanowire Networks as Electrocatalyst for Electrochemical CO₂ Reduction, Technische Universität Darmstadt, 2018.
- (81) Sobczak, I.; Dembowski, E. The Effect of AuAg-MCF and AuAg-NbMCF Catalysts Pretreatment on the Gold-Silver Alloy Formation and the Catalytic Behavior in Selective Methanol Oxidation with Oxygen. *Journal of Molecular Catalysis A: Chemical* **2015**, *409*, 137–148. <https://doi.org/10.1016/j.molcata.2015.08.017>.
- (82) Plieth, W. Electrochemistry for Materials Science. *Electrochemistry for Materials Science* **2008**, 1–410. <https://doi.org/10.1016/B978-0-444-52792-9.X5001-5>.
- (83) Parida, S.; Kramer, D.; Volkert, C. A.; Rösner, H.; Erlebacher, J.; Weissmüller, J. Volume Change during the Formation of Nanoporous Gold by Dealloying. *Physical Review Letters* **2006**, *97* (3), 035504. <https://doi.org/10.1103/PHYSREVLETT.97.035504/FIGURES/3/THUMBNAIL>.
- (84) Scandura, G.; Kumari, P.; Palmisano, G.; Karanikolos, G. N.; Orwa, J.; Dumée, L. F. Nanoporous Dealloyed Metal Materials Processing and Applications—A Review. *Ind. Eng. Chem. Res.* **2023**, *62* (4), 1736–1763. <https://doi.org/10.1021/acs.iecr.2c03952>.
- (85) McCue, I.; Benn, E.; Gaskey, B.; Erlebacher, J. Dealloying and Dealloyed Materials. *Annual Review of Materials Research* **2016**, *46* (Volume 46, 2016), 263–286. <https://doi.org/10.1146/ANNUREV-MATSCI-070115-031739/CITE/REFWORKS>.
- (86) Wittstock, A.; Wichmann, A.; Biener, J.; Bäumer, M. Nanoporous Gold: A New Gold Catalyst with Tunable Properties. *Faraday Discussions* **2011**, *152* (0), 87–98. <https://doi.org/10.1039/C1FD00022E>.
- (87) Earthman, J. C. Corrosion. *Smithells Metals Reference Book* **2004**, 31–1. <https://doi.org/10.1016/B978-075067509-3/50034-8>.
- (88) Ji, C.; Searson, P. C. Fabrication of Nanoporous Gold Nanowires. *Applied Physics Letters* **2002**, *81* (23), 4437–4439. <https://doi.org/10.1063/1.1526920>.
- (89) Burr, L.; Schubert, I.; Sigle, W.; Trautmann, C.; Toimil-Molares, M. E. Surface Enrichment in Au-Ag Alloy Nanowires and Investigation of the Dealloying Process. *Journal of Physical Chemistry C* **2015**, *119* (36), 20949–20956. <https://doi.org/10.1021/acs.jpcc.5b05596>.
- (90) Beane, R. J. Using the Scanning Electron Microscope for Discovery Based Learning in Undergraduate Courses. *Journal of Geoscience Education* **2004**, *52* (3), 250–253. <https://doi.org/10.5408/1089-9995-52.3.250>.
- (91) User, G.; Singh, S.; Krupanidhi, S. B. Delivered by Ingenta to: Fabrication, Structural Characterization, and Formation Mechanism of Ferroelectric SrBi₂Ta₂O₉ Nanotubes. *Nanoscience and Nanotechnology Letters* **2009**, *1*, 8–12. <https://doi.org/10.1166/nnl.2009.001>.
- (92) Goldstein, J. I.; Newbury, D. E.; Michael, J. R.; Ritchie, N. W. M.; Scott, J. H. J.; Joy, D. C. Scanning Electron Microscopy and X-Ray Microanalysis. *Scanning Electron Microscopy and X-ray Microanalysis* **2017**, 1–550. <https://doi.org/10.1007/978-1-4939-6676-9/COVER>.

- (93) Tang, C. Y.; Yang, Z. Transmission Electron Microscopy (TEM). In *Membrane Characterization*; Elsevier Inc., 2017; pp 145–159. <https://doi.org/10.1016/B978-0-444-63776-5.00008-5>.
- (94) Altincicek, F. M. Synthesis and Characterization of Quasi-Two-Dimensional Chromium Sulfides. **2019**.
- (95) Turner, N. H.; Schreifels, J. A. Surface Analysis: X-Ray Photoelectron Spectroscopy and Auger Electron Spectroscopy. *Analytical Chemistry* **1996**, *68* (12). https://doi.org/10.1021/A19600146/ASSET/A19600146.FP.PNG_V03.
- (96) Antolini, E. Catalysts for Direct Ethanol Fuel Cells. *Journal of Power Sources* **2007**, *170* (1), 1–12. <https://doi.org/10.1016/j.jpowsour.2007.04.009>.
- (97) Wang, S.; Jiang, S. P.; Wang, X.; Guo, J. Enhanced Electrochemical Activity of Pt Nanowire Network Electrocatalysts for Methanol Oxidation Reaction of Fuel Cells. *Electrochimica Acta* **2011**, *56* (3), 1563–1569. <https://doi.org/10.1016/j.electacta.2010.10.055>.
- (98) Bard, A. J.; Faulkner, L. R. *Electrochemical Methods : Fundamentals and Applications*.
- (99) Watt-Smith, M. J.; Friedrich, J. M.; Rigby, S. P.; Ralph, T. R.; Walsh, F. C. Determination of the Electrochemically Active Surface Area of Pt/C PEM Fuel Cell Electrodes Using Different Adsorbates. *Journal of Physics D: Applied Physics* **2008**, *41* (17), 174004. <https://doi.org/10.1088/0022-3727/41/17/174004>.
- (100) Lukaszewski, M.; Soszko, M.; Czerwiński, A. Electrochemical Methods of Real Surface Area Determination of Noble Metal Electrodes - an Overview. *International Journal of Electrochemical Science* **2016**, *11* (6), 4442–4469. <https://doi.org/10.20964/2016.06.71>.
- (101) Carrish, J. J. *Three Electrode System in the Generation of Electrostatic Images*; 1978.
- (102) Schott, C. M.; Schneider, P. M.; Song, K. T.; Yu, H.; Götz, R.; Haimerl, F.; Gubanova, E.; Zhou, J.; Schmidt, T. O.; Zhang, Q.; Alexandrov, V.; Bandarenka, A. S. How to Assess and Predict Electrical Double Layer Properties. Implications for Electrocatalysis. *Chemical Reviews* **2024**. https://doi.org/10.1021/ACS.CHEMREV.3C00806/ASSET/IMAGES/LARGE/CR3C00806_0041.JPEG.
- (103) Helmholtz, H. Ueber Einige Gesetze Der Vertheilung Elektrischer Ströme in Körperlichen Leitern Mit Anwendung Auf Die Thierisch-elektrischen Versuche. *Annalen der Physik* **1853**, *165* (6), 211–233. <https://doi.org/10.1002/ANDP.18531650603>.
- (104) Chapman, D. L. LI. A Contribution to the Theory of Electrocapillarity. *The London, Edinburgh, and Dublin Philosophical Magazine and Journal of Science* **1913**, *25* (148), 475–481. <https://doi.org/10.1080/14786440408634187>.
- (105) Stern, O. ZUR THEORIE DER ELEKTROLYTISCHEN DOPPELSCHICHT. *Zeitschrift für Elektrochemie und angewandte physikalische Chemie* **1924**, *30* (21–22), 508–516. <https://doi.org/10.1002/BBPC.192400182>.
- (106) Grahame, D. C. The Electrical Double Layer and the Theory of Electrocapillarity. *Chemical Reviews* **1947**, *41* (3), 441–501. https://doi.org/10.1021/CR60130A002/ASSET/CR60130A002.FP.PNG_V03.
- (107) Zhang, L.; Zhao, X. S. Carbon-Based Materials as Supercapacitor Electrodes. *Chemical Society Reviews* **2009**, *38* (9), 2520–2531. <https://doi.org/10.1039/B813846J>.
- (108) Centeno, T. A.; Stoeckli, F. On the Specific Double-Layer Capacitance of Activated Carbons, in Relation to Their Structural and Chemical Properties. *Journal of Power Sources* **2006**, *154* (1), 314–320. <https://doi.org/10.1016/j.jpowsour.2005.04.007>.
- (109) Srinivasan, S. ELECTRODE/ELECTROLYTE INTERFACES: STRUCTURE AND KINETICS OF CHARGE TRANSFER. In *Fuel Cells*; Springer US, 2006; pp 27–92. https://doi.org/10.1007/0-387-35402-6_2.

- (110) Shao, M.; Odell, J. H.; Choi, S. I.; Xia, Y. Electrochemical Surface Area Measurements of Platinum- and Palladium-Based Nanoparticles. *Electrochemistry Communications* **2013**, *31*, 46–48. <https://doi.org/10.1016/j.elecom.2013.03.011>.
- (111) Morales, D. M.; Risch, M. Seven Steps to Reliable Cyclic Voltammetry Measurements for the Determination of Double Layer Capacitance. *JPhys Energy* **2021**, *3* (3). <https://doi.org/10.1088/2515-7655/abee33>.
- (112) Wang, C.; Yang, C.; Song, Y.; Gao, W.; Xia, X. Adsorption and Direct Electron Transfer from Hemoglobin into a Three-Dimensionally Ordered Macroporous Gold Film. *Advanced Functional Materials* **2005**, *15* (8), 1267–1275. <https://doi.org/10.1002/adfm.200500048>.
- (113) Conway, B. E. Electrochemical Oxide Film Formation at Noble Metals as a Surface-Chemical Process. *Progress in Surface Science* **1995**, *49* (4), 331–452. [https://doi.org/10.1016/0079-6816\(95\)00040-6](https://doi.org/10.1016/0079-6816(95)00040-6).
- (114) Khrushcheva, E. I.; Tarasevich, M. R. Electrochemical Determination of Surface Area of Metals. *Russian Chemical Reviews* **1978**, *47* (5), 416–424. <https://doi.org/10.1070/RC1978V047N05ABEH002227/XML>.
- (115) Hänsch, M. Electrochemical Aspects of Nanoporous Gold, Universität Oldenburg., 2019.
- (116) Leopold, M. C.; Black, J. A.; Bowden, E. F. Influence of Gold Topography on Carboxylic Acid Terminated Self-Assembled Monolayers. *Langmuir* **2002**, *18* (4), 978–980. <https://doi.org/10.1021/la011683e>.
- (117) Schröper, F.; Brüggemann, D.; Mourzina, Y.; Wolfrum, B.; Offenhäusser, A.; Mayer, D. Analyzing the Electroactive Surface of Gold Nanopillars by Electrochemical Methods for Electrode Miniaturization. *Electrochimica Acta* **2008**, *53* (21), 6265–6272. <https://doi.org/10.1016/j.electacta.2008.03.068>.
- (118) Oesch, U.; Janata, J. Electrochemical Study of Gold Electrodes with Anodic Oxide Films—I. Formation and Reduction Behaviour of Anodic Oxides on Gold. *Electrochimica Acta* **1983**, *28* (9), 1237–1246. [https://doi.org/10.1016/0013-4686\(83\)85011-7](https://doi.org/10.1016/0013-4686(83)85011-7).
- (119) Barbir, F. Fuel Cell Applications. In *PEM Fuel Cells*; Elsevier, 2013; pp 373–434. <https://doi.org/10.1016/b978-0-12-387710-9.00010-2>.
- (120) Dharmalingam, S.; Kugarajah, V.; Sugumar, M. Membranes for Microbial Fuel Cells. In *Biomass, Biofuels, Biochemicals: Microbial Electrochemical Technology: Sustainable Platform for Fuels, Chemicals and Remediation*; Elsevier, 2018; pp 143–194. <https://doi.org/10.1016/B978-0-444-64052-9.00007-8>.
- (121) Liu, H.; Song, C.; Zhang, L.; Zhang, J.; Wang, H.; Wilkinson, D. P. A Review of Anode Catalysis in the Direct Methanol Fuel Cell. *Journal of Power Sources* **2006**, *155* (2), 95–110. <https://doi.org/10.1016/j.jpowsour.2006.01.030>.
- (122) Petrucci, R. H.; Harwood, W. S. *General Chemistry: Principles and Modern Applications*; Pearson/Prentice Hall, 2007.
- (123) de Gennes, P.-G.; Brochard-Wyart, F.; Quéré, D. *Capillarity and Wetting Phenomena*; Springer New York, 2004. <https://doi.org/10.1007/978-0-387-21656-0>.
- (124) Priest, C.; Albrecht, T. W. J.; Sedev, R.; Ralston, J. Asymmetric Wetting Hysteresis on Hydrophobic Microstructured Surfaces. *Langmuir* **2009**, *25* (10), 5655–5660. <https://doi.org/10.1021/la804246a>.
- (125) He, Y.; Jiang, C.; Wang, S.; Yin, H.; Yuan, W. Control Wetting State Transition by Micro-Rod Geometry. *Applied Surface Science* **2013**, *285* (PARTB), 682–687. <https://doi.org/10.1016/j.apsusc.2013.08.110>.
- (126) Jin, H.; Li, Y.; Zhang, P.; Nie, S.; Gao, N. The Investigation of the Wetting Behavior on the Red Rose Petal. *Applied Physics Letters* **2016**, *108* (15). <https://doi.org/10.1063/1.4947057>.

- (127) Sudeepthi, A.; Yeo, L.; Sen, A. K. Cassie-Wenzel Wetting Transition on Nanostructured Superhydrophobic Surfaces Induced by Surface Acoustic Waves. *Applied Physics Letters* **2020**, *116* (9). <https://doi.org/10.1063/1.5145282>.
- (128) Bhushan, B.; Nosonovsky, M. The Rose Petal Effect and the Modes of Superhydrophobicity. *Philosophical Transactions of the Royal Society A: Mathematical, Physical and Engineering Sciences* **2010**, *368* (1929), 4713–4728. <https://doi.org/10.1098/RSTA.2010.0203>.
- (129) Ghosh, U. U.; Nair, S.; Das, A.; Mukherjee, R.; DasGupta, S. Replicating and Resolving Wetting and Adhesion Characteristics of a Rose Petal. *Colloids and Surfaces A: Physicochemical and Engineering Aspects* **2019**, *561*, 9–17. <https://doi.org/10.1016/j.colsurfa.2018.10.028>.
- (130) Feng, L.; Zhang, Y.; Xi, J.; Zhu, Y.; Wang, N.; Xia, F.; Jiang, L. Petal Effect: A Superhydrophobic State with High Adhesive Force. *Langmuir* **2008**, *24* (8), 4114–4119. https://doi.org/10.1021/LA703821H/SUPPL_FILE/LA703821H-FILE001.PDF.
- (131) Holmbom, G.; Jacobson, B. E. Incorporation of Gold Cyanide in Electrodeposited Gold. *J. Electrochem. Soc.* **1988**, *135* (3), 787. <https://doi.org/10.1149/1.2095753>.
- (132) Electrodeposition of Alloys: PRINCIPLES and PRACTICE. In *Electrodeposition of Alloys*; Brenner, A., Ed.; Academic Press, 1963; p ii. <https://doi.org/10.1016/B978-1-4831-9807-1.50001-5>.
- (133) Ji, C.; Oskam, G.; Ding, Y.; Erlebacher, J. D.; Wagner, A. J.; Searson, P. C. Deposition of AuAg_{1-x}OAg_{1-y} Multilayers and Multisegment Nanowires. *Journal of The Electrochemical Society*.
- (134) Weil, R.; Nee, C. C.; Chang, J. W. Pulsed Electrodeposition of Layered Brass Structures. *Metall Trans A* **1988**, *19* (6), 1569–1573. <https://doi.org/10.1007/BF02674031>.
- (135) *DOWFAX™ 2A1 Solution Surfactant*. <https://www.dow.com/en-us/pdp.dowfax-2a1-solution-surfactant.23255z.html> (accessed 2025-04-24).
- (136) Kim, K. S.; Winograd, N. X-Ray Photoelectron Spectroscopic Binding Energy Shifts Due to Matrix in Alloys and Small Supported Metal Particles. *Chemical Physics Letters* **1975**, *30* (1), 91–95. [https://doi.org/10.1016/0009-2614\(75\)85505-9](https://doi.org/10.1016/0009-2614(75)85505-9).
- (137) Mamonova, D. V.; Vasileva, A. A.; Petrov, Y. V.; Koroleva, A. V.; Danilov, D. V.; Kolesnikov, I. E.; Bikbaeva, G. I.; Bachmann, J.; Manshina, A. A. Single Step Laser-Induced Deposition of Plasmonic Au, Ag, Pt Mono-, Bi- and Tri-Metallic Nanoparticles. *Nanomaterials (Basel)* **2021**, *12* (1), 146. <https://doi.org/10.3390/nano12010146>.
- (138) Xiong, L.; Sun, Z.; Zhang, X.; Zhao, L.; Huang, P.; Chen, X.; Jin, H.; Sun, H.; Lian, Y.; Deng, Z.; Rümmerli, M. H.; Yin, W.; Zhang, D.; Wang, S.; Peng, Y. Octahedral Gold-Silver Nanoframes with Rich Crystalline Defects for Efficient Methanol Oxidation Manifesting a CO-Promoting Effect. *Nature Communications* **2019**, *10* (1). <https://doi.org/10.1038/s41467-019-11766-w>.
- (139) Camci, M. T.; Ulgut, B.; Kocabas, C.; Suzer, S. In-Situ XPS Monitoring and Characterization of Electrochemically Prepared Au Nanoparticles in an Ionic Liquid. *ACS Omega* **2017**, *2* (2), 478–486. <https://doi.org/10.1021/acsomega.6b00456>.
- (140) Seah, M. P.; Dench, W. A. Quantitative Electron Spectroscopy of Surfaces: A Standard Data Base for Electron Inelastic Mean Free Paths in Solids. *Surface and Interface Analysis* **1979**, *1* (1), 2–11. <https://doi.org/10.1002/SIA.740010103>.
- (141) Powell, C. J.; Seah, M. P. Precision, Accuracy, and Uncertainty in Quantitative Surface Analyses by Auger-electron Spectroscopy and X-ray Photoelectron Spectroscopy. *Journal of Vacuum Science & Technology A* **1990**, *8* (2), 735–763. <https://doi.org/10.1116/1.576956>.

- (142) Baer, D. R.; Engelhard, M. H. XPS Analysis of Nanostructured Materials and Biological Surfaces. *Journal of Electron Spectroscopy and Related Phenomena* **2010**, *178–179* (C), 415–432. <https://doi.org/10.1016/J.ELSPEC.2009.09.003>.
- (143) Artymowicz, D. M.; Erlebacher, J.; Newman, R. C. Relationship between the Parting Limit for De-Alloying and a Particular Geometric High-Density Site Percolation Threshold. *Philosophical Magazine* **2009**, *89* (21), 1663–1693. <https://doi.org/10.1080/14786430903025708>.
- (144) Zielasek, V.; Jürgens, B.; Schulz, C.; Biener, J.; Biener, M. M.; Hamza, A. V.; Bäumer, M. Gold Catalysts: Nanoporous Gold Foams. *Angewandte Chemie - International Edition* **2006**, *45* (48), 8241–8244. <https://doi.org/10.1002/anie.200602484>.
- (145) Schaefer, A.; Ragazzon, D.; Wittstock, A.; Walle, L. E.; Borg, A.; Bäumer, M.; Sandell, A. Toward Controlled Modification of Nanoporous Gold. A Detailed Surface Science Study on Cleaning and Oxidation. *J. Phys. Chem. C* **2012**, *116* (7), 4564–4571. <https://doi.org/10.1021/jp207638t>.
- (146) Wittstock, A.; Neumann, B.; Schaefer, A.; Dumbuya, K.; Kübel, C.; Biener, M. M.; Zielasek, V.; Steinrück, H. P.; Gottfried, J. M.; Biener, J.; Hamza, A.; Bäumer, M. Nanoporous Au: An Unsupported Pure Gold Catalyst? *Journal of Physical Chemistry C* **2009**, *113* (14), 5593–5600. <https://doi.org/10.1021/JP808185V>.
- (147) Schön, G.; Tummavuori, J.; Lindström, B.; Enzell, C. R.; Enzell, C. R.; Swahn, C.-G. ESCA Studies of Ag, Ag₂O and AgO. *Acta Chem. Scand.* **1973**, *27*, 2623–2633. <https://doi.org/10.3891/acta.chem.scand.27-2623>.
- (148) Yu. Klyushin, A.; R. Rocha, T. C.; Hävecker, M.; Knop-Gericke, A.; Schlögl, R. A near Ambient Pressure XPS Study of Au Oxidation. *Physical Chemistry Chemical Physics* **2014**, *16* (17), 7881–7886. <https://doi.org/10.1039/C4CP00308J>.
- (149) Duan, X.; Tian, X.; Ke, J.; Yin, Y.; Zheng, J.; Chen, J.; Cao, Z.; Xie, Z.; Yuan, Y. Size Controllable Redispersion of Sintered Au Nanoparticles by Using Iodohydrocarbon and Its Implications. *Chem. Sci.* **2016**, *7* (5), 3181–3187. <https://doi.org/10.1039/C5SC04283F>.
- (150) Krekeler, T.; Straßer, A. V.; Graf, M.; Wang, K.; Hartig, C.; Ritter, M.; Weissmüller, J. Silver-Rich Clusters in Nanoporous Gold. *Materials Research Letters* **2017**, *5* (5), 314–321. <https://doi.org/10.1080/21663831.2016.1276485>.
- (151) Duya, C. O.; Okumu, F. O.; Matoetoe, M. C. The Electrochemical Properties of Bimetallic Silver-Gold Nanoparticles Nano Film's. *Heliyon* **2024**, *10* (17), e36974. <https://doi.org/10.1016/J.HELIYON.2024.E36974>.
- (152) Bayesov, A.; Tuleshova, E.; Tukibayeva, A.; Aibolova, G.; Baineyeva, F. Electrochemical Behavior of Silver Electrode in Sulphuric Acidic Solution during Anodic Polarization. *Oriental Journal of Chemistry* **2015**, *31* (4), 1867–1872. <https://doi.org/10.13005/OJC/310403>.
- (153) Saleh, M. G. A.; El Wanees, S. A.; Alruwaili, I. D.; Akremi, A.; Elbasiony, A. M.; Brakat, M. Ag/Ag₂O Electrode for Electrocatalytic Oxidation of Ethanol. *International Journal of Electrochemical Science* **2023**, *18* (12), 100372. <https://doi.org/10.1016/j.ijoes.2023.100372>.
- (154) Costentin, C. Cyclic Voltammetry to Study Dynamics of Ion Insertion in Porous Materials. *Advanced Energy and Sustainability Research* **2024**, *5* (5), 2300242. <https://doi.org/10.1002/aesr.202300242>.
- (155) Liu, Y.; Chandresh, A.; Heinke, L. Impact of the Channel Length in Nanoporous Electric Double-Layer Capacitors on the Charge Transport Explored by Metal–Organic Framework Films. *ACS Phys. Chem Au* **2025**. <https://doi.org/10.1021/acsphyschemau.4c00104>.
- (156) McCrory, C. C. L.; Jung, S.; Peters, J. C.; Jaramillo, T. F. Benchmarking Heterogeneous Electrocatalysts for the Oxygen Evolution Reaction. *J. Am. Chem. Soc.* **2013**, *135* (45), 16977–16987. <https://doi.org/10.1021/ja407115p>.

- (157) Lasia, A.; Rami, A. Kinetics of Hydrogen Evolution on Nickel Electrodes. *Journal of Electroanalytical Chemistry and Interfacial Electrochemistry* **1990**, *294* (1), 123–141. [https://doi.org/10.1016/0022-0728\(90\)87140-F](https://doi.org/10.1016/0022-0728(90)87140-F).
- (158) Hampson, N. A.; Latham, R. J.; Lee, J. B.; Macdonald, K. I. Oxidations at Copper Electrodes: Part I. The Differential Capacitance of Polycrystalline Copper in Alkali. *Journal of Electroanalytical Chemistry and Interfacial Electrochemistry* **1971**, *31* (1), 57–62. [https://doi.org/10.1016/S0022-0728\(71\)80042-6](https://doi.org/10.1016/S0022-0728(71)80042-6).
- (159) O'Brien, R. N.; Seto, P. Time Domain Reflectometry, a New Method of Finding Electrical Double-Layer Capacities: 1. The Capacity of the Stainless Steel Electrode in Strong NaOH Solutions. *Journal of Electroanalytical Chemistry and Interfacial Electrochemistry* **1968**, *18* (3), 219–230. [https://doi.org/10.1016/S0022-0728\(68\)80253-0](https://doi.org/10.1016/S0022-0728(68)80253-0).
- (160) Weininger, J. L.; Breiter, M. W. Effect of Crystal Structure on the Anodic Oxidation of Nickel. *J. Electrochem. Soc.* **1963**, *110* (6), 484. <https://doi.org/10.1149/1.2425798>.
- (161) Badawy, W. A.; Gad-Allah, A. G.; Abd El-Rahman, H. A.; Abouromia, M. M. Kinetics of the Passivation of Molybdenum in Acids and Alkali Solutions as Inferred from Impedance and Potential Measurements. *Surface and Coatings Technology* **1986**, *27* (2), 187–196. [https://doi.org/10.1016/0257-8972\(86\)90129-5](https://doi.org/10.1016/0257-8972(86)90129-5).
- (162) Iseki, S.; Ohashi, K.; Nagaura, S. Impedance of the Oxygen-Evolution Reaction on Noble Metal Electrodes. *Electrochimica Acta* **1972**, *17* (12), 2249–2265. [https://doi.org/10.1016/0013-4686\(72\)87016-6](https://doi.org/10.1016/0013-4686(72)87016-6).
- (163) Wu, G.; Li, N.; Zhou, D.-R.; Mitsuo, K.; Xu, B.-Q. Anodically Electrodeposited Co+Ni Mixed Oxide Electrode: Preparation and Electrocatalytic Activity for Oxygen Evolution in Alkaline Media. *Journal of Solid State Chemistry* **2004**, *177* (10), 3682–3692. <https://doi.org/10.1016/j.jssc.2004.06.027>.
- (164) Fournier, J.; Brossard, L.; Tilquin, J.-Y.; Coûté, R.; Dodelet, J.-P.; Guay, D.; Ménard, H. Hydrogen Evolution Reaction in Alkaline Solution: Catalytic Influence of Pt Supported on Graphite vs. Pt Inclusions in Graphite. *J. Electrochem. Soc.* **1996**, *143* (3), 919. <https://doi.org/10.1149/1.1836559>.
- (165) Wittstock, A.; Zielasek, V.; Biener, J.; Friend, C. M.; Bäumer, M. Nanoporous Gold Catalysts for Selective Gas-Phase Oxidative Coupling of Methanol at Low Temperature. *Science* **2010**, *327* (5963), 319–322. https://doi.org/10.1126/SCIENCE.1183591/SUPPL_FILE/WITTSTOCK-SOM.PDF.
- (166) Assiongbon, K. A.; Roy, D. Electro-Oxidation of Methanol on Gold in Alkaline Media: Adsorption Characteristics of Reaction Intermediates Studied Using Time Resolved Electro-Chemical Impedance and Surface Plasmon Resonance Techniques. *Surface Science* **2005**, *594* (1–3), 99–119. <https://doi.org/10.1016/j.susc.2005.07.015>.
- (167) Mahapatra, S. S.; Datta, J. Characterization of Pt-Pd/C Electrocatalyst for Methanol Oxidation in Alkaline Medium. *International Journal of Electrochemistry* **2011**, *2011*, 1–16. <https://doi.org/10.4061/2011/563495>.
- (168) Rahim, M. A. A.; Hameed, R. M. A.; Khalil, M. W. Nickel as a Catalyst for the Electro-Oxidation of Methanol in Alkaline Medium. *Journal of Power Sources* **2004**, *134* (2), 160–169. <https://doi.org/10.1016/J.JPOWSOUR.2004.02.034>.
- (169) Yan, S.; Zhang, S.; Lin, Y.; Liu, G. Electrocatalytic Performance of Gold Nanoparticles Supported on Activated Carbon for Methanol Oxidation in Alkaline Solution. *Journal of Physical Chemistry C* **2011**, *115* (14), 6986–6993. <https://doi.org/10.1021/jp1086834>.
- (170) Prabhuram, J.; Manoharan, R. Investigation of Methanol Oxidation on Unsupported Platinum Electrodes in Strong Alkali and Strong Acid. *Journal of Power Sources* **1998**, *74* (1), 54–61. [https://doi.org/10.1016/S0378-7753\(98\)00012-3](https://doi.org/10.1016/S0378-7753(98)00012-3).

- (171) Rus, E. D.; Wakabayashi, R. H.; Wang, H.; Abruña, H. D. Methanol Oxidation at Platinum in Alkaline Media: A Study of the Effects of Hydroxide Concentration and of Mass Transport. *ChemPhysChem* **2021**, *22* (13), 1397–1406. <https://doi.org/10.1002/cphc.202100087>.
- (172) Zhu, J.; Xia, L.; Yu, R.; Lu, R.; Li, J.; He, R.; Wu, Y.; Zhang, W.; Hong, X.; Chen, W.; Zhao, Y.; Zhou, L.; Mai, L.; Wang, Z. Ultrahigh Stable Methanol Oxidation Enabled by a High Hydroxyl Concentration on Pt Clusters/MXene Interfaces. *J. Am. Chem. Soc.* **2022**, *144* (34), 15529–15538. <https://doi.org/10.1021/jacs.2c03982>.
- (173) Cheng, H.; Dong, B.; Liu, Q.; Wang, F. Direct Electrocatalytic Methanol Oxidation on MoO₃/Ni(OH)₂: Exploiting Synergetic Effect of Adjacent Mo and Ni. *J. Am. Chem. Soc.* **2023**, *145* (49), 26858–26862. <https://doi.org/10.1021/jacs.3c09399>.
- (174) Graf, M.; Haensch, M.; Carstens, J.; Wittstock, G.; Weissmüller, J. Electrocatalytic Methanol Oxidation with Nanoporous Gold: Microstructure and Selectivity. *Nanoscale* **2017**, *9* (45), 17839–17848. <https://doi.org/10.1039/c7nr05124g>.
- (175) Arán-Ais, R. M.; Yu, Y.; Hovden, R.; Solla-Gullón, J.; Herrero, E.; Feliu, J. M.; Abruña, H. D. Identical Location Transmission Electron Microscopy Imaging of Site-Selective Pt Nanocatalysts: Electrochemical Activation and Surface Disorder. *Journal of the American Chemical Society* **2015**, *137* (47), 14992–14998. <https://doi.org/10.1021/JACS.5B09553>.
- (176) Cui, C.-H.; Yu, S.-H. Engineering Interface and Surface of Noble Metal Nanoparticle Nanotubes toward Enhanced Catalytic Activity for Fuel Cell Applications. *Accounts of Chemical Research* **2013**, *46* (7), 1427–1437. <https://doi.org/10.1021/AR300254B>.
- (177) Nakaya, Y.; Furukawa, S. Catalysis of Alloys: Classification, Principles, and Design for a Variety of Materials and Reactions. *Chem. Rev.* **2023**, *123* (9), 5859–5947. <https://doi.org/10.1021/acs.chemrev.2c00356>.
- (178) Du, M.; Li, X.; Pang, H.; Xu, Q. Alloy Electrocatalysts. *EnergyChem* **2023**, *5* (2), 100083. <https://doi.org/10.1016/j.enchem.2022.100083>.
- (179) He, J.; Johnson, N. J. J.; Huang, A.; Berlinguette, C. P. Electrocatalytic Alloys for CO₂ Reduction. *ChemSusChem* **2018**, *11* (1), 48–57. <https://doi.org/10.1002/cssc.201701825>.
- (180) Chen, J.; Zhang, Y.; Zhang, Z.; Hou, D.; Bai, F.; Han, Y.; Zhang, C.; Zhang, Y.; Hu, J. Metal–Support Interactions for Heterogeneous Catalysis: Mechanisms, Characterization Techniques and Applications. *Journal of Materials Chemistry A* **2023**, *11* (16), 8540–8572. <https://doi.org/10.1039/D2TA10036C>.
- (181) Liu, L.; Corma, A. Bimetallic Sites for Catalysis: From Binuclear Metal Sites to Bimetallic Nanoclusters and Nanoparticles. *Chem. Rev.* **2023**, *123* (8), 4855–4933. <https://doi.org/10.1021/acs.chemrev.2c00733>.
- (182) Zeng, S.; Shan, S.; Lu, A.; Wang, S.; Caracciolo, D. T.; Robinson, R. J.; Shang, G.; Xue, L.; Zhao, Y.; Zhang, A.; Liu, Y.; Liu, S.; Liu, Z.; Bai, F.; Wu, J.; Wang, H.; Zhong, C.-J. Copper-Alloy Catalysts: Structural Characterization and Catalytic Synergies. *Catal. Sci. Technol.* **2021**, *11* (17), 5712–5733. <https://doi.org/10.1039/D1CY00179E>.
- (183) Shan, J.; Zhang, S.; Choksi, T.; Nguyen, L.; Bonifacio, C. S.; Li, Y.; Zhu, W.; Tang, Y.; Zhang, Y.; Yang, J. C.; Greeley, J.; Frenkel, A. I.; Tao, F. Tuning Catalytic Performance through a Single or Sequential Post-Synthesis Reaction(s) in a Gas Phase. *ACS Catal.* **2017**, *7* (1), 191–204. <https://doi.org/10.1021/acscatal.6b02054>.
- (184) Zamora Zeledón, J. A.; Stevens, M. B.; Gunasooriya, G. T. K. K.; Gallo, A.; Landers, A. T.; Kreider, M. E.; Hahn, C.; Nørskov, J. K.; Jaramillo, T. F. Tuning the Electronic Structure of Ag-Pd Alloys to Enhance Performance for Alkaline Oxygen Reduction. *Nat Commun* **2021**, *12* (1), 620. <https://doi.org/10.1038/s41467-021-20923-z>.

- (185) Chang, F.; Yu, G.; Shan, S.; Skeete, Z.; Wu, J.; Luo, J.; Ren, Y.; Petkov, V.; Zhong, C.-J. Platinum–Nickel Nanowire Catalysts with Composition-Tunable Alloying and Faceting for the Oxygen Reduction Reaction. *J. Mater. Chem. A* **2017**, *5* (24), 12557–12568. <https://doi.org/10.1039/C7TA03266H>.
- (186) Mahr, C.; Kundu, P.; Lackmann, A.; Zanaga, D.; Thiel, K.; Schowalter, M.; Schwan, M.; Bals, S.; Wittstock, A.; Rosenauer, A. Quantitative Determination of Residual Silver Distribution in Nanoporous Gold and Its Influence on Structure and Catalytic Performance. *Journal of Catalysis* **2017**, *352* (2017), 52–58. <https://doi.org/10.1016/j.jcat.2017.05.002>.
- (187) Silva Olaya, A. R.; Zandersons, B.; Wittstock, G. Effect of the Residual Silver and Adsorbed Lead Anions towards the Electrocatalytic Methanol Oxidation on Nanoporous Gold in Alkaline Media. *Electrochimica Acta* **2021**, *383*. <https://doi.org/10.1016/j.electacta.2021.138348>.
- (188) Mekazni, D. S.; Arán-Ais, R. M.; Ferre-Vilaplana, A.; Herrero, E. Why Methanol Electro-Oxidation on Platinum in Water Takes Place Only in the Presence of Adsorbed OH. *ACS Catal.* **2022**, *12* (3), 1965–1970. <https://doi.org/10.1021/acscatal.1c05122>.
- (189) Dhakar, S.; Mukhopadhyay, S.; Ottakam Thotiyl, M.; Sharma, S. Methanol Assisted Water Electrooxidation on Noble Metal Free Perovskite: RRDE Insight into the Catalyst's Behaviour. *Journal of Colloid and Interface Science* **2024**, *654*, 688–697. <https://doi.org/10.1016/j.jcis.2023.10.072>.
- (190) Chen, L.; Wang, S. Y.; Xiang, X.; Tao, W. Q. Mechanism of Surface Nanostructure Changing Wettability: A Molecular Dynamics Simulation. *Computational Materials Science* **2020**, *171*. <https://doi.org/10.1016/j.commatsci.2019.109223>.
- (191) Kwon, D.; Lee, S.; Yeom, E. Experimental Investigation on Water Repellency and Anisotropic Wettability of Microgrooved Polymer Surfaces. *Experiments in Fluids* **2019**, *60* (11), 1–12. <https://doi.org/10.1007/S00348-019-2805-3/FIGURES/14>.
- (192) Rajab, F. H.; Korshed, P.; Liu, Z.; Wang, T.; Li, L. How Did the Structural ZnO Nanowire as Antibacterial Coatings Control the Switchable Wettability. *Applied Surface Science* **2019**, *469*, 593–606. <https://doi.org/10.1016/j.apsusc.2018.10.249>.
- (193) Zhang, W.; Zhang, R. run; Jiang, C. gang; Wu, C. wei. Effect of Pillar Height on the Wettability of Micro-Textured Surface: Volume-of-Fluid Simulations. *International Journal of Adhesion and Adhesives* **2017**, *74*, 64–69. <https://doi.org/10.1016/J.IJADHADH.2016.12.011>.
- (194) Dawood, M. K.; Zheng, H.; Liew, T. H.; Leong, K. C.; Foo, Y. L.; Rajagopalan, R.; Khan, S. A.; Choi, W. K. Mimicking Both Petal and Lotus Effects on a Single Silicon Substrate by Tuning the Wettability of Nanostructured Surfaces. *Langmuir* **2011**, *27* (7), 4126–4133. <https://doi.org/10.1021/la1050783>.
- (195) Li, H.; Li, A.; Zhao, Z.; Li, M.; Song, Y. Heterogeneous Wettability Surfaces: Principle, Construction, and Applications. *Small Structures* **2020**, *1* (2), 2000028. <https://doi.org/10.1002/sstr.202000028>.
- (196) Kashyap, K. K.; Hazarika, M.; Dhayal, S. S.; Chinnamuthu, P. Synthesis of Metallic Surface Plasmon-Sensitized TiO₂ Nanowire for Wettability Application. *Journal of Materials Science: Materials in Electronics* **2022**, *33* (11), 8674–8682. <https://doi.org/10.1007/s10854-021-06770-0>.
- (197) Bai, W.; Dong, P.; Wu, X. Surface Wettability Studies on Aligned Gold Nanorod Array Substrate. In *2020 IEEE 20th International Conference on Nanotechnology (IEEE-NANO); 2020*; pp 53–56. <https://doi.org/10.1109/NANO47656.2020.9183497>.
- (198) Gruener, S.; Hofmann, T.; Wallacher, D.; Kityk, A. V.; Huber, P. Capillary Rise of Water in Hydrophilic Nanopores. *Physical Review E - Statistical, Nonlinear, and Soft Matter Physics* **2009**, *79* (6). <https://doi.org/10.1103/PhysRevE.79.067301>.

- (199) Geng, W.; Hu, A.; Li, M. Super-Hydrophilicity to Super-Hydrophobicity Transition of a Surface with Ni Micro-Nano Cones Array. *Applied Surface Science* **2012**, *263*, 821–824. <https://doi.org/10.1016/j.apsusc.2012.09.006>.
- (200) Chen, J.; Zhai, F.; Liu, M.; Hou, X.; Chou, K. C. SiC Nanowires with Tunable Hydrophobicity/Hydrophilicity and Their Application as Nanofluids. *Langmuir* **2016**, *32* (23), 5909–5916. <https://doi.org/10.1021/acs.langmuir.6b00430>.
- (201) Wang, M.; Wan, L.; Luo, J. Promoting CO₂ electroreduction on CuO Nanowires with a Hydrophobic Nafion Overlayer. *Nanoscale* **2021**, *13* (6), 3588–3593. <https://doi.org/10.1039/d0nr08369k>.
- (202) Liu, M.; Wang, S.; Jiang, L. Nature-Inspired Superwettability Systems. *Nature Reviews Materials* **2017**, *2* (7), 1–17. <https://doi.org/10.1038/natrevmats.2017.36>.
- (203) Iwata, R.; Zhang, L.; Wilke, K. L.; Gong, S.; He, M.; Gallant, B. M.; Wang, E. N. Bubble Growth and Departure Modes on Wettable/Non-Wettable Porous Foams in Alkaline Water Splitting. *Joule* **2021**, *5* (4), 887–900. <https://doi.org/10.1016/J.JOULE.2021.02.015>.
- (204) Li, J.; Ha, N. S.; Liu, T. ‘Leo’; van Dam, R. M.; ‘CJ’ Kim, C. J. Ionic-Surfactant-Mediated Electro-Dewetting for Digital Microfluidics. *Nature* **2019**, *572* (7770), 507–510. <https://doi.org/10.1038/s41586-019-1491-x>.
- (205) Balasubramanian, K. Challenges in the Use of 1D Nanostructures for On-Chip Biosensing and Diagnostics: A Review. *Biosensors and Bioelectronics* **2010**, *26* (4), 1195–1204. <https://doi.org/10.1016/j.bios.2010.07.041>.
- (206) Erb, R. A. *The Wettability of Gold*.
- (207) Bico, J.; Tordeux, C.; Quéré, D. Rough Wetting. *Europhysics Letters* **2001**, *55* (2), 214. <https://doi.org/10.1209/EPL/I2001-00402-X>.
- (208) Gambaryan-Roisman, T. Liquids on Porous Layers: Wetting, Imbibition and Transport Processes. *Current Opinion in Colloid & Interface Science* **2014**, *19* (4), 320–335. <https://doi.org/10.1016/J.COCIS.2014.09.001>.
- (209) Bormashenko, E. Wetting Transitions on Biomimetic Surfaces. *Philosophical Transactions of the Royal Society A: Mathematical, Physical and Engineering Sciences* **2010**, *368* (1929), 4695–4711. <https://doi.org/10.1098/RSTA.2010.0121>.
- (210) Bormashenko, E. Y. Wetting of Real Surfaces. *Wetting of Real Surfaces* **2013**, 1–170. <https://doi.org/10.1515/9783110583144/EPUB>.
- (211) Almonte, L.; Pimentel, C.; Rodríguez-Cañas, E.; Abad, J.; Fernández, V.; Colchero, J. Rose Petal Effect: A Subtle Combination of Nano-scale Roughness and Chemical Variability. *Nano Select* **2022**, *3* (5), 977–989. <https://doi.org/10.1002/nano.202100193>.
- (212) Gao, L.; McCarthy, T. J. The “Lotus Effect” Explained: Two Reasons Why Two Length Scales of Topography Are Important. *Langmuir* **2006**, *22* (7), 2966–2967. <https://doi.org/10.1021/LA0532149>.
- (213) Yang, S.; Du, J.; Cao, M.; Yao, X.; Ju, J.; Jin, X.; Su, B.; Liu, K.; Jiang, L. Direct Insight into the Three-Dimensional Internal Morphology of Solid–Liquid–Vapor Interfaces at Microscale. *Angewandte Chemie* **2015**, *127* (16), 4874–4877. <https://doi.org/10.1002/ange.201411023>.
- (214) Quéré, D. Wetting and Roughness. *Annual Review of Materials Research* **2008**, *38* (Volume 38, 2008), 71–99. <https://doi.org/10.1146/ANNUREV.MATSCI.38.060407.132434/CITE/REFWORKS>.
- (215) Cho, S. K.; Moon, H.; Kim, C. J. Creating, Transporting, Cutting, and Merging Liquid Droplets by Electrowetting-Based Actuation for Digital Microfluidic Circuits. *Journal of Microelectromechanical Systems* **2003**, *12* (1), 70–80. <https://doi.org/10.1109/JMEMS.2002.807467>.

- (216) Schubert, I.; Huck, C.; Kröber, P.; Neubrech, F.; Pucci, A.; Toimil-Molares, M. E.; Trautmann, C.; Vogt, J. Porous Gold Nanowires: Plasmonic Response and Surface-Enhanced Infrared Absorption. *Advanced Optical Materials* **2016**, *4* (11), 1838–1845. <https://doi.org/10.1002/adom.201600430>.
- (217) Hong, S.; Lee, J.; Do, K.; Lee, M.; Kim, J. H.; Lee, S.; Kim, D. H. Stretchable Electrode Based on Laterally Combed Carbon Nanotubes for Wearable Energy Harvesting and Storage Devices. *Advanced Functional Materials* **2017**, *27* (48). <https://doi.org/10.1002/adfm.201704353>.
- (218) Briot, N. J.; Kosmidou, M.; Dingreville, R.; Hattar, K.; Balk, T. J. In Situ TEM Investigation of Self-Ion Irradiation of Nanoporous Gold. *Journal of Materials Science* **2019**, *54* (9), 7271–7287. <https://doi.org/10.1007/S10853-019-03385-Z/FIGURES/13>.

List of Figures

Figure 2.1 Four times irradiation of the PC membrane ⁶¹	6
Figure 2.2 Schematic drawing of the pore etching cross-section view ¹⁷	7
Figure 2.3 Schematic representation of the electroplating process ⁷⁵	8
Figure 2.4 Schematic representation of a two-electrode setup for electrodeposition of a Au layer on the sputtered gold of the membrane ⁶⁰	10
Figure 2.5 Schematic representation of a three-electrode setup consisting of working, counter, and reference electrodes, connected to a potentiostat ⁶⁰	10
Figure 2.6 CV recorded using a PC template with nanochannel density $d=4 \times 1 \times 10^8 \text{ cm}^{-2}$, and pore diameter 150 nm with a Au back-electrode, in 50 mM KAu(CN) ₂ electrolyte with 1% Doxfax 2A1, at temperature 60 °C.	11
Figure 2.7 Schematic drawing of the deposition process of nanowire networks. ⁸⁰	12
Figure 2.8 Representative I-t curve of NWNW deposition process.	12
Figure 2.9 Working model for porosity evolution in dealloying in the Ag-Au alloy system (Ag, gray; Au, orange). (a) The rate-limiting step is the formation of terrace vacancies, which then grow into lateral vacancy clusters. (b) As dissolution proceeds layer by layer, surface diffusion passivates low-coordination sites with Au, leading to surface roughening. (c, d) As dealloying continues, there is insufficient Au to totally passivate the increasing surface area, leading to undercutting and bifurcation of ligaments. (e) The result of this process is a bicontinuous porous structure in which ligaments have Au-rich surfaces and Ag-rich interiors. (f) As coarsening increases the length scale of the initial structure, residual Ag atoms are exposed and dissolved, leaving a final structure with much reduced Ag content ⁸⁵	14
Figure 2.10 Schematic representation of SEM structure ⁹⁰	16
Figure 2.11 Interaction between the electron beam and sample ⁹⁰	17
Figure 2.12 EDX spectra from a SrBi ₂ Ta ₂ O ₉ nanotube ⁹¹	17
Figure 2.13 Schematic representation of transmission electron microscope ⁹³	18
Figure 2.14 Transmitted and diffracted electrons for (a) bright-field and (b) dark-field images in transmission electron microscope ⁹³	18
Figure 2.15 Diagram and main components of an XPS system ⁹⁴	19
Figure 2.16 Example of a CV curve measurement ¹⁰¹	20
Figure 2.17 The Redoxme BMM EC 15 mL Cell assembly construction.	20
Figure 2.18 Schematic representation of the electrical double-layer using the (a) Helmholtz description, (b) Gouy-Chapman description, and (c) Stern description. IHP stands for the inner Helmholtz plane while OHP refers to the outer Helmholtz plane. ¹⁰⁷	21
Figure 2.19 Cyclic voltammograms (a) recorded for a glassy carbon electrode in argon-purged 0.1 M NaOH aqueous solution in a wide scan range, (b) with different scan rates within the selected measuring window, (c) anodic and cathodic current as a function of scan rate, dot lines correspond to corresponding linear regression fits. The resulting capacitance values are shown with the colors corresponding to their respective data set ¹¹¹	22

Figure 2.20 CV recorded in 0.1 M H ₂ SO ₄ for a 1 cm ² flat Au reference sample ⁵² .	23
Figure 2.21 Schematic figure of a methanol fuel cell ¹²⁰ .	24
Figure 2.22 Schematic of a droplet on a tilted surface showing advancing (θ_{adv}) and receding (θ_{rec}) contact angle (CA). The difference between these angles is the CA hysteresis ¹²⁸ .	26
Figure 2.23 Photo of the Optical Tensiometer Theta Lite.	27
Figure 3.1 (a) Current-vs.-time ($I-t$) curves recorded for various applied potentials during the potentiostatic deposition of Au NWNWs, and the corresponding SEM images, (b) $U = -1.1$ V, (c) $U = -1.0$ V, (d) $U = -0.9$ V, (e) $U = -0.8$ V, (f) $U = -0.7$ V vs. Ag/AgCl. The large magnification SEM images reveal cylindrical monodispersed nanowires.	30
Figure 3.2 SEM images of cross-sections of Au NWNW deposited at (a) $U = -1.1$ V, (b) $U = -1.0$ V (c) $U = -0.9$ V vs. Ag/AgCl. The orange arrows indicate some branches of nanowires grow higher than average, and the inhomogeneity decrease, from a to c, as the deposition potential is less negative.	31
Figure 3.3 EDX spectrum of a Au NWNW deposited at $U = -0.9$ V vs. Ag/AgCl.	31
Figure 3.4 TEM dark-field images of fragments of Au nanowire networks deposited at (a-c) $U = -1.0$ V, (d-f) $U = -0.9$ V, which are high-angle annular dark-field imaging, and (g-i) $U = -0.8$ V vs. Ag/AgCl, are medium-angle annular dark-field imaging. The red lines mark the positions where grain boundaries (GB) were observed.	32
Figure 3.5 SEM images of Au NWNWs with different nanowire diameters, density of 2×10^9 cm ⁻² .	33
Figure 3.6 Cyclic voltammograms for electrolytes containing 50 mM KAu(CN) ₂ / 50 mM KAg(CN) ₂ with 250 mM Na ₂ CO ₃ at 60 °C.	34
Figure 3.7 SEM image and EDX spectrum of Au _{1-x} Ag _x NWNWs deposited at (a) $U = -1.1$ V, (b) $U = -1.0$ V, (c) $U = -0.9$ V, (d) $U = -0.8$ V vs. Ag/AgCl, using electrolyte 50 mM Au + 5 mM Ag.	35
Figure 3.8 Nanowire composition as a function of Ag concentration in the electrolytes at two different deposition potentials. $U = -0.8$ V (brown triangle dot), and $U = -1.1$ V (blue round dot), the error bar comes from the five EDX measurements, and the dashed line is the linear fitting of the data points.	37
Figure 3.9 EDX mapping of a selected area of a representative NWNW, showing the atomic distribution of Au (yellow), Ag (pink), and C (blue).	37
Figure 3.10 EDX spectrums of different composition Au _{1-x} Ag _x NWNWs.	38
Figure 3.11 XPS spectrum survey of five Au _{1-x} Ag _x NWNWs with different compositions.	39
Figure 3.12 XPS spectrum of Au _{1-x} Ag _x NWNWs at Au 4f (left) and Ag 3d (right) peak positions.	40
Figure 3.13 TEM line scan of four single nanowires atomic composition distributions, green lines represent the atomic composition of Au, and the red lines represent the atomic composition of Ag, the black box represents the measurement on the nanowire.	41
Figure 3.14 SEM images of Au _{1-x} Ag _x alloy nanowire dealloying process, with three different composition precursor alloy.	43
Figure 3.15 Nanowire composition change with dealloying time.	44
Figure 3.16 SEM images of 150 nm diameter nanowire dealloying process of nanowire morphology evolution with time (from left to right) of two different composition precursor alloy.	45

Figure 3.17 SEM images of 100 nm diameter nanowire dealloying process of nanowire morphology evolution with time (from left to right) of two different composition precursor alloy.....	45
Figure 3.18 SEM images of 60 nm diameter nanowire dealloying process of nanowire morphology evolution with time (from left to right) of two different composition precursor alloy.....	46
Figure 3.19 Nanowire composition change with dealloying time.....	47
Figure 3.20 Overall XPS survey spectra of precursor Au _{0.3} Ag _{0.7} NWNW sample (black), after dealloy 1 hour (red), and after dealloy 6 hours (blue) in concentrated nitric acid.	48
Figure 3.21 XPS spectra of (a)Ag 3d, and (b) Au 4f peaks of sample Au _{0.3} Ag _{0.7} NWNW (green), after dealloying for 1 hour (purple), and after dealloying 6 hours (orange), all normalized by peak intensity.	49
Figure 3.22 TEM images of nanoporous Au nanowires after dealloying for 1 hour.....	50
Figure 3.23 TEM images of nanoporous Au nanowires after dealloying for 6 hours.	51
Figure 3.24 Diffractogram of dealloyed nanowires: (a) dealloyed for 1 hour, (b) dealloyed for 6 hours.	51
Figure 4.1 SEM image of Au NWNWS with the same density ($4 \times 10^8 \text{ cm}^{-2}$), and different diameters (a) 80 nm, (b) 130 nm, and (c) 170 nm.	54
Figure 4.2 Nanowire diameter distribution charts of Au NWNWs.	54
Figure 4.3 CVs recorded in 0.1 M H ₂ SO ₄ for Au NWNWs of different nanowire diameters: (a) 80 nm, (b) 130 nm, and (c) 170 nm (room temperature, scan rate = 100 mV s ⁻¹). The red dashed line defines the baseline for the reduction peak integration, the yellow area represents the Au oxide reduction peak region providing the electrochemically active surface area. (d) Experimental (ECSA) and calculated (S _{GEO}) surface area values of the Au NWNWs as a function of nanowire diameter. ...	55
Figure 4.4 Cyclic voltammogram of the Ag NWNW in 0.1 M KOH solution at a scan rate of 50 mV/s.	56
Figure 4.5 Cyclic voltammograms (a) recorded for a Au NWNW in argon-purged 0.1 M KOH solution in a wide scan range, (b) with different scan rates within the selected measuring window, anodic and cathodic current difference as function of scan rate, of the low-density (c) and high-density (d) series, dash lines correspond to corresponding linear fits.	57
Figure 4.6 SEM images of (a) Au _{0.3} Ag _{0.7} NWNW before dealloying, (b) dealloyed for 1 h, (c) dealloyed for 6 h, (d) Au _{0.2} Ag _{0.8} NWNW before dealloying, (e) dealloyed for 30 min.....	59
Figure 4.7 Cyclic voltammograms of dealloyed NWNWs, (a) Au _{0.3} Ag _{0.7} NWNW dealloyed 1 h, (b) Au _{0.3} Ag _{0.7} NWNW dealloyed 6 h, (c) Au _{0.2} Ag _{0.8} NWNW dealloyed 30 min, and (d) anodic and cathodic current difference as a function of scan rate of three samples, dash lines correspond to corresponding linear fits.	60
Figure 4.8 CV of Au thin film reference sample in (a) 0.1 M H ₂ SO ₄ , and (b) in 0.1 M/ 1 M KOH solutions.....	62
Figure 4.9 (a) CVs of the planar Au film reference sample in the non-faradic region for DLC measurements with different scan rates, the starting and end points of each cycle were joined by a vertical line, (b) plot of current difference vs. scan rate.	62
Figure 4.10 CV of Au NWNW samples in (a) 0.1 M H ₂ SO ₄ , and (b) in 0.1 M KOH solutions.	63

Figure 4.11 (a) CVs of Au NWNW in the non-faradic region for DLC measurements with different scan rates, (b) plot of current difference vs. scan rate.	64
Figure.12 CVs of DLC measurements of a Au NWNW sample, with three different conditions: (a) narrow scan window, (b) wide scan window, (c) wide scan window with IR compensation.	66
Figure 4.13 (a) CVs of $4 \times 10^8 \text{ cm}^{-2}$ density Au NWNW recorded in 0.1 M KOH with 0/1/2/3 M MeOH with scan rate 50 mV s^{-1} , (b) anodic peak current density and onset potential as a function of the methanol concentration.	69
Figure 4.14 CVs of Au NWNW with nanowire diameter of 150 nm, and density of $2 \times 10^9 \text{ cm}^{-2}$ recorded in (a) 0.1 M KOH, (b) 0.5 M KOH, and (c) 1 M KOH electrolyte, with 0 M (black dash line), 0.5 M (red solid line), 1 M (blue solid line), and 2 M (green solid line) MeOH with scan rate 50 mV s^{-1}	70
Figure 4.15 (a) anodic peak current density, and (b) peak potential as a function of the methanol concentration from Figure 4.14, with three different KOH electrolyte concentration: 0.1 M (red), 0.5 M (blue), and 1 M (green).	71
Figure 4.16 CVs recorded in 0.1 M KOH (black dash line) and in 0.1 M KOH + 0.5 M MeOH electrolyte. The graphs display the 10th cycle (blue solid line), and the 200th cycle (orange dash-dot line) for (a) 80 nm, (b) 130 nm, and (c) 170 nm diameter nanowires. (d) Methanol electro-oxidation peak current density divided by nominal area (blue) and ECSA (shadowed green) for this three Au NWNWs. The orange dash line represents the methanol oxidation peak current density of the smooth Au thin film reference sample.	72
Figure 4.17 SEM images of Au NWNW deposited at $U = -0.9 \text{ V}$ vs. Ag/AgCl with different nanowire diameters, (a) and (d) 80 nm, (b) and (e) 130 nm, (c) and (f) 170 nm, before (a–c) and after (d–f) 200 CV cycles during methanol oxidation reaction measurements.	73
Figure 4.18 SEM images of $\text{Au}_{1-x}\text{Ag}_x$ NWNWs with density of $4 \times 10^8 \text{ cm}^{-2}$, nanowire diameter of 150 nm, and different atomic compositions.	74
Figure 4.19 CVs recorded for (a) $\text{Au}_{0.9}\text{Ag}_{0.1}$, (b) $\text{Au}_{0.8}\text{Ag}_{0.2}$, (c) $\text{Au}_{0.5}\text{Ag}_{0.5}$, (d) $\text{Au}_{0.3}\text{Ag}_{0.7}$, (e) $\text{Au}_{0.2}\text{Ag}_{0.8}$, (f) Au_0Ag_1 NWNWs, in 0.1 M KOH electrolyte with different concentration of methanol, scan rate = 50 mV/s , at room temperature.	76
Figure 4.20 CVs of “as-prepared” NPG (curve in black) and NPG “after cycling in H_2SO_4 ”(curve in blue) in 1 M MeOH + 0.25 M KOH^{187}	77
Figure 4.21 CVs recorded for $\text{Au}_{0.9}\text{Ag}_{0.1}$ NWNW in (a) 0.1 M, (b) 0.5 M, (c) 1 M KOH with different concentration methanol, and $\text{Au}_{0.8}\text{Ag}_{0.2}$ NWNW in (d) 0.1 M, (e) 0.5 M, (f) 1 M KOH with different concentration methanol.	78
Figure 4.22 CVs recorded for (a) $\text{Au}_{0.6}\text{Ag}_{0.4}$, (b) $\text{Au}_{0.4}\text{Ag}_{0.6}$, (c) $\text{Au}_{0.3}\text{Ag}_{0.7}$, (d) $\text{Au}_{0.2}\text{Ag}_{0.8}$ NWNWs in 1 M KOH with different concentration of methanol.	79
Figure 4.23 SEM pictures of $\text{Au}_{1-x}\text{Ag}_x$ NWNWS with different compositions after catalyzing the methanol oxidation reaction.	80
Figure 4.24 EDX mapping and line scan of a $\text{Au}_{0.3}\text{Ag}_{0.7}$ NWNW sample, SEM image (left) with the arrow represents the line scan, elemental mapping (middle) of Au (green) and Ag (blue), and quantitative line scan (right).	81
Figure 4.25 SEM image of $\text{Au}_{0.3}\text{Ag}_{0.7}$ NWNWs dealloyed for (a) 1 h and (b) 6 h.	82

Figure 4.26 CVs recorded for Au _{0.3} Ag _{0.7} NWNW dealloyed for 1 h, tested in (a) 0.1 M KOH, (b) 0.5 M KOH, (c) 1 M KOH with different concentration of methanol.	82
Figure 4.27 CVs recorded for Au _{0.3} Ag _{0.7} NWNW dealloyed for 6 h, tested in (a) 0.1 M KOH, (b) 0.5 M KOH, (c) 1 M KOH with different concentration of methanol.	83
Figure 4.28 CVs recorded for porous Au NWNWs fabricated by dealloying Au _{0.3} Ag _{0.7} NWNWs for (a) 1 h, and (b) 6 h. The CVs were measured in 1 M KOH solution with addition of 3 M MeOH. ...	84
Figure 4.29 DLC measurements of two porous Au NWNW samples before and after the long-term CV tests.	84
Figure 4.30 SEM images of the nanoporous NWNWS after the long-term CV tests.	85
Figure 5.1 Schematics of water droplets sitting on top of the 3D Au NWNW structure with the surface wetting states transition from low contact angle, hydrophilic (left) to high contact angle, hydrophobic (right), as the structural porosity increases ⁵⁹	87
Figure 5.2 Representative SEM images of (a, b) one low-density Au NWNW with 100 nm wire diameter and 95% porosity, and (c, d) one high-density Au NWNW with 200 nm wire diameter and 28% porosity. (a)/(c) and (b)/(d) display top- and side views, respectively.	88
Figure 5.3 (a) Contact angle measured for low-density NWNWs with tailored nanowire diameter between 60 and 210 nm, and porosity ranging between 98% and 86%, respectively. SEM images show selected networks with nanowire diameter (b) 60 nm, (c) 100 nm, (d) 160 nm, (e) 210 nm, the scale bar is 200 nm. The insets show the sessile drop on the corresponding sample surface. The error bars are given by the standard deviation of five contact angle measurements on various positions of the same sample.	89
Figure 5.4 (a) Contact angle measured for high-density Au NWNWs with tailored nanowire diameter between 40 and 200 nm, and porosity ranging between 96% and 28%, respectively. SEM images show selected networks with nanowire diameter (b) Ø 40 nm, (c) Ø 60 nm, (d) Ø 110 nm, (e) Ø 180 nm, the scale bar is 200 nm. The insets show the sessile drop on the corresponding sample surface. The error bars are given by the standard deviation of five contact angle measurements on various positions of the same sample.	90
Figure 5.5 SEM images of (a) Au sputtered silicon wafer, and (b) Au substrate layer with insets of sessile drop for contact angle measurement.	90
Figure 5.6 Measured contact angle values versus the NWNW porosity visualizing the influence of the network porosity on wetting state transition. The corresponding values estimated with the models of Cassie-Baxter (solid blue line) and Cassie-Baxter impregnating (dash green line) are also shown.	92
Figure 5.7 Photos of a 5 µL droplet on top of a hydrophobic nanowire network sample by Keyence optical microscope, scale bar is 1 mm. Nanowire diameter 104 nm, density 2.3*10 ⁸ cm ⁻² , with porosity of 97%.	93
Figure 5.8 Photos of the sessile drop contact angle measurement by the high-speed camera on the Biolin Scientific Theta-lite tensiometer. On a hydrophilic NWNW sample, with nanowire diameter 106 nm, density 1.3*10 ⁹ cm ⁻² , and porosity of 80%.	93
Figure 5.9 Photos of a 5 µL droplet on top of a hydrophilic nanowire network sample by Keyence optical microscope, a wetted ring around the droplet can be observed, scale bar is 1 mm. Nanowire diameter 120 nm, density 1.3*10 ⁹ cm ⁻² , with porosity of 74%.	94

Figure 5.10 (a) 4 μL and (b) 15 μL water droplet sitting on Au NWNW surface with different tilting angles, (c) plots of two volume water droplets advancing (green) and receding (purple) contact angles as a function of stage tilting angle, (d) optical image of a rose with multiple droplets attached on the petals, (e, f) images of a 4 μL water droplet on one rose petal surface (e) horizontal position, and (f) tilted 90° with advancing (green) and receding (purple) angles..... 95

List of Tables

Table 2.1 Au _{1-x} Ag _x alloy nanowire network deposition conditions	13
Table 3.1 Au _{1-x} Ag _x NWNWs electrodeposition conditions and the corresponding nanowire composition	36
Table 3.2 Comparison of the atomic composition values determined for Au _{1-x} Ag _x NWNWs by XPS and EDX.....	41
Table 3.3 Pristine and dealloyed NWNWs composition analysis by XPS and EDX.....	49
Table 4.1 Double-layer capacitance and the corresponding ECSA of Au _{1-x} Ag _x NWNWs.....	58
Table 4.2. Measured DLC and ECSA values of pristine and dealloyed NWNWs.....	60
Table 4.3 ECSA measurement comparison from two methods.....	65
Table 4.4 DLC values obtained from CVs in Figure.12.....	66
Table 4.5 Dealloyed nanoporous NWNWs composition change before and after the long-term CV test	85

Abbreviations

3D	three-dimensional
Ag	silver
Au	gold
CA	contact angle
Cu	copper
CV	cyclic voltammogram
DCM	dichloromethane
DI	deionized
DLC	double-layer capacitance
ECSA	electrochemically active surface area
EDX	energy dispersive x-ray spectroscopy
HRSEM	high resolution scanning electron microscopy
NPG	nanoporous gold
NWNW	nanowire network
PC	polycarbonate
PET	polyethylene terephthalate
SEM	scanning electron microscopy
S _{GEO}	theoretically calculated geometrical surface area
TEM	transmission electron microscopy
UV	ultraviolet
XPS	x-ray photoelectron spectroscopy
XRD	x-ray diffraction

Acknowledgements

It has been a long and interesting journey since I have decided to pursue a PhD degree, and finally this journey has come to an end.

I hope many years later, when I read this acknowledgment again, I can still remember all the fun I have had, during exploring the unknown science, thinking about the problems and difficulties I have encountered and solved. The excitements when I have discovered a new phenomenon, and the thrills when I have finally figured out the truths hidden behind.

It has been a real fortunate for me, that in the best years of my life, I can work freely in a scientific field that I am truly interested in, and develop my own research in multiple directions, and being supported by so many supervisors, mentors, colleagues, friends, and family members. To whoever is reading this, natural science is really lively and fun, being able to work towards the unknown of human kind, and getting paid to do it, is a real privilege, if you have the chance to do it, don't hesitate.

First, I would like to thank my PhD supervisor, Dr. Maria Eugenia Toimil-Molares, if not for her continuous support and guidance, I could not have accomplished so much. She has been very supportive for my always-appearing new ideas, she can help me organize my chaotic thoughts, and clear the way towards the goal, and help me find collaboration partners to upgrade my research. She always encourages me to participate in many conferences and workshops, so I can communicate with many scientists, and gain deeper understandings of what is good science and what is good research.

Second, I would like to thank my PhD supervisor, Dr. Christina Trautmann, she has helped me so much at the beginning of my PhD, she has introduced me into the fun but challenging fields of nuclear physics and radiation physics. This was not part of the initial plan for my PhD, but I do find it very interesting, I am now able to understand the challenging problems and open questions in the field, the values of fundamental science, and learn the way of how physicists think and study.

I would like to thank Dr. Jan Philipp Hofmann for being the second referee of my thesis, with his expertise in materials science, surface science, and electrochemistry. Thanks for reading and grading my thesis, and thanks for all the XPS analysis conducted by your group members, Dr Harol Anibal Moreno-Fernandez and Dr. Jona Schuch.

I would like to thank Dr. Robert Stark and Dr. Eva Maria Pellicer-Vila, for joining my PhD examination committee, and examining my results.

I would like to thank Dr. Bernhard Kaiser, for his expert advice in the electrochemistry part of my thesis.

I would like to thank Dr. Wilfried Sigle, Dr. Peter Kopold, and Dr. Peter van Aken, for conducting the TEM analysis for my samples, allowing me to gain more insights in my materials.

I would like to acknowledge the financial support by the HGS-HIRe for FAIR graduate school, and for the various helpful workshops and soft skill courses they provided.

I would like to thank my colleagues Dr. Kay Obbe Voss, Mr. Elko Schubert, and Mr. Arne Siegmund, for their continuous help in solving experimental problems. A special thanks give to Elko, thanks for helping me design and construct many different electrochemical cells, and many other experimental setups, that allowed me to always improve my experiments. Also thank Sabine Seubert for helping me with the complicated administration problems.

I would like to thank my office mates, Dr. Nils Ulrich and Dr. Pascal Simon, for the nice atmosphere, and helpful discussions.

Acknowledgements

I would like to thank my colleagues from the MAT group, for discussing my questions, helping me solve problems, and the good working environment: Dr. Ina Schubert, Dr. Michael Florian Peter Wagner, Dr. Frieder Koch, Dr. Daniel Severin, Dr. Vanina Cayón, Dr. Dila Kaya, Dr. Luo Jia, Dr. Ioannis Tzifas, Christopher Schröck, Leon Kirsch, Dr. Verena Velthaus, Dr. Philipp Bolz, Pui Lap Jacob Lee, Michelle Schäfer, Daniel Zellner, Sinan Orkunt, Isabel Armstrong-Cowell.

I would like to thank my friends for the companion and pleasure in my free time (sequencing does not matter):

Liu Dongyao	Chen Mingyu	Wang Sijia	Guo Jia	Zhu Tingting
Dr. Yu Xiao	Dr. Zhao Jianwei	Sun Tianchen	Zhou Pei	Dr Zhang Xiao
Dr. Fang Likun	Shi Ruirui	Dr. Yu Jiajun	Tian Yi	Dr Sheng Yinxiangzi
Wang Zicheng	Li Xiawen	Xu Chen	Zheng Lanlan	Dr. Ge Zhuang
Zhao He	Philip Hirschle	Dr. Anahid Amiri	Guo Yaqian	Dr. Russel Wilson
Iuliia Romanenko	Miguel Hevia	Yang Jiangyan	Ran Yunjia	Dr. Yang yangyiwei
Zhang Yuqing	Chen Jiale	Luo Liyi	Li Yuanyuan	Niloofar Hoseinpour

Finally, I would like to thank my family, my grandparents, and our dog Berdi, especially my mom and dad, for their love, support, encouragement, and confidence in me.

Last but not least, I would like to thank myself for all the efforts, time, energy, struggling, and enduring that I have put in this thesis and work. Good job Mohan!

Curriculum Vitae

Mohan Li

李默涵

Education

01.2021- 08.2025	Materials Science, Dr. rer. nat. Technische Universität Darmstadt, Germany GSI Helmholtz Center for heavy ion research, Germany.
10.2017- 08.2020	Materials Science, M.Sc. Technische Universität Darmstadt, Germany.
08.2014- 06.2017	Materials Science and Engineering, B.Sc. Northeastern University, China.
02.2016- 07.2016	Materials Science and Engineering, Exchange program University of Queensland, Australia.

Research Expertise

- **Electrodeposition of various metal and alloys**
Including Fe, Co, Ni, Cu, Pd, Ag, Sb, Pt, Au, Bi, both surface coating and nanostructures
- **Heavy ion irradiation of various materials**
Ion penetration depth calculation, high dose and single-ion irradiation, including metal, alloy, semi-metal, plastic
- **Materials Analysis Techniques**
SEM, EDX, XRD, TEM, XPS, Raman Spectroscopy, Optical Microscopy, Mechanical Test, Nanoindentation, Surface Wettability Test, Electrochemistry Test
- **Fuel cell catalysis test**
Half-cell test in controlled conditions, long-term stress test, with failures detection and optimization

Work Experience

01.2021- 2025	Scientific Researcher Development and Characterization of 3D Au_{1-x}Ag_x Nanowire Networks by Ion-Track Nanotechnology as Catalysis Department of Materials Research, GSI Helmholtz Center for Heavy Ion Research, Darmstadt, Germany
------------------	--

	Department of Materials and Earth Sciences, Technische Universität Darmstadt, Germany
01.2020-08.2020	Master thesis Electrodeposition of Au/Au-Ag Nanowire Networks GSI Helmholtz Center for Heavy Ion Research, Darmstadt, Germany Department of Materials and Earth Sciences, Technische Universität Darmstadt, Germany
03.2019-02.2020	Industrial Internship and working student Mechanical tests and SEM analysis of Klett welding and Klettsintering techniques Nanowired GmbH, Griesheim, Germany
Award	
<ul style="list-style-type: none">• Electrochemistry Society 244th Meeting Travel Grant, 2023• Giersch Excellence Award, 2022• Helmholtz Best Scientific Image Contest Annual Award, 2021	

List of Publications

Parts of the results of this thesis were already published in the following publications:

1. **Li, Mohan**, Henning Bonart, Daniel Zellner, and Maria Eugenia Toimil-Molares. "3D Gold Nanowire Networks with Tailorable Surface Wetting State: From Rose-Petal Effect to Super-Hydrophilicity." *Small* (2025): 2411971.
2. **Li, Mohan**, Nils Ulrich, Ina Schubert, Wilfried Sigle, Michael Florian Peter Wagner, Christina Trautmann, and Maria Eugenia Toimil-Molares. "Three-dimensional free-standing gold nanowire networks as a platform for catalytic applications." *RSC advances* 13, no. 7 (2023): 4721-4728.
3. Fernández, Harol Moreno, Julia Gallenberger, Crizaldo Mempin Jr, Isobel Khalek, Marie Neumann, Soroush Lotfi, Sun Myung Kim, **Mohan Li**, Chuanmu Tian, and Jan P. Hofmann. "Phase transitions in NiO during the oxygen evolution reaction assessed via electrochromic phenomena through operando UV–Vis spectroscopy." *Electrochimica Acta* 498 (2024): 144626.
4. Gallenberger, Julia, Harol Moreno Fernández, Achim Alkemper, **Mohan Li**, Chuanmu Tian, Bernhard Kaiser, and Jan Philipp Hofmann. "Stability and decomposition pathways of the NiOOH OER active phase of NiO x electrocatalysts at open circuit potential traced by ex situ and in situ spectroscopies." *Catalysis Science & Technology* 13, no. 16 (2023): 4693-4700.

Academic Conferences Contributions

Talk Presentations:

12.2024	12th international symposium on swift heavy ions in matter, SHIM 2024 Canberra, Australia
05.2024	From Matter to Materials and Life, MML RT2 workshop: catalysis Hamburg, Germany
10.2023	244 th Electrochemistry Society Meeting, ECS 2023 Gothenburg, Sweden
09.2023	17 th European Congress and Exhibition on Advanced Materials and Processing, FEMS EUROMAT 2023 Frankfurt, Germany
04. 2023	From Matter to Materials and Life, MML Workshop- Materials Research Jülich, Germany
10.2022	242 nd Electrochemistry Society Meeting, ECS 2022 Atlanta, USA
06.2022	14 th International Workshop on Electrodeposited Nanostructures, EDNANO 2022 Krakow, Poland.
10.2021	240 th Electrochemistry Society Meeting, ECS 2021 Online
03.2021	German Ion Beam Workshop 2021 Online

Poster Presentations:

05.2025	16th International Workshop on Electrodeposited Nanostructures, EDNANO 2025 Florence, Italy.
09.2022	German Conference for Research with Synchrotron Radiation, Neutrons and Ion Beams at Large Facilities, SNI 2022 Berlin, Germany
06.2022	11th international symposium on swift heavy ions in matter, SHIM 2022 Helsinki, Finland
11.2021	From Matter to Materials and Life, MML Workshop2021 Online

